R-06-99

Groundwater flow and transport modelling during the temperate period for the SR-Can assessment

Laxemar subarea – version 1.2

Lee Hartley, Andrew Hoch, Peter Jackson,
Steve Joyce, Rachel McCarthy, Ben Swift
Serco Assurance

Björn Gylling and Niko Marsic
Kemakta Konsult AB

December 2006

Svensk Kärnbränslehantering AB
Swedish Nuclear Fuel
and Waste Management Co
Box 5864
SE-102 40 Stockholm Sweden
Tel 08-459 84 00
+46 8 459 84 00
Fax 08-661 57 19
+46 8 661 57 19

ISSN 1402-3091
SKB Rapport R-06-99

Groundwater flow and transport modelling during the temperate period for the SR-Can assessment

Laxemar subarea – version 1.2

Lee Hartley, Andrew Hoch, Peter Jackson,
Steve Joyce, Rachel McCarthy, Ben Swift
Serco Assurance

Björn Gylling and Niko Marsic
Kemakta Konsult AB

December 2006

Executive summary

Nuclear waste in Sweden is handled by Svensk Kärnbränslehantering AB (SKB), the Swedish Nuclear Fuel and Waste Management Company. Within SKB's programme for spent nuclear fuel management, an interim storage facility and a transportation system are already in operation. SKB's concept for the final stage of the nuclear fuel cycle, based on several decades of research and development, is to place spent fuel inside a cast iron insert inside copper canisters. These are then deposited in a repository, about 500 m deep in saturated, granitic rock, with the canisters surrounded by bentonite clay. This method is referred to as the KBS-3 concept.

Two principal remaining tasks in SKB's programme are to locate, build and operate i) the deep repository and ii) an encapsulation plant in which the spent fuel will be emplaced in canisters to be deposited in the deep repository.

SKB is currently carrying out site investigations for a deep repository in the municipalities of Östhammar and Oskarshamn. The investigations will be conducted in two stages; an initial site investigation (ISI) phase followed, if the expected site suitability is confirmed, by a complete site investigation (CSI) phase. The aim is to build a deep repository at one of these candidate sites, provided that the bedrock and other relevant conditions are found to be suitable. An application to build a deep repository will be made at the end of 2009 according to the current timetable.

The favoured alternative for the location of the encapsulation plant is at Oskarshamn, where it would operate in conjunction with the existing interim storage facility. An application to build an encapsulation plant will be made in 2006.

The final planning application requires a report on the long-term safety of the deep repository, referred to as SR-Site, which will be based on data from the completed site investigations. This is an obvious requirement for the application to build the repository. SR-Can is a preparatory stage for the SR-Site report. The main[1] purposes are to obtain a first assessment of long-term safety of a repository at the Forsmark and Laxemar sites, based on data from the initial site investigation stage, and to foster a dialogue with concerned authorities regarding interpretations of applicable regulations. SR-Can will be based on site data from the initial site investigation phase.

The overall purposes of the safety assessment SR-Can are the following:

1. Primarily, to investigate whether canisters of the envisaged type are suitable for disposal in repositories at Forsmark and Laxemar, given the host rock conditions at the sites in so far as they can be specified after the initial site investigation phase.
2. Secondarily, to provide feedback to design development, to SKB's R&D programme, to further site investigations and to future safety assessment projects.

An Interim report of the SR-Can project was published in 2004 to demonstrate the methodology to be used in the assessment, so that it could be reviewed and commented prior to use. There, groundwater flow and transport modelling were performed using the Forsmark site as an illustration and based on data from the Version 1.1 site descriptive modelling. As part of SR-Can

[1] The SR in the acronym SR-Can stands for Safety Report and Can is short for canister. This title of the present report was chosen since it was originally intended to support the application to build an encapsulation plant. As a result of the formal consultation process with concerned authorities regarding safety assessments during SKB's site investigation phase, such a report is no longer required for that application. For practical reasons, this altered purpose of the SR-Can report has not been reflected in a change of the name of the report, since it is long well established.

assessment, this methodology has been applied for the Version 1.2 Site Descriptive Models (SDM) firstly for the site Forsmark, followed by the Laxemar site which is reported here. Some enhancements have been made in the methodology to support the final SR-Can report.

The methodology for the assessment of the groundwater pathway makes use of both Continuum Porous Medium (CPM) models, including Equivalent Continuum Porous Medium (ECPM) models, and Discrete Fracture Network (DFN) models on a range of scales to investigate the groundwater flow and radionuclide transport from a deep disposal facility to the biosphere. SKB's methodology refers to three scales of modelling: 'Regional' (~ 10 km); 'local' (~ 1 km); and 'repository/block' (10–100 m). Using models at these scales, it is necessary to simulate the transient, variable-density groundwater flow in sufficient detail to enable the groundwater flux and radionuclide transport paths to be determined. For example, flows from deposition holes into adjacent small-scale fractures represent one release route for radionuclides into the geosphere. Further transport through fractures of increasing size, up to regional-scale deformation zones, is the most likely route through the geosphere to the biosphere. Due to significant developments both in computational tools and in hardware it has been possible to integrate some of these scales and include more detail in each individual model. However, due to the requirement to simulate processes such as transients and rock matrix diffusion it was still necessary to use several types of models to address the relevant issues. Key outputs from the modelling are the groundwater flux through the repository, the definition of flow-paths and values for parameters describing the transport of radionuclides along the paths. The results from the groundwater flow modelling will feed into the assessment of radionuclide transport, and ultimately into biosphere calculations of radiological risks to man.

The focus of the study described in this report has been to perform numerical simulations of the geosphere from post-closure and throughout the temperate period up until the beginning of the next permafrost period at around 20,000 AD for the Laxemar area. Together with providing quantitative results for the immediate temperate period following post-closure, these results are also intended to give a qualitative indication of the evolution of the groundwater system during future temperate periods within an ongoing cycle of glacial/inter-glacial events.

The groundwater pathway

As part of the assessment of the groundwater pathway, models on two different scales were constructed: regional-scale transient porous medium models, and more detailed repository-scale steady-state models using a DFN representation. The regional-scale was used to assess the effects of transient processes such as land-rise and the evolution of hydro-geochemistry coupled to groundwater flow, as well as to perform a sensitivity study of transport performance measures (PM's) to conceptual and parameter uncertainties. The repository-scale modelling was performed with much more detail to resolve the flow around individual deposition holes and calculate flow-paths to the surface for input to Safety Assessment (SA) calculations. For all models, transport was characterised by four main PM's for each canister position in terms of travel-time, initial Darcy velocity, path-length and F-factor along flow-paths started from each canister position. Additional PM's were derived for the DFN repository-scale models such as distances and travel-times in the EDZ and tunnels, as well as equivalent flow-rates, *Qeq*, used in near-field models. Finally, the DFN model is also used to simulate the deposition hole screening process to give three extra PM's to be used in SA analyses.

The reference case from the SDM L 1.2 has been utilised here to quantify SA performance measures based on particle tracking for a release from the canister positions at times in the past, present and future to study the evolution of discharge areas and performance measures over the current temperate climatic period, and to be used as an analogue for future temperate periods. The model uses an ECPM conceptual model, where hydraulic properties are based on upscaling a Hydro-DFN. The simulations are transient and model the effects of shore-level displacement and changes in the salinity in the Baltic Sea on groundwater flow and hydro-geochemical

mixing. The time period modelled is from 8,000 BC to 20,000 AD. At chosen release times, particles are released from the canister positions to calculate pathlines using the instantaneous velocity field at the chosen times.

It was found that least favourable performance measures are found between about 2,000 BC and 1,000 BC. This time-frame coincides with that at which the coastline is directly above the starting positions. After the present-day, the performance measures are generally very constant. The only significant changes take place in the 20–30% of flow-paths that discharge at the shoreline which slowly retreats in the future. Based on the evolution of performance measures and exit locations, 6,000 BC 2,000 BC, 2,020 AD and 6,000 AD were chosen as representative times to be used in the more detailed repository-scale modelling.

A series of variants have been simulated to explore the sensitivity of the SA performance measures, exit locations and groundwater chemistry to various uncertainties that were highlighted in the SDM or were considered important for SA. One group of simulations were performed to study the sensitivity to the deterministic deformation zones, including cases with spatial variability within deformation zones, and with low confidence zones absent. Another group included variants based on variations in the Hydro-DFN model. A third group investigated sensitivities to transport parameters. Finally, the sensitivity to the hydraulic soil domain model was addressed. One variant that stood out has a higher transmissivity in the sub-vertical Set_C giving greater heterogeneity than the reference case since it gave the least favourable performance measures of the cases explored, although the predicted salinities for this case suggest it perhaps has implausibly high hydraulic conductivities. The variants with stochastic variability within the deterministic deformation zones suggested that plausible variants are found when the standard deviation in transmissivity is reduce by subtracting 0.5 from $\log(T)$ to give values of std. $\log(T)$ around 1.0. A variant with a correlated relationship between fracture transmissivity-size resulted in slightly worse performance measures than the reference case with a semi-correlated model. Not surprisingly, the case with low confidence deterministic deformation zones removed gave improved performance measures.

Consideration was given to the difference in starting particles in the different hydraulic rock domains. The initial Darcy velocity in HRD(A) is significantly higher than HRD(D, E, M) and has less spread between the 25th and 75th percentiles. Similarly the F-factor has a median about 0.5 in log-space higher in HRD(D, E, M) than HRD(A). Considering how performance measures vary between tunnel locations, the shortest travel times occur in repository subareas 2 and 3, and the longest travel times are in the southern part of subarea 1, subareas 5 and 7.

Detailed repository-scale models have been used to derive near-field and far-field performance measures for input to SA calculations. A DFN conceptual model has been applied to represent the entire repository and flow in the bedrock around each deposition hole down to the scale of a few metres or less. Groundwater flow-paths are calculated at the representative times 6,000 BC 2,000 BC, 2,020 AD and 6,000 AD with boundary conditions and the salinity distribution being interpolated on to the steady-state repository-scale models from ECPM transient regional-scale coupled groundwater flow and salt transport models based on a consistent underlying DFN. Particles are released from three points around each canister position to provide equivalent flow rates for the near-field (COMP23) SA models, and transport statistics along the pathway to the surface for input to far-field (FAR31) SA models. The release points give the three paths: Q1, a release in a fracture abutting the deposition hole; Q2, a release point in the EDZ at the top of the deposition hole; Q3, a release in the tunnel above the canister.

In terms of the SA performance measures for a release at 2,020 AD, the DFN model predicts travels times with a median about 60 years; initial velocity has a median around $2 \cdot 10^{-4}$ m/y with a standard deviation of 1.3 orders of magnitude; the F-factor has a median of $5.4 \cdot 10^{5}$ y/m with a standard deviation of about 1.0 in log-space. At later times in the future, the performance measures are very similar. At 2,000 BC the performance measures are less favourable with a median travel time of 32 years, median initial velocity of $3 \cdot 10^{-4}$ m/y and an F-factor of $4.8 \cdot 10^{5}$ y/m. At 6,000 BC when the site is covered by a shallow sea, the performance measures are the best.

The DFN is sparsely connected, especially in hydraulic rock domain HRD(D, E, M), and so there is not always an advective pathway through a fracture that intersects the deposition holes via the fracture network to the surface. Overall, about 52% of deposition holes have a Q1 path, i.e. a path to the surface via an intersecting fracture. Of these, only about 47% of canisters are intersected by a connected fracture above the PFL detection limit of around 10^{-9} m^2/s. For the releases in the EDZ and the tunnel, Q2 and Q3, over 80% make it to the surface of the model. The ones that do not are associated with areas of stagnant flow in the tunnel and EDZ since the end of each deposition tunnel opposite the main tunnel is essentially a dead-end. Travel-time and F-factor are almost identical for each of the release points around the canister, which suggests that the flow-path is the same for each release point and that flow does not diverge down different flow conduits around the repository. For the individual rock domains, HRD(A) has 74% of deposition holes with an advective Q1 path to the surface via and adjoining fracture, while HRD(D, E, M) has only 40%.

Generally flow-paths tend to be focussed toward the deterministic deformation zones and the larger stochastic fractures since these are more connected, have higher transmissivity, and hence carry more flow. Typically, there are few long horizontal flow-paths that discharge away from the site area. This is due to the limited horizontal connectivity and geometry of the fracture network. One clear characteristic of this overall picture of path trajectories is the greater dispersion of paths in the northern and eastern parts of the repository which correspond with rock domain HRD(A) compared with the southern part where particles concentrate on a small number of discrete conduits in rock domain HRD(D, E, M). The cause is the difference in fracture connectivity. In HRD(A) the network is relatively connected, so particles tend to be dispersed through the many connections through the network, while in HRD(D, E, M), particles tend to follow the tunnel or EDZ before they find a connection to a handful of deformation zones or large stochastic fractures that provide the only connections to the surface.

PM's measures were found to be generally insensitive to the tunnel and EDZ properties considered as well as the relationship used between fracture transmissivity and size.

For the current fracture model, avoiding locations where fractures intersect the full perimeter of a tunnel seems to be a sufficient test for screening out the worst deposition hole locations without having to perform flow tests of fracture transmissivity in deposition pilot holes.

Gas migration and its effects on groundwater flow

The consequences of the production of gas from iron corrosion in a small proportion of canisters that potentially have manufacturing defects allowing water ingress were addressed.

Gas is generated in defective canisters by anaerobic corrosion of the cast iron insert as a result of water ingress through the defect. The rate of gas generation is determined by the iron corrosion rate, the iron surface area exposed to water, and the availability of water. Assuming that the whole surface of the iron insert is exposed to an unlimited supply of water, the rate of hydrogen production would be $2.1 \cdot 10^{-2}$ m^3 y^{-1} at STP. This is an upper bound to the rate of gas production from a canister as in practice water availability will be limited by the flow capacity of the bentonite, the build up of gas pressure in the canister opposing water ingress through the defect, and the capacity of the geosphere to supply groundwater. The generation rate for these is unlikely to exceed ~ 10^{-2} m^3 y^{-1} at STP, and the build up of gas pressure is likely to reduce the rate to less than ~ 10^{-4} m^3 y^{-1} at STP. Bear in mind that no gas escapes from the defective canister until the gas pressure has reached at least hydrostatic. Gas generation will continue, but possibly only at these very low rates, for at least 250,000 years.

Gas released from a defective canister needs to pass through the bentonite buffer if it is to escape from the vicinity of the canister. Even at the constrained gas generation rates discussed above, gas transport through the bentonite by diffusion in solution from the small defect will be inadequate to remove all the gas generated. However, if the gas pressure opens a gap between

the canister and the buffer into which the gas can spread, the contribution of diffusion of dissolved gas to gas transport through the buffer may become more significant. In any event, it is expected that, if the gas pressure rises sufficiently, movement of a free gas phase through the bentonite buffer will occur.

Once the gas has passed through the bentonite, it might collect in the tunnel and the EDZ associated with the tunnel, and it might enter the fracture network either from the tunnel or directly from the deposition hole. Some of the gas will dissolve in the groundwater and be transported away by the groundwater flow. However, the groundwater flow at the repository depth is very slow, and it is unlikely that gas generated at the upper bound generation rate of $2.1 \cdot 10^{-2}$ m^3 y^{-1} at STP could all dissolve and be transported away in groundwater flowing through the neighbourhood of the repository. If, as seems quite probable for most defective canisters, the gas release rate is 1–2 orders of magnitude less than the upper bound, it is possible that much if not all of the gas could be transported away in solution.

Should the gas not all dissolve, simple estimates show that the gas transport capacity of the fracture network, assuming that it is sufficiently connected between the location of the defective canister and the surface, should be more than adequate to easily transport the gas to the surface without any significant increase in gas pressure in the neighbourhood of the repository.

Should free gas phase migration be sustained between the repository and the surface, this would be capable of transporting volatile radionuclides relatively rapidly from the repository to the surface. The only significant such radionuclides identified in the waste canisters are ^{14}C and ^{222}Rn. Direct release of the volatile ^{14}C in defective canisters to the surface has been previously assessed as not causing a significant radiological hazard and so the capacity of migrating gas to transport this radionuclide is immaterial. Similar conclusions were reached for ^{222}Rn release, although it may be desirable to assess the consequences of ^{222}Rn release into an occupied dwelling.

Migrating gas may also affect the movement of groundwater and hence the transport of dissolved radionuclides. Such transport is mitigated by the following observations:

- With a small defect, it is not possible to get release of dissolved radionuclides and gas at the same time. The situation may be different if a large hole develops.
- Gas migration can only affect transport of dissolved radionuclides released from a nearby different canister, and the probability of two defective canisters being present close together must be quite small.
- Migrating gas is only likely to affect groundwater flows in the neighbourhood of a small number of canisters local to the canister generating gas, and there is a low probability that one of these also may be defective and releasing radionuclides.

Contents

1 Introduction

1.1 SKB's programme for spent fuel and the SR-Can project

Nuclear waste in Sweden is handled by Svensk Kärnbränslehantering AB (SKB), the Swedish Nuclear Fuel and Waste Management Company. Within SKB's programme for spent nuclear fuel management, an interim storage facility and a transportation system are already in operation. SKB's concept for the final stage of the nuclear fuel cycle, based on several decades of research and development, is to place spent fuel inside a cast iron insert inside copper canisters. These are then deposited in a repository, about 500 m deep in saturated, granitic rock, with the canisters surrounded by bentonite clay. This method is referred to as the KBS-3 concept.

Two principal remaining tasks in SKB's programme are to locate, build and operate i) the deep repository and ii) an encapsulation plant in which the spent fuel will be emplaced in canisters to be deposited in the deep repository.

SKB is currently carrying out site investigations for a deep repository in the municipalities of Östhammar and Oskarshamn. The investigations will be conducted in two stages; an initial site investigation (ISI) phase followed, if the expected site suitability is confirmed, by a complete site investigation (CSI) phase. The aim is to build a deep repository at one of these candidate sites, provided that the bedrock and other relevant conditions are found to be suitable. An application to build a deep repository will be made at the end of 2009 according to the current timetable.

The favoured alternative for the location of the encapsulation plant is at Oskarshamn, where it would operate in conjunction with the existing interim storage facility. An application to build an encapsulation plant will be made in 2006.

The final planning application requires a report on the long-term safety of the deep repository, referred to as SR-Site which will be based on data from the completed site investigations. This is an obvious requirement for the application to build the repository. SR-Can is a preparatary stage for the SR-Site report. The main purposes are to obtain a first assessment of long-term safety of a repository at the Forsmark and Laxemar sites, based on data from the initial site investigation stage, and to foster a dialogue with concerned authorities regarding interpretations of applicable regulations. SR-Can will be based on site data from the initial site investigation phase and SR-Site on data from the complete site investigation.

1.2 SR-Can: scope and objectives

The overall purposes of the safety assessment SR-Can are the following:

1. Primarily, to investigate whether canisters of the envisaged type are suitable for disposal in repositories at Forsmark and Laxemar, given the host rock conditions at the sites in so far as they can be specified after the initial site investigation phase.
2. Secondarily, to provide feedback to design development, to SKB's R&D programme, to further site investigations and to future safety assessment projects.

An Interim report of the SR-Can project was published in 2004 /SKB 2004a/ to demonstrate the methodology to be used in the assessment, so that it could be reviewed and commented prior to use. As part of that work, groundwater flow and transport modelling was performed /Hartley et al. 2004/ using the Forsmark site as an illustration and based on data from the Version 1.1 site descriptive modelling (SDM) /SKB 2004b/. The Forsmark SDM was updated

for the Version 1.2 data freeze, F 1.2, /SKB 2005/ in part to support the SR-Can assessment at Forsmark. Based on the conceptual models and data developed in the SDM, groundwater flow and transport calculations were performed to support the SR-Can assessment and main report for Forsmark /Hartley et al. 2006b/.

A SDM has been developed for the Laxemar site based on data freeze version 1.2, L 1.2, /SKB 2006b/. The work reported here provides numerical simulations of groundwater flow and transport at the Laxemar site to support the final SR-Can report. The methodology used here follows that developed in the interim study, and enhanced further in the SR-Can assessment of Forsmark.

The methodology developed in the interim assessment of the groundwater pathway makes use of both Continuum Porous Medium (CPM) and Discrete Fracture Network (DFN) models on a range of scales to investigate the groundwater flow and radionuclide transport from a deep disposal facility to the biosphere. There it was stated that the modelling should address the effects of variable groundwater density and transients. Significant transients occur naturally as a consequence of changes in climate states associated with glacial events and during the construction, operation (e.g. dewatering by pumping) and immediate post-closure phases of the repository. Key outputs from the modelling are the groundwater flux through the repository, the definition of flow-paths and values for parameters describing the transport of radionuclides along the paths. The results from the groundwater flow modelling will feed into the assessment of radionuclide transport using the PROPER chain of codes, and ultimately into biosphere calculations of radiological risks to man.

SKB's methodology refers to three scales of modelling: 'Regional' (~ 10 km); 'local' (~ 1 km); and 'repository/block' (10–100 m). Using models at these scales, it is necessary to simulate the transient, variable-density groundwater flow in sufficient detail to enable the groundwater flux and radionuclide transport paths to be determined. For example, flows from deposition holes into adjacent small-scale fractures represent one release route for radionuclides into the geosphere. Further transport through fractures of increasing size, up to regional-scale fracture zones, is the most likely route through the geosphere to the biosphere. Research into ways of effectively coupling the geosphere and biosphere through near-surface and surface hydrology models is ongoing within the SKB programme. Due to significant developments both in computational tools and in hardware it has been possible to integrate some of these scales and include more detail in each individual model. However, due to the requirement to simulate processes such as transients, rock matrix diffusion, and thermal effects, it was still necessary to use several types of models to address the relevant issues.

The focus of the study described in this report has been to perform numerical simulations of the geosphere from post-closure and throughout the temperate period up until the beginning of the next permafrost period around 20,000 AD for the Laxemar area. Together with providing quantitative results for the immediate temperate period following post-closure, these results are also intended to give a qualitative indication of the evolution of the groundwater system during future temperate periods within an ongoing cycle of glacial/inter-glacial events.

The output from the groundwater flow models forms some of the important input to repository Safety Assessment (SA) calculations. These outputs are described as performance measures (PM's) and are generally tables of data associated with the exit location, canister-flux, travel-time, and transport resistance (F-factor) along paths for particles released at or around each of the canister locations within the repository. These PM's provide a means for quantifying the sensitivity of the SA input to various features, uncertainties and processes. Hence, they provide a way of answering some of the key questions to be asked of the groundwater flow and transport modelling, such as:

1. What is the distribution of groundwater discharge areas and how does this evolve in the future?
2. What are the distributions of PM's, and how do these evolve in the future?

3. Under what conditions do the backfilled tunnels and Engineered Damage Zone (EDZ) acts as potential pathways for groundwater flow?
4. What are the key sensitivities of PM's to model parameters?
5. What uncertainties in the Version 1.2 site descriptive modelling (SDM) have the greatest impact on PM's?
6. What effect do uncertainties in the conceptual model for groundwater flow have on PM's?

1.3 Setting and limitations

The setting for groundwater flow modelling for Laxemar Version 1.2 (abbreviated to L 1.2) has been identified in the site modelling performed by /Hartley et al. 2006a/ and /Follin et al. 2006/.

The Laxemar investigation area, Simpevarp area and cored boreholes used in L 1.2 are illustrated in Figure 1-1. It should be noted that only partial data was available for boreholes KLX05 and KLX06 as of L 1.2. A larger area was used in the CONNECTFLOW L 1.2 regional-scale modelling studies, the domain was chosen on the basis of surface water catchments in the area with dimensions about 21 km, 13 km and 2.3 km in the Easting (x), Northing (y), and Elevation (z) directions respectively.

Figure 1-1. *The Laxemar investigation area (within the grey boundary centre-left), and the Simpevarp area (within the grey boundary centre-right). The positions of cored boreholes are shown.*

An updated geological model of the deformation zones was produced for L 1.2, and the hydro-geological properties of the zones were re-interpreted. Significantly, these updates introduced the concept of depth dependence in hydraulic properties based on evidence from the site. In terms of the rock mass, depth dependence in the hydraulic conductivity was also interpreted along with a dependence on rock domain. Hence, a significantly more complex model of the hydrogeological properties was specified for L 1.2 than was implemented in earlier studies of the Simpevarp area. The motivation being to honour the observed differences in hydraulic properties measured at the boreholes. However, there are only one or two boreholes within each rock domain and hence it is difficult to quantify the variability within domains compared to that between rock domains.

A significant amount of hydraulic data from boreholes was available for L 1.2 SDM, such as KLX03 and KLX04 together with some re-interpretation of data from older boreholes such as KLX01, KLX02, KSH01A and KAV01. The cored boreholes distributed throughout the candidate area gave fracture intensities from boremap data, Posiva Flow-Log (PFL) hydraulic data, together with Pipe-String System (PSS) double packer-test injection. Using previously developed techniques for conditioning hydrogeological fracture models (Hydro-DFN), a parameterisation of the fractured bedrock was developed for each rock domain along with equivalent porous medium properties on various scales. Some uncertainties associated with the assumptions made in interpreting the data were quantified, such as the relationship between fracture transmissivity and size, and anisotropy.

Large quantities of hydro-geochemical data were also available for calibration of the L 1.2 regional flow models. These were provided for cored boreholes and for a series of shallower percussion drilled boreholes. The data were provided in terms of interpreted mixing fractions for reference waters, concentrations of major ions, stable isotope ratios in addition to the salinity data that had been supplied previously. The hydro-geochemical information is used to calibrate simulations of palaeo-hydrogeology and to help understand the key sensitivities of present-day chemistry profiles observed in the boreholes. This calibration proved to be an important step in building confidence in the interpreted hydrogeological properties and conditions at the site. Using the properties based on the interpreted hydrogeological DFN (Hydro-DFN) and an assumed topographic head condition were found to predict too much flushing at repository depth and below. In consequence, a number of changes had to be made in the SDM hydrogeological models that included a lower watertable, anisotropy between fracture sets and a slightly reduced hydraulic conductivity below –600 m elevation. The hydro-geochemical data motivated the development of transient groundwater flow models coupled to transport of multiple reference waters of the palaeo-hydrogeological situation from 8,000 BC until 2,020 AD. All these models were either Continuum Porous Medium (CPM) or Equivalent Continuum Porous Medium (ECPM) models based on an underlying DFN model, and were on the regional-scale with grid resolution only going down to 50 m. A number of uncertainties were studied and quantified with the SDM modelling. However, additional uncertainties were identified of potential importance for safety assessment which has been addressed by sensitivity studies completed here.

For this study it is necessary to continue the transient simulations up to 20,000 AD to consider the future evolution of the site in the temperate period, and to consider models with a much higher resolution to represent flow around individual deposition holes and in the adjoining tunnels and EDZ. For the reference case, transient simulations were continued up to 20,000 AD to assess the effect of long-term transients associated with land-rise. The rate of land-rise falls to around 0.4 mm/year which means the effects on groundwater flow at Laxemar become diminishingly small. Therefore, transients were only considered up to 9,000 AD for variant cases on a regional scale. It should be noted that the periods involving the open repository and resaturation are not considered here. They are dealt with elsewhere in the SR-Can project /Svensson 2006/.

1.4 Organisation of work and structure of report

The approach taken was to use the regional-scale ECPM models developed in the SDM regional-scale modelling to address issues relating to the future evolution of the site. A wider variety of variant simulations were run to better quantify sensitivities than was possible in the SDM hydrogeological modelling. In the SDM hydrogeological modelling, sensitivities were measured in terms of both the calibration against hydraulic data and current hydro-geochemistry data, as well as transport PM's based on releasing particles in the current groundwater flow situation from a regular grid of points within the site release-area. In SR-Can, sensitivities were measured solely in terms of transport PM's for particles released at the 7,483 canister locations, but at different release times in the past and future also. Measuring sensitivities in this way, the regional-scale models were used to rank the most important sensitivities. This is a useful exercise in its own right, but it also helped identify which key variants should be propagated in to the second stage of modelling where much more detailed models were used to consider flow-paths with greater resolution. For practical reasons only a restricted set of cases could be considered with detailed models.

The detailed models include the use of discrete fracture network (DFN) models or combined CPM/DFN to give a more realistic and accurate description of flow in the vicinity of a repository and represent flow-paths through a fracture system. Two different types of combined model are used to nest the calculation of flow-paths within a DFN model. The first type of model (DFN/CPM) is used to represent the detailed flows and transport around individual canister volumes using repository-scale models that sub-divide the repository according to distinct tunnel areas within the layout. These can be used to track particles for several hundred metres, often to the top surface, but some particles exit the sides of these models. To provide a means to continue these particles to the surface, a second type of model (ECPM/DFN) is constructed which extends the DFN representation to the local-scale such that it captures the vast majority of discharge points. In this, way the whole transport pathway is represented within a DFN model to give PM's, such as F-factor, that are calculated with a consistent conceptual model.

Significant advances since the interim assessment in the capabilities of combined models have made it possible to model variable-density flow in DFN and/or combined models. It is also possible to construct much larger models containing many thousands of deposition holes and around 1 million of the surrounding fractures, whereas in the interim assessment it was only possible to model a few hundred deposition holes at a time. The former option addresses some problems encountered in how to define boundary conditions in DFN models to approximate variable-density flow, while the latter option makes it possible to provide input to SA for the entire repository rather than just a fraction.

Calculations to support the assessment of gas migration have been performed based on analytical models using data from the numerical groundwater flow calculation as input.

All the work presented in this report was conducted by the *CONNECTFLOW Team* involving modelling experts from Serco Assurance and Kemakta Konsult using the CONNECTFLOW code that is developed and maintained by /Serco Assurance 2005abc/.

This report presents the general concepts and methodology used in groundwater flow simulations in Section 2. Regional-scale flow simulations using CPM and ECPM models and the ranking of sensitivities are described in Section 3. The more detailed repository-scale modelling to give PM's for input to SA calculations is reported in Section 4. Assessment of gas generation and migration is covered in Section 5. The work is summarised in Section 6.

A glossary of abbreviations used in the report is included in Appendix A. Statistics of PM's for the regional-scale modelling are tabulated in Appendix B. Appendix C presents tables of PM's derived from the detailed modelling for use in SA calculations.

2 Hydrogeological concepts, methodology and data from site descriptive modelling

2.1 Conceptual model types

There are two main types of groundwater flow model relevant to a description of the granitic bedrock at Laxemar: continuum porous medium (CPM) models and discrete fracture network (DFN) models. CPM groundwater flow models treat the rocks through which the groundwater flows as a continuum characterised by quantities defined at all points in a 3D region; DFN models explicitly model the water conducting fractures through which groundwater flows in some rocks, and are characterised by quantities associated with the fractures. For crystalline hard rocks groundwater flow generally takes place through an interconnected network of fractures. Hence, the DFN approach is a natural conceptual model to apply at Laxemar. Also, much effort has been placed in the site investigations on obtaining the relevant geometrical and hydraulic data required to describe fracture characteristics.

At suitable scales the overall flow through a fracture network can be modelled (to a reasonable approximation) using CPM models by appropriate choice of bulk properties (e.g hydraulic conductivity and kinematic porosity). Such models tend to be heterogeneous and have anisotropic block properties in order to represent an underlying stochastic DFN model. Here and elsewhere in SKB's SDM exercises these models are referred to as Equivalent Continuum Porous Medium (ECPM) models.

For the purposes of the SDM characterisation, the hydrogeological structures and properties are divided into following three hydrogeological units:

HCD Hydraulic Conductor Domains – deterministically represented deformation zones of generally relatively high conductivity.

HRD Hydraulic Rock Domains – the bedrock between the deformation zones.

HSD Hydraulic Soil Domains – the surface hydrological units.

This distinction is made because different modelling concepts, field investigations, and interpretation techniques are applied to each.

2.1.1 Continuum Porous Medium (CPM) representation

CPM models are considered the appropriate models for certain types of rock in which flow is predominantly through an interconnected network of pores in the rock matrix, such as many sandstones, or for soils and unconsolidated deposits. The model assumes continuity in 3D and hence a high degree of connectivity between points in the model domain. Connectivity is only reduced when very low conductivity layers or flow barriers are incorporated in the model. The flow through such models is modelled by Darcy's Law, which relates the specific discharge (volumetric flux) to the driving force, i.e. the pressure gradient and/or buoyancy force. There are several distinct types of CPM models depending on how properties are assigned to a finite-element, finite-difference/volume grid. These include: a piecewise homogeneous model where uniform properties are used within to define hydrogeological domains; a stochastic continuum model where properties are defined according to a stochastically sampled spatial process; or an equivalent porous medium model where properties are obtained by upscaling the properties of an underlying DFN model.

To keep consistency with the SR-Can work for Forsmark, the term CPM model is used to refer specifically to models with properties which are uniform within defined rock volumes with spatial heterogeneity only arising due to the implicit representation of fracture zones. This type

of model was only used early in the SDM modelling to perform an initial calibration of transport parameters. Figure 2-1 shows an example of a CPM model used in regional-scale SDM modelling. The figure shows how the hydrogeological rock domains are defined in CONNECTFLOW on which hydraulic properties are specified. It should be noted that depth dependency of hydraulic conductivity and other properties was introduced in the SDM for L 1.2, and so the hydrogeological rock domains were each subdivided into three vertical layers: above –200 m elevation, between –200 m and –600 m, and below –600 m.

2.1.2 Discrete Fracture Network (DFN) representation

The discrete fracture network (DFN) concept assumes flow through a fractured rock is predominantly through an inter-connected network of flow-conductive fractures with groundwater moving from one fracture to another at the intersections between them. The properties of the network are usually characterized in terms of:

- Spatial distribution (e.g. Poisson, fractal, clustered around points or lineaments).
- Fracture intensity (and its spatial variation).
- Number of fracture sets distinguished by orientation.

The properties of deterministic or stochastic individual fractures are primarily:

- Length.
- Orientation (strike and dip).
- Transmissivity (and possibly spatial variability within the plane).
- Transport aperture.
- Storativity.

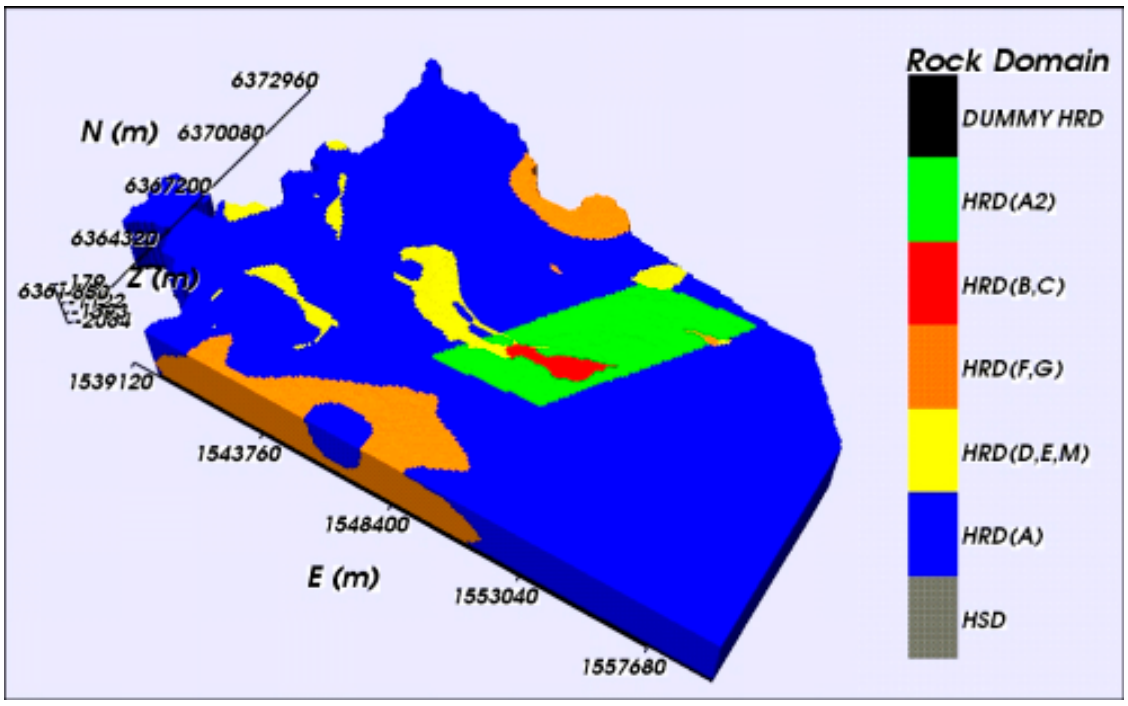

Figure 2-1. *An example of a CPM regional-scale model used for L 1.2. The regional model domain is divided into the HRDs: HRD(A), HRD(A2), HRD(B,C), HRD(D,E,M) and HRD(F,G). The key gives the name of the HRD and the depth interval. The HRD in the depth interval 2,100 m to 2,300 m provides a buffer between the bottom of the HCD's and the bottom of the model. The HSD layers have been removed.*

In CONNECTFLOW, fractures are rectangular, or may be right-angle triangles where a complex surface has been triangulated into many pieces. For stochastic fractures, the properties are sampled from probability distribution functions (PDFs) specified for each fracture set. The properties may be sampled independently or correlated.

The DFN concept is very useful since it naturally reflects the individual flow conduits in fractured rock, and the available field data. However, to understand flow and transport on the regional-scale it is often necessary to consider larger-scale bulk properties in the context of an ECPM continuum concept. This requires methods (i) to convert the properties of a network of discrete fractures of lengths less than the continuum blocks into equivalent continuum porous medium (CPM) block properties, known as upscaling, and (ii) to represent larger scale features such as fracture zones by appropriate properties in a series of continuum blocks, i.e. a down-scaling method. The implementation of upscaling and downscaling in CONNECTFLOW is described in subsections 2.1.3 and 2.2.2, respectively.

As part of the site modelling a parameterisation of a Hydro-DFN model was developed using the field data for L 1.2. The purposes of the Hydro-DFN modelling exercise were:

- Checking the fracture distributions in the boreholes based on the Geo-DFN.
- Deriving transmissivity distributions to match the observed flows in the Posiva flow-log (PFL) and Pipe-string system (PSS) data.
- Deriving the statistical distributions of equivalent porous medium (ECPM) properties on specified block scales for addressing design issues using flux-based upscaling.
- Creating realisations of the regional-scale ECPM model based on upscaling regional-scale DFN models.

An example of a regional-scale DFN model constructed for the L 1.2 SDM study /Hartley et al. 2006a/ is shown in Figure 2-2. Here, fractures were generated in the “small regional-scale” area of approximately 12 km by 6 km by 2 km with radii between 14 and 560 m. The stochastic fractures are square, but the deterministic fracture zones are defined as more complex non-planar surfaces. SDM L 1.2 defined different DFN parameters in terms of geometry, intensity and transmissivity for each hydrogeological rock domain, which has to be honoured in the model. Hence, spatial variability arises both from the stochastic generation of the DFN and from piecewise variations in the fracture statistics.

2.1.3 Equivalent Continuum Porous Medium (ECPM) representation

In order to assess the implications of the DFN model on flow and transport on the regional-scale, it is often necessary for practical reasons to convert the DFN model to an ECPM model with appropriate properties. The resulting parameters are a directional hydraulic conductivity tensor, fracture kinematic porosity and other transport properties (such as the fracture surface area per unit volume). In CONNECTFLOW a flux-based upscaling method is used that requires several flow calculations through a DFN model in different directions.

Figure 2-3 shows an illustration of how flow is calculated in a DFN model (a 2D network is shown for simplicity). To calculate equivalent hydraulic conductivity for the block shown, the flux through the network is calculated for a linear head gradient in each of the axial directions. Due to the variety of connections across the network, several flow-paths are possible, and may result in cross-flows non-parallel to the head gradient. Cross-flows are a common characteristic of DFN models and can be approximated in an ECPM by an anisotropic hydraulic conductivity. In 3D, CONNECTFLOW uses six components to characterise the symmetric hydraulic conductivity tensor. Using the DFN flow simulations, the fluxes through each face of the block are calculated for each head gradient direction. The hydraulic conductivity tensor is then derived by a least-squares fit to these flux responses for the fixed head gradients. Other authors /La Pointe et al. 1995/ have only considered the components of the equivalent hydraulic conductivity parallel to the coordinate axes using a head difference between opposite faces

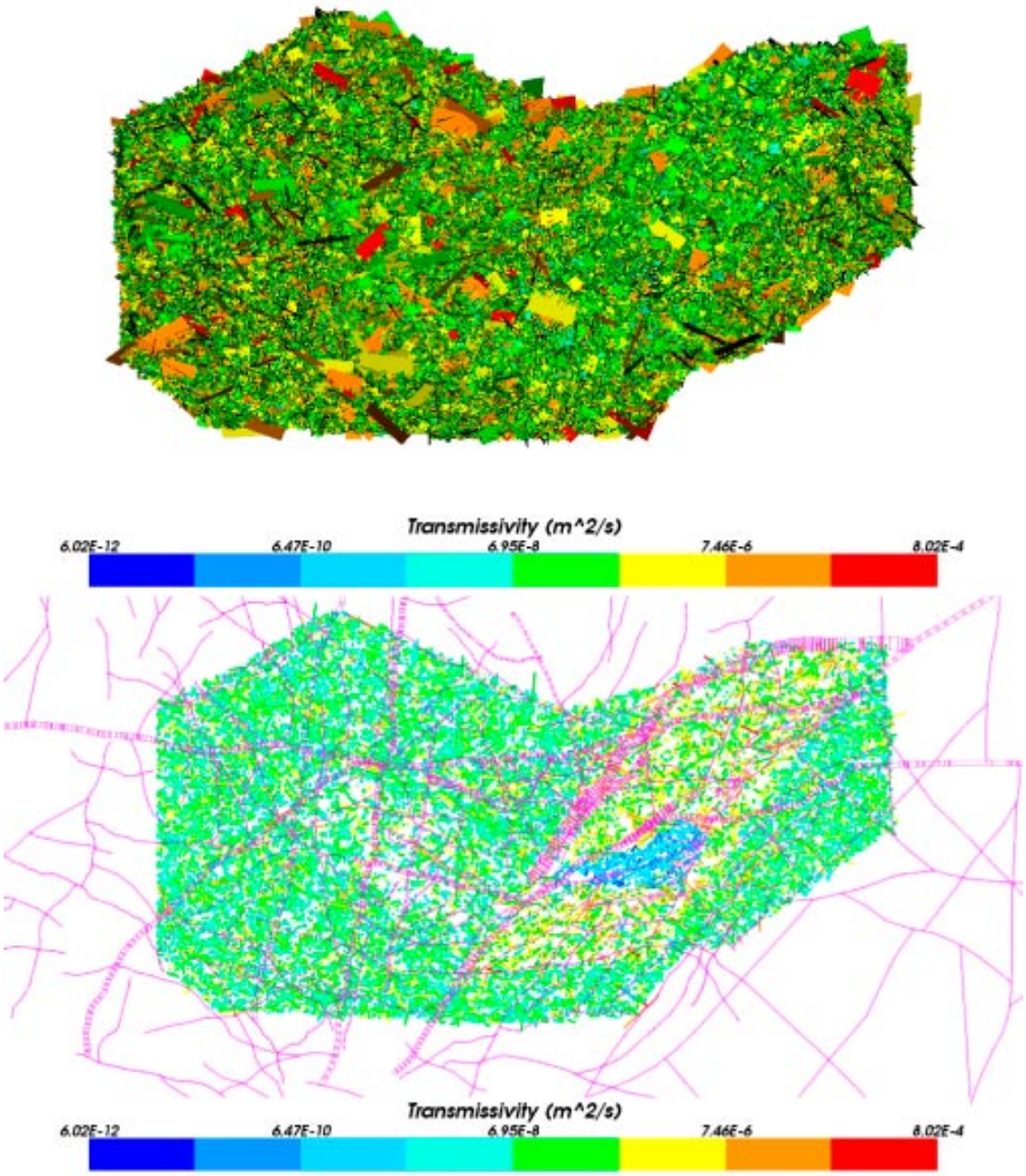

Figure 2-2. *An example of a regional-scale DFN model of Laxemar showing stochastic fractures coloured by log(transmissivity). The domain shown is the small regional-scale model used in the SDM L 1.2 studies /Hartley* et al. *2006a/. Top: 3D network shown from above. Bottom: a horizontal slice through the network at –500 m illustrating the different fracture intensities and transmissivities assigned to different hydrogeological rock domains. In the lower plot a slice through the deterministic deformation zones is superimposed. Here, the minimum fracture radius is 14 m.*

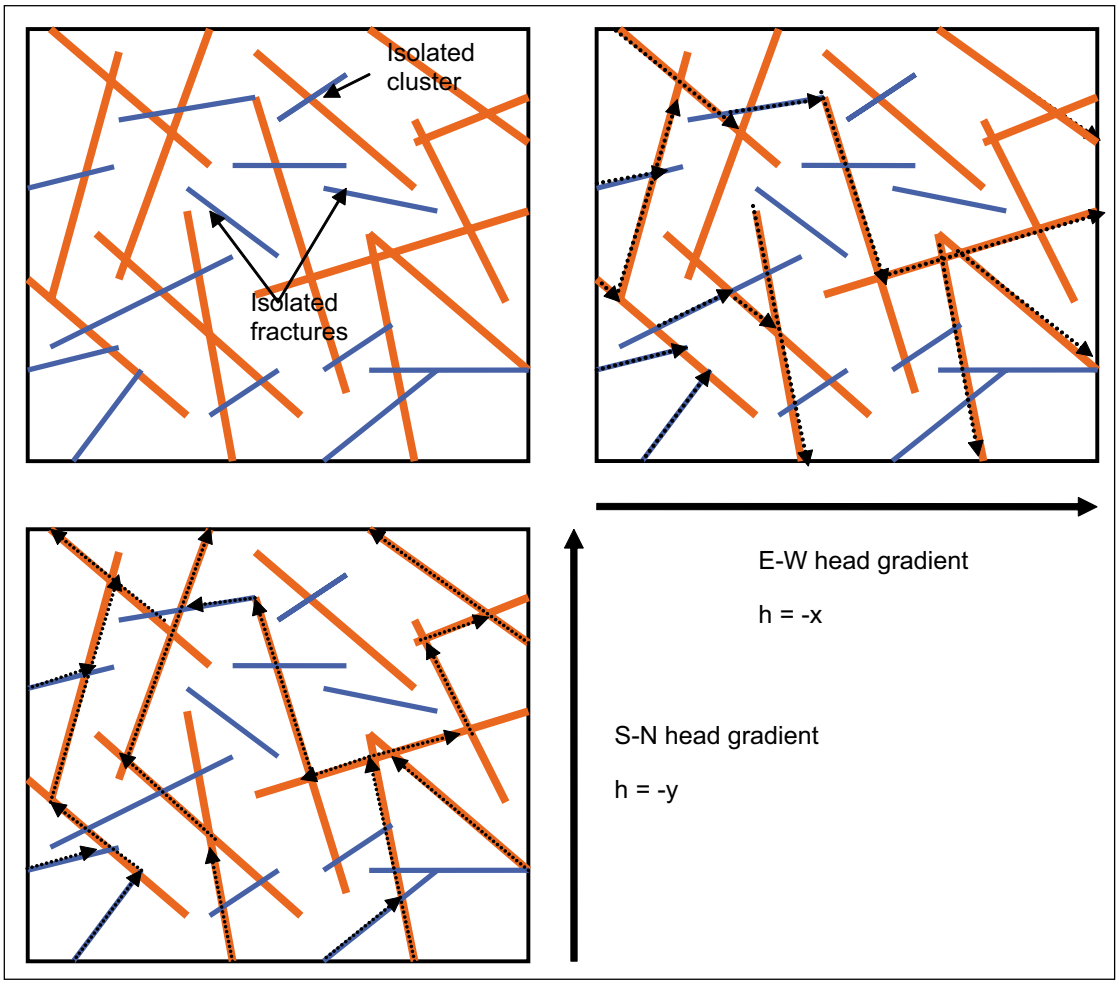

Figure 2-3. *2D illustration of flow through a network of fractures. A random network of fractures with variable length and transmissivity is shown top left (orange fractures are large transmissivity, blue are low). Top right: flow-paths for a linear head gradient E-W decreasing along the x-axis. Bottom left: flow-paths through the network for a linear head gradient S-N decreasing along the y-axis.*

and no-flow on the other faces. This leads to a very poor representation of blocks in which the network connections, and hence flow, are mostly between adjacent faces rather than between opposite faces. The effective hydraulic conductivity assigned to such blocks may be essentially zero, even though the flow-paths through the block may contribute significantly to the overall flow through the network.

In 3D, the blocks have to be hexahedra (cuboids), but the upscaling method can be applied to an array of sub-blocks within a much larger DFN domain by performing the upscaling on each sub-block in sequence. The upscaling method is typically used in one of two ways:

1. To obtain the statistical distribution of hydraulic conductivity on a given block scale a DFN model is generated for a much larger domain, and then ECPM properties are calculated for an array of sub-blocks of equal size and shape to give an ensemble of properties.
2. To obtain an ECPM model for a local- or regional-scale grid, a DFN model is generated within the grid domain, and the upscaling is performed within each grid element to derive the ECPM properties element by element.

A detailed description of the upscaling method to calculate the ECPM hydraulic conductivity tensor is given in /Jackson et al. 2000/. Briefly, the method can be summarised by the following steps:

- Define a sub-block within a DFN model.
- Identify the fractures that are either completely inside or cut the block.
- Calculate the connections between these fractures and their connection to the faces of the block.
- Remove isolated fractures and isolated fracture clusters, and dead-end fractures if specified.
- Specify a linear head gradient parallel to each coordinate axis on all the faces of the block.
- Calculate the flow through the network and the flux through each face of the block for each axial head gradient.
- Fit a symmetric anisotropic hydraulic conductivity tensor that best fits (least-squares) the flux response of the network.
- Fracture kinematic porosity is calculated as the sum (over all fractures that are connected on the scale of the block) of fracture area within the block multiplied by the transport aperture of the fracture.

Hence, to calculate the ECPM properties for a finite-element grid with 1 million elements, say, involves 3 times 1 million DFN flow calculations. One important aspect of this approach is that the properties are calculated on a particular scale, that of the blocks, and that a connectivity analysis of the network is performed only on the scale of the block. Bulk flows across many blocks will depend on the correlation and variability of properties between blocks.

One refinement of the upscaling methodology is to simulate flow through a slightly larger domain than the block size required for the ECPM properties, but then calculate the flux responses through the correct block size. The reason for this is to avoid over-prediction of hydraulic conductivity from flows through fractures that just cut the corner of the block but that are unrepresentative of flows through the in situ fracture network. This method is illustrated in Figure 2-4. The area around the block is known as a 'guard-zone', and an appropriate choice for its thickness is about half a fracture length. The problem is most significant in sparse

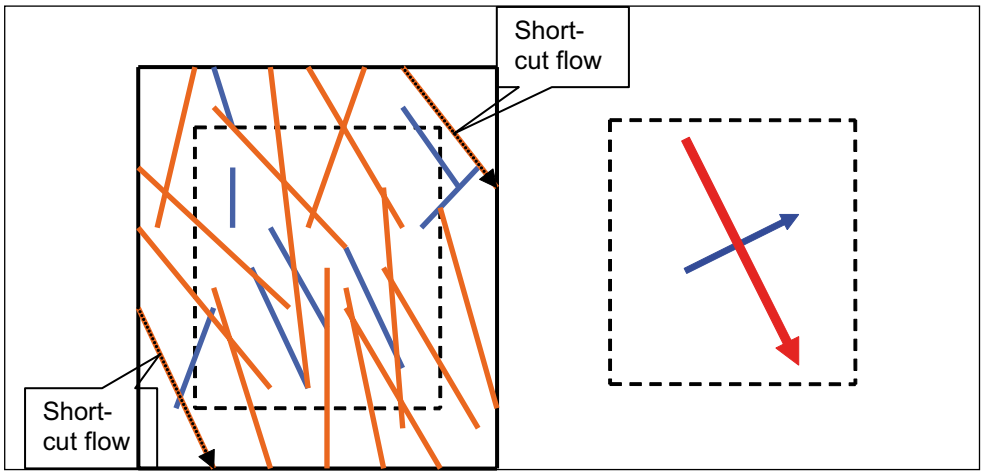

Figure 2-4. *2D sketch of how block-scale hydraulic conductivity can be over-estimated using a linear head gradient by high transmissivity fractures that cut across a corner of the block. By simulating flow through a larger domain, but only calculating the flux through the required block size (dashed block) then fluxes more consistent with flow through an in situ network are obtained. The ECPM hydraulic conductivities are then calculated for the dashed block to give principal components (right). The red arrow is the maximum component, blue the minimum.*

heterogeneous networks in which the flux through the network of fractures is affected by 'bottlenecks' through low transmissivity fractures, and is quite different to the flux through single fractures. This approach is simple to implement for the upscaling of block properties for simple geometries such as an array of adjacent cubes, but becomes more complex when performing upscaling on a more complex regional-scale grid with irregular boundaries. Since the key issue is to ensure that the connectivity of the network is calculated on an appropriate scale, another approach is to generate a stochastic network within an appropriately large volume, remove any isolated or dead-end fractures, and then calculate the fluxes through the required sub-volume of block to provide input to the upscaling calculation. This approach is used for calculating the upscaled properties for each finite-element of a regional-scale ECPM model. That is, a realisation of the DFN is generated on the full regional model, any fracture isolated from the boundaries of the model are then removed, and finally upscaling is performed element-by-element on the remaining network. This avoids over-predicting the equivalent hydraulic conductivity within an element due to fractures that are isolated from a source of water at the surface of the regional model.

An example of an ECPM model used in the regional-scale modelling is illustrated by Figure 2-5. The long linear features with high hydraulic conductivities occur in finite-elements crossed by a deterministic deformation zone (HCD). Between these, properties are heterogeneous due to stochastic variations in the generation of a particular realisation of the fracture network. One can see some short linear features of about 1 km length with hydraulic conductivities around 10^{-6} m/s corresponding to the longest stochastic fractures and some elements with values around 10^{-10} m/s. The spatial variations of properties around the centre of the model are created by differences in the underlying DFN parameters between the different HRDs shown in Figure 2-1. The lowest fracture intensities and transmissivities occur in HRD(D, E, M) and HRD(B,C) (see Figure 2-1).

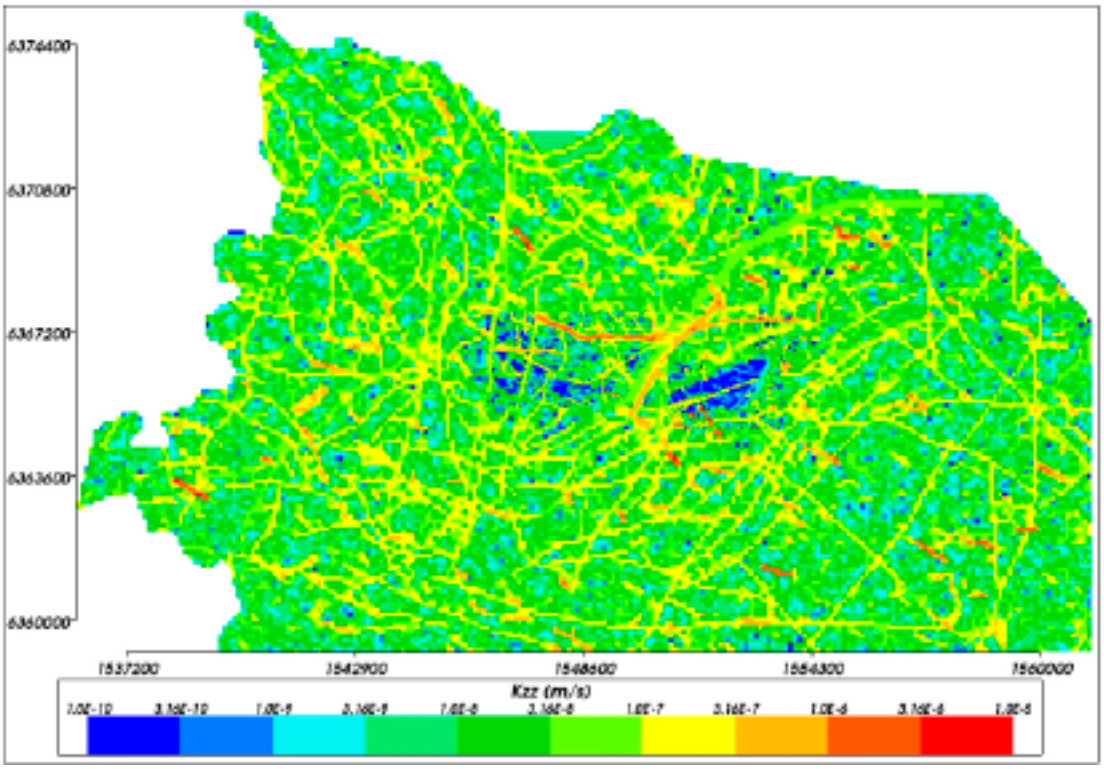

Figure 2-5. *An example of an ECPM regional-scale model based on a horizontal slice at –500 m through the L 1.2 model. Each finite-element is coloured by vertical hydraulic conductivity. The properties are based on upscaling a DFN description of the HRDs and an implicit representation of the deterministic deformation zones (see Figure 2-2).*

2.1.4 Combined CPM/DFN models

In addition, to the ability to create distinct models based on the concepts described above, CONNECTFLOW offers the option to construct combined models that integrate sub-models of different types. That is, the model can be split into 2 different domains: one that uses the CPM concept, and one that uses the DFN concept. However, DFN and CPM sub-models have to be exclusive, i.e. the approaches cannot be used simultaneously in any part of the domain.

Two quite different examples are included below to illustrate some of the possible models that can be constructed. Figure 2-6 shows an example of a combined model where a local-scale DFN model is nested within a larger regional-scale ECPM model. The DFN sub-model is used to provide detailed flow and transport calculations around a repository, while the ECPM sub-model provides a representation of the regional-scale flow pattern that control the boundary conditions on the DFN model. The interface between these two sub-models is on the six faces of the DFN model.

The converse example is to nest a CPM sub-model within a DFN sub-model as shown in Figure 2-7. In this case, a CPM sub-model is used to represent flow in backfilled access and deposition tunnels, while the surrounding fractured rock is represented by a DFN sub-model. The interface between the two sub-models has a complex geometry corresponding to the outer surface of the tunnel system.

In summary, combined models make it possible to represent different regions in different ways and then combine the regions into a single model. This is different from the case where discrete fracture objects co-exist in the same space with a porous medium model of the rock matrix. Representations of the interaction between fractures and the rock matrix within the same domain can be represented in CONNECTFLOW by modelling rock matrix diffusion (RMD) within CPM/ECPM models, but it should be recognised that this is quite a different issue. It may be

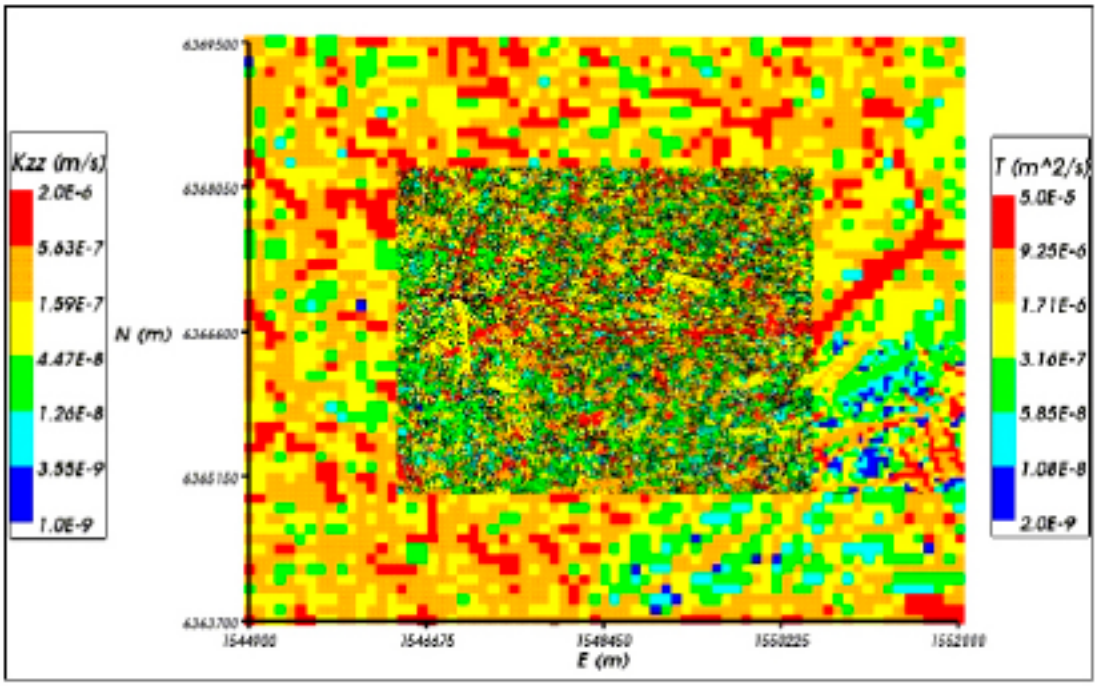

Figure 2-6. *An example of a combined ECPM/DFN CONNECTFLOW model using a DFN sub-model in the centre to represent the detailed fractures around a repository and nested within a larger regional-scale ECPM sub-model. In this map view fractures are coloured by transmissivity while elements are coloured by vertical hydraulic conductivity. Here, the interface between the two sub-models is on the boundary of the DFN model.*

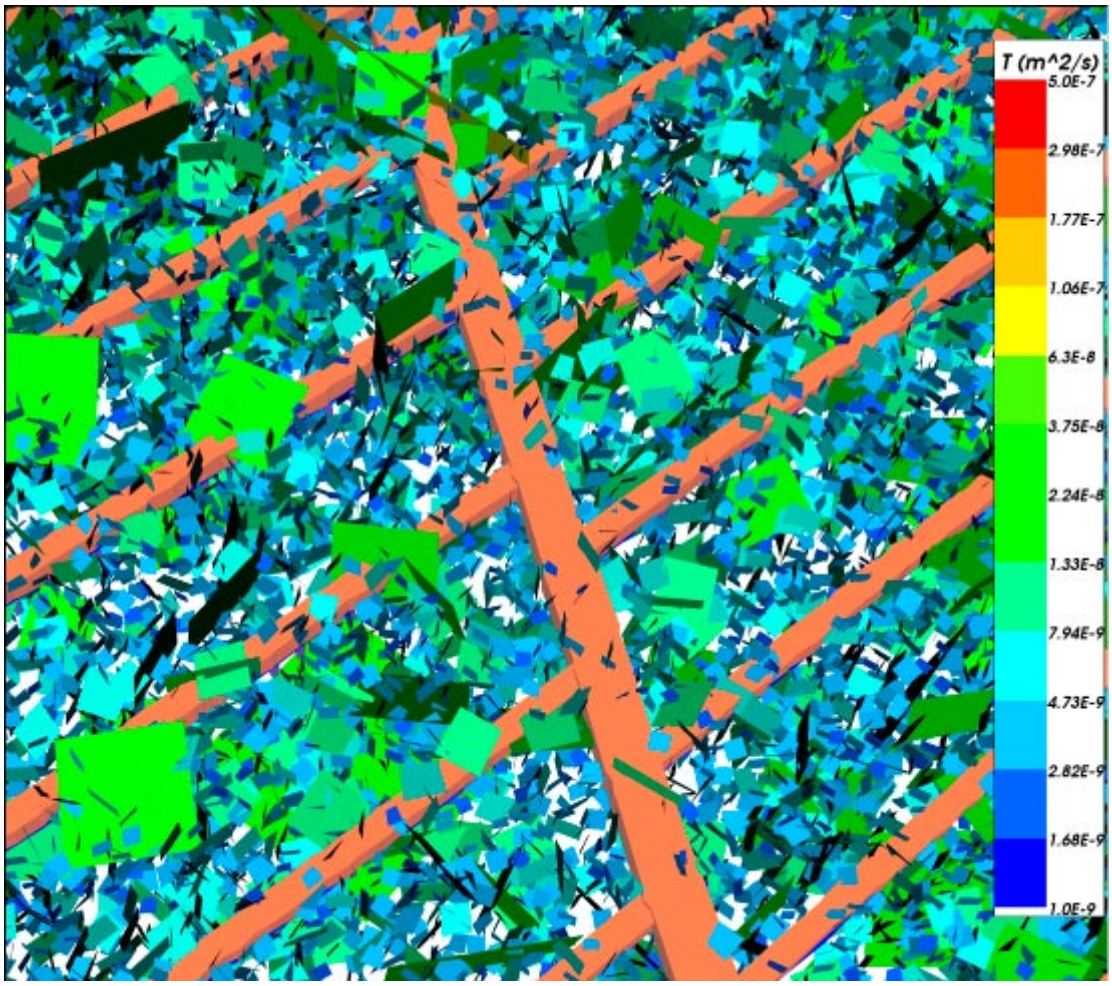

Figure 2-7. *An example of a combined DFN/CPM CONNECTFLOW model using a CPM sub-model of deposition and access tunnels nested within a DFN sub-model. Some fractures have been removed to reveal the tunnels. Here, the interface between the two sub-models is on the boundary of the CPM model.*

noted that RMD of salinity is not represented within the DFN domain, whilst RMD within the fracture system of radionuclides can be accounted for either in the particle tracking algorithm or later in the PROPER radionuclide transport calculations.

In a combined DFN/CPM model, flow in the DFN and CPM models is nested formally by internal boundary conditions at the interface between the two sub-models. These boundary conditions are implemented as equations that ensure continuity of pressure and conservation of mass at the interface between the two sub-regions. On the DFN side of the interface, these boundary conditions are defined at nodes that lie along the lines (traces) that make up the intersections between fractures and the interface surface. On the CPM side, the boundary conditions are applied to nodes in finite-elements that abut the interface surface. Thus, extra equations are added to the discrete system matrix to link nodes in the DFN model to nodes in the finite-element CPM model. Figure 2-8 shows this configuration. By using equations to ensure both continuity of pressure and continuity of mass, then a more rigorous approach to nesting is obtained than by simply interpolating pressures, say, between separate DFN and CPM models.

In order to construct nested models of the same fractured rock (mixing DFN and CPM sub-models), then the data used for the DFN and CPM models should be self-consistent. For example, if a repository scale DFN model is nested within an ECPM model, then flow statistics on an appropriate scale (the size of the elements in the ECPM model) need to be consistent. This is achieved by the fracture upscaling techniques described in Section 2.1.3.

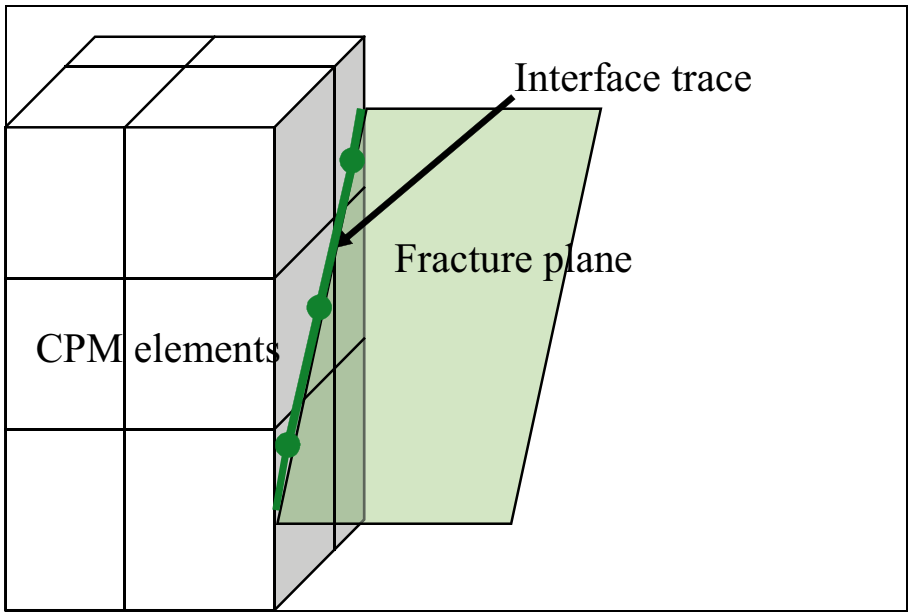

Figure 2-8. *Sketch of coupling between DFN and CPM sub-models. A finite-element CPM mesh is shown on the left. The right hand surface is intersected by a single fracture plane. Extra equations are used to link the DFN to the CPM. These equations are applied at fracture global nodes (dark green points) in the fracture plane along the intersection (dark green line).*

The steps in coupling the two regions are:

1. Calculate the intersections of fractures with the boundary of the DFN region.
2. Select the surfaces of the DFN region that abut the CPM region and specify a coupling type boundary condition.
3. For each fracture that intersects these DFN region surfaces, identify the CPM finite-elements that abut the fracture. A single fracture may abut several elements, or several fractures may abut the same element.
4. Add extra equations to the discrete system matrix to link the pressure values at nodes on the fracture intersections with the pressure values in the adjoining finite-elements.
5. Solve the discrete system matrix.

Hence, extra internal boundary conditions have to be specified for a CONNECTFLOW model to link DFN and CPM regions.

A particle tracking algorithm is used in combined models to represent advective transport of solutes. In CPM models, particles are tracked in a deterministic way by moving along a discretised path with the local finite-element velocity-field. In DFN models, a stochastic 'pipe' network type algorithm is used. Particles are moved between pairs of fracture intersections stepping from one intersection to another. At any intersection there may be several possible destinations that the particle may potentially moved to next as flow follows different channels through a fracture. A random process weighted by the mass flux between pairs of intersections (connected by a 'pipe') is used to select which path is followed for any particular particle. Hence, there is an explicit hydrodynamic dispersion process built into the transport algorithm used in the DFN. The time taken to travel between any two intersections, the distance travelled and flow-wetted surface are calculated for each pipe based on flow rates and geometries. In a combined model, particles are traced through both DFN and CPM regions continuously using the appropriate algorithm according to the region the particle is currently in. An example of this is shown in Figure 2-9. The implication is that particle tracks are deterministic until they enter a DFN sub-model, and are then stochastic afterwards, even if the particle goes back into a CPM sub-model.

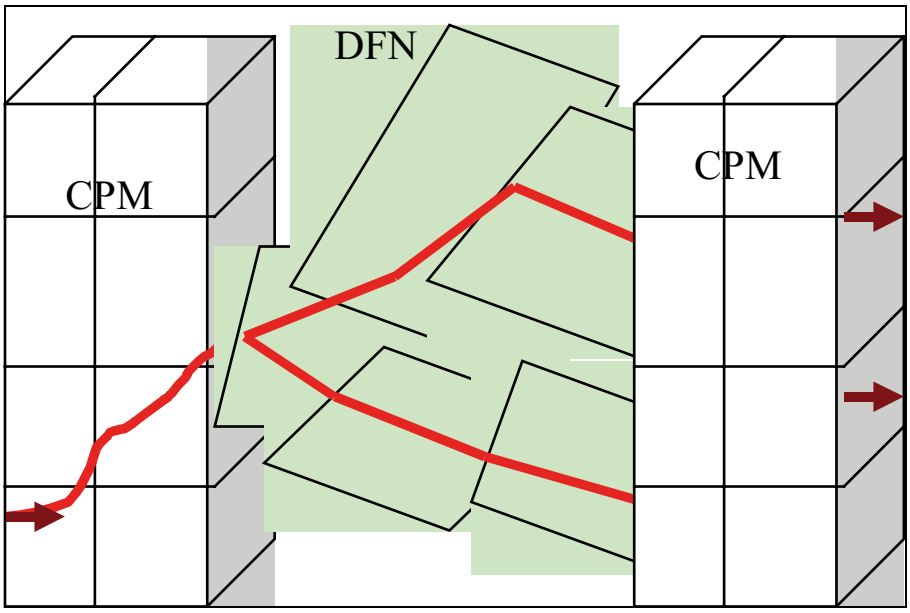

Figure 2-9. *Illustration of particle tracking through a combined DFN/CPM to show the different particle tracking methods in the two regions: deterministic in CPM, stochastic in DFN.*

2.2 Modelling methodology

An appropriate conceptual model for flow and transport is a DFN model since flows observed in the boreholes using the Posiva flow log (PFL-f) technique can be tied with the locations of open fractures identified in the Boremap (integrated BIPS and core) data. The geometrical fracture parameters (Geo-DFN) originate from the SDM geological modelling /Hermanson et al. 2005/ which were further developed to include hydrogeological parameters (Hydro-DFN) by simulating the flow responses in boreholes /Hartley et al. 2006a/. A DFN concept can be implemented in several ways as appropriate to the scales and physical processes of interest. Generally, for issues on fine scales, such as flows around deposition holes or tunnels, it is important to retain the geometry and details of the DFN down to the individual fractures, whereas for large scale regional flow, considering such process as transient mixing of different water types, it may be acceptable and necessary to use an ECPM representation of an underlying DFN model. In fact, this study requires that flow and transport be considered on a variety of scales from the canister (a few metres) to the several kilometres associated with shoreline movements over the next 18,000 years. Hence, a key issue in the modelling is how to integrate or 'nest' these scales when providing input to SA. Important aspects that have to be considered in how to go about nesting different scales are:

1. How to nest different scales of model either as 'embedded' models where different scales or types of model are combined and are linked by internal boundary conditions or as separate models where boundary conditions have to be transferred from the larger scale to the small.
2. How to represent features such as fracture zones that cross the boundary consistently between the different scales.
3. How to model processes such as variable-density flow and rock matrix diffusion on the different scales.
4. How to represent transient processes on the different scales.
5. How to perform particle tracking continuously across the different scales.

Aspects 1, 2 and 3 are dealt with in Sections 2.2.1, 2.2.2 and 2.2.5, respectively. In respect to transients (Aspect 4), the site modelling has already developed a methodology for understanding the current hydrogeological situation by regional-scale modelling of the palaeo-hydrogeology

over the last 10,000 years. For SR-Can we continue this approach to calculate the evolution of groundwater flow at the Laxemar site up to 20,000 AD and also the transport of dissolved species in the groundwater. For more detailed fine-scale models it is not practicable to consider transient processes in a continuous manner. Instead several 'snapshots' in time are considered chosen on the basis of distinct changes in the groundwater flow pattern as calculated in the regional-scale modelling. The methodology used for transport (Aspect 5) is described in Section 2.2.4. A final aspect is how to represent the repository, and this is covered in Section 2.2.5.

2.2.1 Nesting of models

Several different methods of nesting different scales of model have been applied in this project. The methods fall into two main types: either embedded models where only a single model is constructed, but areas of the model have a finer resolution or different type of conceptual model (e.g. DFN) and internal boundary conditions are required to ensure continuity of variables and conservation of flux; or two separate scales of model where boundary conditions have to be transferred more manually from the larger scale to the small. The embedded method of nesting has the advantage that it ensures both continuity of variables and fluxes at the interface between the two scales, whereas separate models only ensure continuity of variables. In CONNECTFLOW the embedded method is used to embed a fine-scale CPM models inside coarser CPM models, or to embed DFN models inside CPM models (CPM/DFN), or vice versa (DFN/CPM). Where one type of conceptual model is embedded within another type, we call these 'combined' models to make a distinction. A schematic of how the nesting works in shown in Figure 2-10. Some real examples of embedded models, both pure CPM and combined, have already been given in Section 2.1.

Because of the complex requirements of this project a variety of nesting methods had to be used and often combined. Figure 2-11 presents an illustration of the overall workflow and interactions between models. Boxes are used to indicate distinct types of model, and arrows to show the flow of data between them. All phases of the process are shown including those from the site-modelling from geological data and data interpretation to site investigation modelling to repository-scale modelling through to SA calculations. The models described by the green boxes are the ones constructed as part of this project and described in this report. Regional-scale ECPM models of the transient evolution of groundwater flow and reference water mixing are used to supply boundary conditions at selected times to finer scale models. Repository-scale DFN models that represent the flow down to the scale of individual deposition holes and the surrounding tunnels and EDZ are used to provide accurate and realistic input to SA calculations.

Because of the computational size of the DFN models, two different scales of DFN model are required. The first is a detailed repository-scale model that models the repository explicitly as a CPM surrounded by a DFN model with fractures down to a scale of order 1 m radius to resolve the release of particles from a canister and then advect them through the surrounding rock. However, this type of model has a limited domain, so it cannot necessarily model transport to ground surface for all flow-paths, particularly long horizontal paths. Hence, a second type of nested model is constructed where a local-scale DFN model is embedded within a regional-scale ECPM model as illustrated by the configuration in shown in the bottom left of Figure 2-10. In this case, the repository is modelled as equivalent fractures with appropriate properties. In this case, it is only possible to include fractures down to a radius 8 m. This approach allows flow-paths to be continued from the repository-scale to the regional-scale within a consistent DFN representation to maintain realism in the calculation of performance measures such as the F-factor.

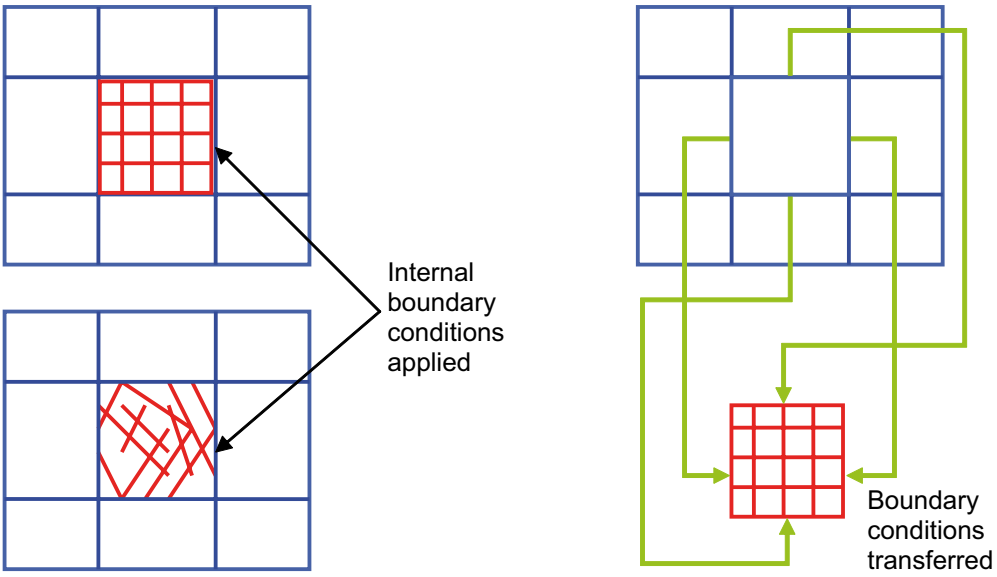

Figure 2-10. *Examples of different methods for nesting models. Top left: an embedded fine-scale CPM model inside a coarser CPM model. Bottom left: a combined fine-scale DFN model embedded within a coarser CPM model. Right: two separate CPM models with boundary conditions transferred from the larger to smaller scale.*

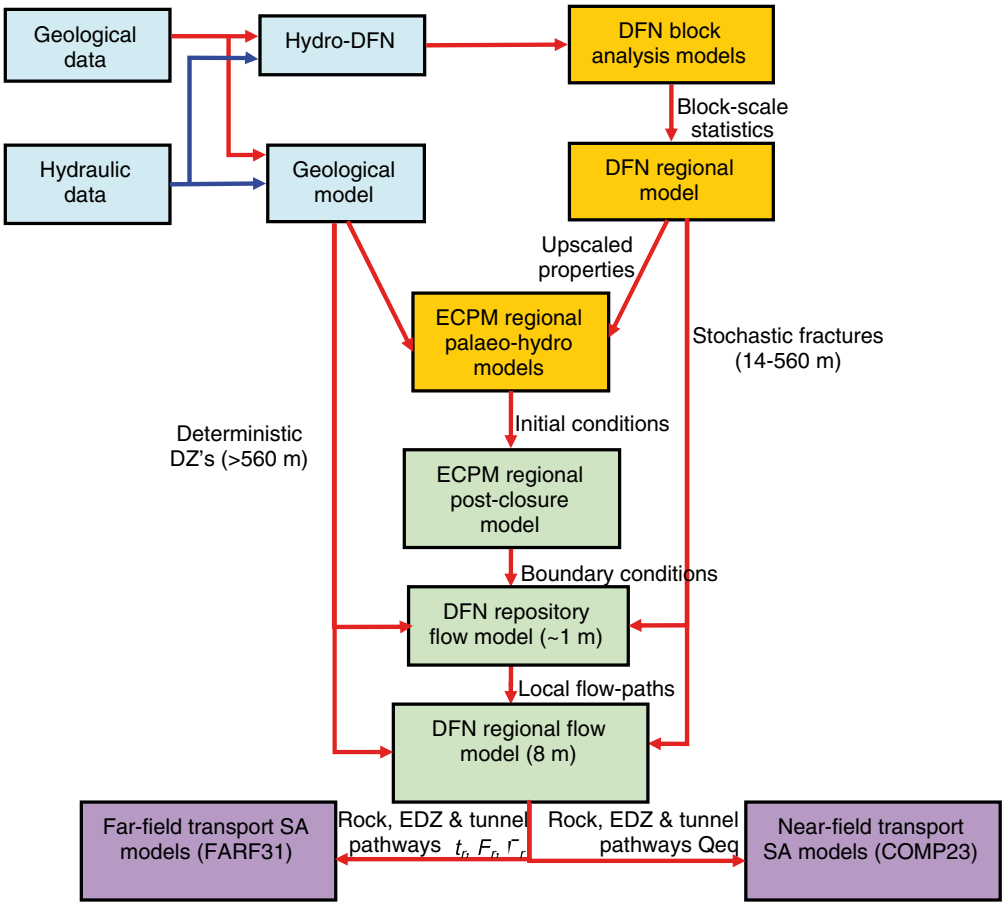

Figure 2-11. *Schematic illustration of model chain developed for the SR-Can methodology. Models coloured blue were supplied as part of the site modelling (SDM) L 1.2 Exercise. Models coloured orange were an overlap between work done as part of the SDM and SR-Can. Models coloured green have been created solely within SR-Can. Models coloured purple relate to the SA modelling phase of SR-Can. The range of fracture radii within each model is indicated in metres.*

2.2.2 Representation of DZ's and the implicit representation of fracture zones (the 'IFZ' method)

For Laxemar version 1.2, the basic concept is that fractures exist on a continuous range of length scales, which motivates a methodology to generate sub-lineament-scale fractures stochastically on scales between tens of metres to about 1 km, and then combine this DFN by superposition with the larger scale deterministic DZ's modelled using SKB's Rock Visualisation System (RVS). The approach used to represent the deterministic DZ's was different in DFN and ECPM models. In the ECPM models, the deterministic DZ's were represented by modifying the hydraulic properties of any finite-elements intersected by one or more zones to incorporate the structural model in terms of the geometry and properties of zones using the Implicit Fracture Zone (IFZ) method in CONNECTFLOW as described in /Marsic et al. 2001/. In a ECPM model, the methodology is to first create one or more realisations of the stochastic network on the regional-scale and then, using the upscaling methods described in Section 2.1.3, to convert this to a realisation of the ECPM model, minus the deterministic DZ's. The ECPM model properties are then modified to incorporate the effect of the deterministic DZ's as shown in Figure 2-5. The IFZ method is described below.

The IFZ downscaling method identifies which elements are crossed by a fracture zone and combines a hydraulic conductivity tensor associated with the fracture zone with a hydraulic conductivity tensor for the background stochastic network. For each element crossed by the fracture zone the following steps are performed:

1. The volume of intersection between the fracture zone and the element is determined.
2. The hydraulic conductivity tensor of the background rock is calculated in the coordinate system of the fracture zone.
3. The combined conductivity tensor of the background rock and the fracture zone is calculated in the coordinate system of fracture zone.
4. The effective hydraulic conductivity tensor that includes the effect of the fracture zone is determined in the original coordinate system.

The methodology is illustrated diagrammatically in Figure 2-12. In 3D, the resultant hydraulic conductivity is a 6-component symmetric tensor in the Cartesian coordinate system. The tensor can be diagonalised to give the principal components and directions of anisotropy.

Similarly, a combined scalar block-sale porosity is calculated for the element based on combining the fracture zone porosity and the background block-sale porosity using a weighting either based simply on either the relative volume or on relative transmissibility (total channel flow capacity, which is transmissivity times flow length [$m^3\ s^{-1}$]). The latter weighting can be suitable for transport since it weights the combined porosity toward the fracture zone porosity if this is of a relatively high hydraulic conductivity. The result of this step is to produce a spatial distribution of ECPM element properties (hydraulic conductivity tensor and porosity) that represent the combined influence of both the deterministic fractures zones and background stochastic fractures.

It may be noted, the term "background conductivity" here means the equivalent conductivity of the stochastic fracture network. No extra component for matrix conductivity or micro-fracturing is added. However, the stochastic DFN is necessarily truncated in some way e.g. based on fracture size which in consequence means that some elements may not contain a connected network of fractures or may only be connected in some directions. To avoid this just being a result of the choice of truncation limit and chance, a minimum block conductivity and porosity is set for any elements that have zero properties following the fracture upscaling and IFZ methods. Appropriate minimum properties were derived in the SDM Hydro-DFN studies /Hartley et al. 2006a/ by calculating the minimum values seen when the DFN is truncated only at very small fractures relative to the block size, and so are essentially free from the truncation effect.

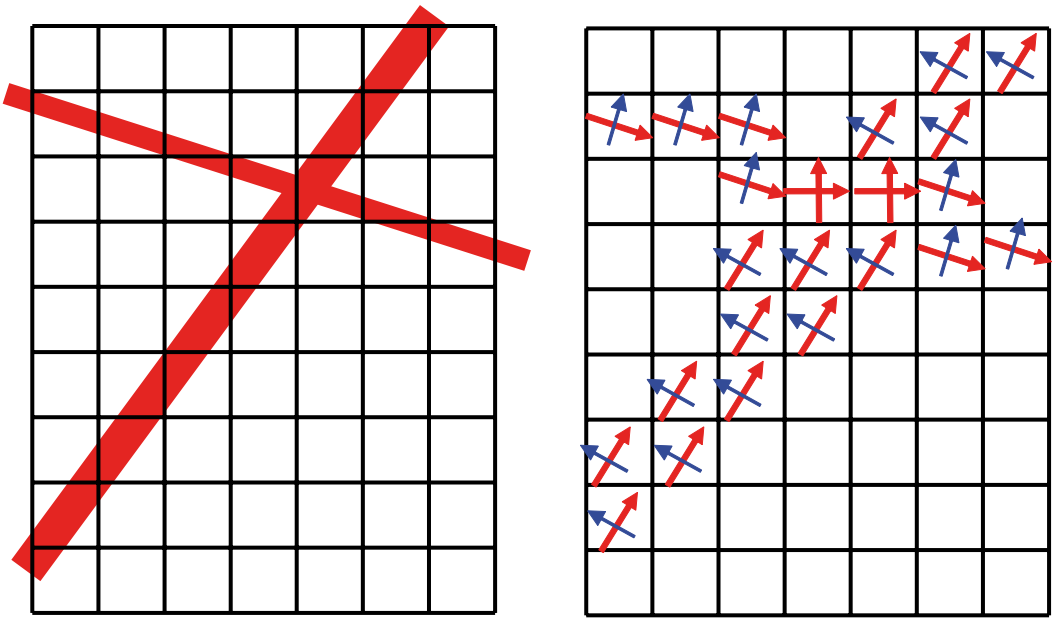

Figure 2-12. *Schematic illustration of the modification of the hydraulic conductivity tensor by the IFZ method. A finite-element grid crossed obliquely by two fracture zones of different thickness (left). The effect on the equivalent porous medium hydraulic conductivity (right). Elements with a large IFZ effect are coloured pink. Ones with a lesser effect, where the fracture zone only crosses one corner, are coloured orange. The principal directions of the resultant anisotropic hydraulic conductivity tensor are shown by arrows (red for major component, blue for minor).*

In DFN models, the deterministic DZ's are modelled as surfaces (i.e. no volume). The surfaces are composed of many rectangular or triangular fractures to discretise the geometry and hydraulic properties. The site modelling L 1.2 prescribed a depth dependent transmissivity that decreased significantly with depth. Therefore, it was necessary to sub-divide the zones into relatively small triangular sub fractures, 200 m, to represent the property variations. An example is shown in Figure 2-13.

In combined models it is important to ensure that the deterministic DZ geometries are represented consistently where they cross between DFN and CPM models. This is to ensure continuity of flow across the interface where the zone crosses the interface, otherwise artificial barriers to flow may be introduced. It is achieved in CONNECTFLOW by specifying the deterministic DZ's using the same input file in the DFN and CPM sub-models. The parts of a fracture within each sub-model are calculated automatically. Figure 2-14 shows an illustration of how a large deterministic fracture that crosses between DFN and CPM sub-models can be modelled in such a way as to ensure there is continuity in its representation, and hence in flow between the regions. An example of how this was applied in the SR-Can study is shown in Figure 2-6.

2.2.3 Variable density groundwater flow and salt transport

Variations in groundwater composition create variations in groundwater density and hence buoyancy-driven flow that modifies the pattern of groundwater flows. Since gradients in the watertable at Laxemar are relatively weak, then buoyancy forces arising from the presence of salt have some importance at depth. In particular the Brine encountered below about 1,000 m depth essentially forms a lower barrier to deep vertical flows. Important advances in the modelling capabilities for handling variable-density flow have been made since the interim SR-Can assessment, namely:

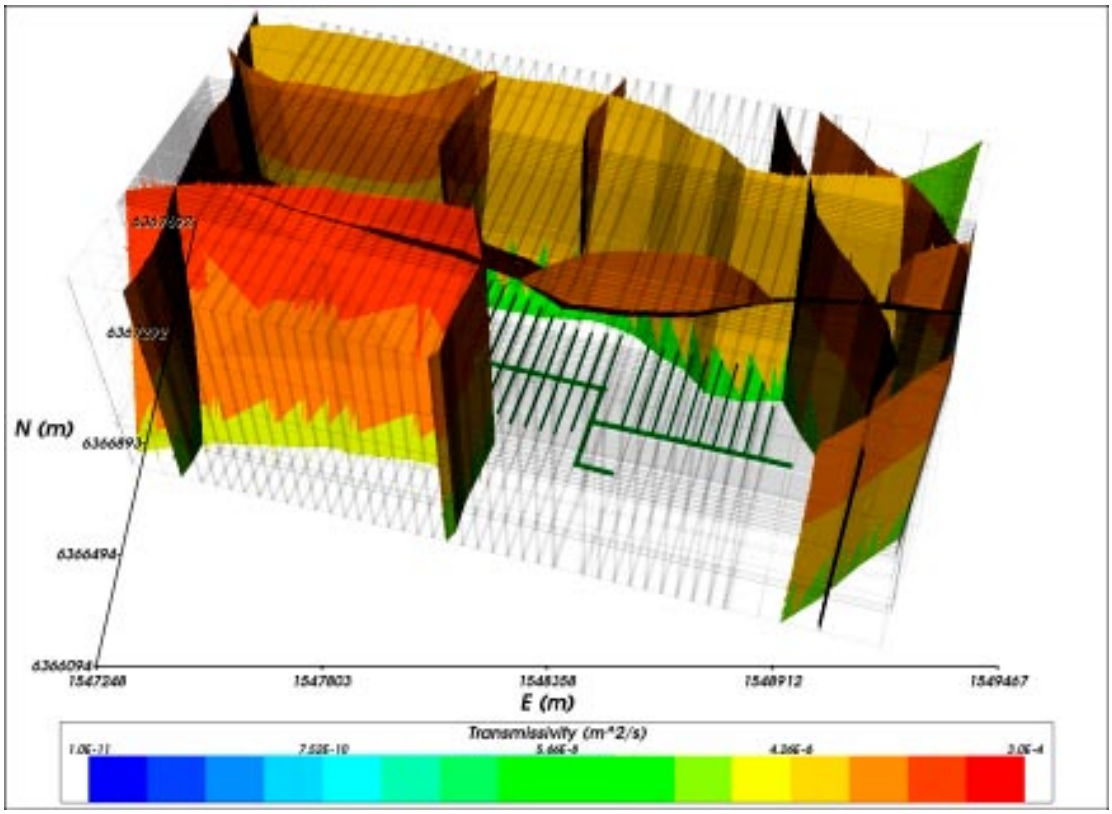

Figure 2-13. *Deterministic deformation zones (DZ's) modelled as surfaces in a repository-scale DFN model with depth dependent transmissivity.*

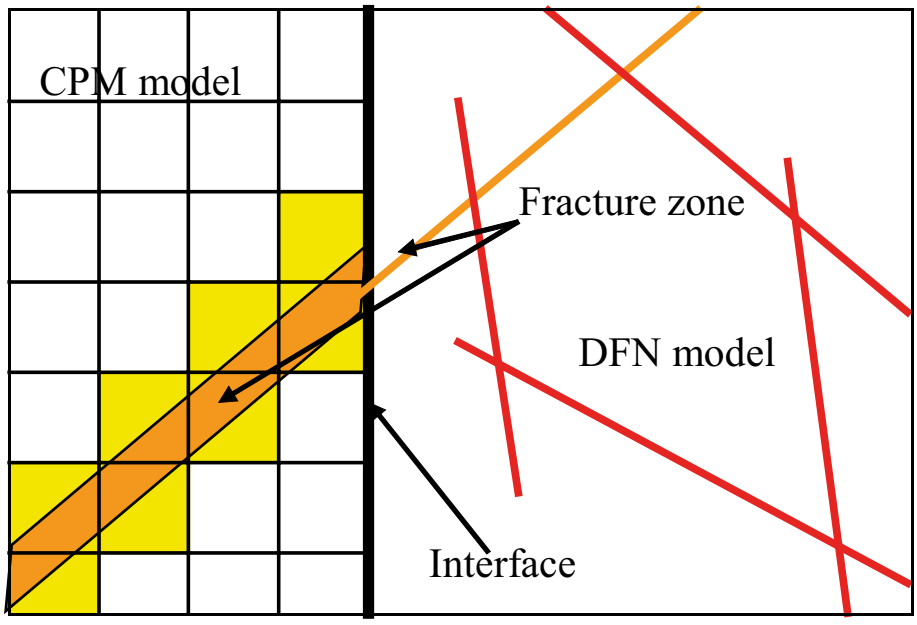

Figure 2-14. *Schematic illustration of continuity of DZ's across a CPM/DFN interface in a CONNECT-FLOW model. The DFN region is to the right with a CPM grid to the left. A few fractures are shown in red and orange in the DFN region. The red fractures may be stochastic for example. The orange fracture is a deterministic DZ that crosses the interface. On the DFN side it is shown as a plane, while on the CPM side it is drawn with its actual thickness. The elements crossed by the DZ's are coloured yellow. Hydraulic conductivity in these elements will be modified in the IFZ method to represent the effect of the fracture zone on flow and transport.*

1. An option in ECPM models to simulate flow in a porous medium for groundwater of variable salinity, where the salinity arises from a number of groundwater constituents. This can be modelled either in terms of transport of mass fractions of the basic hydro-geochemical constituents (such as chloride, sodium, oxygen isotope ratio), which are taken to be conservative, or in terms of transport of fractions of selected reference waters. Either way, the transport equations are coupled with the overall mass conservation equation for groundwater. In addition, rock matrix diffusion (RMD) is included in the transport of each groundwater constituent.
2. An option to calculate groundwater flow for specified spatial variations in groundwater density in DFN models and combined models. That is, the groundwater density has to be interpolated onto the fracture system from another model, but then the consistent pressure distribution and flow-field is calculated with buoyancy forces included. The groundwater density is typically interpolated from a ECPM model at a selected time. Particle tracking through both DFN and combined models with the calculated flow field can then be performed.

The first option was applied in the site modelling to simulate the transport and mixing of four reference waters (Rain 1960, Marine, Glacial, and Brine) in line with the conceptual model for hydro-geochemistry. This helped in the calibration of the model in terms of hydraulic properties and boundary conditions using data from the results of the Mixing and mass-balance modelling (M3) geochemical analysis /Laaksoharju et al. 1999/ and the various ionic species, oxygen and hydrogen isotope ratios. The same option is used here to model the future evolution of groundwater constituents up to 20,000 AD. Not only is this necessary for calculating groundwater flow and flow-paths in the future, but it also gives a prediction of how groundwater chemistry will evolve around the repository and some more general indication of how groundwaters evolve over cycles of glacial and inter-glacial periods.

The option also makes it possible to model diffusion of the reference waters between groundwater flowing in fractures and immobile water in the rock matrix between the fractures (RMD). The numerical approach used /Hoch and Jackson 2004/ is based on a method developed by /Carrera et al. 1998/ enhanced to enable potentially larger time steps to be taken. The approach combines an approximation that is accurate for small times with one that is accurate for long times, to give a representation of the diffusion into the rock matrix that is accurate for all times. At early times, the diffusion is represented in terms of the inverse of the square root of time, and at long times it is represented as a series of decaying exponentials. The main parameter that controls the rate of RMD is the facture surface area per volume of rock, a_r [m^2/m^3], which is also the key parameter in determining the F-factor. Therefore, calibrating models against groundwater constituents in the fracture and matrix systems may help condition the selection of a_r and hence reduce the uncertainties in predictions of F-factor. A more direct estimation of a_r can be derived based on fracture hydraulic data such as PFL data (see Section 2.3.3).

The second option addresses an outstanding issue from the interim assessment of how to define boundary conditions for repository-scale or local-scale DFN models when buoyancy-driven flows are significant. In the interim study quite different flow-paths were predicted by DFN models than the corresponding ECPM models, and it was not clear whether this was due to deficiencies in the choice of boundary conditions used to approximate variable-density flows in the DFN or an innate difference in connectivity for flow through a sparse fracture network compared to a continuum model. Here, groundwater density was exported from the regional-scale ECPM models at selected times and then interpolated onto the fracture systems in either the repository-scale DFN/CPM combined models or the regional-scale ECPM/DFN models and used to calculate the consistent groundwater flow throughout the model, and then flow-paths were computed using particle tracking. This was done at several different instances in time to capture changes in the regional flow boundary conditions. The groundwater density is interpolated on to each fracture intersection and then within each fracture on every finite-element used to discretise the flow in individual fractures, and so variable-density flow is resolved on a fine-scale.

2.2.4 Nesting of transport and calculation of performance measures: travel time (t_r), canister Flux (U_r), path-length (L_r) and F-factor (F_r)

A major objective of the SR-Can modelling is to compute groundwater flow-paths from each deposition hole (there are 7,483 in total) to the surface. The approach taken was to track particles moving with the advective flow velocity from release points around the deposition holes until they reach the top surface. In doing this, two key issues that have to be addressed are how to do this when two scales of model are being used, and how to deal with the transient evolution of the flow-field.

There is a potential nesting issue because the repository-scale models are very detailed around the repository but have limited extent. Vertically the model extends from –700 m elevation almost to the surface, 0 m elevation, but does not extend horizontally far beyond the edge of the repository footprint. The vertical path was found to be an important one in the combined DFN/CPM model, but still some paths exit the vertical sides of the model. The solution is to track particles along a first leg from the release points to the outer boundary of the repository-scale model, and then restart the particle tracking in the corresponding regional-scale DFN model on a second leg from the points where the particles hit the repository-scale model to the top surface. PM's such as travel-time are calculated as the cumulative travel-time along both legs of the path.

In terms of transients, it is possible in CONNECTFLOW to track particles as they move through a flow-field that evolves in time. However here it is preferred to use fixed instantaneous flow-fields from selected times in the future to obtain a qualitative assessment of the potential impact of releases at different times or evolutions in the flow-field. The objective is to establish whether flow-paths are sensitive to the retreat of the shoreline and if so whether flow-paths stabilise once the shoreline becomes remote to the site. Part of the reason for taking this approach is a practical one that to consider radionuclide transport for a range of radionuclides each with different retardation rates and different release times becomes a huge sequence of calculations. Hence, in order to compare transport at different release times, and between different concepts and variants, in a simpler and more quantifiable way, we perform a series of particle-tracking calculations at an appropriate set of release times. These release times are chosen carefully to represent different phases when the flow-field appears to be either changing significantly, or when there are periods of relative stability. Hence, for most transport calculations reported here, PM's are calculated based on fixed flow-fields at several selected times. Another motivation is the fact that the radionuclide transport code (FARF31) used in the SA calculations is based on a stream-tube formulation that assumes a steady-state flow-field.

For the case where the shoreline is retreating away from the site, such that a major discharge area is getting further away in time, then it is expected that flow-paths and travel-times are getting longer, and hence using the instantaneous flow-field at the release time is considered a conservative approximation for the subsequent evolution. When travel-times become longer than the temperate climate period due to retention (e.g. due to sorption), then one needs to consider transport in the wider context of the climate evolution, which is outside the remit of the study reported here.

To provide input to SA calculations, tables of performance measures are produced for each case using the four performance measures (PM's). In a continuum model these are defined as:

1. Travel-time [y], $t_r = \sum_l \frac{n_e \delta l}{q}$, where δl [m] is a step in distance along the path, for example through one finite-element, n_e [–] is the kinematic porosity, and q [m/y] the Darcy velocity.
2. Initial Darcy velocity [m/y] at the release point (Canister flux), $U_r = U_{0,r}$.
3. Path-length [m], $L_r = \sum_l \delta l$.
4. F-factor [y/m], $F_r = \sum_l \frac{a_r \delta l}{q}$, where a_r [m^2/m^3] is the fracture surface area per unit volume.

The subscript "*r*" indicates that the PM is calculated in the rock. That is, they only represent cumulative PM's for those parts of paths within the rock and exclude parts of flow-paths that pass through the EDZ or tunnel backfill. PM's are calculated for sections of paths within the EDZ and tunnels, but these are computed as separate PM's for each path and distinguish by a "*EDZ*" or "*t*" subscript, respectively.

In a DFN model the PM definitions are slightly different:

1. Travel-time [y], $t_r = \sum_f \frac{e_{t,f} w_f \delta l}{Q_f}$, where δl [m] is a step in distance along the path, between a pair of fracture intersections, $e_{t,f}$ [m] is the fracture transport aperture, w_f [m] is the flow width between the pair of intersections, and Q_f [m^3/y] is the flux between the pair of intersections in the fracture.
2. Initial Darcy velocity [m/y] at the release point (Canister flux), $U_r = \frac{1}{w_c} \sum_f \frac{Q_f}{\sqrt{a_f}}$, where the sum is over fractures intersecting a deposition hole, a_f is the area of the fracture [m^2] and w_c [m] is the height of the deposition hole.
3. Path-length [m], $L_r = \sum_f \delta l$.
4. F-factor [y/m], $F_r = \sum_f \frac{2 w_f \delta l}{Q_f} = \sum_f \frac{2 t_{r,f}}{e_{t,f}}$, $t_{r,f}$ [y] is the travel time in a fracture along the path.

The results from the particle tracking are then used to produce ensemble statistics for the performance measures, as well as locating the discharge areas. The ensemble is over the set of 7,483 particle start locations, one for each canister, as shown in the L 1.2 repository (Alternative "500 Centralt", see Figure 2-16). Apart from the work done on the repository layout by Design, no further attempt is made to avoid starting particles in either deterministic fracture zones or high transmissivity stochastic fractures in the DFN or ECPM models. In reality such features are likely to be avoided during repository construction, and hence the model may tend to see particles start in a wider range of possible fracture transmissivities than might be encountered in reality.

2.2.5 Flow and transport in the repository and Engineered Damage Zone (EDZ)

The repository is a large hydraulic feature with a potentially large impact on the local groundwater flow given the low hydraulic conductivity of the bedrock. In order to account for these effects it is necessary to represent the repository appropriately in the model. The potential conduits for flow within the repository are the deposition tunnels, access tunnels, ramp and shafts, together with the EDZ around the tunnels created during construction of the repository. The operational and resaturation phases are not considered here, so it is assumed that we only need consider saturated flow and that all tunnels have been backfilled with a mixture of bentonite and crushed rock to give homogeneous properties. For the EDZ, the most realistic scenario suggested by the Design Team is that hydraulic conductivity parallel to the axis of the tunnel will be enhance by about half an order of magnitude over a thickness of 0.3 m, but due to the drill and blast techniques used, the EDZ will occur in 5 m sections with intact sections of 0.5 m in-between (see /SKB 1997/, for example). The short intact sections arise due to the cycle of blasting with a short intact section around the cut of the previous blast round. A discontinuous EDZ as such obviously gives very little impact on groundwater flow, since the EDZ is a discontinuous hydraulic feature of small volume and only slightly enhanced conductivity. For this reason the EDZ was neglected in the regional-scale modelling, and in the repository-scale modelling, more pessimistic scenarios were assessed such as a continuous EDZ since otherwise it had negligible effect. For both the tunnel backfill and EDZ, values for hydraulic conductivity, porosity, and flow-wetted surface, a_r, were required. Only a single porosity was used for the tunnels and EDZ since RMD of groundwater constituents was neglected in the EDZ and backfill for the groundwater flow modelling. Likewise, a_r was set to zero for the same reason.

In terms of SA calculations, the near-field concept for KBS-3 considers three potential paths for radionuclides to leave the canister:

1. **Path_Q1**, diffusion into the mobile water in fractures surrounding the deposition hole.
2. **Path_Q2,** diffusion into mobile water in the EDZ.
3. **Path_Q3**, diffusion into tunnel pore-water.

Figure 2-15 shows three pathways considered in the KBS-3 concept. A fourth path, Q4, relates to diffusion through the floor of the tunnel to a fracture, but this is generally found to be negligible compared to the advective pathways.

In order to study each of these paths, the detailed repository-scale models have to represent the deposition holes, tunnels and EDZ explicitly, and flow-paths have be computed for a release at 3 appropriate positions around each canister. Hence, the PM's defined in Section 2.2.4 are calculated for 3 paths for each canister. It is possible that the 3 particles may follow very similar trajectories, such that t_r, L_r and F_r for the same paths are similar, but U_r will vary. Further for each path, the PM's are calculated for portions of the path spent in the rock, tunnels, and EDZ separately. Because a_r is set to 0 in the tunnel and EDZ, F_{EDZ} and F_T are zero, and therefore only t_{EDZ}, L_{EDZ}, t_t and L_t are calculated. Clearly a_r in the EDZ (and possibly in the tunnel) is none zero in reality. However, we do not include retention in EDZ and tunnel as retention mechanisms; and hence a_r is assumed to be zero since there is no need to quantify this retention.

In terms of the hydraulic properties, the hydraulic conductivity of the backfill is around 10^{-10} m/s which is smaller than the minimum block hydraulic conductivity for a 100 m block in rock domain HRD(A) at repository depth, and similar to the minimum hydraulic conductivity in HRD(D, E, M) /Hartley et al. 2005/. Hence, in terms of representing the repository in the regional-scale ECPM model, the repository is not expected to have an impact on effective properties in the vicinity of the repository. Further, the cross-sectional area of the repository is much smaller than that of a 50 m square finite-element, and so the tunnel system has negligible effect on the regional-scale hydraulic conductivity. For this reason the repository is ignored in the forward simulations between 2,020 AD and 20,000 AD.

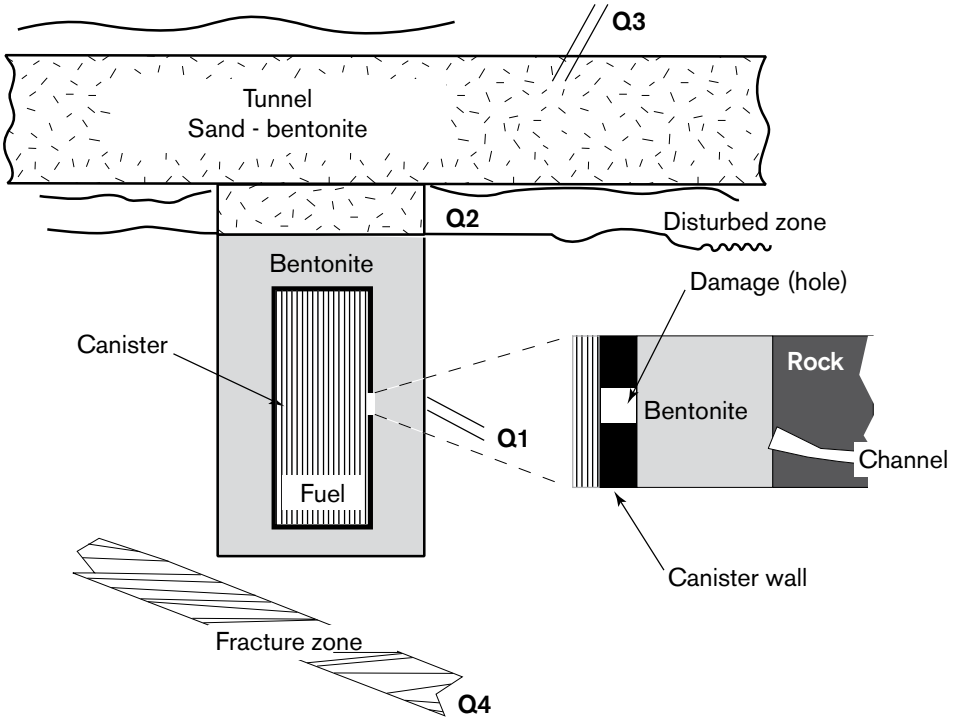

Figure 2-15. *Schematic view of the KBS-3 repository design, showing the small hole in the canister and the location of the various possible transport path into near-field rock.*

The geometrical representation of the repository was simplified slightly by making all cross-sections in the repository (tunnel, ramps and shafts) rectangular using the dimensions listed in Table 2-1. Also, the curved structure of the ramp was simplified by using linear connections instead of more proper bends. The implications of these simplifications are considered negligible.

The deposition tunnels are defined by a start and an end point for each tunnel. The start point of each deposition tunnel is geometrically connected to the main tunnels. The main tunnels, transport tunnels and the ramp are defined by smaller parts all connected to each other to form a hydraulically connected system. The shafts are five vertical features that have a diameter between 2.5 and 5.5 m but are represented as square sections with the equivalent cross-section area. The hydraulic parameter values assigned to the repository are given in Table 2-2. All different parts of the tunnel and ramp system are assigned the same values.

In the repository-scale models the EDZ was modelled explicitly as shown in Figure 2-17. In the continuum models the EDZ is modelled by a layer of elements below the base of the tunnel, whereas in the nested DFN/CPM models it is represented as an equivalent fracture beneath the tunnel. The EDZ 'fracture' is subdivided into 6 m sections to improve discretisation, and is assumed to be continuous as a conservative approximation. Table 2-3 gives the properties used in the EDZ. An example of how the tunnels are modelled in the nested DFN/CPM model was shown in Figure 2-7.

Finally, in the regional-scale combined ECPM/DFN both the tunnel system and EDZ are represented by equivalent fractures as shown in Figure 2-18. The EDZ 'fracture' and tunnel 'fractures' are orthogonal to give a hydraulic connection between the tunnels and EDZ. Similarly, the sections of tunnels, ramps and shafts are all linked to ensure they are hydraulically connected.

Table 2-1. Dimensions of different sections of the Laxemar Repository Layout "500 Centralt" as used in the model.

Section	Width [m]	Height [m]
Deposition tunnel	4.9	5.4
Main tunnel	10.0	7.0
Transport tunnel	7.0	7.0
Ramp	5.5	6.0
Shaft	2.5–5.5	–

Table 2-2. Summary of hydraulic parameter values used for the Laxemar Repository Layout "500 Centralt".

Parameter	Value
Tunnel hydraulic conductivity	10^{-10} m/s
Deposition hole hydraulic conductivity	10^{-11} m/s
Backfill porosity	0.35

Table 2-3. Summary of hydraulic parameter values used for the EDZ.

Parameter	Value
Thickness	0.3 m
Hydraulic conductivity	$3 \cdot 10^{-8}$–$3 \cdot 10^{-7}$ m/s
Kinematic porosity	10^{-4}

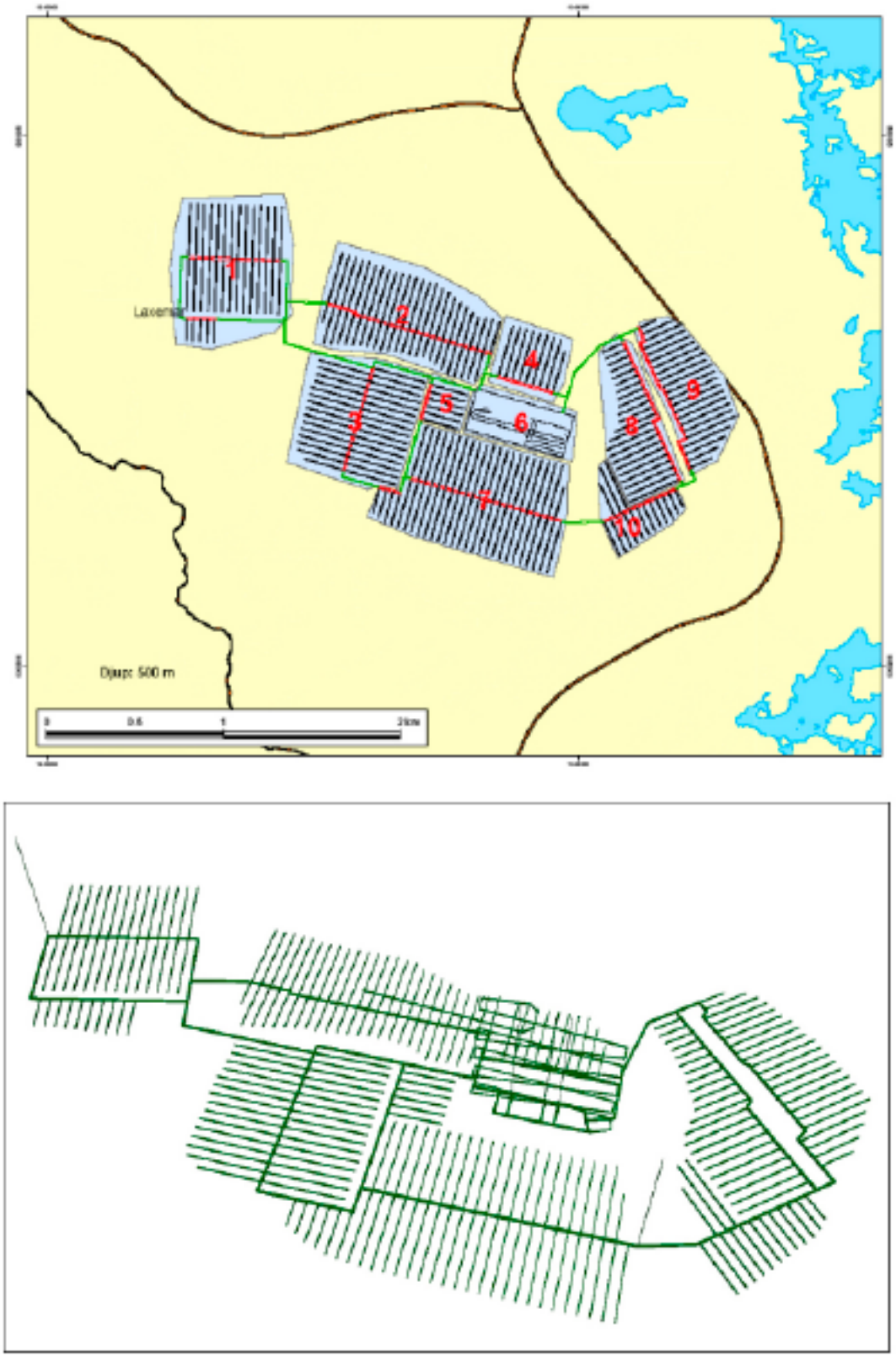

Figure 2-16. *Top: Plan view of the Laxemar repository layout at reference depth 500 m showing the numbered sub-areas. Bottom: Oblique view of the Laxemar repository layout, showing ramps and shafts.*

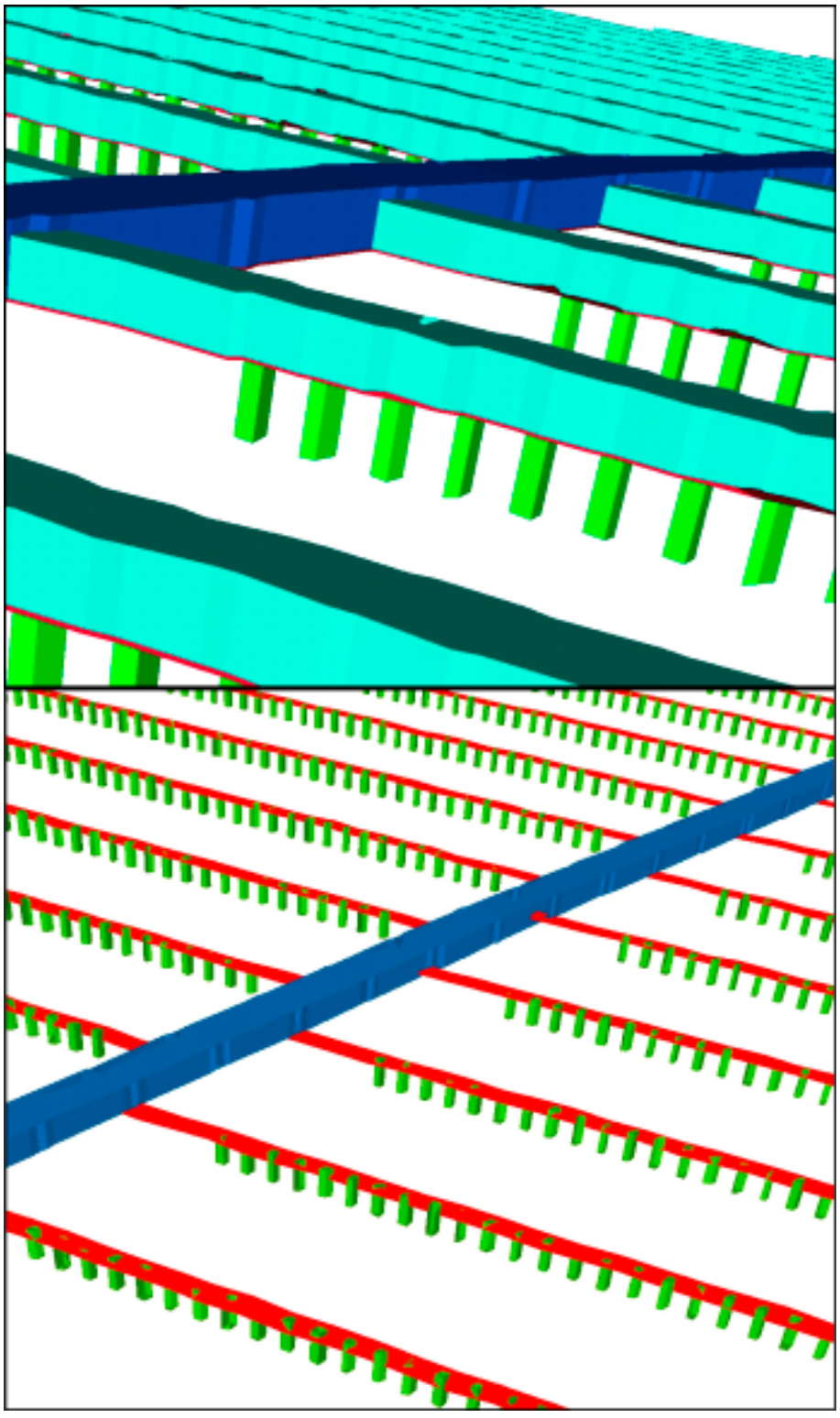

Figure 2-17. *Methods used to represent the tunnels and EDZ in the repository-scale models. Top: the continuum models showing a close up of the tunnels (blue, deposition holes (green) and EDZ (red). Bottom: the combined DFN/CPM model showing the access tunnel (blue), EDZ modelled as a set of equivalent fractures (red), and deposition holes (green).*

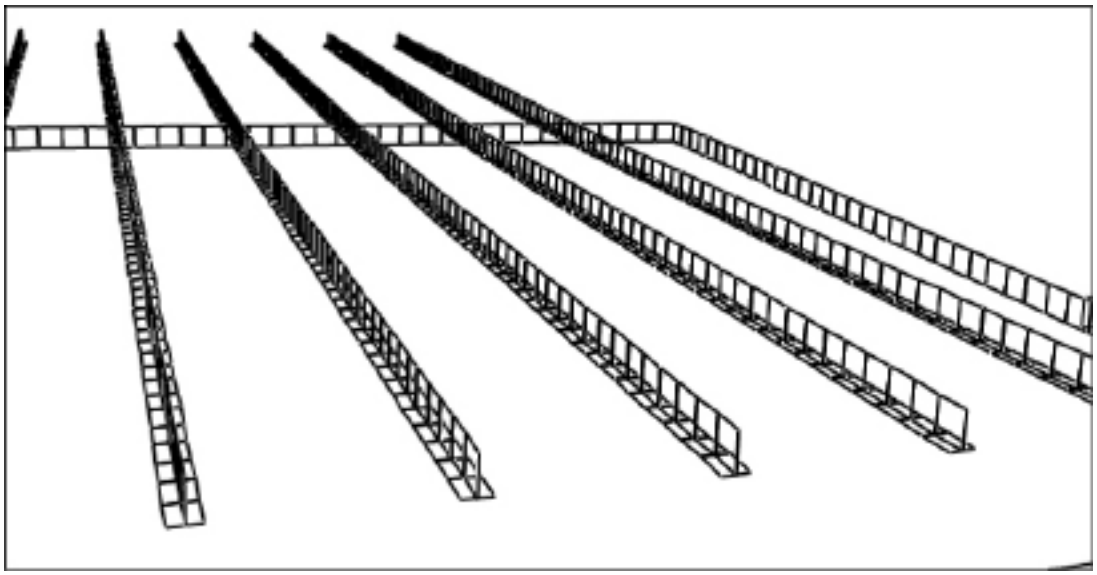

Figure 2-18. *Representation of tunnels and EDZ in regional-scale combined ECPM/DFN model. The plot shows a close up of a section of tunnels (vertical) and EDZ (horizontal).*

2.3 Data from Site descriptive modelling L 1.2

The data analysis and site modelling is documented in /SKB 2006b/ and /Hartley et al. 2006a/ and /Follin et al. 2006/. Here, a brief summary of the main assumptions from the site modelling adopted in this study, and key data such as the Hydro-DFN is given.

2.3.1 DFN assumptions and concepts

Few characteristics of the DFN can be determined uniquely and directly. Therefore it is necessary to assume a framework of conceptual models, and then derive parameters that best match the field-data.

Continuous power-law length distribution

One of the most difficult fracture characteristics to measure directly in the sub-surface is fracture size. Fracture trace lengths on outcrops can be measured on the scale of metres to tens of metres, and additional data are available for lineaments on the scale of 500 m to several kilometres, but this leaves a gap between the scales. A widely used assumption is one of a continuum of fracturing that spans all scales and that can be described by a power-law relationship between fracture intensity and size. The key parameters for the power-law distribution are the slope, k_r, and reference fracture radius, r_0. Often the distribution is defined only in a truncated range, $r_{min} < r < r_{max}$, either because the concept is only valid on a certain range or for practical reasons. As for the site modelling, it will be assumed that fractures with radial dimension greater than 564 m will be modelled deterministically having been detected as lineaments or fracture zones, whereas fractures with radial dimension less than 564 m will have to be modelled stochastically based on the Hydro-DFN.

It should be noted that CONNECTFLOW represents fractures as squares, rectangles or triangulated surfaces, and fracture size is defined in terms of side length L. Elsewhere in SKB's programme fractures are represented by discs of radius, r. Therefore, in this report, fracture size is described in terms of the equivalent radius. Assuming a consistent area between both representations implies a conversion $r = L/\sqrt{\pi}$.

A useful formula /Munier 2004/ associated with the power-law distribution is the fracture intensity, P32, for fractures in some truncated radius range $r_{max} > r > r_{min}$ based on the $P32_{tot}$ for the range $r > r_0$:

$$P32(r_{\max} > r > r_{\min}) = \frac{P32_{\text{tot}}\left(r_{\max}^{(2-k_r)} - r_{\min}^{(2-k_r)}\right)}{r_0^{(2-k_r)}}, \qquad \text{Equation (2-1)}$$

where k_r is the power-law slope. It was used extensively in this work to calculate the fracture intensity of additional small-scale fractures to be added to the regional-scale DFN, for example.

Fracture transmissivity models

One important uncertainty considered in the SDM studies for L 1.2 is the relationship between fracture transmissivity and size. In order to illustrate the implications of this assumption, three alternative concepts for fracture transmissivity, T, and its relationship to fracture radius, r, were considered in this study (as shown in Figure 2-19):

- Uncorrelated: Log-normal distribution for T,

  $$T = 10^{\mu+\sigma \text{N'}(0,1)}, \qquad \text{Equation (2-2)}$$

  where μ is the mean of $\log_{10}(T)$, σ is the standard deviation of $\log_{10}(T)$, and N'(0,1) is a normalised normal distribution, truncated between –2 and +2.

- Correlated: Power-law relation between T and r,

  $$T = a \times r^b, \qquad \text{Equation (2-3)}$$

  where a and b are the factor and exponent respectively describing the power-law relation.

- Semi-correlated: Random lognormal distribution about a mean that is based on a correlation,

  $$T = 10^{\log\left(a \times r^b\right)+\sigma \text{N'}(0,1)}, \qquad \text{Equation (2-4)}$$

  where a and b are the factor and exponent respectively of the deterministic part of the relation between r and T, σ is the standard deviation of $\log_{10}(T)$, and N'(0,1) is a normalised normal distribution, truncated between –2 and +2.

All three cases were simulated in the development of the Hydro-DFN, but the semi-correlated case was used as the main case.

The correlated case was originally proposed in /Dershowitz et al. 2003/. One argument for it is that, at least for deformation zones, the zone width often increases with length, and thus generally the number of individual conductive fractures associated with a zone. If the transmissivity distribution for individual fracture is the same, then based on the above assumption it follows that the effective transmissivity for the fracture zone should increase with the length of the fracture zone. Each of these concepts has an associated set of parameters which were derived in the Hydro-DFN to match the hydrogeological data.

Fracture kinematic porosity models

As part of the modelling, it is intended to derive fracture kinematic porosity as part of the block properties, as these will be needed in the regional flow modelling. There are no new data such as tracer tests to try to interpret, so the model for the porosity of an individual fracture will be based on Äspö Task Force 6c results /Dershowitz et al. 2003/. This approximates a direct correlation between the transport aperture e_t, and the transmissivity, such that:

$$e_t = aT^b \qquad \text{Equation (2-5)}$$

The values for the constants suggested from Äspö Task Force 6c are $a = 0.46$ and $b = 0.5$. For ECPM models, these parameters affect the kinematic porosity and hence travel-time for particle tracks. For DFN models, the transport aperture affects travel time directly. In both

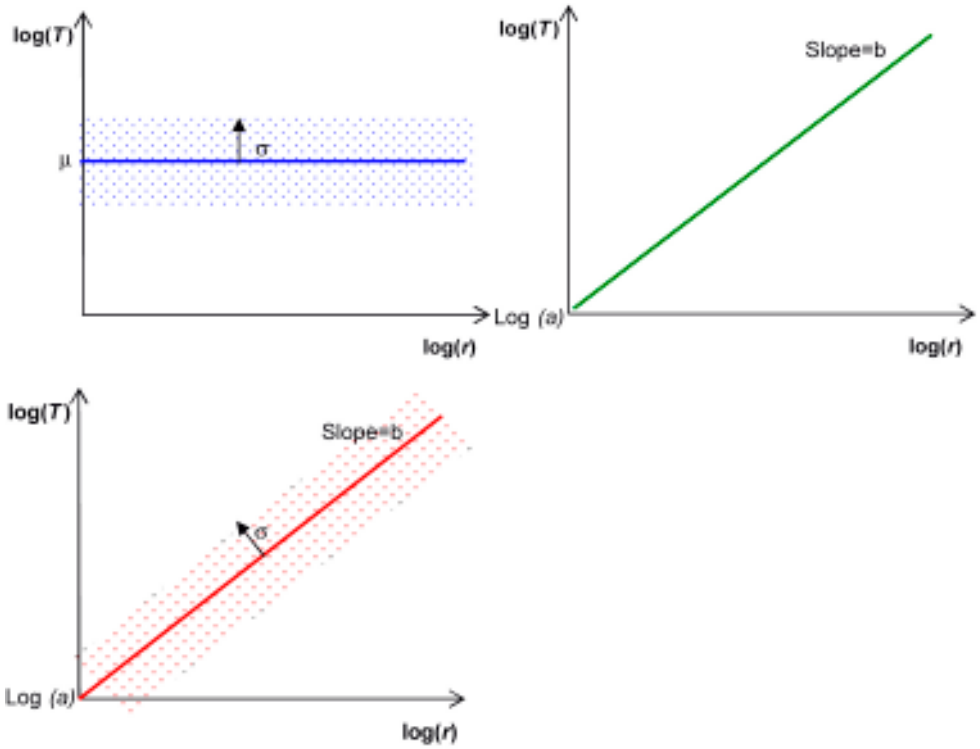

Figure 2-19. *Schematic of transmissivity models, top left to bottom: Uncorrelated, correlated, and semi-correlated. Note that for the Hydro-DFN models, the values of the parameters a and b used for the semi-correlated case are not necessarily the same as those used for the correlated case.*

cases the relationship is linear between transport aperture and travel-time. In this study, explicit sensitivities to the transport aperture are only calculated for the deterministic deformation zones. The sensitivity to properties of the background fractures can be estimated simply from the linear relationship.

2.3.2 Hydrogeological DFN properties (Hydro-DFN)

Spatial variability and rock volumes

The Geo-DFN model /Hermanson et al. 2005/ defined variations in fracture intensity, orientations and size distribution between the geological rock domains which are shown in Figure 2-20 and Figure 2-21. The geological definitions of rock domains were grouped together based on available or sub-divided as in the case of Ävrö Granite according to hydrogeological observations into the hydrogeological rock domains shown in Figure 2-1 /Hartley et al. 2006a/. Based on variations in fracture intensity and the frequency of PFL-anomalies down the bore-holes, most hydrogeological rock domains were further sub-divided into vertical layers above –200 m elevation, between –200 m and –600 m, and below –600 m. The exception was HRD(A2) which does not have the layer below –600 m. The properties of these layers are such that the equivalent block hydraulic conductivity decreases with depth.

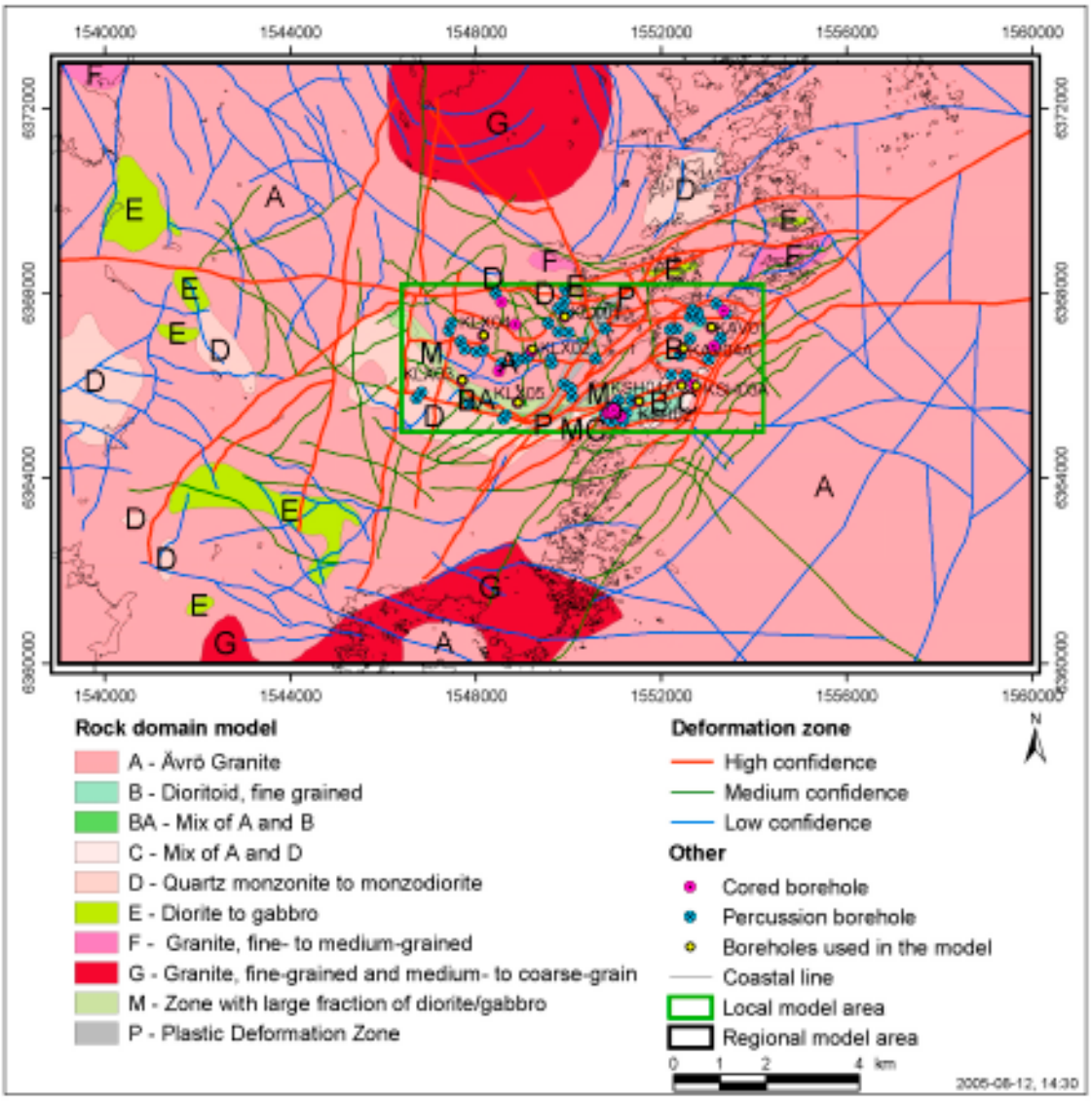

Figure 2-20. *Rock domain model for the regional model area. The local area for which the rock domains are illustrated in* Figure 2-21 *are shown by the green box.*

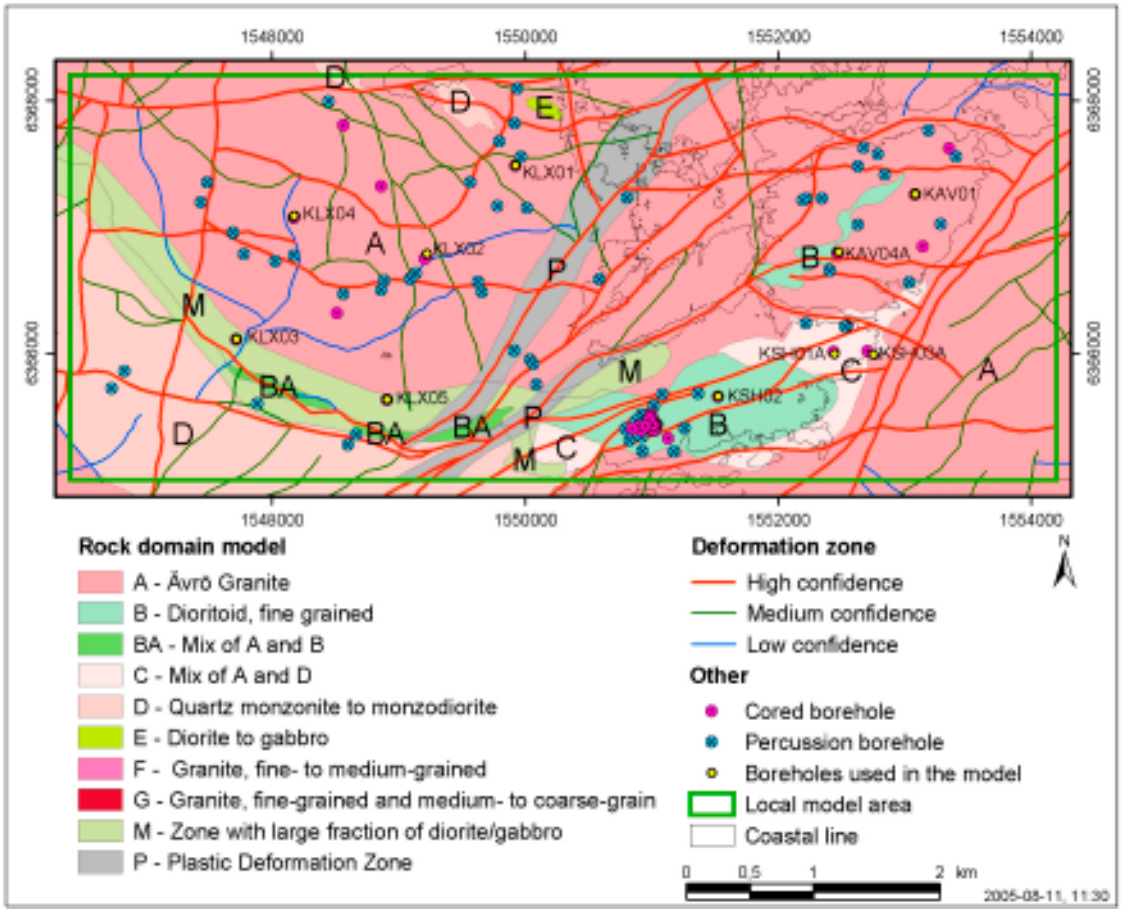

Figure 2-21. *Rock domain model for the local model area.*

Model parameters of the Hydro-DFN model with uncertainties

The SR-Can simulations are based on the reference case in the SDM modelling /Hartley et al. 2006a/. This uses the semi-correlated transmissivity model (Equation 2-4). Another feature introduced during the SDM regional modelling studies was to have anisotropy in transmissivity between the fracture sets. The transmissivity of the sub-horizontal set and the sub-vertical set parallel to the maximum horizontal stress is higher than that of the other sub-vertical sets. This was one of the changes made to achieve a better calibration against borehole hydrogeochemistry. The final Hydro-DFN regional case parameters used for the reference case are summarised in Table 2-4 to Table 2-7.

The site-modelling concluded the key uncertainties in the Hydro-DFN model were:

- The correlation between transmissivity and size. This has been addressed here by considering three alternative transmissivity models on regional scale (two on the repository scale).
- The slope of the power-law distribution as parameterised by k_r and r_0 that potentially effects fracture connectivity.
- Anisotropy between the fracture sets. This has been partly tested here by considering a variant with ten times higher transmissivity in the sub-vertical set parallel to the maximum horizontal stress.
- The spatial variability between boreholes means the uncertainty in how representative it is to extrapolate a single borehole to an entire rock domain needs to be quantified, but as of L 1.2 too few boreholes have been drilled and interpreted.
- Depth dependency in hydraulic parameters.

Table 2-4. Description of the Hydro-DFN input parameters for rock domain HRD(A).

Fracture set name	Orientation set pole: (trend, plunge), concentration	Fracture radius model power-law (*r0*, *kr*)	Intensity P32 (m^2/m^3); valid radius interval (*rmin, rmax*)	Relative intensity of P32	Semi-correlated transmissivity model parameters *(a,b,σ)*
Set_A	(338.1, 4.5) 13.06	(0.28, 2.73)	Above –200 m: 50% of open = 1.70	0.18	$(3.5 \cdot 10^{-9}, 1.0, 0.9)$ z > –200
Set_B	(100.4, 0.2) 19.62	(0.28, 2.83)		0.19	$(3.5 \cdot 10^{-10}, 1.0, 0.9)$ –200 > z > –600
					$(1.1 \cdot 10^{-10}, 1.0, 0.9)$ z < –600
Set_C	(212.9, 0.9) 10.46	(0.28, 2.73)	Below –200 m: 35% of open = 1.19	0.19	$(3.5 \cdot 10^{-8}, 1.0, 0.9)$ z > –200
Set_d	(3.3, 62.1) 10.13	(0.28, 2.76)		0.27	$(3.5 \cdot 10^{-9}, 1.0, 0.9)$ –200 > z > –600
Set_f	(243, 24.4) 23.52	(0.40, 3.6)	(0.28, 564)	0.17	$(1.1 \cdot 10^{-9}, 1.0, 0.9)$ z < –600

Table 2-5. Description of the Hydro-DFN input parameters for rock domain HRD(D, E, M). The recommended transmissivity model is highlighted in bold.

Fracture set name	Orientation set pole: (trend, plunge), concentration	Fracture radius model power-law (*r0*, *kr*)	Intensity P32 (m^2/m^3); valid radius interval (*rmin, rmax*)	Relative intensity of P32	Semi-correlated transmissivity model parameters *(a,b,σ)*
Set_A	(338.1, 4.5) 13.06	(0.28, 2.63)	Above –200 m: 60% of open = 0.84	0.22	$(1.8 \cdot 10^{-9}, 1.0, 0.9)$ z > 200
Set_B	(100.4, 0.2) 19.62	(0.28, 2.68)		0.15	$(3.5 \cdot 10^{-10}, 1.0, 0.9)$ –200 > z > –600
					$(1.1 \cdot 10^{-10}, 1.0, 0.9)$ z < –600
Set_C	(212.9, 0.9) 10.46	(0.28, 2.59)	Below –200 m: 30% of open = 0.42	0.17	$(1.8 \cdot 10^{-8}, 1.0, 0.9)$ z > 200
Set_d	(3.3, 62.1) 10.13	(0.28, 2.63)	(0.28, 564)	0.36	$(3.5 \cdot 10^{-9}, 1.0, 0.9)$ –200 > z > –600
Set_f	(243, 24.4) 23.52	(0.40, 3.6)		0.09	$(1.1 \cdot 10^{-9}, 1.0, 0.9)$ z < –600

Table 2-6. Description of the Hydro-DFN input parameters for rock domain HRD(B,C). The recommended transmissivity model is highlighted in bold.

Fracture set name	Orientation set pole: (trend, plunge), concentration	Fracture radius model power-law (*r0*, *kr*)	Intensity P32 (m^2/m^3); valid radius interval (*rmin, rmax*)	Relative intensity of P32	Semi-correlated transmissivity model parameters *(a,b,σ)*
Set_A	(330.3, 6.1) 16.80	(0.28, 2.77)	Above –200 m: 27% of open = 1.40	0.24	$(1.4 \cdot 10^{-9}, 1.2, 0.9)$ z > 200
Set_B	(284.6, 0.6) 10.78	(0.28, 2.91)		0.15	$(1.6 \cdot 10^{-11}, 0.8, 0.9)$ –200 > z > –600
					$(5.1 \cdot 10^{-12}, 0.8, 0.9)$ z < –600
Set_C	(201.8, 3.7) 14.60	(0.28, 2.92)	Below –200 m: 27% of open = 1.40	0.26	$(1.4 \cdot 10^{-8}, 1.2, 0.9)$ z > 200
Set_d	(84.6, 81.8) 6.98	(0.28, 2.87)		0.26	$(1.6 \cdot 10^{-10}, 0.8, 0.9)$ –200 > z > –600
Set_f	(67.1, 15.5) 11.73	(0.21, 3.27)	(0.28, 564)	0.10	$(5.1 \cdot 10^{-11}, 0.8, 0.9)$ z < –600

Table 2-7. Description of the Hydro-DFN input parameters for rock domain HRD(A2). The recommended transmissivity model is highlighted in bold.

Fracture set name	Orientation set pole: (trend, plunge), concentration	Fracture radius model power-law (*r0*, *kr*)	Intensity P32 (m^2/m^3); valid radius interval (*rmin, rmax*)	Relative intensity of P32	Semi-correlated transmissivity model parameters *(a,b,σ)*
Set_A	(330.3, 6.1) 16.80	(0.28, 2.78)	Above –200 m: 28% of open = 1.43	0.24	($4.5\cdot10^{-9}$, 0.7, 0.9) z > –200
Set_B	(284.6, 0.6) 10.78	(0.28, 2.87)		0.16	($7.5\cdot10^{-9}$, 0.7, 0.9) z < –200
Set_C	(201.8, 3.7) 14.60	(0.28, 2.90)	Below –200 m: 22% of open = 1.13	0.22	($4.5\cdot10^{-8}$, 0.7, 0.9) z > –200
Set_d	(84.6, 81.8) 6.98	(0.28, 2.85)		0.27	($7.5\cdot10^{-8}$, 0.7, 0.9) z < –200
Set_f	(67.1, 15.5) 11.73	(0.21, 3.27)		0.11	
			(0.28, 564)		

2.3.3 Fracture connectivity and flow-wetted-surface (FWS)

The flow-wetted-surface, or a_r, is required to calculate the F-factor along flow-paths in continuum models. It is also used in the calculation of rock matrix diffusion (RMD) for the reference water transport. There are several possible approaches to estimating a_r. One possibility is to obtain a value by calibrating the models of palaeo-hydrogeology in terms of the RMD process to estimate a value of a_r that gives a reasonable reproduction of the measured hydro-geochemistry data. Two other possible approaches are either to perform a connectivity analysis of the Hydro-DFN to calculate the fracture intensity of the connected network, $P32_c$, or to use the hydraulic PFL-f data directly. Each of these approaches was considered in the SDM modelling /Hartley et al. 2006a/.

Starting with the PFL approach, the vertical frequency of PFL-anomalies, $P10_{PFL,}$ is first computed, then two formulae are needed to estimate a_r. Firstly, $a_r = 2\times P32_c$, where $P32_c$ is the connected fracture intensity. The factor 2 comes from the two rock surfaces either side of the fracture at which matrix diffusion and sorption can take place. Secondly, $P32_c = \alpha\times P10_c$ relates the areal fracture intensity of connected fractures to the vertical frequency of connected fractures, $P10_c$. For example, for a single horizontal set and a vertical borehole, α would be 1.0. The factor α can be estimated based on the average Terzaghi correction from borehole fracture orientation data. Here, it is evaluated in a more specific way as a function of the geometrical parameters of the DFN model.

The approach based on DFN modelling is to use the relationship $a_r = 2\times P32_c$, and calculate $P32_c$ from a connectivity analysis of the Hydro-DFN model. In performing the connectivity analysis, it is informative to calculate both $P32_c$ and the vertical frequency of connected fractures, $P10_c$, since this gives an estimate of the number of connected fractures intersecting a vertical deposition hole. $P32_c$ is calculated by generating a network of fractures within a given block-size, removing all isolated fractures and isolated clusters that have no connection to the boundary, removing all dead-end fractures (those with only one intersection), and then the surface area per volume of the remaining fractures is calculated. To calculate $P10_c$, fractures are generated within a given block-size, all isolated and dead-end fractures are removed, and then an array of 25 equally spaced vertical boreholes is used to sample the fracture spacing in the block. This means the total simulated core length is 25 multiplied by the block size. $P10_c$ is then calculated as the average connected fracture frequency over the 25 simulated cores. The calculated $P32_c$ and $P10_c$ can be sensitive to the block size and minimum fracture size truncation used since they both affect connectivity. A fracture size truncation of $r_{min} = 0.5$ m was used compared to the r_0 of 0.28 m for Set_A-Set_d. This was close to the lower limit for what was computationally feasible for a 200 m block.

Using the Hydro-DFN models for boreholes KLX03, KLX04, KAV04 and KSH01A, the connected $P32_c$ and $P10_c$ were calculated above and below –200 m. The ratio of $\alpha = P32_c/P10_c$ was found to be 2.5 on average. The a_r values calculated by both methods are summarised in

Table 2-8. The vertical frequency of connected fractures, $P10_c$ may also be compared directly with $P10_{PFL}$ in Table 2-9. The a_r values calculated using $P32_c$ are generally similar to the a_r values calculated using $P10_{PFL}$ for all boreholes, except for the lower sections of KLX04 and KSH01A where they are higher. In KLX03 and KLX04 both approaches give consistent values, predict a much higher a_r in KLX04 than in KLX03, and higher values in the upper rock. It should be noted that the a_r values given by the model are sensitive to the choice of r_{min}, and if all fractures were included down to r_0, then a_r would increase.

Based on considering other boreholes with PFL-anomaly data in the L 1.2 data freeze, minimum, average and maximum values of a_r values were estimated based on the variations with the rock domains as presented in Table 2-10.

Table 2-8. Comparison of a_r values calculated in two different ways based on the Hydro-DFN model and the PFL-f data.

Elevation interval	Borehole	a_r (m^2 m^{-3}) a_r = 2×P32c (model)	a_r = 2×α×P10PFL (PFL)
Above –200 m elevation	KAV04A (HRD(A2))	1.1	1.2
	KLX04 (HRD(A))	1.7	1.2
	KLX03 (HRD(D, E, M))	0.6	0.6
	KSH01A (HRD(B,C))	1.0	1.5
Below –200 m elevation	KAV04A (HRD(A2))	0.7	0.8
	KLX04 (HRD(A))	1.0	0.5
	KLX03 (HRD(D, E, M))	0.2	0.2
	KSH01A (HRD(B,C))	1.0	0.1

Table 2-9. Comparison of $P10_{PFL}$ and $P10_c$.

Elevation interval	Borehole	P10 P10c (model)	P10PFL (PFL)
Above –200 m elevation	KAV04A (HRD(A2))	0.20	0.23
	KLX04 (HRD(A))	0.35	0.24
	KLX03 (HRD(D, E, M))	0.13	0.12
	KSH01A (HRD(B,C))	0.20	0.29
Below –200 m elevation	KAV04A (HRD(A2))	0.14	0.15
	KLX04 (HRD(A))	0.20	0.09
	KLX03 (HRD(D, E, M))	0.04	0.05
	KSH01A (HRD(B,C))	0.20	0.03

Table 2-10. Average, minimum and maximum a_r values for each rock domain, calculated from PFL-anomaly data.

	Rock domain	average a_r (m^2 m^{-3})	min a_r (m^2 m^{-3})	max a_r (m^2 m^{-3})
Above –200 m elevation	HRD(A2)	1.9	1.2	2.4
	HRD(A), HRD(F,G)	1.4	1.2	1.6
	HRD(D,E,M)	0.6	0.6	0.6
	HRD(B,C)	0.9	0.4	1.5
Below –200 m elevation	HRD(A2)	0.6	0.3	0.8
	HRD(A), HRD(F,G)	0.3	0.2	0.5
	HRD(D,E,M)	0.2	0.2	0.2
	HRD(B,C)	0.4	0.1	0.5

2.3.4 Hydraulic Conductor Domain (HCD) models with uncertainties

The geometry of the deformation zones were supplied to the SDM studies by Geology using the Rock Visualisation System (RVS). This HCD model contains 37 zones that have been classified as high confidence zones. 65 zones are classified as intermediate confidence zones, and 98 as low confidence DZ's. This is illustrated in Figure 2-22. Most zones are vertical, though there are some gently dipping DZ's, such as the ZSMEW007A DZ that runs just north of the repository layout. Hydraulic thickness is based on geological estimates of the width of the DZ. If no value is given by the geologist, the thickness is approximated with a default value of 20 m.

For 24 of the zones, an explicit transmissivity is interpreted on the basis of the hydraulic tests in the HCD's. The interpretation of the hydraulic measurements in the DZ's suggested a significant depth trend in zone transmissivity. Three different functional forms were derived based on a step-change, power-law and exponential. The step-change function was used in the SDM reference case for consistency with the description of fracture transmissivity in the stochastic fractures sets. The mean transmissivity is given as:

- $-300 \le z \le 0$: $T = 2.0 \cdot 10^{-5}$ m^2 s^{-1}.
- $-600 \le z \le -300$: $T = 1.2 \cdot 10^{-5}$ m^2 s^{-1}.
- $-2{,}100 \le z \le -600$: $T = 7.1 \cdot 10^{-7}$ m^2 s^{-1}.

For deterministic DZ's with one or more measured transmissivities, the geometric mean T and the representative 'mean elevation' of these observations were used to modify the suggested depth trend curve for transmissivity (T) defined above, by adding/subtracting a number to/from the given equation so that it passes through the given point. After the depth trends are implemented, the values are calibrated against PSS data. Where there is a discrepancy between the modelled and observed transmissivity, the zones are modified indvidually to

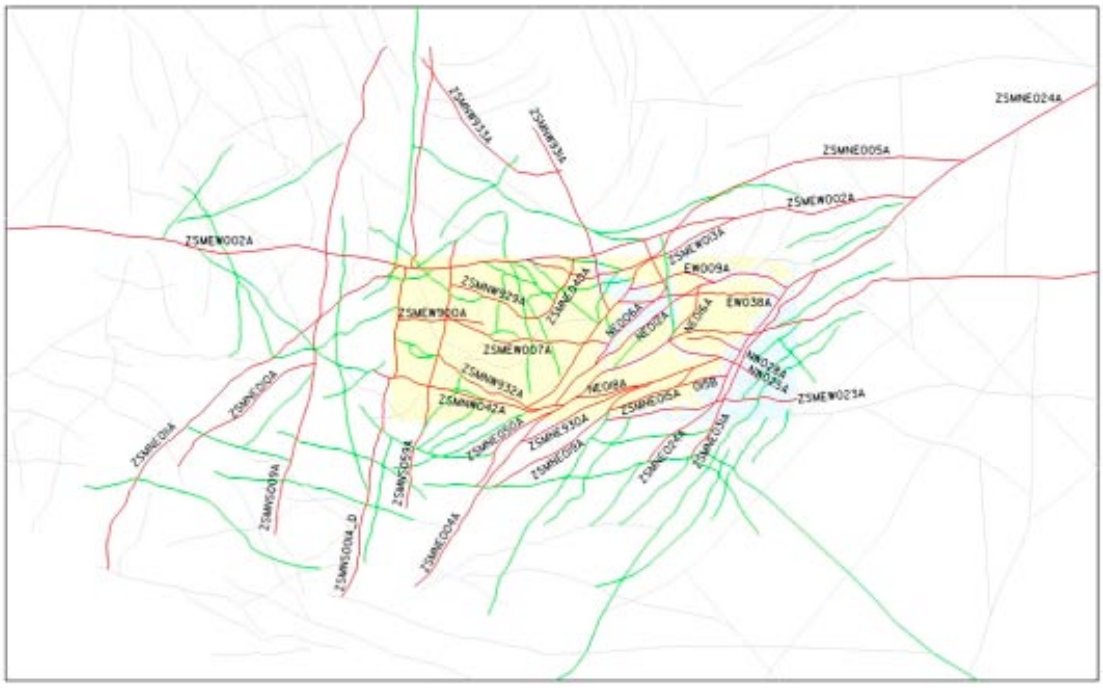

Figure 2-22. *HCD used in the SDM and SR-Can studies for L 1.2. Deformation zones coloured red have been verified and are high confidence. Lineaments are coloured green and have intermediate or low confidence.*

obtain a better match. Based on the data, intersections of the boreholes with the deformation zones were identified and the intersected horizontal segment of the zone was calibrated against corresponding PSS data. For each intersected deformation zone, the depth trend curve was adjusted such that it passes through the interpreted transmissivity at the "mean elevation" in the provided data file. In the calibration step, only the horizontal segment with the PSS data was modified, whilst checking that the transmissivities remained within the suggested range. For deterministic DZ's without any measurements, the given depth trends for T are used. Global maximum and minimum T values are also provided and these are used to limit the resulting T values. The deformation zones were divided into triangles of side no more than 200 m to make their discretisation more spatially uniform. An example of the implementation of the HCD model is illustrated in Figure 2-23. It is also stipulated that all deterministic DZ's should be in hydraulic contact with the overburden (the modelled HSD). The HCD kinematic porosity was set to10^{-3} for zones less than 100 m thick and 10^{-2} for zones thicker than 100 m. In the reference case, all deterministic DZ's are retained since it is a conservative assumption with respect to radionuclide transport.

Due to the uncertainties in the HCD model, the following variants were considered:

- Confidence levels – a variant with only DZ's of high and intermediate confidence of existence.
- Heterogeneity – variants that have spatial variability in the transmissivity within a DZ.

For the variants with spatial variability, two different values for the magnitude of spatial variability was consider for a correlation length of 200 m, and three realisations were performed for each case. An example with spatial variability is shown in Figure 2-24.

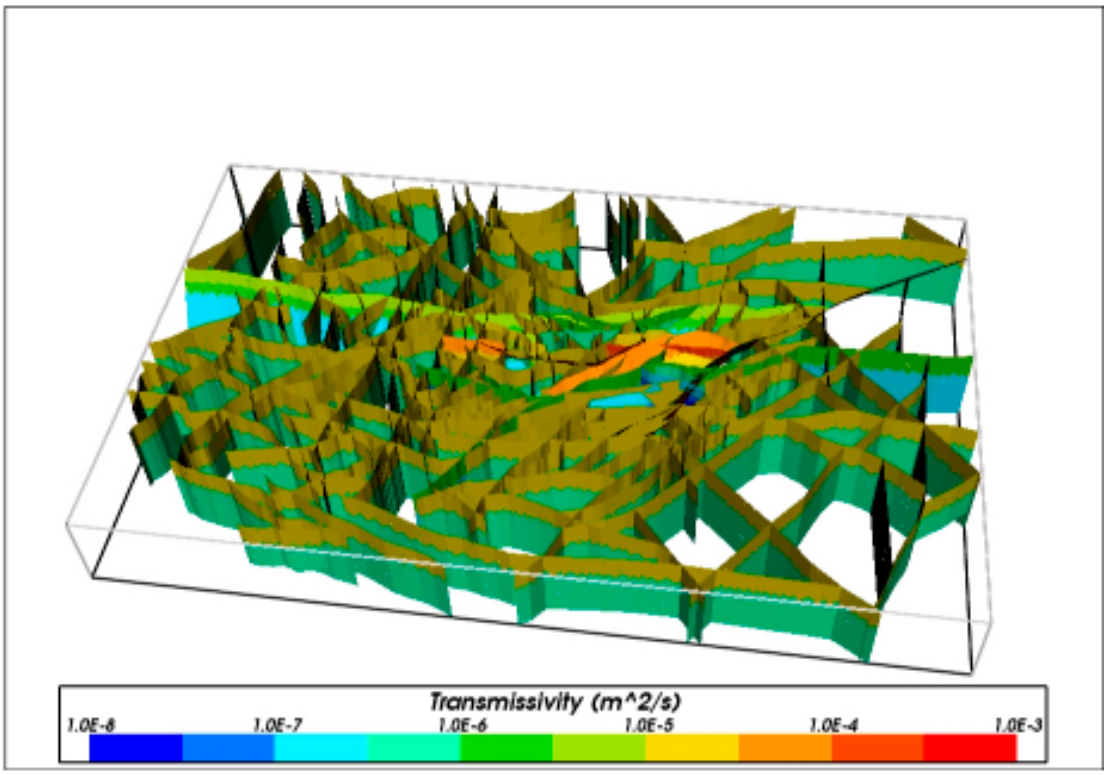

Figure 2-23. *HCD for regional-scale modelling in 3D. The zones are coloured by transmissivity, where red is high and blue is low.*

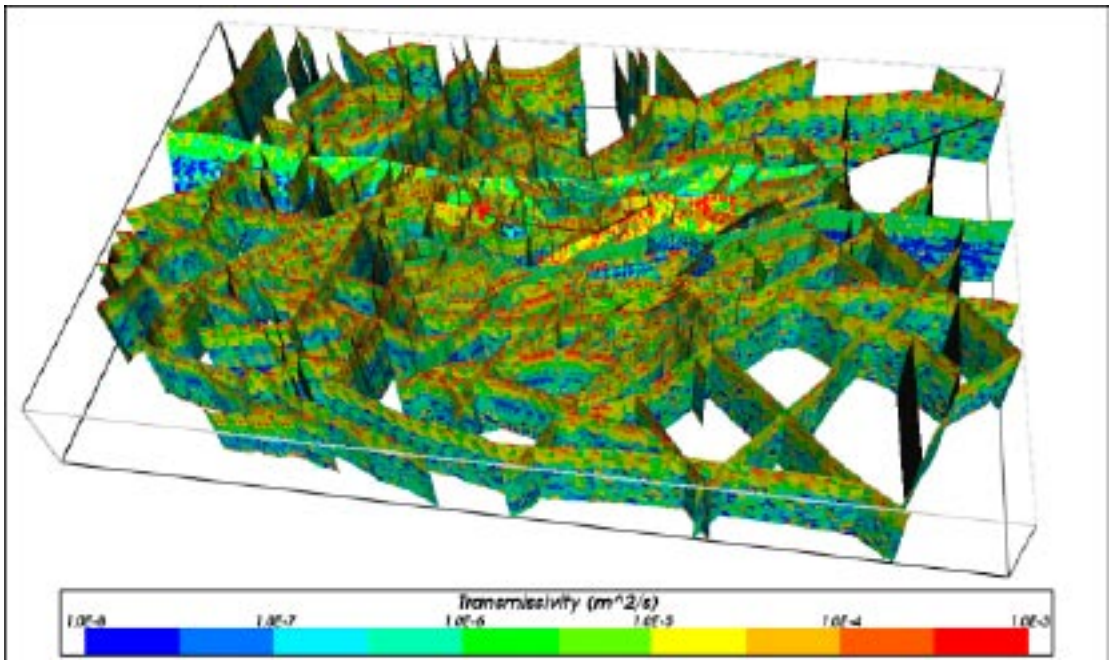

Figure 2-24. *HCD model with all zones and stochastic hydraulic properties. The zones are coloured by transmissivity, where red is high and blue is low.*

3 Regional-scale modelling of the post-glacial and temperate climatic periods (8,000 BC to 22,000 AD)

The continuum modelling for SDM L 1.2 developed a coupled model of groundwater flow and reference water transport with rock matrix diffusion (RMD) from 8,000 BC to the present-day to study conditions and parameters consistent with measured borehole profiles of hydraulic conductivity and hydro-geochemistry. This supported some conditioning of the model, but significant uncertainty still remains due to a sparsity of borehole data.

As mentioned in Section 2.2 above, one requirement for the safety assessment calculations is to extend the regional-scale ECPM models developed for SDM L 1.2 to consider the future evolution of flow-paths and groundwater chemistry over the period up to 20,000 AD when a transition to permafrost conditions are expected. In addition, it is necessary to consider a wider range of sensitivities appropriate to safety assessment than was possible in SDM L 1.2, such as considering a lower flow-wetted-surface, a higher transmissivity in the sub-vertical Set_C, different relationships between fracture size and transmissivity, and removing low confidence deformation zones. Some of these issues will later be re-quantified and cross-verified against DFN model on the local- and repository-scales in Section 4. However, current capabilities within CONNECTFLOW means that a greater diversity of processes such as transient transport of reference waters coupled to variable-density flow can be modelled using CPM/ECPM models than in DFN models.

The regional-scale hydrogeological properties, such as a hydraulic conductivity tensor and kinematic porosity, for the ECPM model are obtained by upscaling an underlying DFN model. Implicit representations of the deterministic large-scale deformation zones (HCD's) are included.

In SDM L 1.2 /Hartley et al. 2006a/ it was found difficult to obtain an acceptable match to the hydro-geochemical data based on the initial interpretation of Hydro-DFN properties from hydraulic data for KLX04. Improved results were achieved once the top surface flow boundary had been derived from surface water data to give a reduced driving head, and half order of magnitude reduction in hydraulic conductivity below –600 m elevation. Sensitivities to parameters and conditions were quantified in terms of the predictions of hydro-geochemical constituents in the site boreholes. Sensitivities considered were to the size of model, initial and boundary conditions, stochastic variability in the HRD, the relationship between fracture size and transmissivity, the confidence in interpreting the HCD, depth dependency in both HRD and HCD, spatial variability in the HCD, the incorporation of a more detailed HSD model, and some transport properties including the flow wetted surface (FWS). Many of these uncertainties are also explored here, but in the context of the sensitivity of the SA performance measures and exit locations. The SDM suggested that uncertainties with respect to spatial variability of the HCD, anisotropy between the fracture sets, flow-wetted-surface, and the kinematic porosity are of particular importance to safety assessment.

3.1 Model set-up and specification

To some extent the main model and the outer boundaries of the model are based on earlier modelling work of the site /Hartley et al. 2005/. The model was developed further in the SDM L 1.2 project /Hartley et al. 2006a/. The final model obtained from the SDM modelling as used as the central case for use in sensitivity analysis is referred to as the "Reference case" and its properties are summarised in Table 3-1.

Table 3-1. Description of the Reference Case.

Property	Description	Uncertainties and parameter ranges
Domain	Extended regional model domain with 50 m element-size embedded grid in Laxemar, Simpevarp and Ävrö release areas, and 100 m element-size elsewhere.	
Initial condition	Initial condition is set to full glacial melt water conditions between ground surface and an elevation of –700 m; then linear gradient to no Glacial and full Brine at –1,500 m elevation. Between –700 m and –1,500 m elevation, the Brine increases linearly from 0 to 100%. Below –1,500 m elevation, a full Brine condition is applied.	Brine at shallower depths in Simpevarp subarea?
Top surface flow boundary condition	Top-surface head equals simulated watertable +30% of the difference between the simulated watertable and the topographic surface (see /Rhén et al. 2006/)	Watertable level or flux boundary condition.
Top surface waters	Surface groundwaters are: Glacial and Littorina during early Baltic Ice Lake, Yoldia Sea and Ancylus Lake periods; Meteoric water and Littorina during the Littorina Sea and current Baltic Sea phases. The provided sea-water salinity history is used to determine relative fractions of Littorina and Meteoric waters at the top surface of the model offshore.	
Density and viscosity	Density and viscosity a function of salinity (transient), temperature (fixed), and total pressure (transient).	
Tranmissivity model	Hydraulic properties obtained from an upscaled regional-scale DFN that is based on the semi-correlated cases of the Hydro-DFN models.	Alternative *T* models are correlated or uncorrelated.
Anisotropy	Anisotropy has been introduced by decreasing the transmissivity of fracture sets Set_A and Set_B by a factor of 10.	Anisotropy has not been fully investigated. Other possibilities include increasing transmissivity of Set_C.
HCD confidence	HCD included all zones.	Alternative is exclusion of low confidence zones.
Depth dependency	HRD: The underlying DFN has a step change in properties according to the Hydro-DFN, although a transition elevation of –200 m is used instead of –300 m. For all HRD except HRD(A2), the upscaled conductivity is then reduced by half an order of magnitude below an elevation of –600 m. HCD: Implemented as a step function in elevation (0 to –300 m, –300 m to –600 m, < –600 m), conditioned at boreholes against measured transmissivities.	Borehole data suggests that levels of the two step changes could be within the ranges –200 m to –350 m and –500 m to –650 m. Alternative depth trend functions for HRD and HCD are exponential and power-law.
HSD	Homogeneous 3 layer HSD of uniform 1 m thickness per layer.	Overburden model from /Werner et al. 2005/ with uncertainty in hydraulic conductivities.
Flow-wetted surface and salinity matrix diffusion length	Flow-wetted-surface (FWS) per unit volume for RMD above –200 m elevation: a_r = 2.0 m^2/m^3.for HRD(A2), a_r = 1.0 m^2/m^3 for HRD(D,E,M), a_r = 1.5 m^2/m^3 elsewhere. For all rock domains below –200 m elevation, a_r = 1.0 m^2/m^3 (see /Hartley et al. 2006a/) Matrix diffusion length into matrix blocks: $L_D = 1/a_r$	Other possibilities are FWS based on PFL-f or P32c analysis.
Kinematic porosity	HRD kinematic porosity is taken from the upscaled regional-scale DFN that is based on the semi-correlated cases of the Hydro-DFN models. However, the 10th percentile values for the 20 m block scale kinematic porosity obtained from the appropriate Hydro-DFN are used as minima of *ne,b*. HCD porosity 10^{-3} for zone thickness $W < 100$ m and 10^{-2} for $W \geq 100$ m.	An alternative for HCD is a depth-dependent porosity based on the transmissivity and thickness of the zones.

Property	Description	Uncertainties and parameter ranges
Diffusion accessible porosity	Diffusion accessible porosity from /Byegård et al. 2006/ upper limit n_m = 5.9·10^{-3}.	1.3·10^{-3}–5.9·10^{-3} (Byegård)
Diffusion coefficient	Intrinsic diffusion coefficient into matrix *De* = 1.5·10^{-13} m^2/s.	1.5·10^{-13} (Byegård) – 3.1·10^{-13} (ChemNet)
Dispersion lengths	*al* = 40 m, *at* = 5 m	

3.1.1 Model domain and properties

To a large extent the boundaries are based on surface water catchments for the present-day inland areas and large deformation zones in the present-day sea areas. The extent of the model domain is shown in Figure 3-1.

In the SDM L 1.2 project, several model cases for the HCD, as formulated in /Hartley et al. 2006a/ and based on data in /Rhén et al. 2006/, have been modelled and analysed. These cases have been analysed at a regional model scale, matching results of the simulated hydro-geochemical evolution to measured hydro-geochemical data, see /Hartley et al. 2006a/. The hydraulic properties were derived single-hole PFL and PSS test data. As of L 1.2, no hydraulic interference test data was available to support simulations or calibrations to adjust the assigned hydraulic properties of the HCD's.

The reference case in /Hartley et al. 2006a/ includes all HCD's (i.e. deformation zones with high, medium and low confidence). A depth trend, as a three-step function in elevation (0 to –300 m, –300 to –600 m, deeper than –600 m), was also applied to the transmissivity in the HCD. However, in order to honour measured values of transmissivity, for each hydraulically tested deformation zone, the depth trend curve was adjusted such that it passed through the interpreted *T* value at a representative depth in the data set, and the mean transmissivity was then estimated for the three elevation intervals. If no tests were available for a HCD, then the

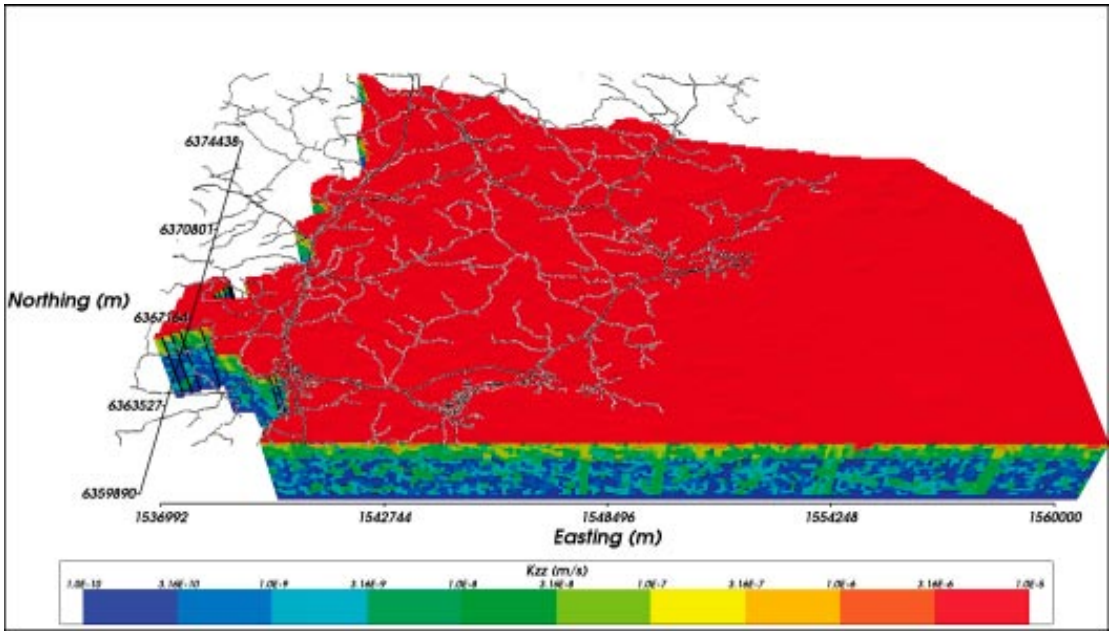

Figure 3-1. *The distribution of hydraulic conductivity in the reference case. The high hydraulic conductivity red layer represents the 3 m thick hydraulic soil domain. The depth trend in hydraulic conductivity may be seen, together with longer linear vertical features corresponding to the deformation zones.*

mean values for the three-step depth trend were used. Hence, the transmissivities of the HCD's were conditioned to measured values (PSS transient injection tests, test scale 100 m) in a horizontal band along the HCD at elevations corresponding to the HCD intersection with the borehole.

Efforts were made in the SDM study to find suitable Hydro-DFN models based on borehole data. A number of hydraulic rock domains were identified based on variations in fracture properties between boreholes that intercept the different rock domains. Different geological and hydraulic fracture properties were interpreted for the different rock domains to give the parameters defined in Section 2.3.2, and some uncertainties were quantified explicitly such as the relationship between fracture size and transmissivity. The best fit was found for the semi-correlated transmissivity model (Equation 2-4). The Reference case ECPM model described in this section uses HRD hydraulic conductivities from an upscaled DFN model divided into several volumes. The hydraulic properties (hydraulic conductivity tensor, kinematic porosity and transport flow-wetted surface) of the HRD of the Reference case are obtained from one realisation of the Hydro-DFN as parameterised in Section 2.3.2.

Transport performance measures: canister flux (q_r), travel time (t_r), path-length (L_r) and F-factor (F_r)

One objective of the SR-Can modelling is to assess the characteristics of groundwater pathways from a repository to the surface. The approach taken is to track particles moving with the advective flow velocity from a range of release points until they reach the top surface. Although it would be possible in CONNECTFLOW to track particles as they move through a velocity field that evolves in time, it is preferred here to use the instantaneous velocity fields at a number of selected release times. This is mainly because particle tracks released in a transient velocity field would be sensitive to both the release time and the kinematic porosity, making it more difficult to interpret the results due to the added uncertainties. One uncertainty that it is important to address here is the effect of the stochastic DFN on regional-scale pathways. Hence, several realisations of the DFN model, and corresponding ECPM model, are considered here to quantify the sensitivity of transport performance measures to particular realisations. The four performance measures required are listed in Section 2.2.4.

The approach to calculating the performance measures based on the ECPM model is to release one particle from each canister position and use these to produce ensemble statistics for the performance measures, as well as locating the discharge areas. Since the canister positions are based on a layout produced by the Design Group, no particle will start within a certain distance of a high or medium confidence deterministic deformation zones. However, some particles are starting in deterministic deformation zones with low confidence.

Modelling strategy

A key philosophy in developing the groundwater models described in the SDM L 1.2 work has been to calibrate model parameters against field data within a margin appropriate to the quality and availability of the data. Equally, it is important that any variants considered here for the purposes of quantifying uncertainties are equally calibrated to data, rather than being arbitrary parameter variations, so that in a sense they are equally possible realisations. Many models were created during the SDM L 1.2 study, but in the reporting we focused on the combinations of parameters and conditions that give predictions consistent with field data. The variants reported are therefore the ones that have been constructed to demonstrate the uncertainties that remain in the model concepts and parameters, and consequent model predictions, due to the lack of constraint by the available data. These variants were used to quantify sensitivities and form the basis for recommending important uncertainties that may need to be evaluated in the SR-Can safety assessment calculations.

3.2 Flow simulations using the ECPM reference case

3.2.1 Description of past evolution

In the SDM Laxemar 1.2 transient simulations were carried out from 8,000 BC to 2,000 AD /Hartley et al. 2006a/. The simulations include density driven flow, shore-level displacement and salinity changes in the sea. One result from the SDM calculations is that a Reference Case, with acceptable simulations in terms of e.g. reference waters and salinity, was established. The obtained reference case is propagated to the prevailing SR-Can study. Some simulations of the hydro-geochemistry from the resulting present-day conditions are given below.

Initial and boundary conditions

The boundary conditions used must represent the transient processes of shore displacement due to post-glacial rebound and the variations in the salinity of the Baltic Sea. The general modelling approach was to hold the model domain fixed (i.e. same x, y and z coordinates), but modify the head and salinity on the top surface in time.

The evolution of shore displacement over the post-glacial period is shown in Figure 3-2 and compared with that used in the Simpevarp version1.2 modelling /Hartley et al. 2005/. The shore displacement data used for L 1.2 covers the time period from 10,000 BC until present and includes very sharp changes early on, although it is smoother than the curves used for S 1.2. The early sharp changes in shoreline correspond to rapid melting at the end of the ice age. The simulations were started at 8,000 BC, well before the start of the Littorina phase and after the initial rapid changes in sea-levels that resulted in the area around Laxemar beginning to rise out of the sea. The uncertainty in the shoreline displacement curve is about ±1 m for the last few thousand years.

The salinity progress in the Baltic Sea at Oskarshamn is shown in Figure 3-3 /Westman et al. 1999/. The data used in the modelling is represented by the blue line. The uncertainty is shown by the maximum and minimum values along the curve in orange. The present-day salinity at Oskarshamn (6.8 ‰) is represented by a straight blue line in the figure.

The evolution of salinity in the Baltic informs how the Glacial, Littorina and Meteoric reference waters have mixed in differing fractions over time. It is also important to have a more general hypothesis of the evolution of surface and sub-surface reference waters. The current understanding is based on /SKB 2006a/.

In the reference case, the head on the top surface was set to an estimated watertable height, which evolves in time due to changes in the head relative to the shoreline (see Figure 3-2). The watertable is based on interpolating measurement data in the area and an assumed varying offset from the interpolated water surface (30% of the difference between topography and the interpolated water surface). The watertable for past times was approximated as the present-day watertable minus the shoreline displacement. Offshore, the head was equal to the depth of the sea multiplied by the relative density of the Baltic Sea compared to freshwater.

Based on the surface hydro-geochemistry concept shown in /SKB 2006a/, the definition of reference water boundary conditions were specified according to the following stages:

- Baltic Ice Lake: Full Meteoric water onshore; Full Glacial water offshore.
- Yoldia Sea: Full Meteoric water onshore; Offshore a mixture of Littorina and Glacial reference waters according to the ratio of TDS shown in Figure 3-3 to the TDS of the Littorina reference water.
- Ancylus Ice Lake: Full Meteoric water onshore; Full Glacial water offshore.

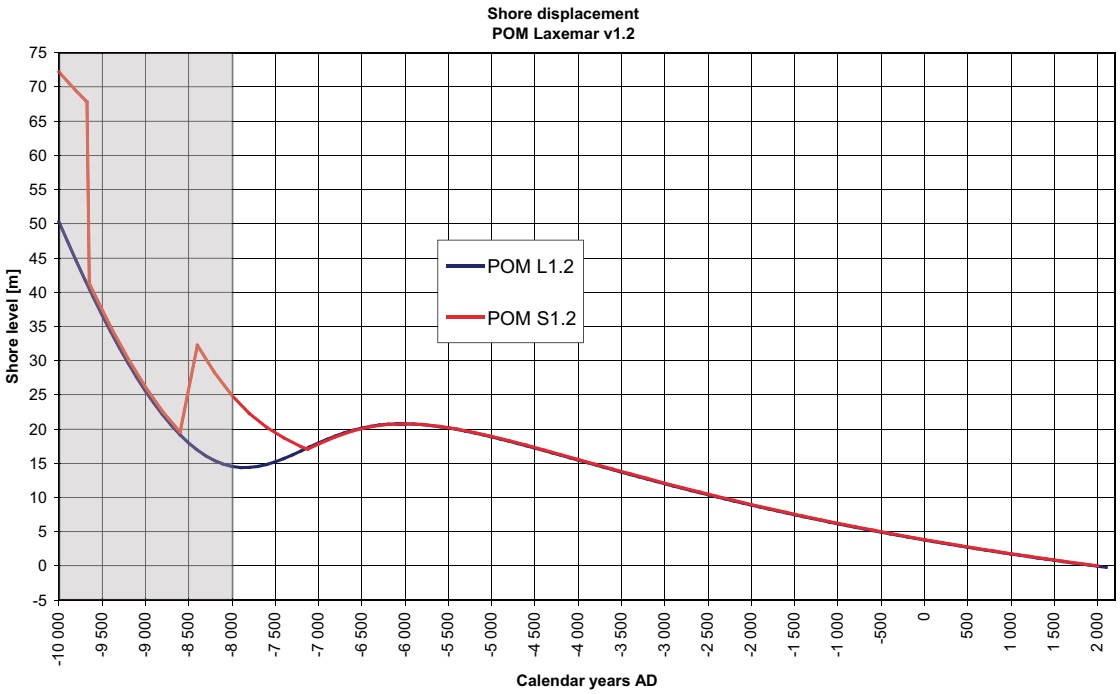

Figure 3-2. *The shore displacement used for POM Laxemar v1.2 (blue). The data used for POM Simpevarp v 1.2 are shown for comparison (red). Only data from –8,000 AD and onwards are used.*

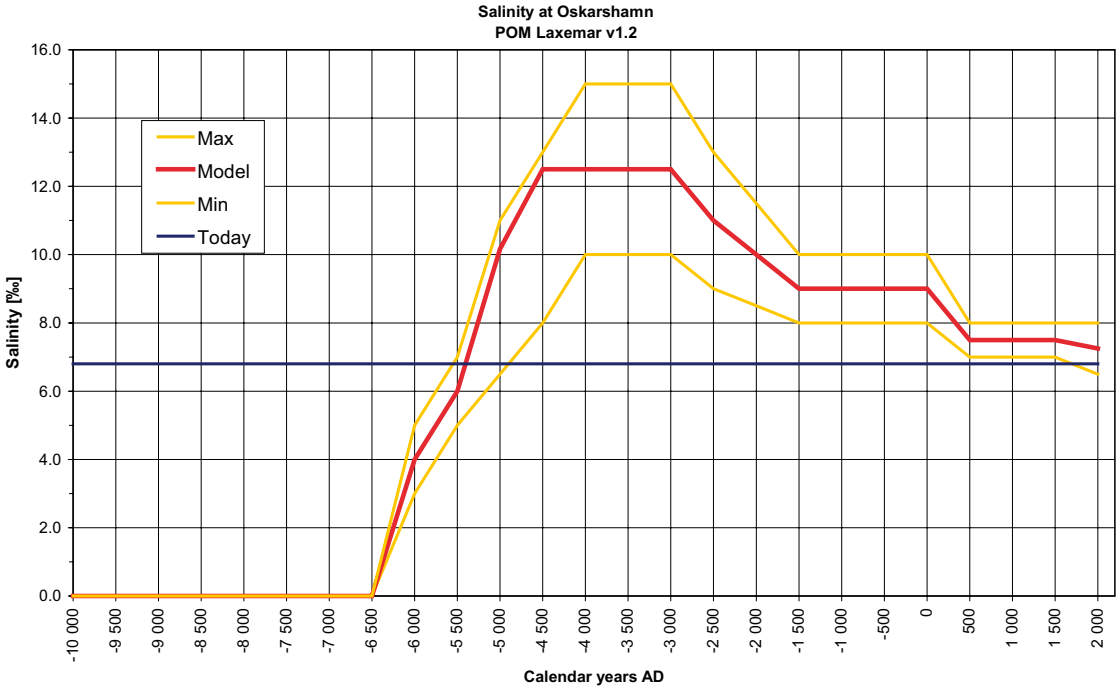

Figure 3-3. *The salinity progress in the southern Baltic Sea. The red line shows the data used in the model and the orange lines indicate the maximum and minimum intervals. The present-day salinity is indicated by the blue line.*

- Littorina Sea to present-day: Full Meteoric water onshore; offshore a mixture of Marine and Meteoric reference waters according to the ratio of TDS shown in Figure 3-3 to the TDS of the Littorina reference water.

The boundary conditions on the sides are no-flow and zero flux of reference waters. At the bottom of the model, at z = –2,300 m, there is a no-flow condition and groundwater is set to pure Brine, i.e. Brine fraction = 1.0, all other fractions = 0.

The initial conditions for the reference waters assume a profile of Brine at depth and Glacial water at the surface, with a start time of –8,000 AD. The results from Simpevarp v1.2 suggest a piecewise linear initial condition (IC 1) with full Glacial water down to 700 m depth, and then a gradual rise in Brine to full Brine at 1,500 m depth. This profile was based on the present-day profile of Brine and Glacial water in KLX02, the only borehole deep enough to measure the full Brine reference water.

In the SDM report for L 1.2 /Hartley et al. 2006a/, an alternative initial condition (IC 2) with full Glacial to 300 m depth increasing to full Brine at 1,500 m depth was tested in an attempt to improve the calibration of Cl in boreholes KLX01 and KSH01A where saline water is found above 600 m depth.

Hydro-geochemical comparison

One of the end products of the transient simulations is the reference water distributions, and salinity profiles. In addition, profiles for natural tracers along boreholes are obtained. Below are some illustrations for water compositions at 2,000 AD for the Reference Case. Figure 3-4 and Figure 3-5 are examples of the comparison in reference water fractions between those simulated and interpreted from the hydro-geochemical data. Examples of the modelled and measured salinity are also presented for the Laxemar (Figure 3-6), Simpevarp (Figure 3-7), Ävrö (Figure 3-8) and Äspö (Figure 3-9) subareas. More illustrations may be found in the SDM report by /Hartley et al. 2006a/ albeit based on a slightly different model case.

Flow-paths

By releasing particles from canister positions, flow-paths are simulated using the instantaneous velocity fields for chosen time steps. The particles are released from canister positions based on the proposed repository layout. This means that we release 7,483 particles from repository depth, which is at a depth of about 500 m. The particles are released at the centre of the canister positions. For these flow-paths, discharge points superimposed on head field are shown for the past in Figure 3-10 and the present-day in Figure 3-11. Up to 4,000 BC the release-area is predominantly under the sea, so particles tend to travel slowly vertically upwards in the deformation zones. After that, the surface above the release-area rises above the sea allowing infiltration by meteoric water, and consequentially the discharge areas become concentrated in a valley directly above the site and along the shoreline, which in turn retreats to expose two more valleys to the north and south where discharge congregates. By 2,020 AD the discharge areas lie in these 3 valleys, in the bay near to Äspö, and the shoreline to the south of Simpevarp.

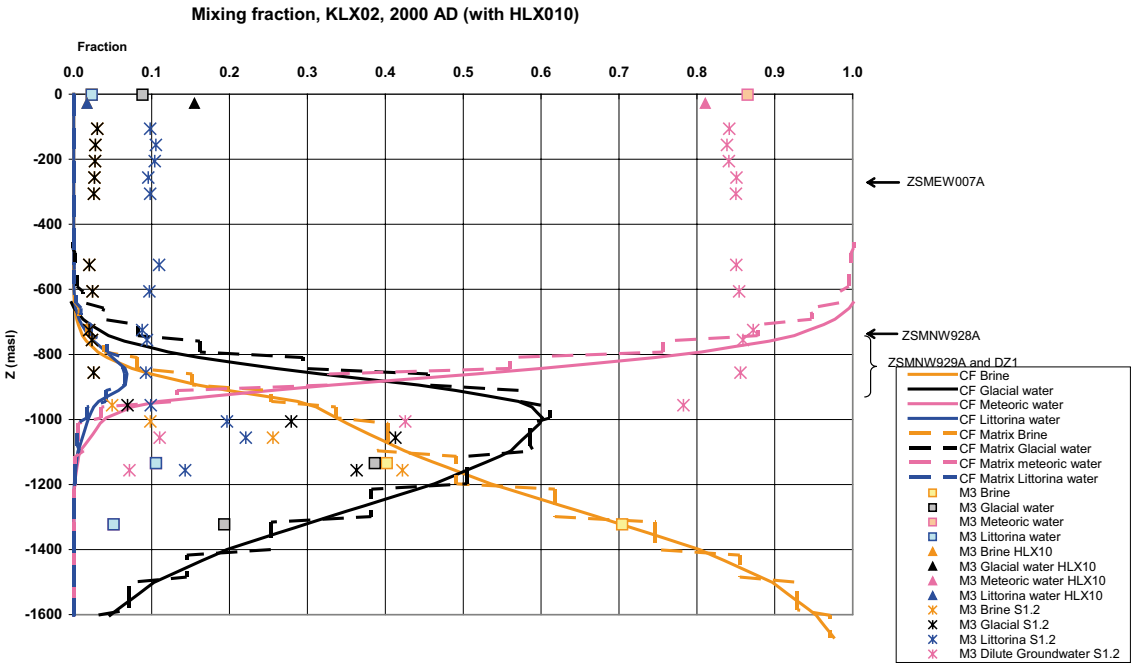

Figure 3-4. *Comparison of 4 reference water fractions in KLX02 for the reference case. The mixing fractions in the fracture system are shown by solid lines, in the matrix it is dashed, and the data by points. Only representative data is shown.*

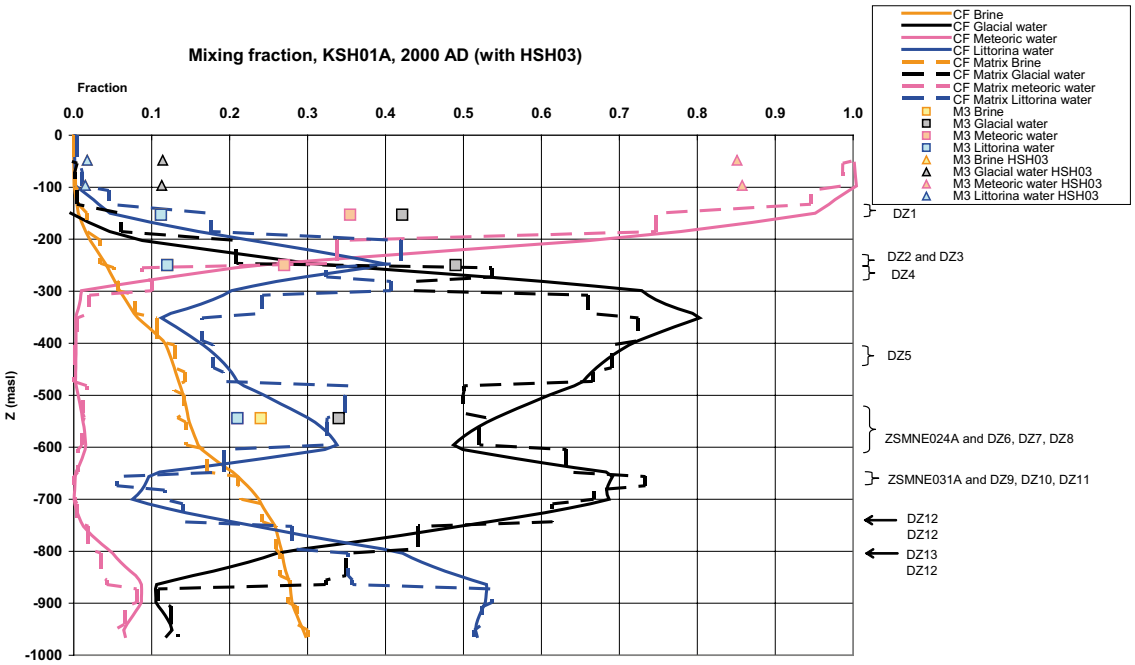

Figure 3-5. *Comparison of 4 reference water fractions in KSH01A for the reference case. The mixing fractions in the fracture system are shown by solid lines, in the matrix it is dashed, and the data by points. Only representative data is shown.*

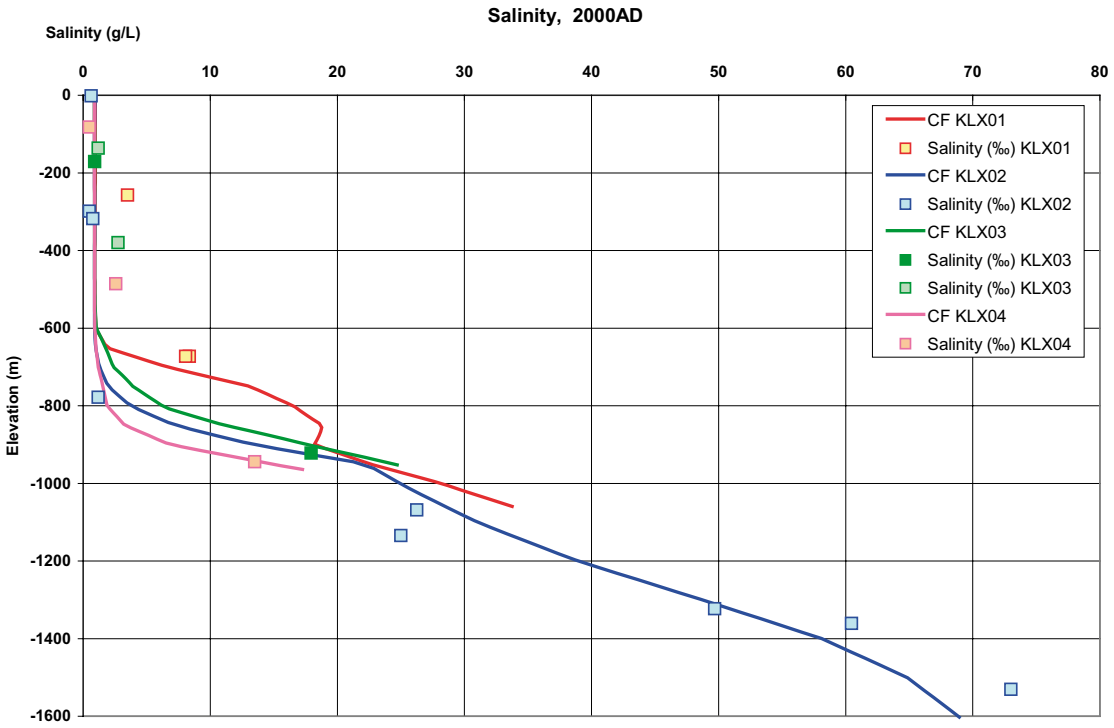

Figure 3-6. *Comparison of salinity in KLX01, KLX02, KLX03 and KLX04 for the reference case. The salinity in the fracture system is shown by solid lines, and the data by points. Only representative data is shown.*

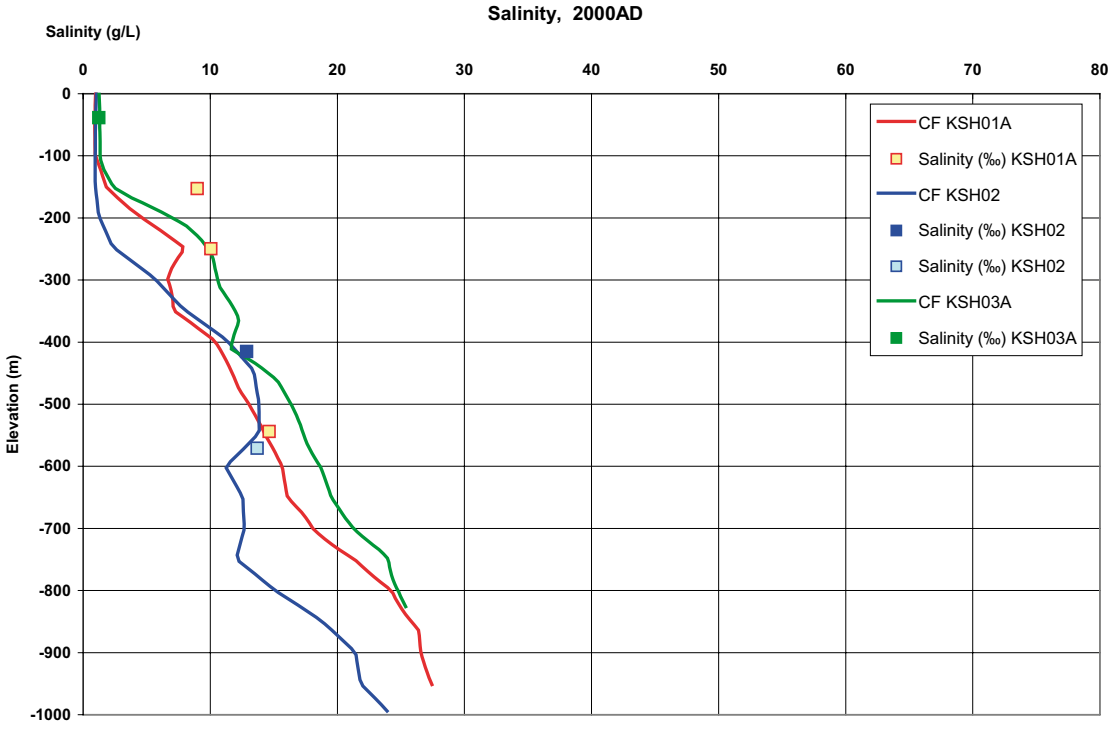

Figure 3-7. *Comparison of salinity in KSH01A, KSH02, and KSH03A for the reference case. The salinity in the fracture system is shown by solid lines, and the data by points. Only representative data is shown.*

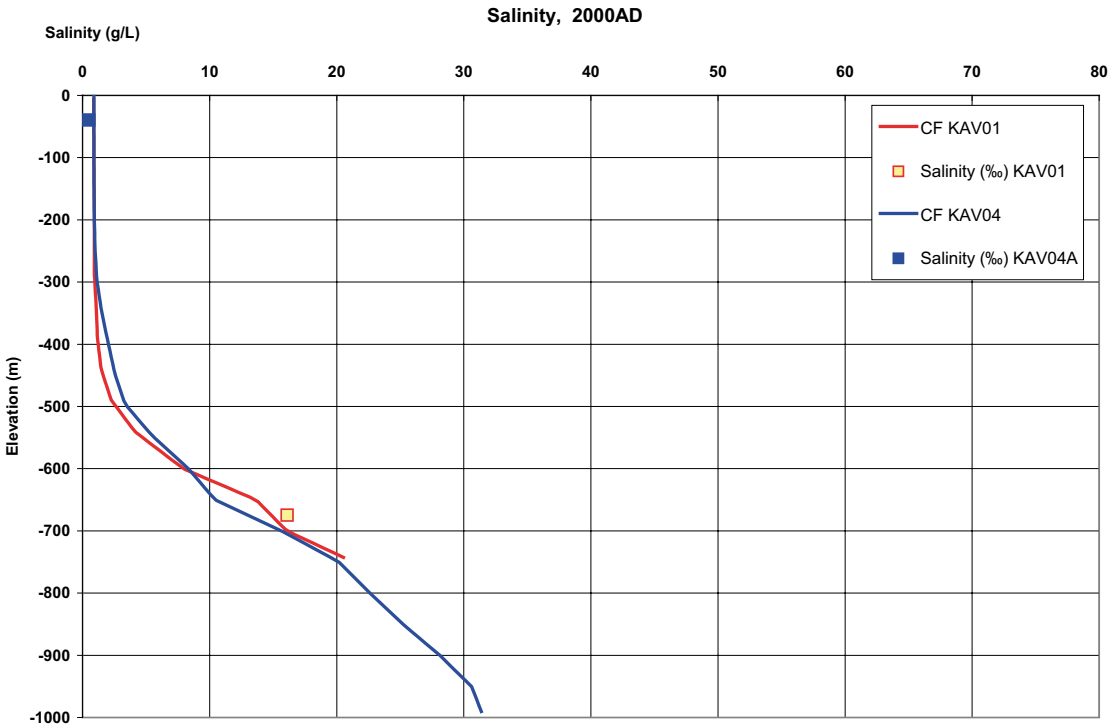

Figure 3-8. *Comparison of salinity in KAV01, and KAV04 for the reference case. The salinity in the fracture system is shown by solid lines, and the data by points. Only representative data is shown.*

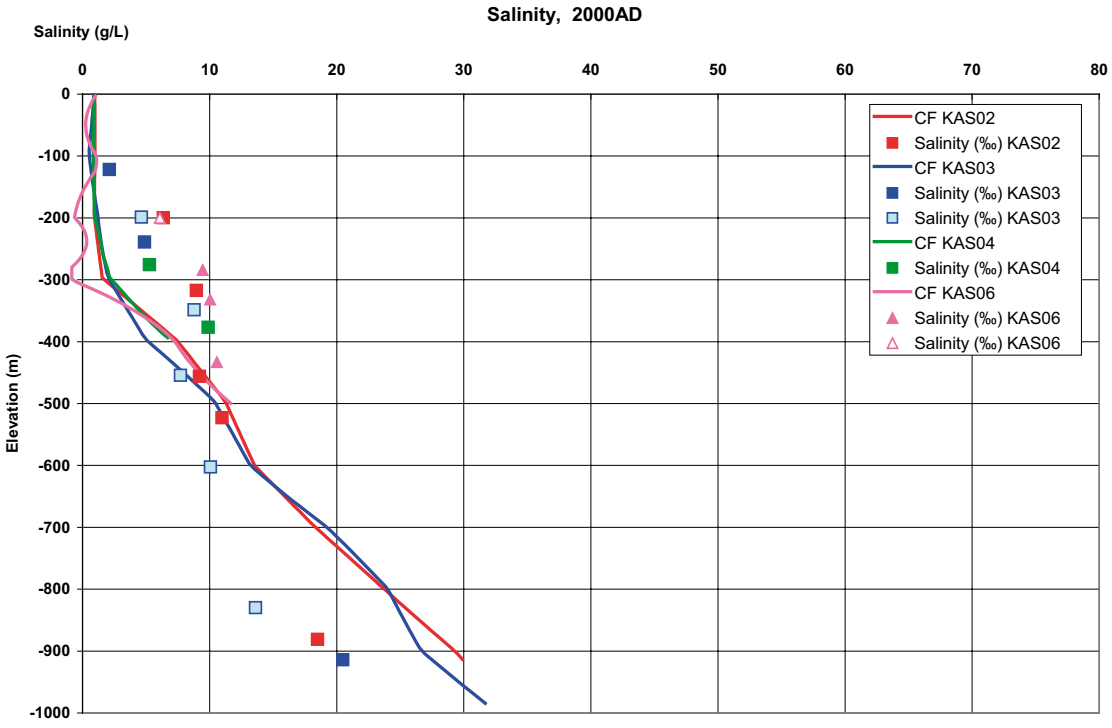

Figure 3-9. *Comparison of salinity in KAS02, KAS03, KAS04 and KAS06 for the reference case. The salinity in the fracture system is shown by solid lines, and the data by points. Only representative data is shown.*

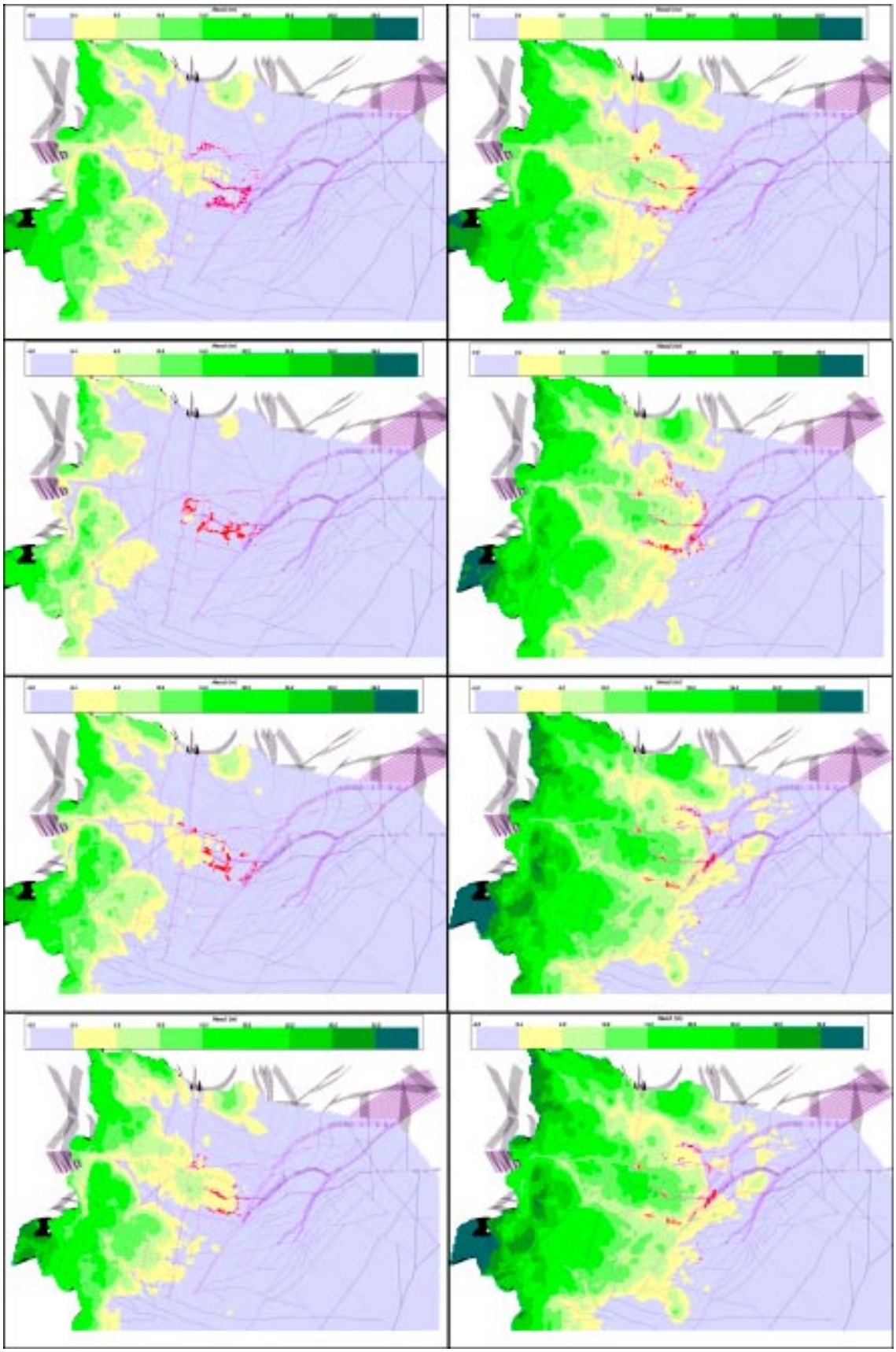

Figure 3-10. *Particle exit locations of pathlines released at canister positions for releases at 8,000 BC, 6,000 BC, 4,000 BC, 3,000 BC, 2,000 BC, 1,000 BC, 0 AD, 1,000 AD (top left-bottom right) for the reference case. The background colours show groundwater head and DZ's.*

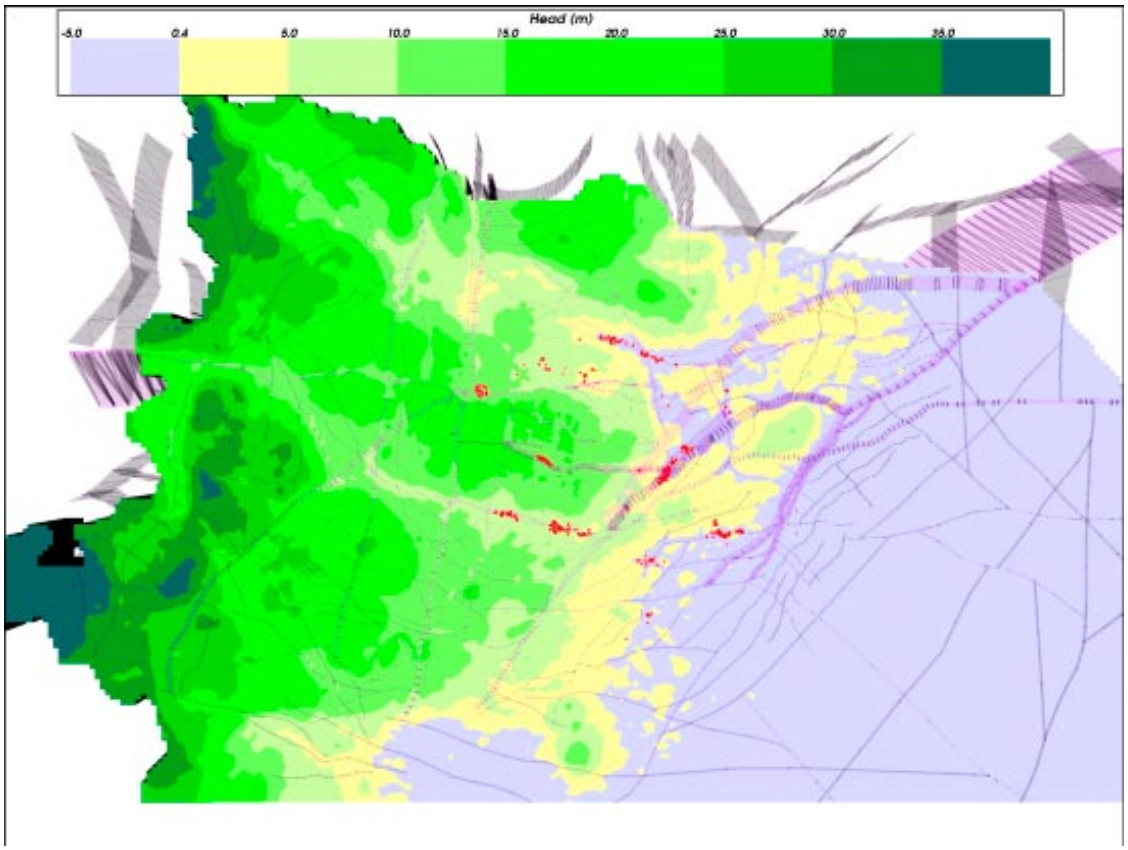

Figure 3-11. *Particle exit locations of pathlines released at canister positions for releases at 2,020 AD for the reference case. The background colours show groundwater head and DZ's.*

3.2.2 Description of future evolution

In order to continue the simulations for predictions, some assumptions have to be made regarding the top boundary conditions. One assumption is related to the shore-level displacement and another is related to the future salinity in the Baltic Sea. For the shore-level displacement it was decided to use the same relationship as was used for the past evolution /Påsse 1997/. This is illustrated in Figure 3-11.

The values used for the salinity in the Baltic Sea are shown in Figure 3-13. As may be seen it was decided to use a constant value for the future evolution. It is assumed that this has a low influence on the results, and if it were to change, it would probably be to a lower salinity in the Baltic Sea, which means it would influence the results even less.

From the same pathline calculations a number of performance measures are calculated, and flow path exit locations are obtained. The performance measure results are given below. In Figure 3-14 the exit locations are shown for different time steps up to 20,000 AD. The positions are superimposed on the head field used, and the deterministic deformation zones. The rate of land-rise becomes decreasingly small in the future, such that shoreline to the south of Simpevarp persists up until 16,000 AD, and the associated discharge area remains for a very long time. Even at 20,000 AD the particle exit locations are quite similar to those for the present-day.

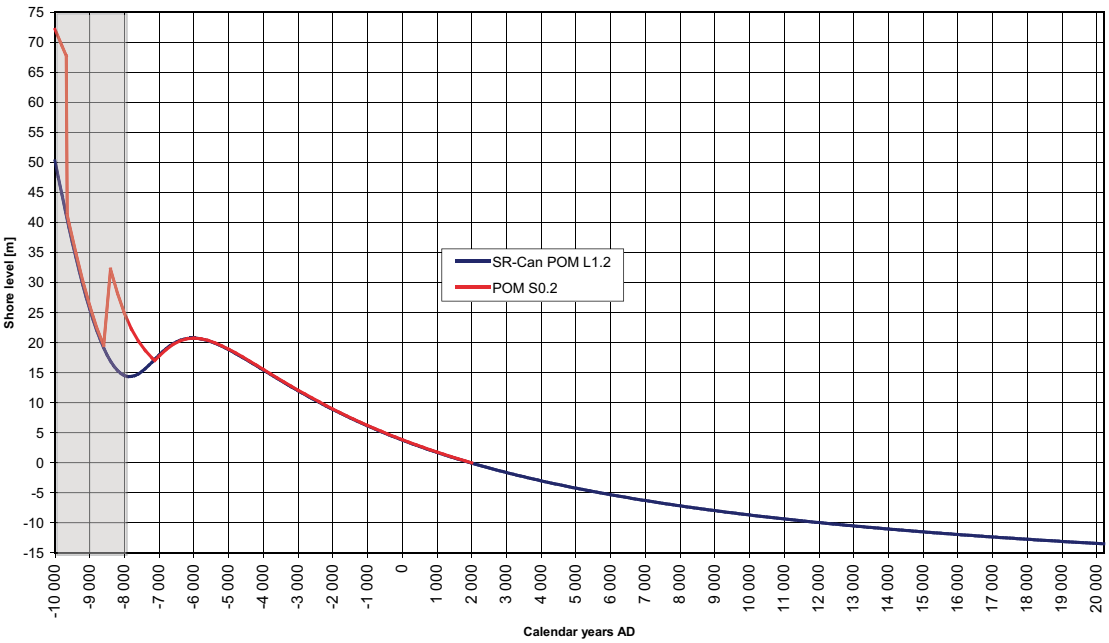

Figure 3-12. *Blue curve: Shore Level Displacement as in SDM POM L 1.2, but continued from 2,000 AD to 20,000 AD and therefore denoted "SR-Can POM L 1.2". Red curve: Shore Level Displacement as in SDM POM S1.2 /Hartley et al. 2005/.*

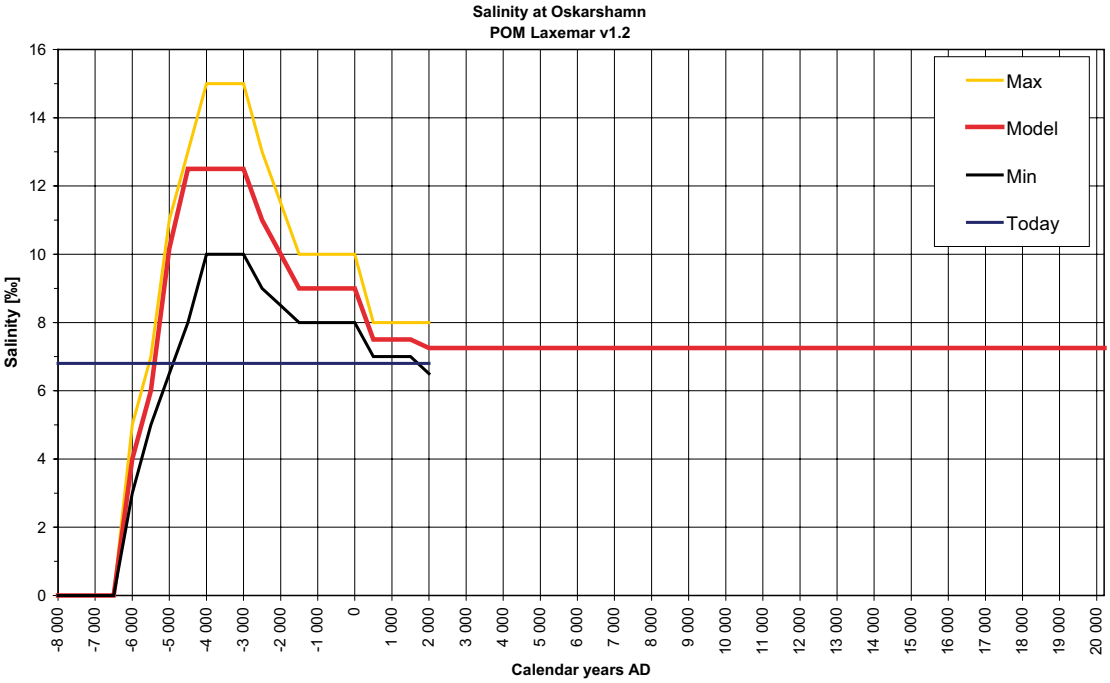

Figure 3-13. *The salinity progress used in the southern Baltic Sea. The red line shows the values used in the model, the orange and black lines indicate the maximum and minimum intervals. The present-day salinity is indicated by the blue line.*

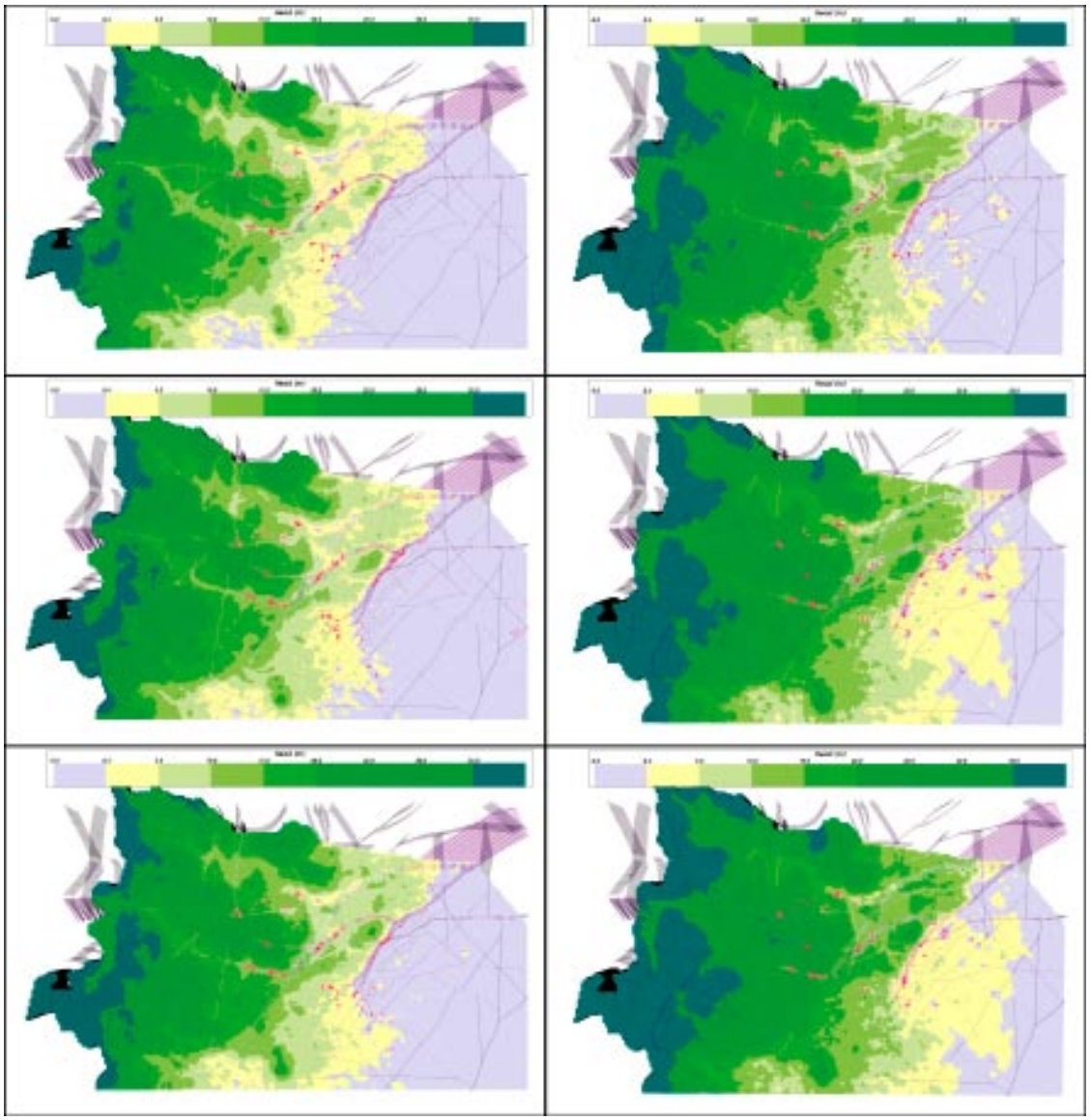

Figure 3-14. *Particle exit locations of pathlines released at canister positions at 4,000 AD, 6,000 AD, 8,000 AD, 12,000 AD, 16,000 AD and 20,000 AD (top left to bottom right) for the reference case. The background colours show groundwater head and deformation zones.*

3.2.3 Performance measures

Performance measures are calculated in terms of travel times, initial Darcy velocity, path-lengths, and F-factor values (see Section 2.2.4). The performance measures are calculated for chosen time steps using the instantaneous velocity fields and for an ensemble of pathlines. The ensemble of particles represents all the defined canister positions, which means that particles start at repository depth, i.e. in the centre of the deposition hole. In the layout used there are 7,483 deposition holes.

Performance measure statistics are calculated for the ensemble of pathlines. In the current project, the tool @STAT has been developed even further. As before, statistical tables and a vast number of plots are produced. Typically, box plots, histograms, cumulative distribution plots, and scatter plots are produced. Examples of the plots are given below for most of the performance measures.

The developments make it possible to study statistics of groups of particles as well. The groups may be based on starting positions, e.g. different hydraulic rock domains and tunnel sections.

Starting positions

On the basis of the repository design provided, a starting position for each canister is defined. The starting positions are located in three different areas, rock domain HRD(A), mixed rock domain HRD(D,E,M), and low confidence deformation zones HCD. The deformation zones are classified as low confidence zones. The percentages of starting positions within these hydraulic domains are 39%, 58%, and 3%, respectively. The three categories of starting position areas are illustrated in Figure 3-15.

Travel time

The ensemble results in terms of travel times are illustrated for different time release times below using cumulative distribution plots and histograms. In the cumulative distributions it is perhaps easier to compare the distributions for different release times in the past and future. Cumulative distributions for the travel time, t_r, are shown for release times 8,000 BC to 20,000 AD in Figure 3-16 to Figure 3-21. Apart from reduced travel times at 7,980 AD, the travel time distributions are very stable. Marginally shorter travel times occur for release times between about 3,000 BC and 1,000 BC when the shoreline is located directly above the release-area. The lowest 10th percentile for travel time occurs at this time period. At later times it is only the "tail" of the distribution, greater than about the 70th percentile, that varies significantly. This corresponds to changes in the discharge area associated with the long paths that clearly continue to respond to changes in the shoreline position in the future. The shorter paths that discharge in three valleys close to the release area are not affected by the land-rise. This leads to a bi-model distribution for travel time associated with these two type of paths as illustrated by the histograms in Figure 3-22.

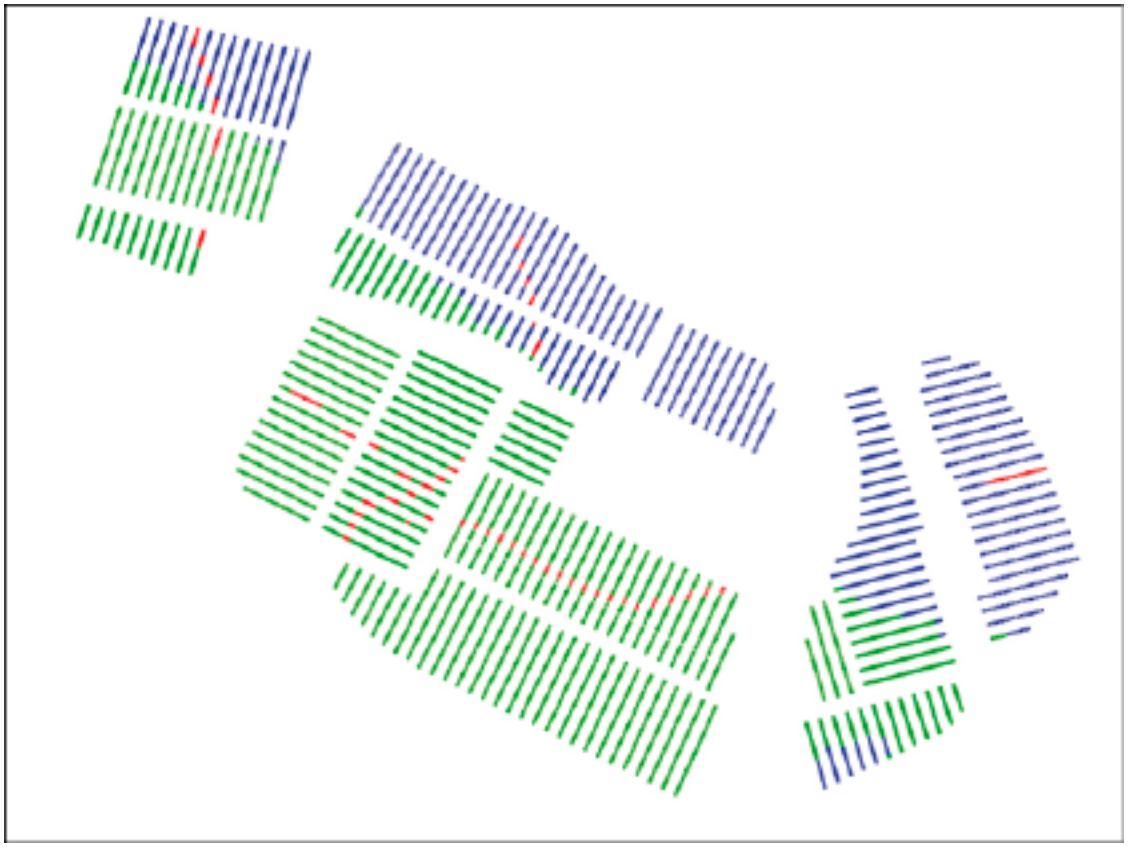

Figure 3-15. *Three categories of starting positions, blue is rock domain HRD(A), green is rock domain HRD(D,E,M) and red is low confidence zones HCD.*

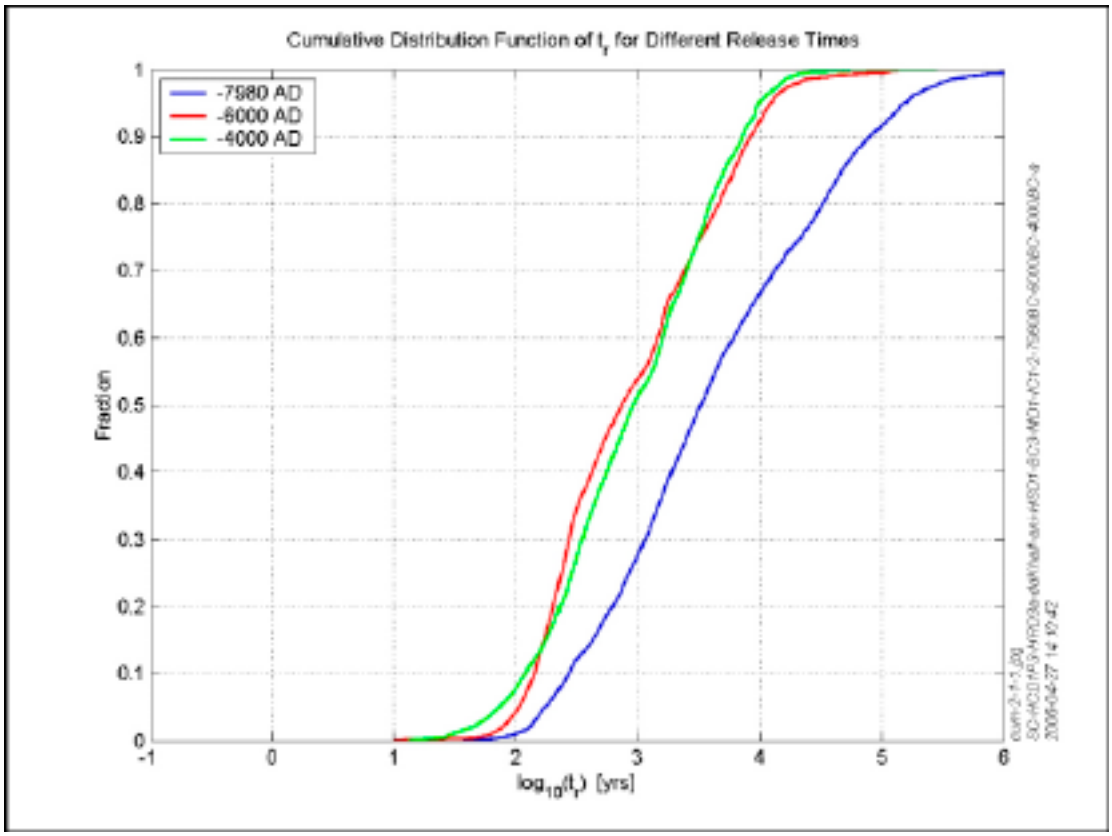

Figure 3-16. *Cumulative distribution of travel times for three release times.*

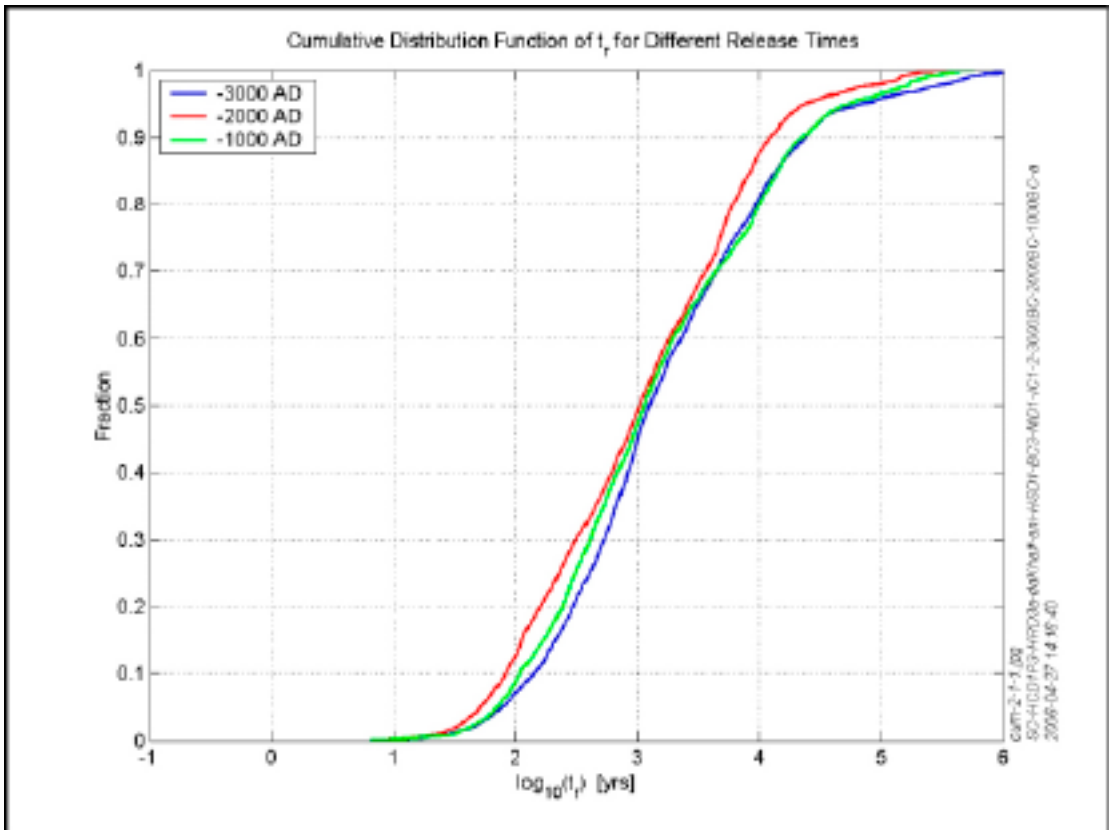

Figure 3-17. *Cumulative distribution of travel times for three release times.*

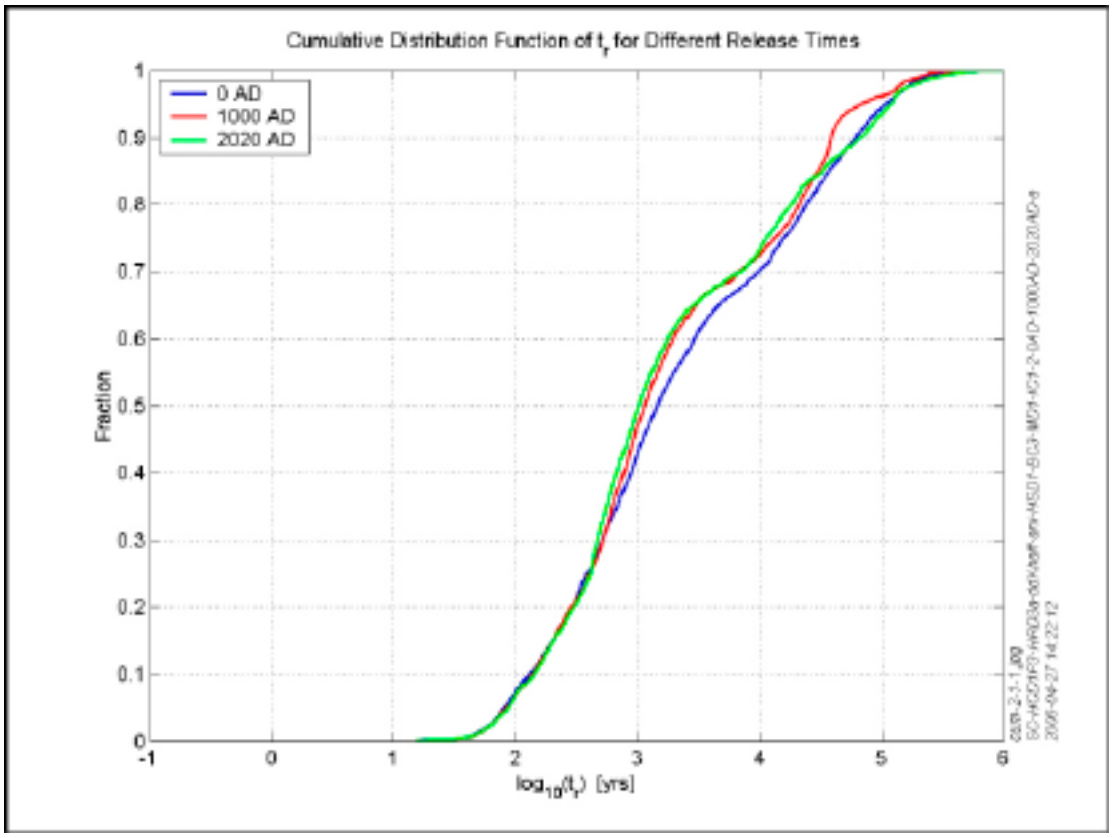

Figure 3-18. *Cumulative distribution of travel times for three release times.*

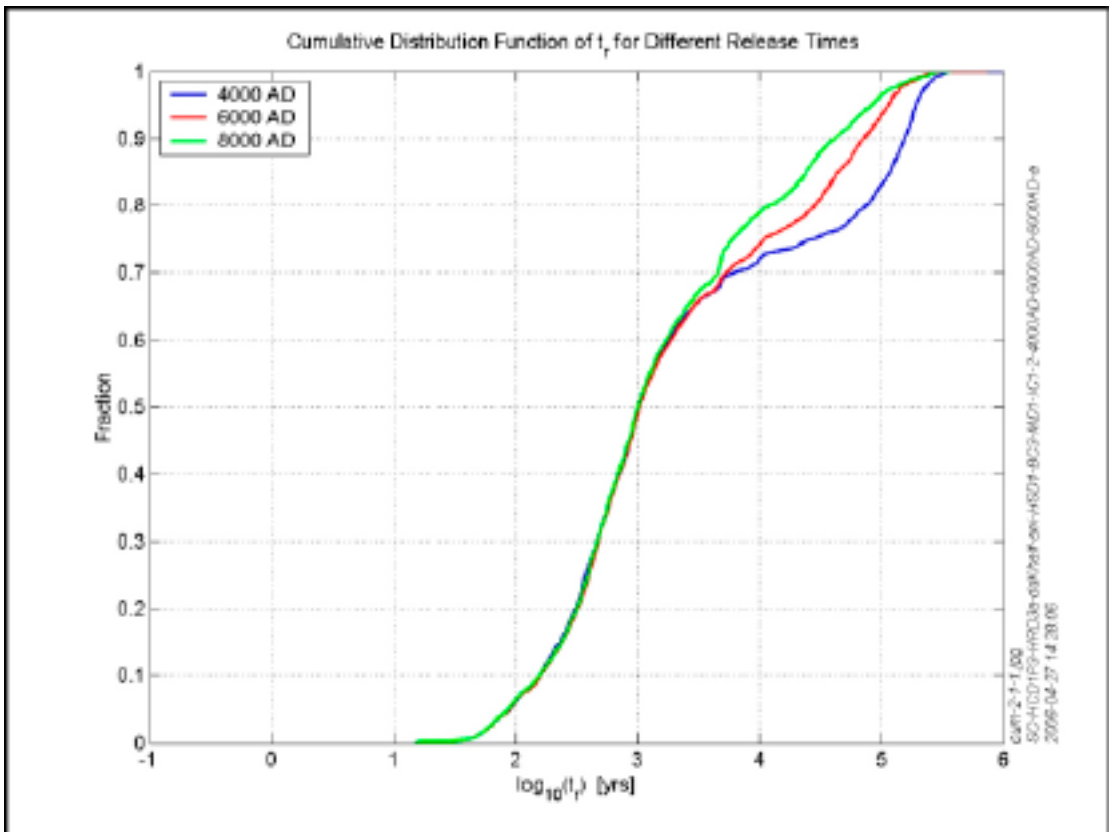

Figure 3-19. *Cumulative distribution of travel times for three release times.*

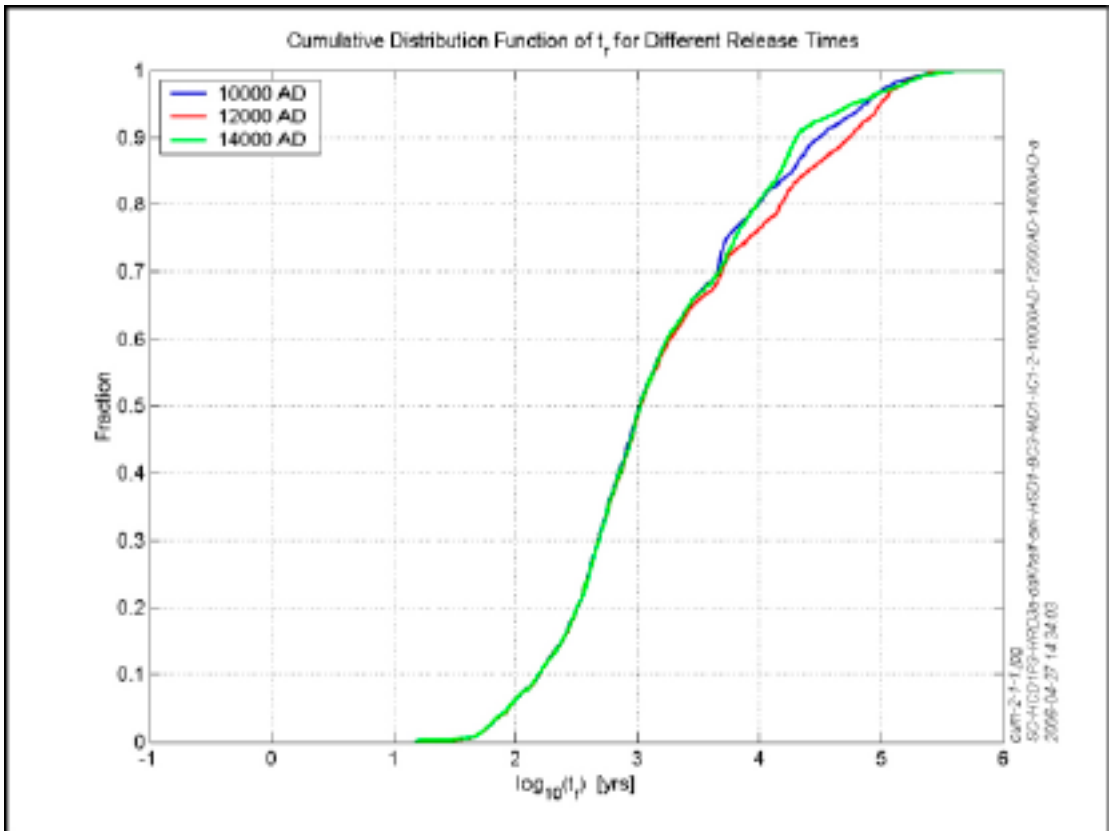

Figure 3-20. *Cumulative distribution of travel times for three release times.*

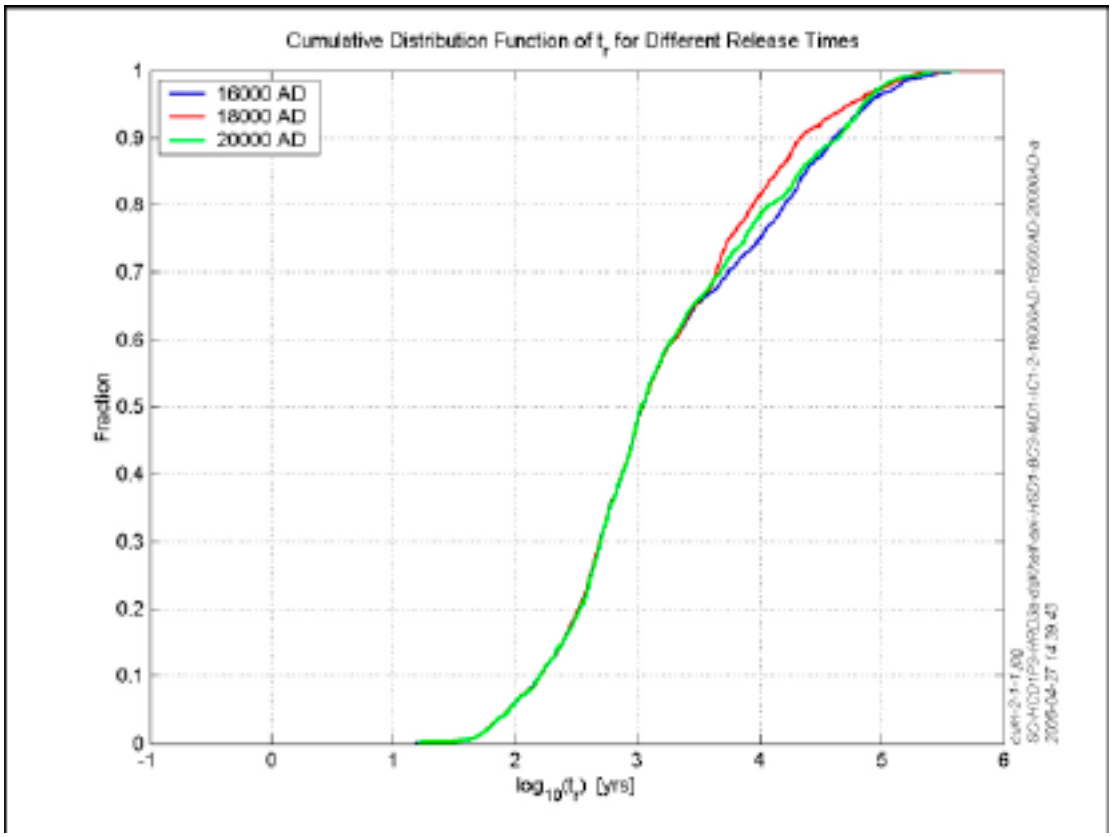

Figure 3-21. *Cumulative distribution of travel times for three release times.*

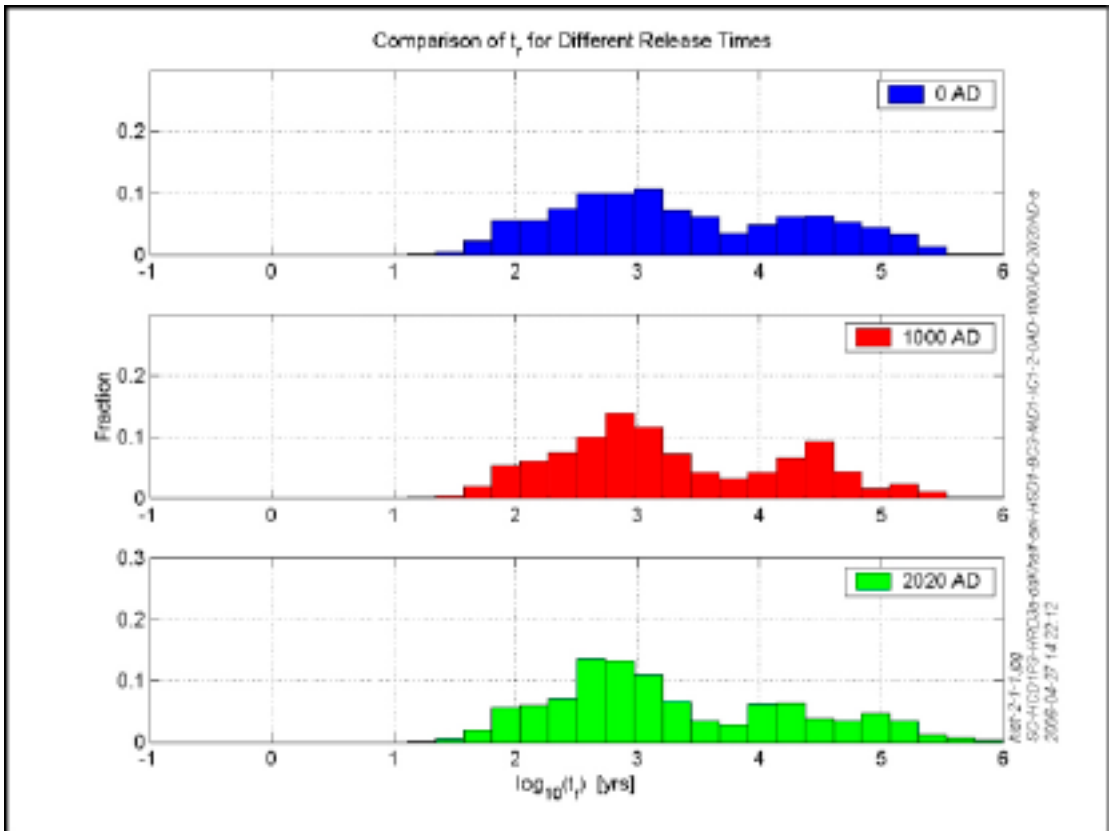

Figure 3-22. *Example of histograms for travel times for three release times.*

Initial Darcy velocity

The distribution of initial Darcy velocity at the canister locations is perhaps even more stable with respect to the shoreline displacement. A histogram of Darcy velocity is shown in Figure 3-23. Even for the ECPM model, the spread in values is very large from about 10^{-7} m/yr to 10^{-1} m/yr with a median around 10^{-3} m/yr. The histograms show a distinct group of canisters associated with very low Darcy velocities around 10^{-7} m/yr to 10^{-5} m/yr. This is associated with areas that have a low hydraulic conductivity due to areas of poor fracture network connectivity that occur for stochastic networks with a low fracture intensity. This is particularly apparent in rock domain HRD(D, E, M) as is shown in Figure 3-33. The median initial Darcy velocity actually increases from about $\log(U_r) = -4.3$ at 8,000 BC to $\log(U_r) = -3.4$ at 1,000 BC, after which time it is essentially constant.

F-factor

The distribution of F-factor along the flow-paths is shown in Figure 3-24 to Figure 3-27. Again, the distributions are very stable with respect to the shoreline evolution. The F-factor is highest around 8,000 BC before the Littorina phase. There then follows a reduction in F-factor around 6,000 BC to 4,000 BC when the sea temporarily advances coincident with Littorina phase (see Figure 3-12 and Figure 3-13) which leads to short vertical flow-paths. The F-factor distribution then becomes very stable until eventually around 4,000 AD, the retreat of the shoreline starts lengthen some flow-paths that exit at the shore giving higher F-factor values. The range is consistently between about 10^5 yr/m to 10^8 yr/m with a median around 10^6 yr/m. The biggest fluctuations occur in the tail of the distribution above about the 70th percentile which is due to the evolution of the long paths that follow the changes in shoreline around the bay near Äspö and to the south of Simpevarp. There are at most around 10% of particles with F-factors less than 10^5 yr/m.

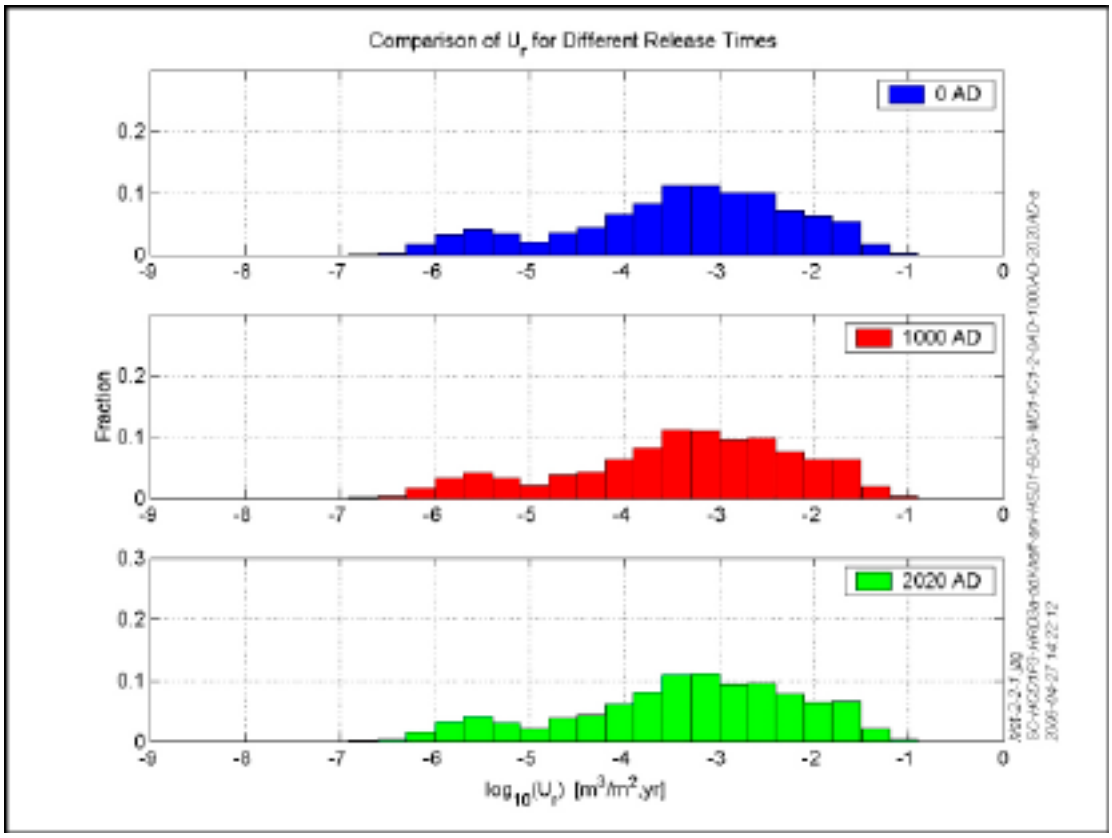

Figure 3-23. *Example of histograms for initial Darcy velocity for three release times.*

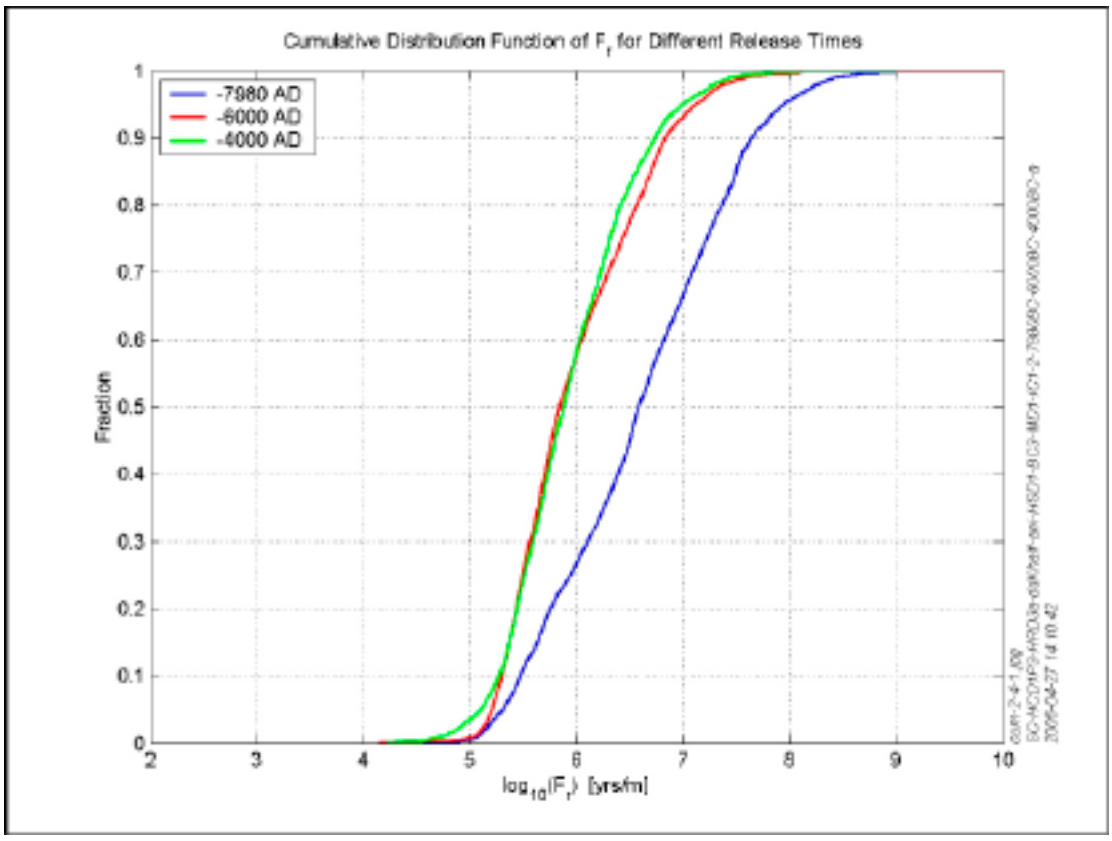

Figure 3-24. *Cumulative distribution of F-factor for the three release times 7,980 BC, 6,000 BC, and 4,000 BC.*

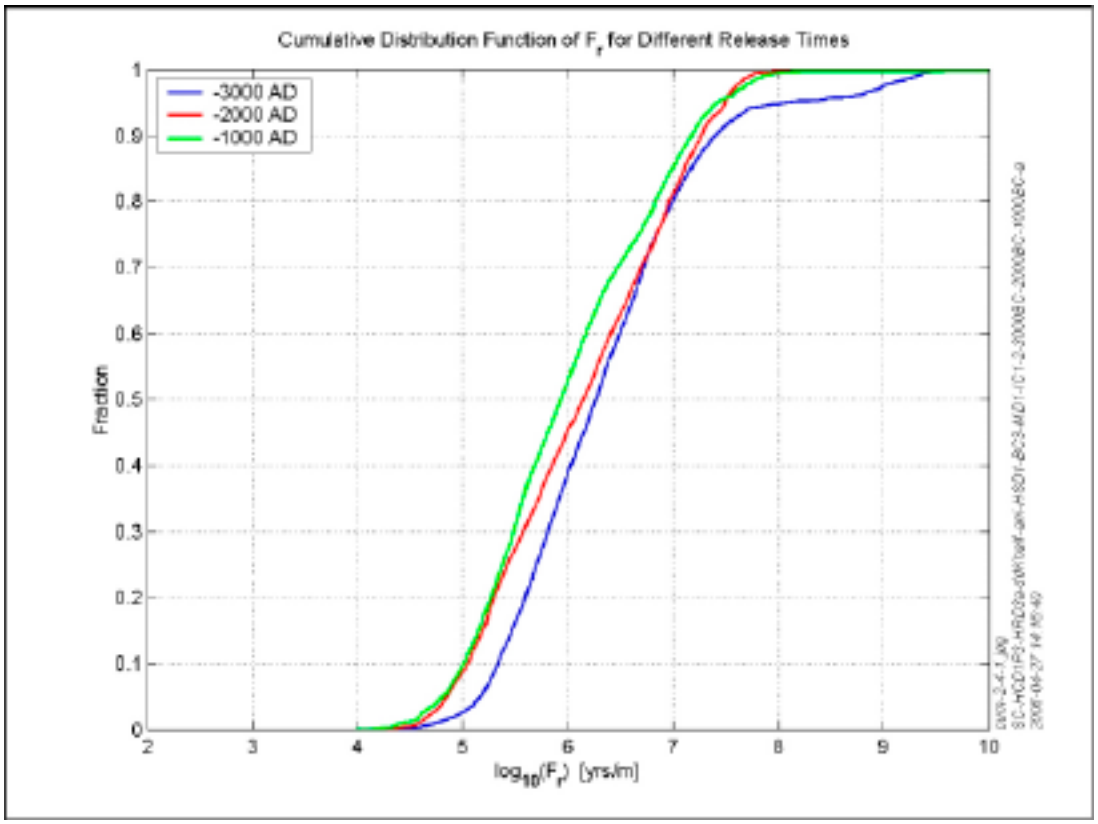

Figure 3-25. *Cumulative distribution of F-factor for the three release times 3,000 BC, 2,000 BC, and 1,000 BC.*

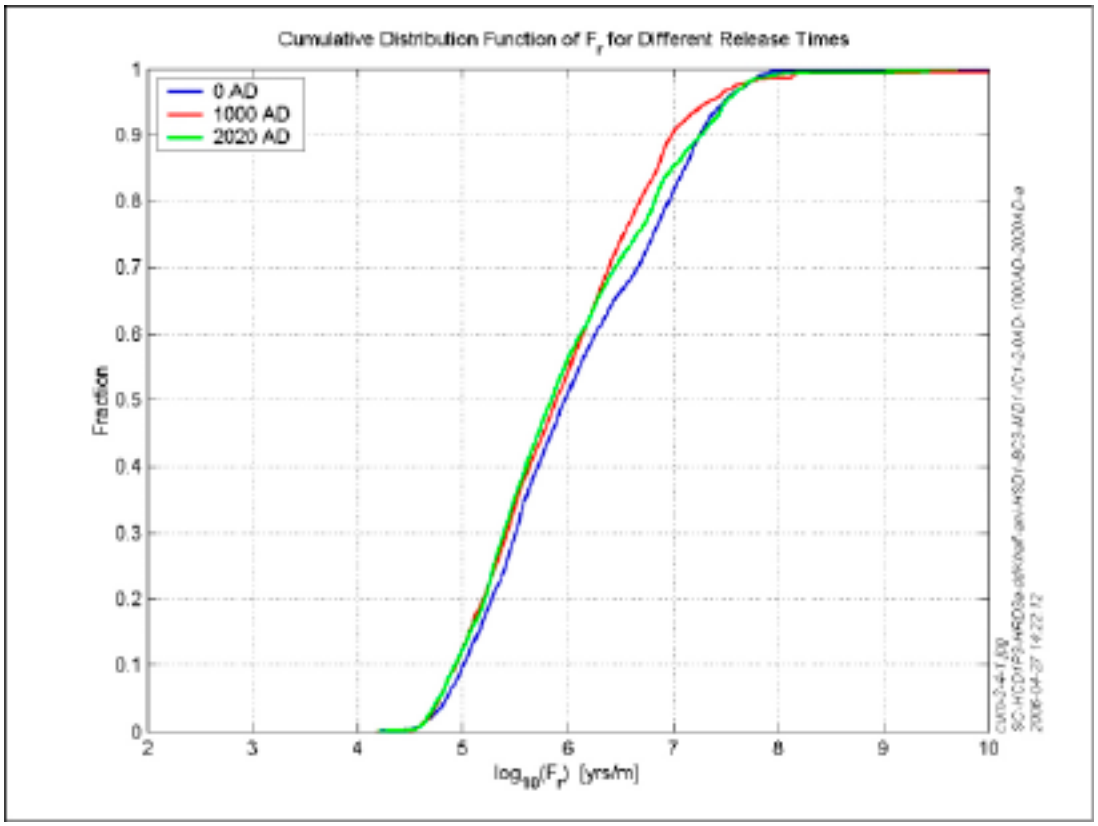

Figure 3-26. *Cumulative distribution of F-factor for the three release times 0 AD, 1,000 AD, and 2,020 AD.*

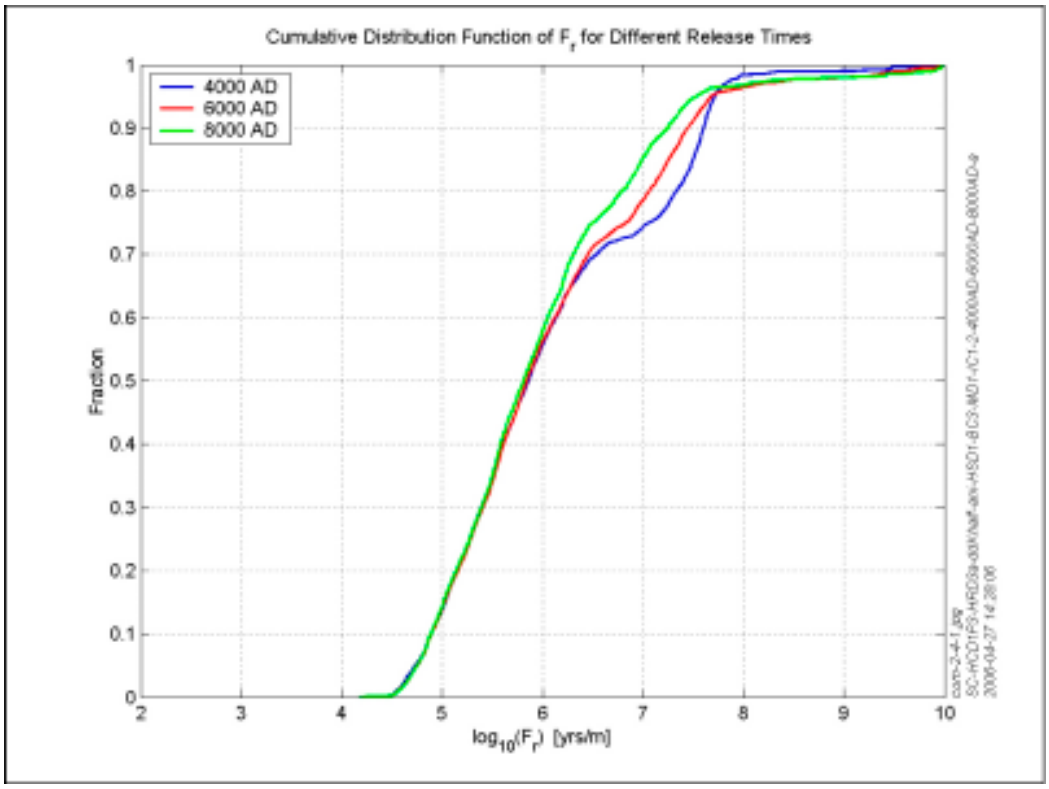

Figure 3-27. *Cumulative distribution of F-factor for the three release times 4,000 AD, 6,000 AD, and 8,000 AD.*

Performance measures at 2,020 AD

The performance measures are calculated for release times from 8,000 BC to 20,000 AD in 1,000 years intervals. As an example, a summary of the performance measures at 2,020 AD is given in Table 3-2. The performance measures for other release times are summarised in Appendix B. The variance in travel time, Darcy velocity and F-factor are between 0.8 to 1.4 in Log10 space, which reflects the spatial variability in the properties arising from the different hydrogeological domains and the underlying stochastic DFN.

Table 3-2. A summary of the performance measures for the reference case at release time 2,020 AD.

Statistical entity	Log10(*tr*)	Log10(*Ur*)	Log10(*Fr*)	Log10(*Lr*)
Mean	3.16	–3.50	6.02	3.25
Median	3.05	–3.35	5.93	3.16
5th percentile	1.85	–5.81	4.82	2.89
10th percentile	2.03	–5.43	5.00	2.93
25th percentile	2.49	–4.15	5.38	3.03
75th percentile	3.85	–2.63	6.67	3.44
90th percentile	4.31	–2.10	7.15	3.67
95th percentile	4.67	–1.82	7.40	3.84
Std deviation	0.89	1.18	0.83	0.30
Variance	0.79	1.38	0.70	0.09
Max value	5.93	–1.13	10.09	4.32
Min value	0.80	–7.04	3.98	2.78
Fraction OK	0.99	1.00	0.99	0.99

3.2.4 Exit locations, performance measures and GIS information

Exit location for particles released at the repository at different times, past and future, are used in the assessment to support the development of appropriate biosphere models for the present and future temperate climatic periods. In Figure 3-28 to Figure 3-30, the exit locations for release time 2,020 AD are presented together with GIS (Geographical Information System) data, e.g. forests, fields, marsh lands, rivers, lakes, and parts of the Baltic. In addition, the location of the repository is indicated by its projection on the ground surface.

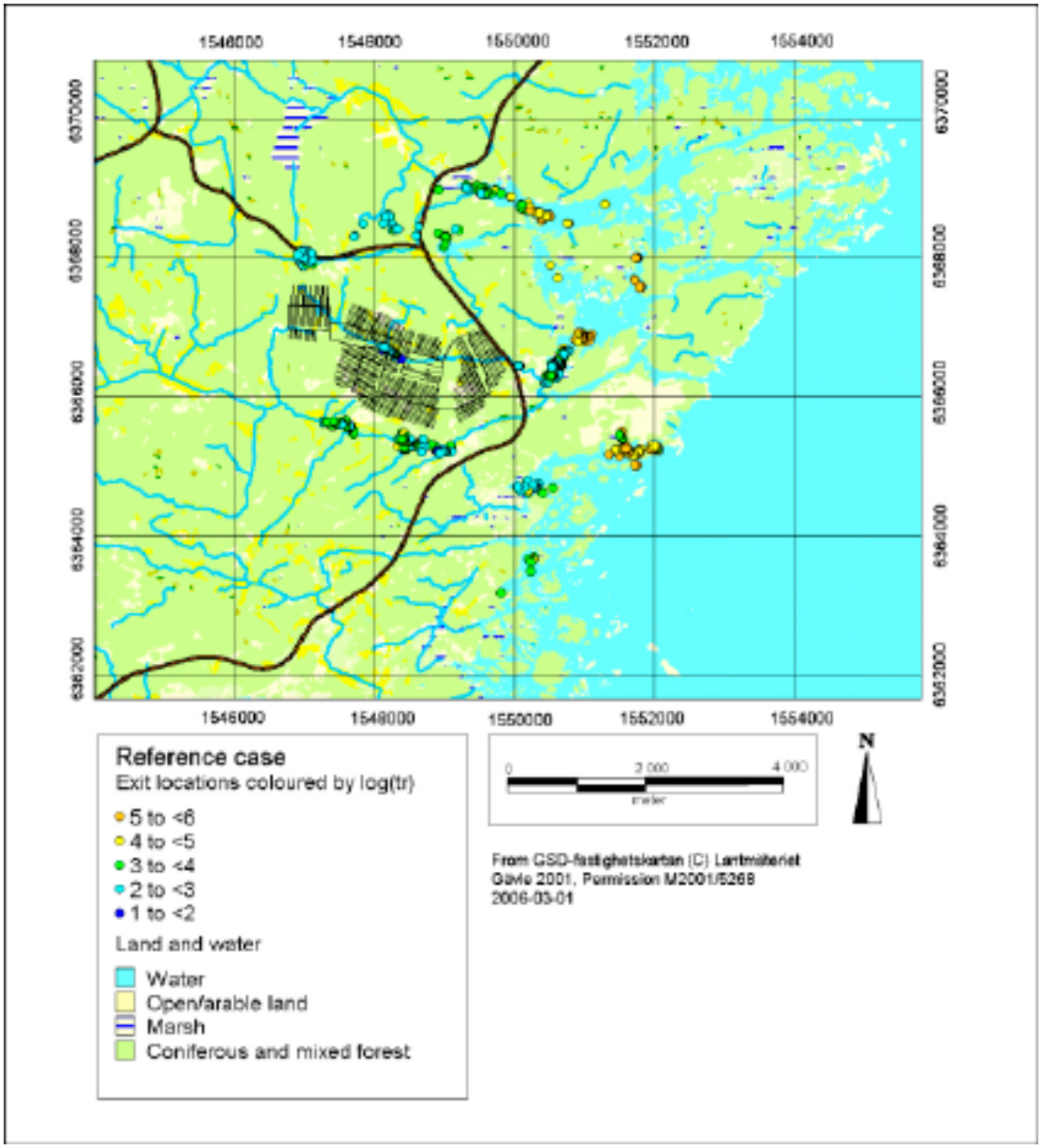

Figure 3-28. *Particle exit locations coloured by travel time [yr] of pathlines released at 2,020 AD for the reference case, plotted together with GIS data. The repository tunnels are projected on the ground surface.*

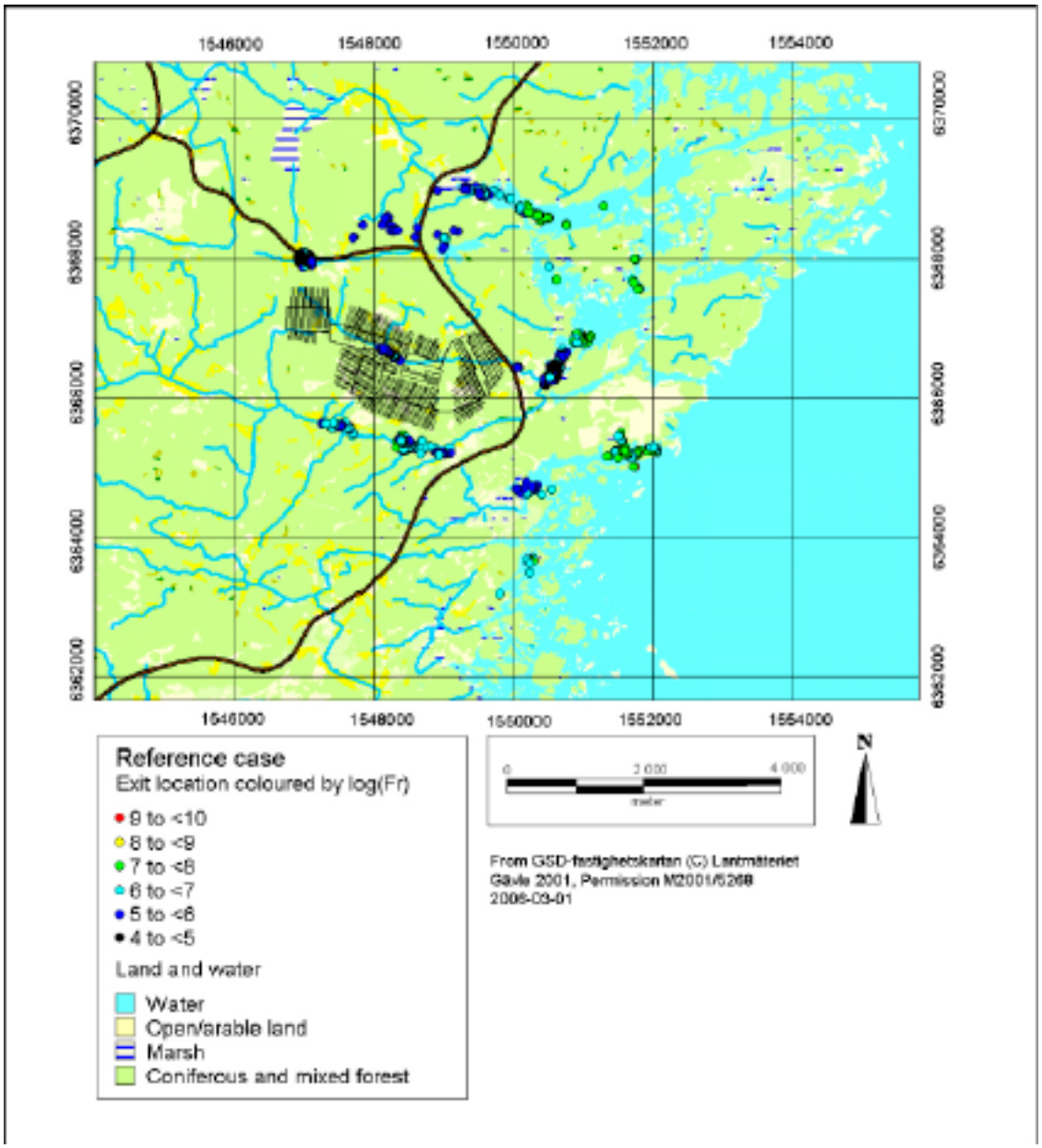

Figure 3-29. *Particle exit locations coloured by F-factor values [yr/m] of pathlines for release time 2,020 AD for the reference case, plotted together with GIS data. The repository tunnels are projected on the ground surface.*

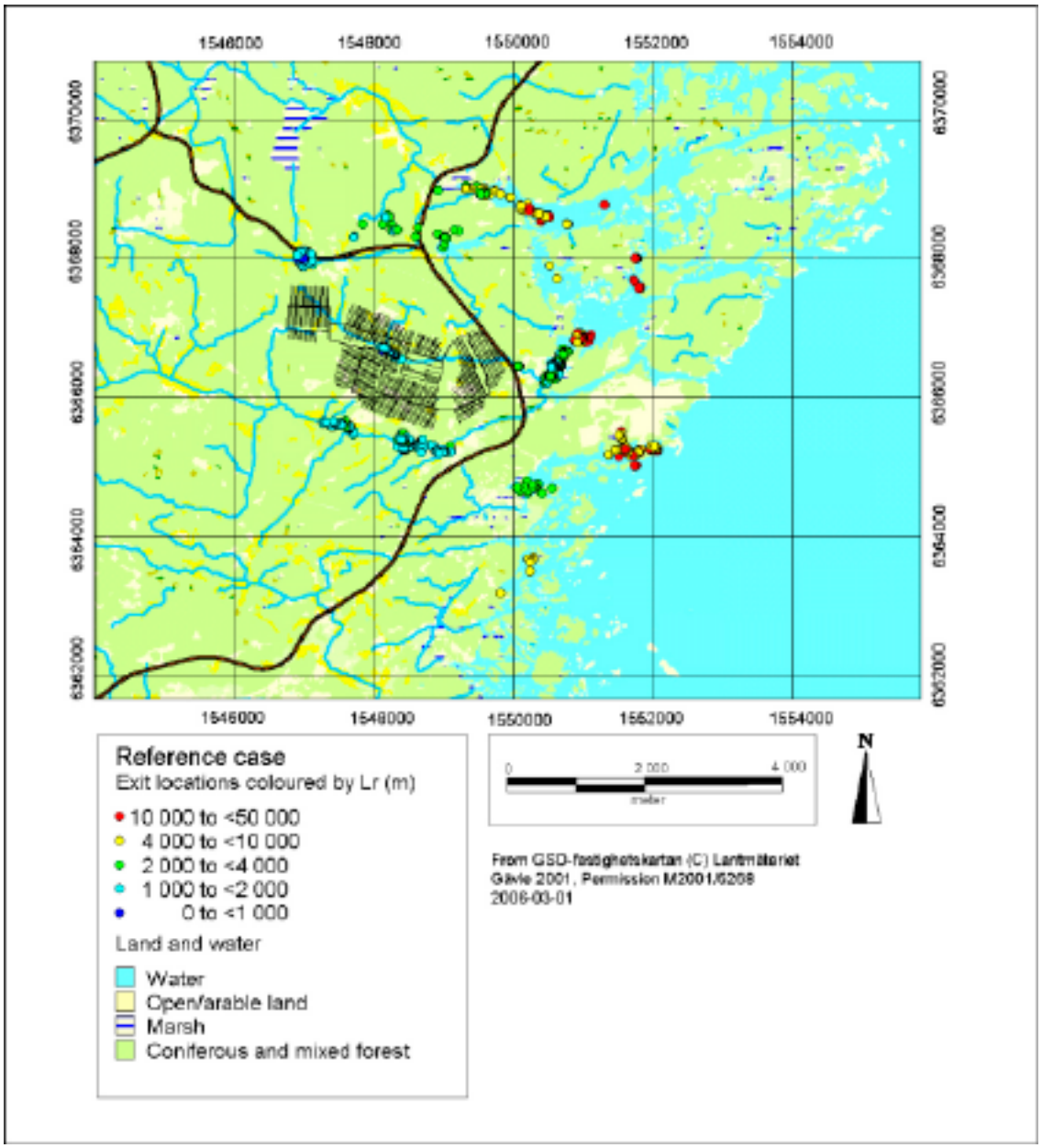

Figure 3-30. *Particle exit locations coloured by path-lengths [m] of pathlines for release time 2,020 AD for the reference case, plotted together with GIS data. The repository tunnels are projected on the ground surface.*

The distribution of travel times as shown at exit locations on the top surface is shown in Figure 3-28. This shows that the shortest travel times are associated with discharge to the stream running directly above the repository footprint. The next shortest are distributed over the streams to the north, north south and east of the repository. The longest travel times are to the bay near Äspö and to the shore south of the Simpevarp peninsula.

The F-factor at the exit locations is shown in Figure 3-29. This follows a similar pattern to travel time with the lowest F-factors associated with discharge to the streams in the centre, north and just east of the repository. Slightly higher F-factors are calculated for the discharge to the stream to the south, and the highest are to the bay near Äspö and to the shore south of the Simpevarp peninsula. The slight increase in F-factor to the south may be due to reduced Darcy velocities through the lower conductivity in HRD(D, E, M) that occurs in the south west part of the repository. The path-length shown in Figure 3-30 follows a consistent pattern. Some of the long paths that exit at the shoreline also reach down to depths of around 1 km before discharging.

Analysis of Hydraulic Domains

The pathlines were studied according to the hydraulic domain the particles were released in. In the reference case, there are particles that start in the Ävrö granite, rock domain HRD(A), and in the mixed rock domain HRD(D,E,M). In addition, there are a number of particles that start in low confidence deformation zones, HCD. The percentages for particles starting in these hydraulic domains are 39%, 58%, and 3% respectively. In Figure 3-31, the hydraulic domains HRD(A), HRD(D,E,M), and HCD are denoted A, MD, and DZ, respectively. Rock domain HRD(D, E, M) is encountered mainly in the south west part of the repository , see Figure 3-15. Generally, particles starting in HRD(A) discharge to the north and east, while particles starting in HRD(D, E, M) discharge in the south or south east. Hence, the exit locations associated with HRD(D, E, M) tend to be the ones that have longer travel times and larger F-factors.

Figure 3-32 to Figure 3-34 compare the performance measures for releases in the 3 different hydraulic domains as box-plots showing the 5^{th}, 25^{th}, 50^{th}, 75^{th} and 95^{th} percentiles based on the ensemble of particles released within each hydraulic domain. The travel times shown in Figure 3-32 have similar distributions for each hydraulic domain although some longer times are seen in HRD(D, E, M). This suggests that perhaps the travel time is more dependent on hydraulic gradients and flow directions rather than rock properties. A much more dramatic picture is seen for the initial Darcy velocity in Figure 3-33. The initial Darcy velocity in the HCD is much higher, and the initial Darcy velocity in HRD(A) is significantly higher than HRD(D, E, M) and has less spread between the 25^{th} and 75^{th} percentiles. Similarly the F-factor shown in Figure 3-34 has a median about 0.5 in log-space higher in HRD(D, E, M) than HRD(A).

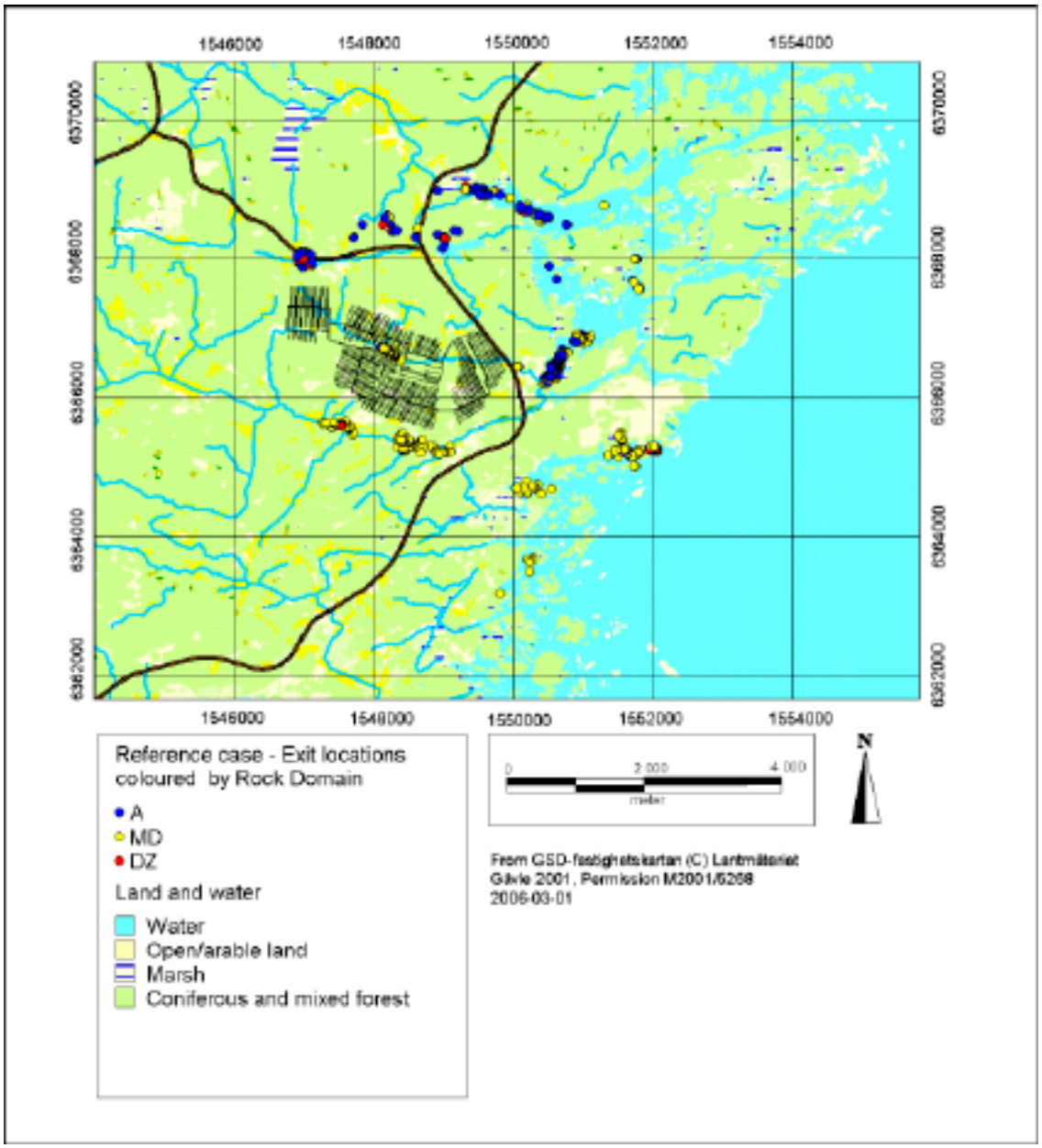

Figure 3-31. *Particle exit locations coloured by the hydraulic domain that the particle release point lies within: Rock domain HRD(A) is denoted A, mixed rock domain HRD(D,E,M) is denoted MD, and HCD is denoted DZ. Particles were released at 2,020 AD in the reference case model. GIS data is also plotted. The repository tunnels are projected on the ground surface.*

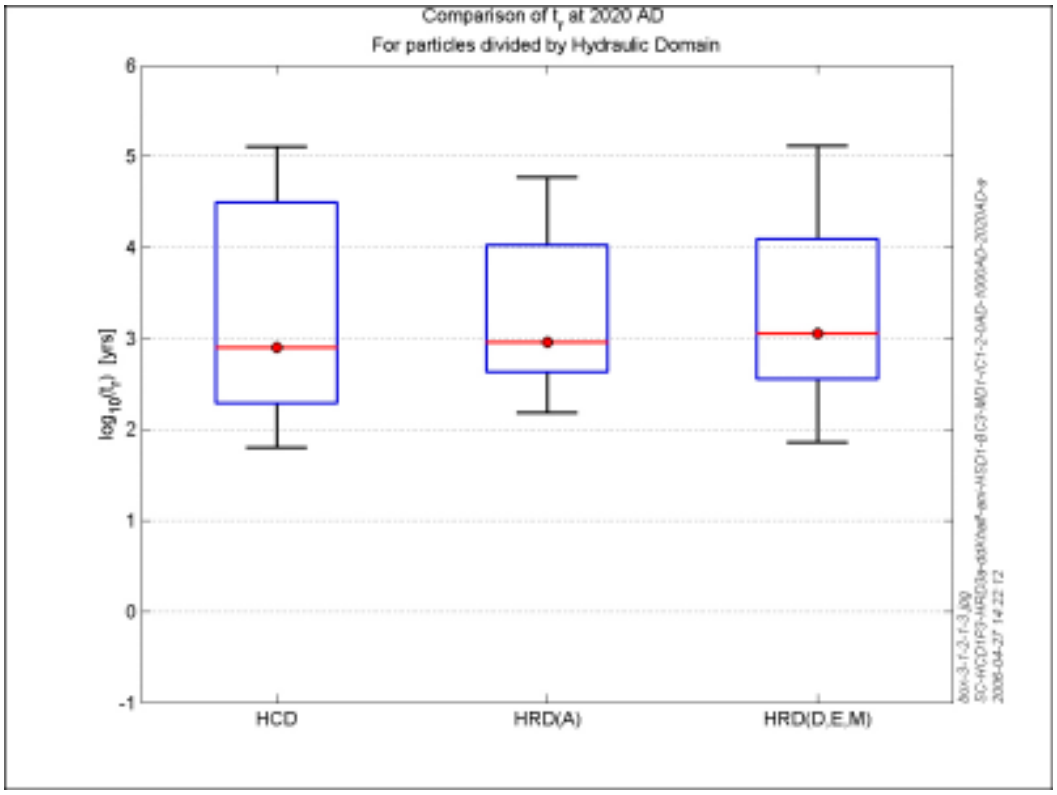

Figure 3-32. *Travel time results shown as box plots for the three categories of hydraulic domain. The red line with marker indicates the median value, the blue box indicates the range from the 25th to the 75th percentile, and the black whiskers show the 5th and 95th percentiles.*

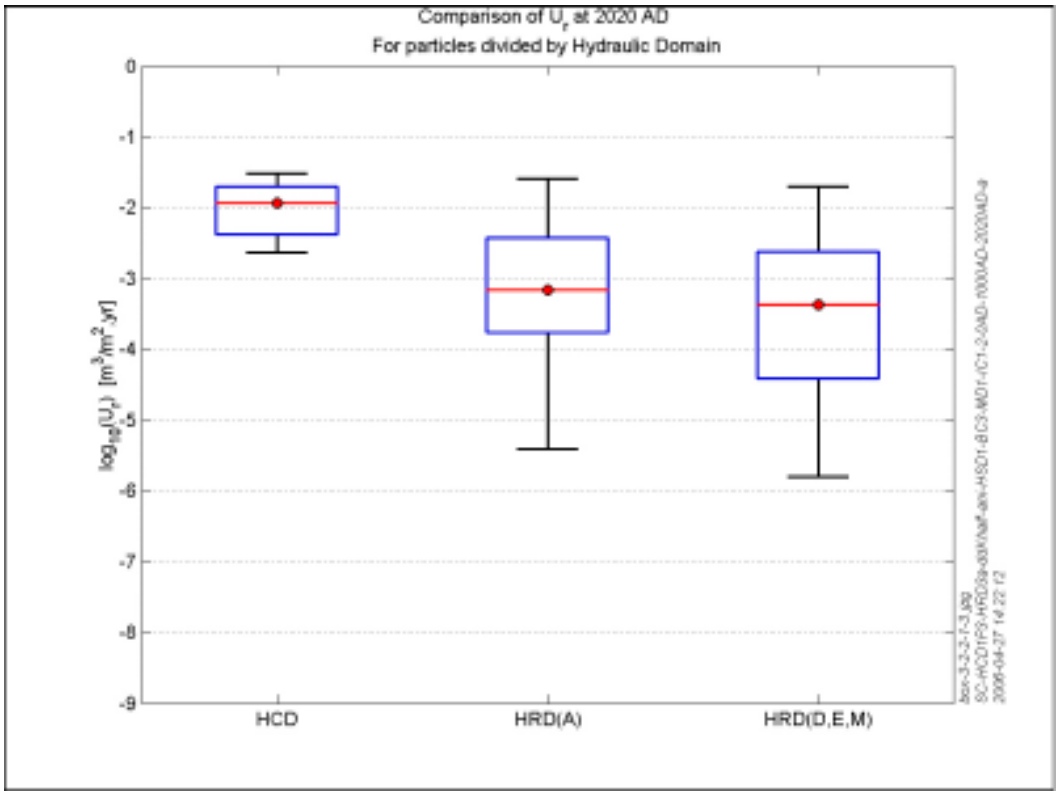

Figure 3-33. *Initial Darcy velocity results shown as box plots for the three categories of hydraulic domain. The red line with marker indicates the median value, the blue box indicates the range from the 25th to the 75th percentile, and the black whiskers show the 5th and 95th percentiles.*

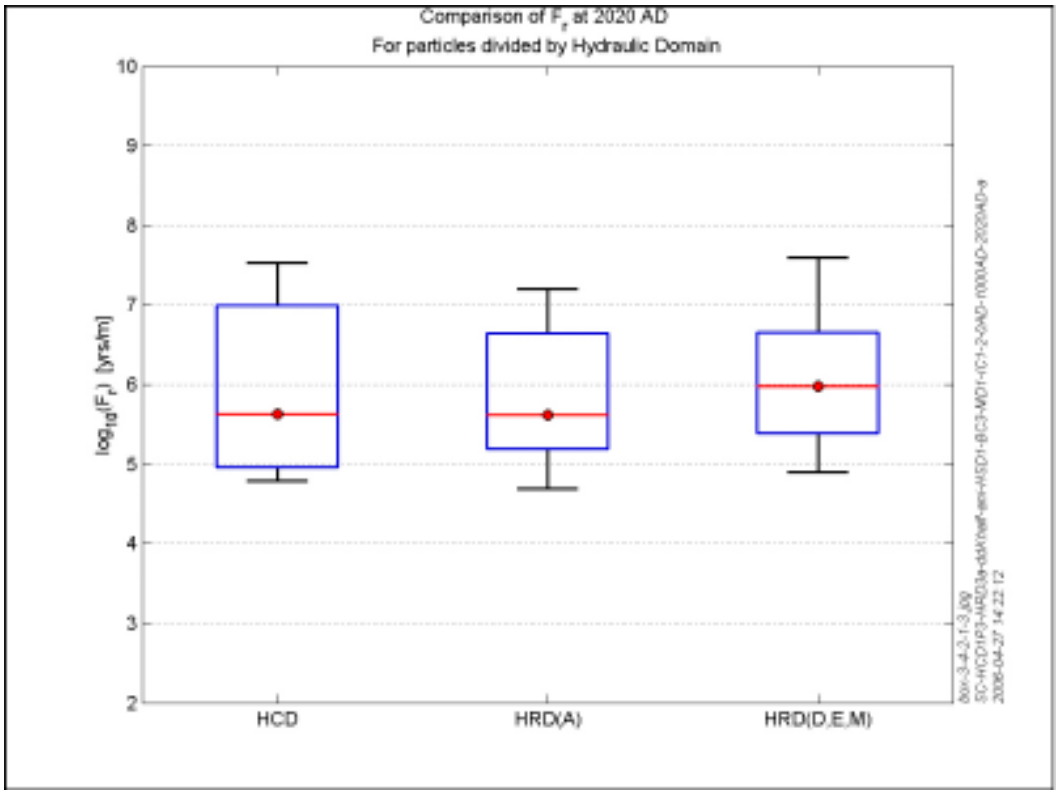

Figure 3-34. *F-factor results shown as box plots for the three categories of hydraulic domain. The red line with marker indicates the median value, the blue box indicates the range from the 25th to the 75th percentile, and the black whiskers show the 5th and 95th percentiles.*

Study of tunnel characteristics

The results were also analysed based on tunnel position, i.e. statistics for each tunnel are calculated. For all of the 244 tunnels, minimum, maximum, mean, standard deviation, median and 5th to 95th percentiles are obtained for the different performance measures. The lowest number of canister positions in a tunnel is 11, and the highest number of canisters in a tunnel is 38. This means that the comparison is approximate, but may still give some indication on where the least and most favourable canister positions are located. In Figure 3-35, the repository is divided into 10 subareas as defined by the layout delivered by the Design group, and the tunnel numbers are indicated for each repository subarea.

The tunnel characteristics are shown in Figure 3-36 and Figure 3-37, where the PM quantity for each tunnel is represented as a box with whiskers. The box is delimited by the 25th and 75th percentiles, and the median value is shown within the box. The whiskers show the 5th and the 95th percentiles. The boxes are by necessity vary thin to fit on all 244 tunnels. The tunnels are plotted in an order that is sorted according to their name. The names are built up by the label "BTD" and a number, where the number relates to the repository area and a specific number for the tunnel. The statistics are also available as tables for all performance measures and statistical entities. In Table 3-3 and Table 3-4 respectively, the least and most favourable tunnels according to the median travel time are listed. One can see some patterns, such as the shortest travel times occur in repository subareas 2 and 3, and the longest travel times are in the southern part of subarea 1, subareas 5 and 7.

The type of information shown in Figure 3-36 is accompanied by statistical results in tables for the calculated performance measures. For each tunnel, the performance measures are grouped and the statistics are calculated. This is illustrated by the two tables below, in which the median travel times are sorted and only the ten shortest median travel times are shown in addition to the ten longest median travel times.

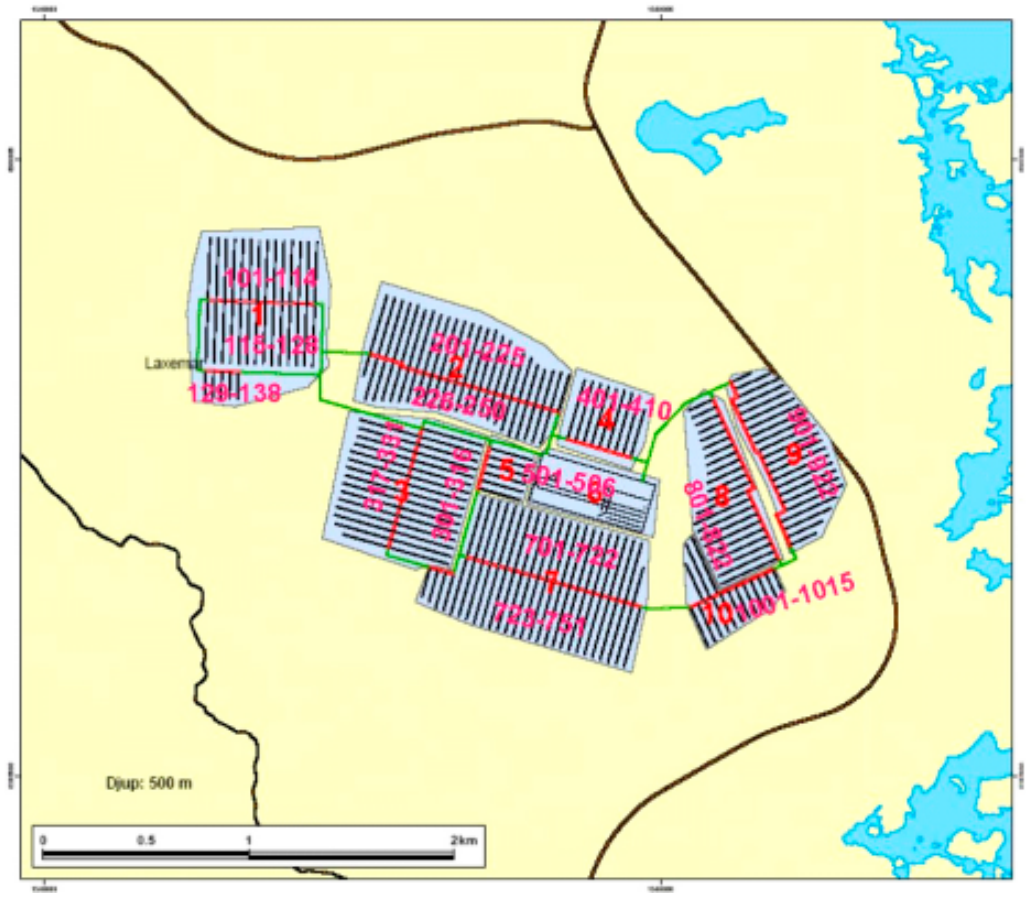

Figure 3-35. *Repository sub-areas and tunnel numbers.*

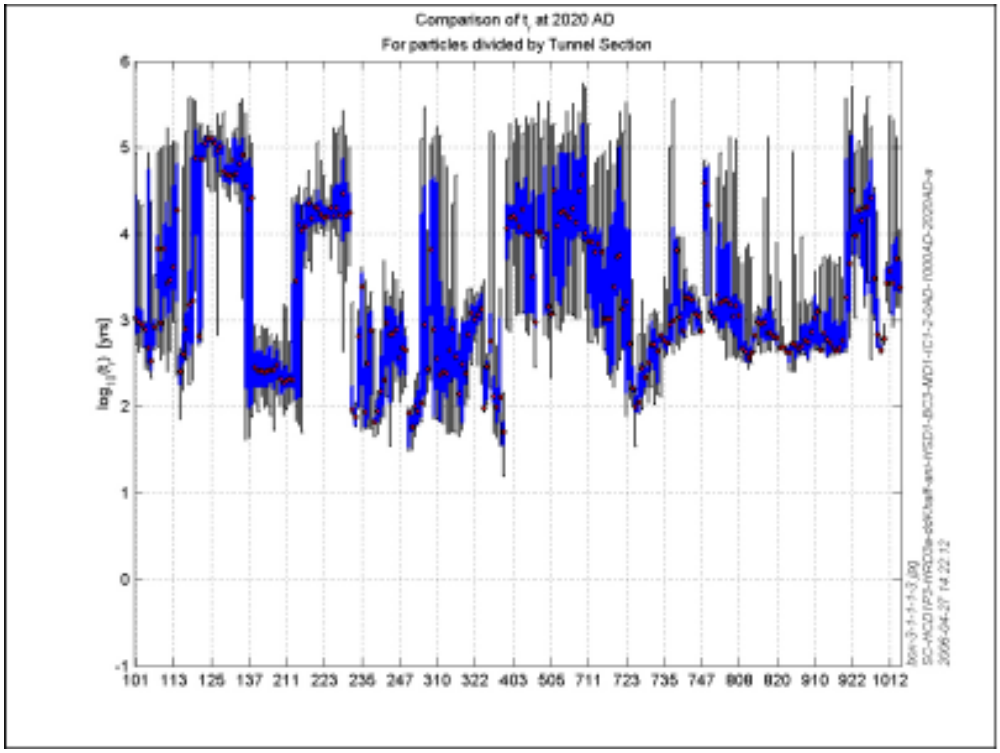

Figure 3-36. *Travel time statistics for the tunnels in the repository. The values are sorted by tunnel names. Each tunnel is represented by a thin box including median (red dot), range from 25th to 75th percentiles (blue bar), and 5th and 95th percentiles (black bars at the ends).*

Table 3-3. The ten tunnels with the shortest median travel times.

Tunnel	Median log10 (t_r)
BTD331C	1.71
BTD302C	1.77
BTD239C	1.82
BTD233C	1.88
BTD301C	1.92
BTD236C	1.94
BTD304C	1.94
BTD240C	1.95
BTD232C	1.97
BTD325C	1.99

Table 3-4. The ten tunnels with the longest median travel times.

Tunnel	Median log10 (tr)
BTD132C	4.86
BTD122C	4.87
BTD120C	4.88
BTD135C	4.92
BTD127C	4.97
BTD128C	5.01
BTD123C	5.05
BTD126C	5.05
BTD124C	5.10
BTD125C	5.11

Observing the travel time statistics and Figure 3-35, it seems like the southern half of repository subarea 1 is the most favourable, whereas the subareas 2 and 3 result in the shortest median travel time values. Several factors play a role here, such as the local gradient, distance to a deformation zone, rock domain, and distance to exit locations. Particle pathlines suggests that there is a discharge area on top of north-eastern corner of subarea 3.

It may be seen in Figure 3-37 that some tunnels in the southern part of subarea 1 have low Darcy velocity corresponding to HRD(D, E, M), whereas others just to the north have a much higher Darcy velocity. However, the reason seems to relate to a downward velocity in this area as well as the difference in rock domain. In subarea 2, the fluxes are about average, with some exceptions. In subarea 3, the fluxes seem generally to be above average, but also here exceptions may be found. Subarea 2 is mainly in HRD(A), while subareas 7, 10 and some of subarea 3 are HRD(D,E,M), but at least two low confidence zones are intersecting subarea 3.

3.3 Sensitivities

To explore a number of uncertainties in the definition of the reference case based on site data, a number of model variants have been used to quantify the sensitivity to different concepts and entities. One group of simulations are performed to study the sensitivity in the geological model. In this group, we define variants with spatial variability within each deterministic deformation zone, and the removal of low confidence zones. In another group, we define variants with

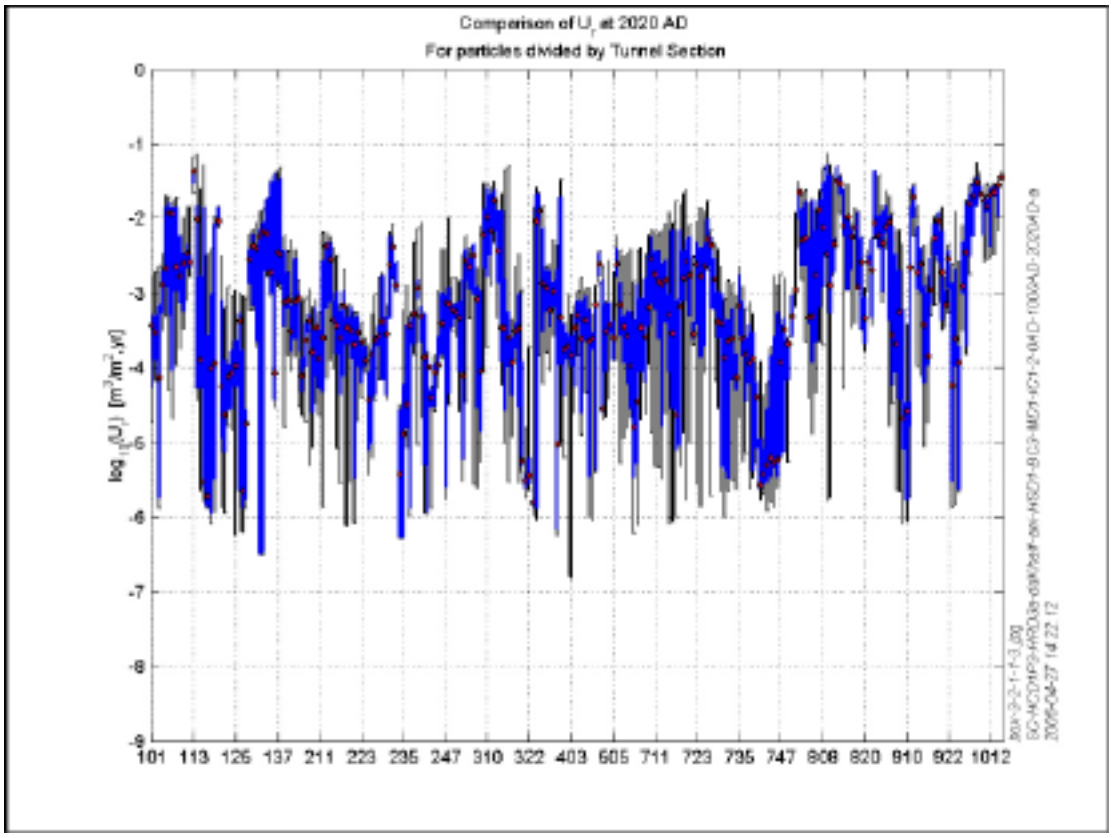

Figure 3-37. *Initial Darcy velocity statistics for the repository tunnels. The values are sorted by tunnel names. Each tunnel is represented by a box including median (red dot), range from 25th to 75th percentiles (blue bar), and 5th and 95th percentiles (black bars at the ends).*

properties obtained from other Hydro-DFN models than in the reference case. In a third group, the sensitivity to transport parameters is tested. Finally, a more elaborate model for the hydraulic soil domain based on maps of the Quaternary deposits is considered. The simulated cases are summarised in Table 3-5.

For two sets of simulations stochastic hydraulic properties are used to model spatial variability within each deterministic deformation zone. In all models the deterministic deformation zones are divided into three vertical sections depending on depth. A simplified step function is used to assign the hydraulic properties for each section. In these stochastic cases, the mean is based on the values used in the HCD for the reference case and a standard deviation for each vertical section is defined based on an interpretation of the data. Each deterministic deformation zone is then triangulated into triangles of side approximately 200 m and the transmissivity is sampled independently for each sub-triangle based on the appropriate mean and standard deviation depending on in which vertical section its centre lays. The standard deviations interpreted from the PSS 100 m interval data in the HCD's were (1.40, 1.08, 1.71) for ($z > -300$ m, -300 m $> z > -600$ m, $z < -600$ m). One set of realisations were performed with this set of standard deviations, and a second was performed with the standard deviations reduced by subtracting 0.5 from the std. in log(T) to (0.90, 0.58, 1.21). Another aspect to test with respect to uncertainty in the deterministic deformation zones is to remove deformation zones with low confidence.

All the sensitivity cases use HRD hydraulic properties from up-scaled DFN models. The properties of the HRD hydraulic properties of the reference case are obtained from one realisation where a semi-correlated transmissivity-size concept is used. The sensitivity to realisation is checked by repeating the simulation with realisations 2 and 3 of the underlying DFN model, i.e. only changing the random number seed.

Table 3-5. Summary of simulated cases.

Cases for SR-can Laxemar version 1.2	Properties or characteristics
SC_HCD1P3_HRD3a_ddKhalf_ani_HSD1_BC3_MD1_IC1_1	Reference case adopted from SDM L 1.2
SC_HCD1P3S1_HRD3a_ddKhalf_ani_HSD1_BC3_MD1_IC1	Stochastic HCD, std = (0.90, 0.58, 1.21), Rel. 1
SC_HCD1P3S2_HRD3a_ddKhalf_ani_HSD1_BC3_MD1_IC1	Stochastic HCD, std = (0.90, 0.58, 1.21), Rel. 2
SC_HCD1P3S3_HRD3a_ddKhalf_ani_HSD1_BC3_MD1_IC1	Stochastic HCD, std = (0.90, 0.58, 1.21), Rel. 3
SC_HCD1P3S1i_HRD3a_ddKhalf_ani_HSD1_BC3_MD1_IC1	Stochastic HCD, std = (1.40, 1.08, 1.71), Rel. 1
SC_HCD1P3S2i_HRD3a_ddKhalf_ani_HSD1_BC3_MD1_IC1	Stochastic HCD, std = (1.40, 1.08, 1.71), Rel. 2
SC_HCD1P3S3i_HRD3a_ddKhalf_ani_HSD1_BC3_MD1_IC1	Stochastic HCD, std = (1.40, 1.08, 1.71), Rel. 3
SC_HCD5P3_HRD3a_ddKhalf_ani_HSD1_BC3_MD1_IC1	Low confidence zones removed
SC_HCD1P3_HRD3a_ddKhalf_ani-S_C_HSD1_BC3_MD1_IC1	10 times higher T in Set_C
SC_HCD1P3_HRD3b_ddKhalf_ani_HSD1_BC3_MD1_IC1	Realisation 2 of DFN model
SC_HCD1P3_HRD3c_ddKhalf_ani_HSD1_BC3_MD1_IC1	Realisation 3 of DFN model
SC_HCD1P3_HRD4_ddKhalf_ani_HSD1_BC3_MD1_IC1	Correlated
SC_HCD1P3_HRD5_ddKhalf_ani_HSD1_BC3_MD1_IC1	Un-correlated
SC_HCD1P3_HRD3a_ddKhalf_ani_HSD2_BC1_MD1_IC1	Elaborate Overburden model
SC_HCD1P3_HRD3a_ddKhalf_ani_HSD1_BC3_MD1_MP_IC1	Lower matrix porosity
SC_HCD1P3_HRD3a_ddKhalf_ani_HSD1_BC1_MD1_FWS_IC1	Modified FWS in HRD

In the reference case there is already anisotropy in the transmissivity between fracture sets in the Hydro-DFN model prior to the up-scaling (see Section 2.3.2). In one variant the anisotropy is enhanced more by increasing the transmissivity in the sub-vertical Set_C which is aligned parallel to the maximum horizontal insitu stress. This is based on a potential scenario identified in the SDM work due to uncertainties in interpreting the transmissivity of vertical fractures from vertical boreholes. Other variants address the uncertainty in the transmissivity-size relationship. Variants are constructed based on Hydro-DFN models using the correlated and uncorrelated transmissivity-size concepts.

The sensitivity to transport parameters is tested by variation of the matrix porosity and flow-wetted surface area for the HRD. The matrix porosity case uses a value in the lower end of the suggested range of matrix porosity. In the flow-wetted surface variant, the values are obtained from Posiva flow log measurements (see Table 2-10).

Finally, the sensitivity to using a more elaborate hydraulic soil domain model based on mapping of the Quaternary deposits is addressed. In the reference case, the hydraulic soil domain is simplified to three 1 m thin layers with homogeneous conductive properties, and therefore it is suggested to test a soil model based on detailed measurements.

3.3.1 Sensitivity to deterministic deformation zones (HCD)

Two sets of variants with stochastic spatial variability of transmissivity within the deterministic deformation zones are evaluated each using three realisations as described above. Another case quantifies the geological uncertainty by removing deterministic deformation zones with low confidence.

Stochastic deformation zones

In order to quantify the sensitivity to spatial variability within each deterministic deformation zone, two sets of variants with high and moderate variability in transmissivity were simulated. The high variability case is based directly on the interpretation of PSS 100 m test intervals performed in DZ's, which gives standard deviations in log transmissivity ranging from 1.1 to 1.7. This will result in a huge spread of transmissivities over perhaps 10 orders of magnitude.

The moderate case reduces the standard deviation by subtracting 0.5 from std. log(T). Three realisations of each set of variances were performed.

The variant with lower standard deviations seems to give reasonable reference water compositions, whereas the case with higher standard deviation leads to unrealistic reference water profiles. In terms of performance measures for the ensemble of path-lines, the cases with moderate standard deviation give similar mean travel times as for the reference case, even slightly longer mean travel time for one realisation. The mean initial Darcy velocity seems to be higher in general for the cases with the moderate standard deviations. In terms of mean F-factors, the stochastic versions yield somewhat better performance than the reference case. One explanation is that by adding the stochastic component to the transmissivity, the flow-paths have to follow less direct routes through the HCD, and therefore increasing the path-length and F-factor. Figure 3-38 illustrates effect of HCD spatial variability on exit locations and F-factor to be compared with the reference case in Figure 3-29. Exit locations are slightly more dispersed in the stochastic case, especially realisation 3. Generally, though the exit locations are the same, and only a slight improvement in F-factor can be perceived from these plots.

In general, the mean performance measures have a higher variance for the simulations with a stochastic HCD transmissivity, than for the reference case. Out of all variants considered, the simulations with the higher standard deviations yield the worst and best performance in terms of median F-factor. However, since this set of cases results in unstable highly variable reference water simulations, then these cases should not be given too much credibility. Perhaps a standard deviation of about 1.0 is about the limit of what can reasonably simulated when a correlation length as large as 200 m is assumed.

Confidence level of deformation zones

In this variant, all the deterministic deformation zones that are classified as low in confidence are removed. Not surprisingly, the mean performance measures are generally better than in the reference case. In fact, it seems to be the most favourable case of all the simulated variants. The exit locations for this variant are shown in Figure 3-39 coloured by travel time, as this shows the greatest difference compared with the reference case in Figure 3-28. The exit locations are largely the same, except that a small lake in the north is no longer a discharge area here. The travel increases for most exit locations apart from perhaps in the stream that runs through the centre of the repository footprint.

3.3.2 Sensitivity to DFN interpretation

The variants in the Hydro-DFN properties considered were:

- 2 extra realisations of the reference case Hydro-DFN using semi-correlated T model,
- anisotropy in Set-C by increasing the transmissivity by a factor 10,
- a correlated T model,
- an uncorrelated T model.

DFN realisations 2 and 3

The HRD properties in the reference case are based on upscaling DFN models to obtain the corresponding ECPM values. In order to study the stochastic sensitivity, two other realisations of the Hydro-DFN were simulated. As reported in the SDM L 1.2 /Hartley et al. 2006a/, the salinities in the boreholes are relatively insensitive to the DFN realisation. Equally, overall PM statistics do not vary much between realisations. However, looking at individual exit locations

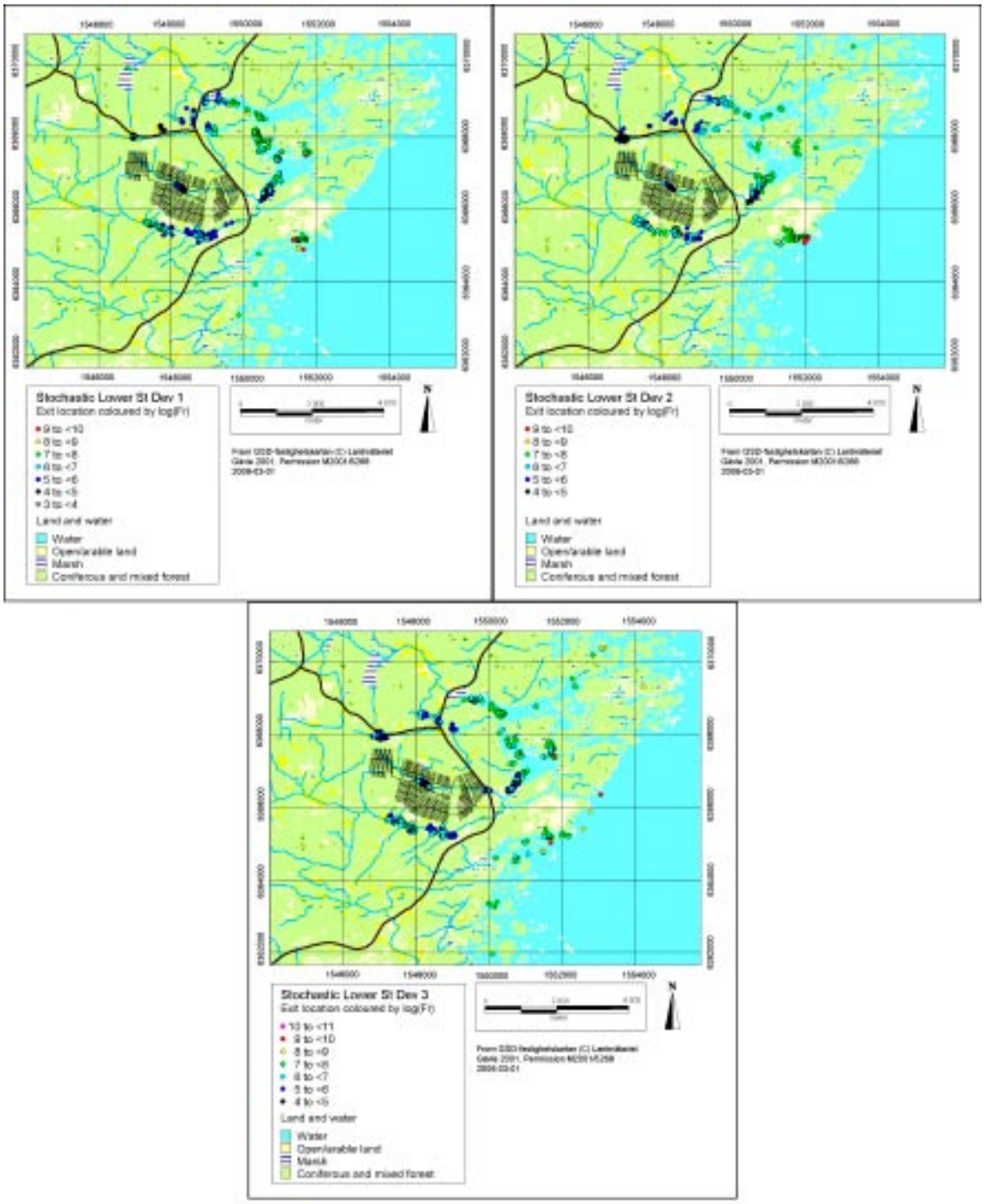

Figure 3-38. *Particle exit locations coloured by F-factor [yr/m] of pathlines released 2,020 AD for three realisations of the case with moderate spatial variability within each deterministic deformation zone. Together with GIS data, the repository tunnels are projected on the ground surface.*

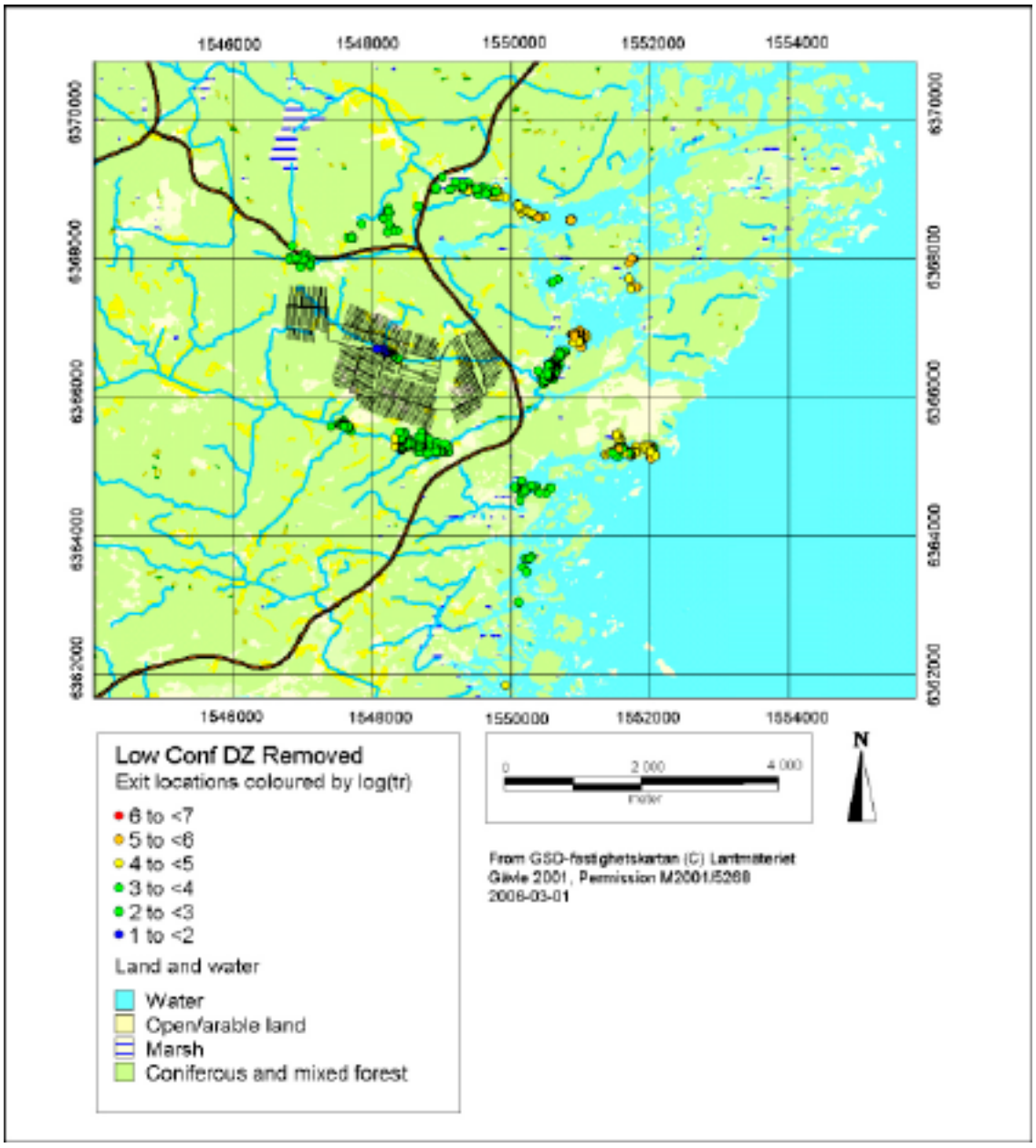

Figure 3-39. *Particle exit locations coloured by travel time [yr] of pathlines released 2,020 AD for the case with removed low confidence zones. Together with GIS data, the repository tunnels are projected on the ground surface.*

for the realisations shown in Figure 3-40 and compared with the reference case (realisation 1) in Figure 3-29, there is considerable variability. For example, both realisations show more dispersion of exit locations around the shoreline, especially realisation 2. Also, the discharge area to a stream to the north west of the repository present in realisation 1 moves 500 m east in realisation 3. The differences in statistics though are limited to the 90th and 95th percentiles suggesting the sensitivities in the PM's are mainly associated long paths that exit at the shoreline.

Anisotropy, increased transmissivity in Set_C

In this variant the transmissivity in Set_C is increased in the Hydro-DFN model prior to the upscaling. The transmissivity is 10 times higher than in the corresponding set in the reference case. This variant resulted in the shortest median travel time (by about 0.4 in Log10(t_r)) for the ensemble of path-lines (excluding the stochastic HCD variant with high standard deviation).

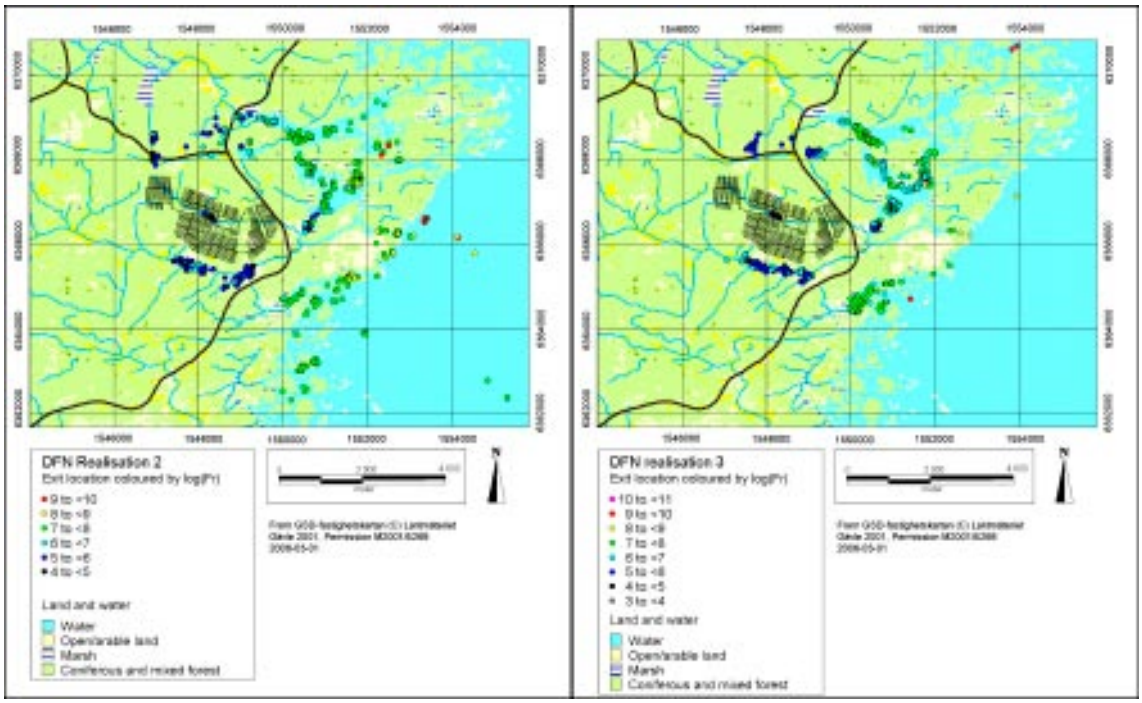

Figure 3-40. *Particle exit locations coloured by F-factor [yr/m] of pathlines released 2,020 AD for two additional realisations of the reference case. Together with GIS data, the repository tunnels are projected on the ground surface.*

This case also results in the highest mean initial Darcy velocity (by about 0.5 in Log10(U_r)) and lowest F-factor (by about 0.5 in Log10(F_r)). The reduction in F-factor is illustrated in Figure 3-41 along with exit locations. The reductions occur in the discharge areas associated with the streams to the north, south, east and centre. The exit locations themselves are less effected.

Correlated transmissivity-size model

In the reference case, a semi-correlated relationship between transmissivity and fractures size is used in the Hydro-DFN models. In this variant, a correlated fracture transmissivity-size model is used. The correlated case is similar to the reference case in terms of mean performance measures t_r and U_r. However, the F-factor values deviate more, about 0.3 lower in median Log10(F_r). The exit locations for this case coloured by F-factor along the flow-path are shown in Figure 3-42. In general, the case seems to be less favourable than the reference case. In addition, the spread in exit locations around the shoreline is larger than in the reference case. The changes are likely to be caused by the direct correlation giving more long continuous high transmissivity paths that will lead to some faster and more direct paths, though it also means there may be more potential for long horizontally connected paths that perhaps accounts for the greater number of discharge points around the shoreline.

Uncorrelated transmissivity-size model

In this variant, an uncorrelated fracture transmissivity-size model is used. The uncorrelated case is very similar to the reference case in terms of mean performance measures t_r, U_r *and* F_r. Performance is slightly worse than the semi-correlated reference case as median Log10(F_r) is 0.2 lower, for example. The exit locations for this case coloured by F-factor along the flow-path are shown in Figure 3-43. The exit locations are very similar to the semi-correlated case, i.e. less dispersed around the shoreline than for the correlated case. The distribution of F-factor values is also very similar to the reference case.

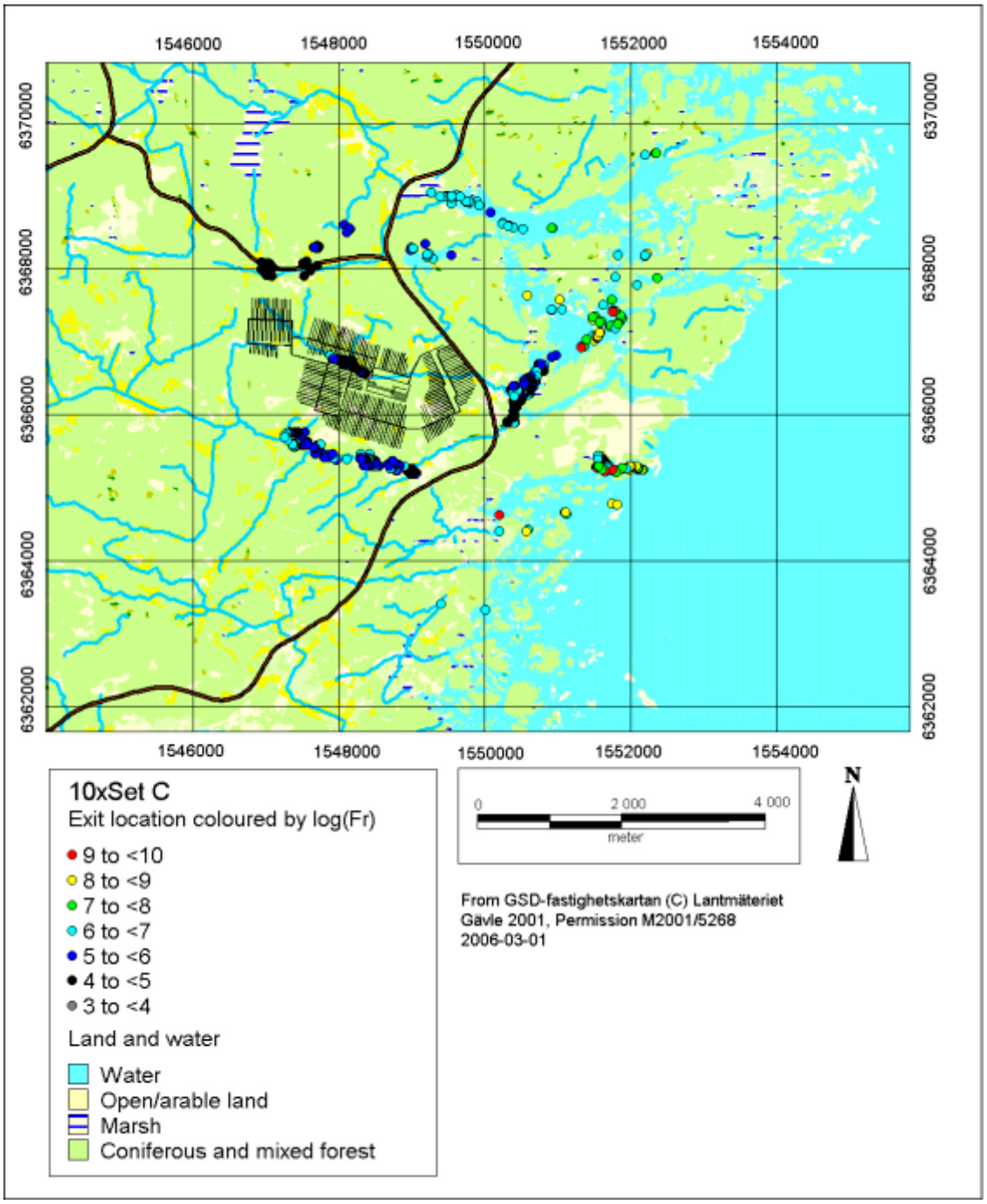

Figure 3-41. *Particle exit locations coloured by travel time [yr] of pathlines released 2,020 AD for the increased anisotropy case with ten times higher transmissivity in Set_C. Together with GIS data, the repository tunnels are projected on the ground surface.*

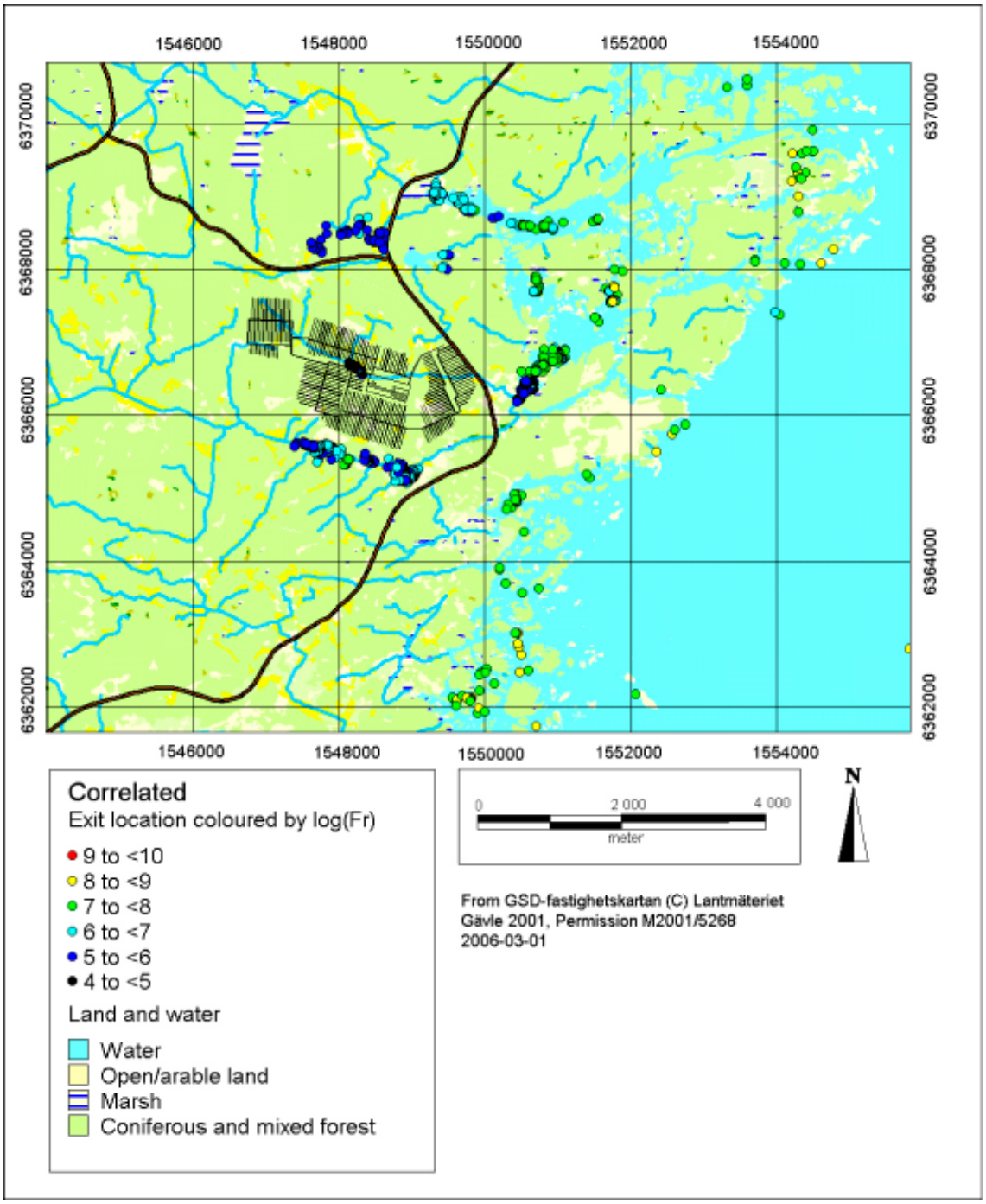

Figure 3-42. *Particle exit locations coloured by travel time [yr] of pathlines released 2,020 AD for the case with block HRD properties based on a Hydro-DFN model with a correlated T-size relationship. Together with GIS data, the repository tunnels are projected on the ground surface.*

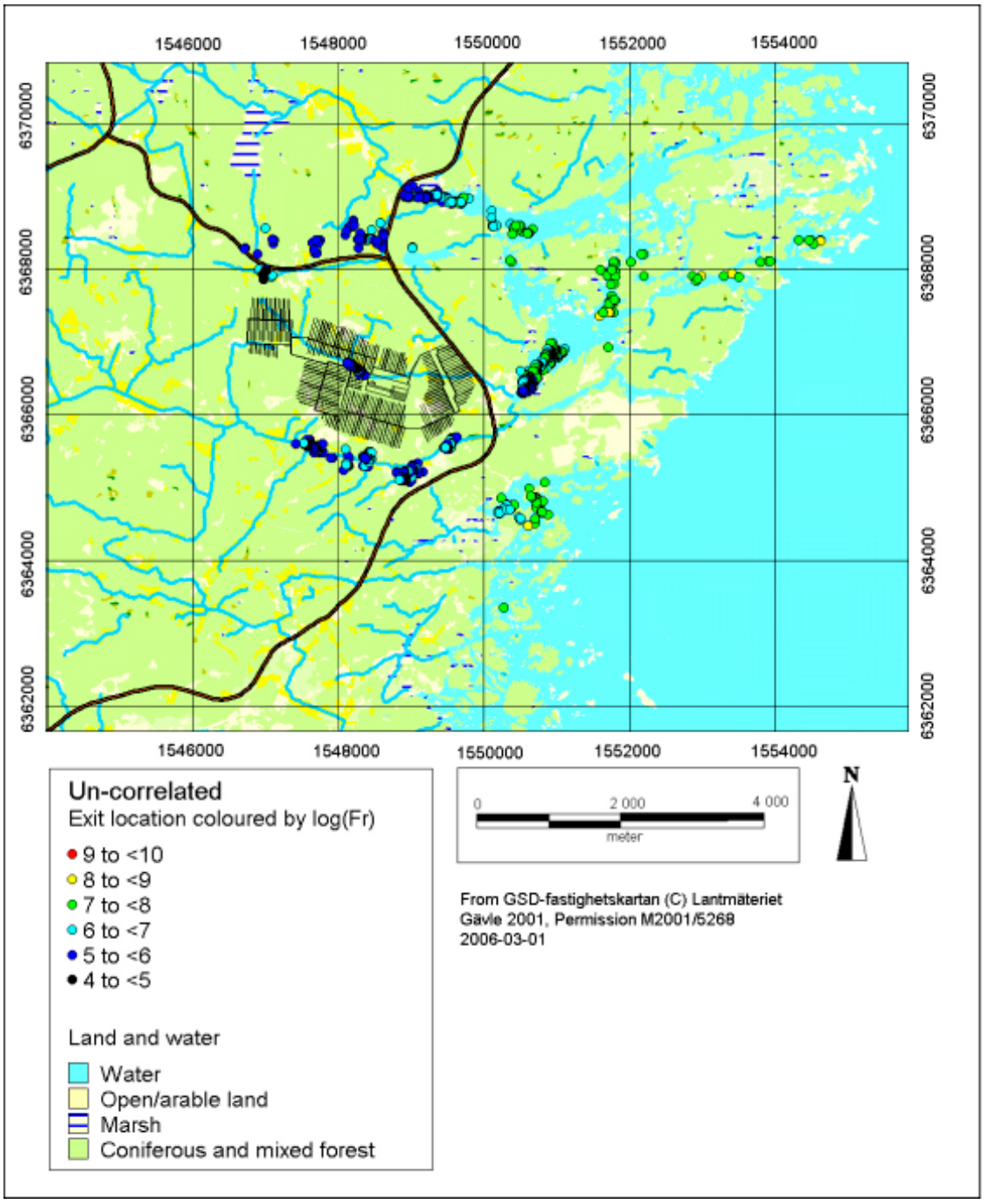

Figure 3-43. *Particle exit locations coloured by travel time [yr] of pathlines released 2,020 AD for the case with block HRD properties based on a Hydro-DFN model with an uncorrelated T-size relationship. Together with GIS data, the repository tunnels are projected on the ground surface.*

3.3.3 Sensitivity to transport properties

The sensitivity to transport parameters is tested by varying the matrix porosity and flow-wetted-surface area for the HRD. The matrix porosity case uses a value in the lower end of the suggested range of matrix porosity given in Table 3-1. In the flow-wetted-surface variant, the values are obtained from Posiva flow log measurements, as given in Table 2-10.

Matrix porosity

In this case the matrix porosity is lower than in the reference case. The result is that the median performance measures are similar to the reference case. The median Log10(F_r) is only 0.1 lower in this case.

Flow-wetted surface

In this case, the flow-wetted surface values are based on the PFL data that are used in rock-matrix diffusion model for transport of reference waters /Hoch and Jackson 2004/. These values are homogeneous within each hydraulic rock domain and are only used to calculate the rate of exchange between the reference water concentrations in the fracture system and rock matrix. An independent flow-wetted-surface parameter is used in the calculation of the F-factor in the pathline calculations that is derived from the connected fracture intensity of the underlying DFN within each finite-element. In terms of the median for ensemble travel times, this case is similar to the reference case. The median initial velocity is very slightly higher, and the median Log10(F_r) slightly lower, but the differences are about 0.1, or less, in log-space. The small difference is unsurprising since the values of flow-wetted-surface based on the modelled Hydro-DFN connectivity used in the reference case are similar to those derived from the PFL data, see Table 2-9.

3.3.4 Sensitivity to overburden interpretation

In the reference case, a 3 m thick layer with homogeneous properties is used to represent the overburden. In this variant, a more elaborate overburden model is used based on mapping and interpolation of the Quaternary deposits thickness and their properties as divided into distinct soil types. Again, the changes in median performance measures were about 0.1, or less, in log-space.

3.4 Summary

Here we summarise the evolution of PM's through the temperate period, PM statistics and the sensitivity of salinity in the Laxemar area.

3.4.1 Evolution of performance measures through the temperate climatic period

The hydrogeological conditions at Laxemar change over the temperate climatic period due to land-rise and changes in the chemical composition of surface and sub-surface waters. As well as studying the evolution of exit locations, it is also important to study how PM's evolve and identify any least favourable release times. The evolutions of mean travel times and F-factor over the ensemble of canister locations as a function of release time are plotted in Figure 3-45 and Figure 3-46, respectively. As can be seen, large changes occur in the past when the shoreline retreats over the top of the site. After about 0 AD, the changes are very gradual and small in magnitude, especially after 4,000 AD.

For the repository-scale modelling, it is only possible to study particular instances in time, due to the large numerical sizes of models. Hence, some representative release times need to be selected to quantify variations in PM's as the hydrogeological conditions evolve. At these

selected times, boundary conditions and fluid density profiles are transferred to the repository-scale models to allow flow and transport to be investigated on a finer scale. Based on plots such as Figure 3-45 and Figure 3-46, the representative times selected were:

- 6,000 BC – a time at the start of the Littorina period when there is a local maxima in the shore-level height around when the first minima occurs in travel times and F-factors.
- 2,000 BC – a time when a second minima occurs when the Littorina salinity is starting to reduce in mean travel times and F-factors.
- 2,020 AD – present-day.
- 6,000 AD – a time when the land rises above sea-level around Äspö.

3.4.2 PM statistics and sensitivities

In order to compare the different variants, the sensitivities of the PM statistics are collated in Table 3-6 to Table 3-8 for t_r, U_r and F_r. Corresponding plots of the median PM's for each variant are shown in Figure 3-46 to Figure 3-48. The variant denoted 10xSet_C with higher transmissivity in Set_C gives the shortest median log travel times and F-factor. The variant "S2, higher standard deviation" also gives relatively low median log travel time, but since the simulated reference water compositions seem unrealistic, then this case is not plausible. The model based on a Hydro-DFN with a correlated transmissivity-size relationship is also significantly worse than the reference case. Not surprisingly, the variant where the low confidence zones are excluded from the model give the most favourable median travel times.

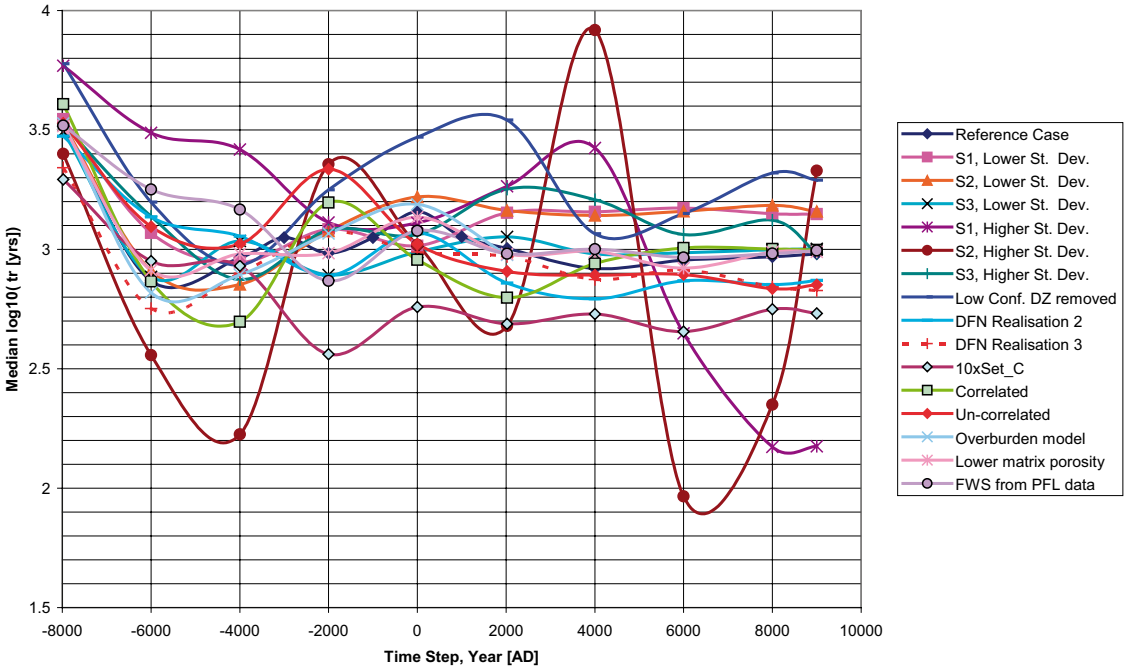

Figure 3-44. *Comparison of mean travel times [yrs] for the modelled cases. Performance measure values presented as log_{10} for different release times.*

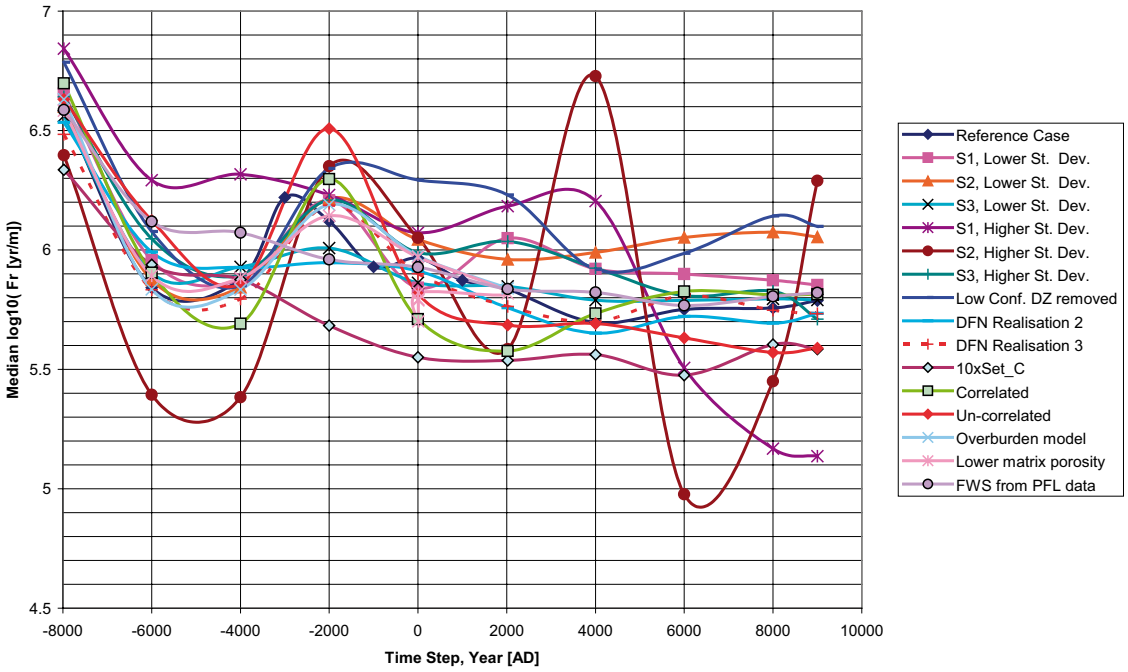

Figure 3-45. *Comparison of mean F-factor values [yr/m] for the modelled cases. Performance measure values presented as log_{10} for different release times.*

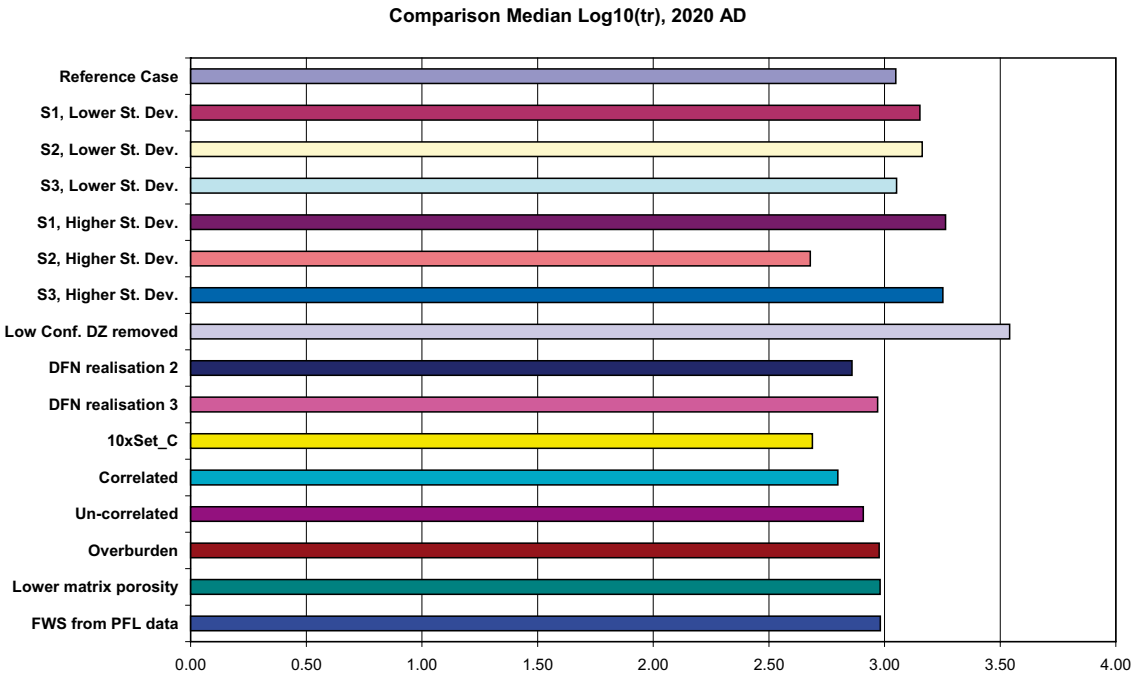

Figure 3-46. *Comparison of median travel time, t_r [yr], for the calculated cases. Results for a release at 2,020 AD.*

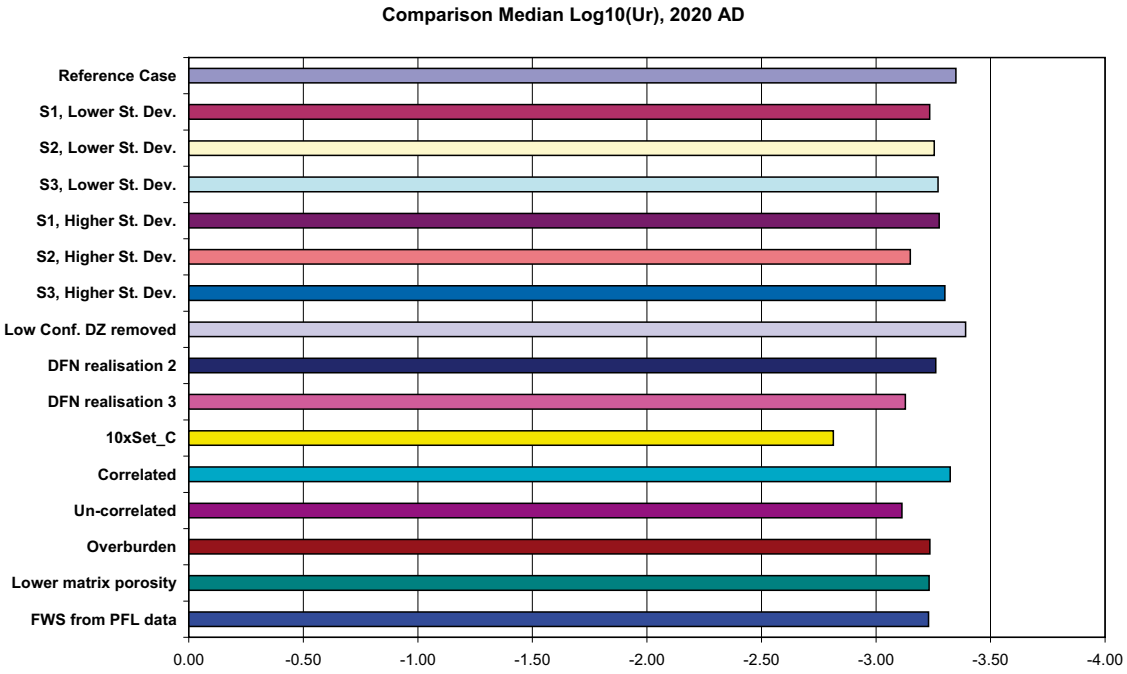

Figure 3-47. *Comparison of median initial Darcy velocity, U_r [m/yr], for the calculated cases. Results for a release at 2,020 AD.*

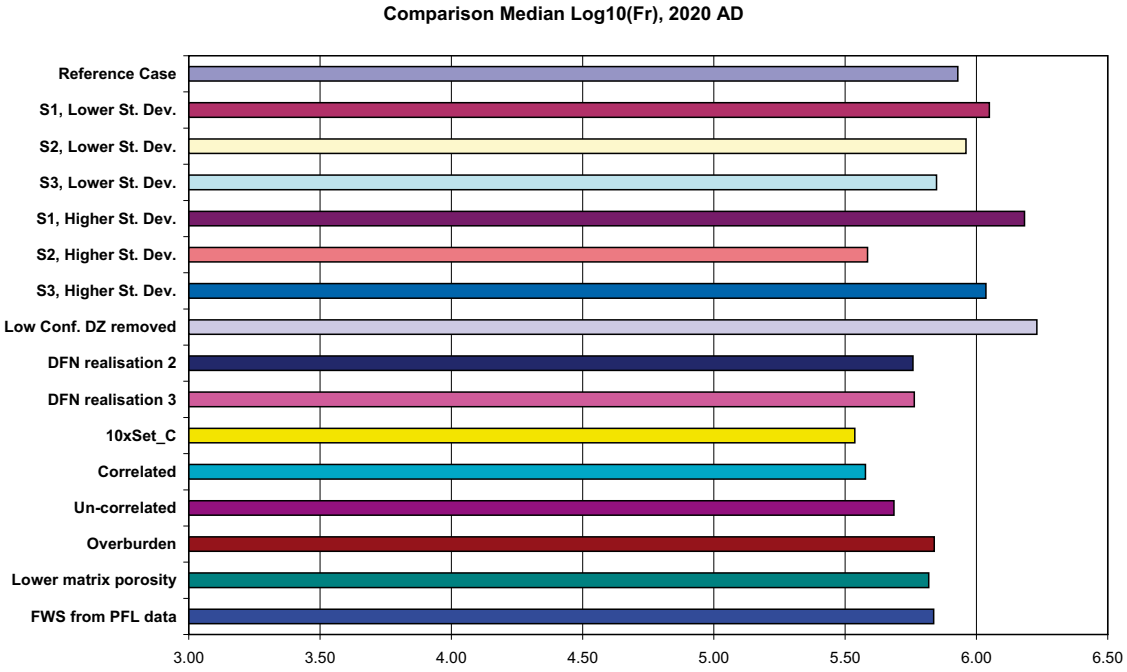

Figure 3-48. *Comparison of median F-factor values, F_r [yr/m], for the calculated cases. Results for a release at 2,020 AD.*

Table 3-6. Cases sorted on ascending median $Log_{10}(t_r)$. Results for a release at 2,020 AD.

Case	Median	5th percentile	95th percentile	Mean	Std deviation
S2, Higher St. Dev.	2.68	0.73	5.17	2.82	1.38
10xSet_C	2.69	1.48	4.74	2.93	1.01
Correlated	2.80	1.73	5.23	3.12	1.11
DFN realisation 2	2.86	1.79	5.15	3.16	1.04
Un-correlated	2.91	1.83	5.01	3.20	1.02
Overburden	2.98	1.94	5.07	3.20	0.91
Lower matrix porosity	2.98	1.93	5.05	3.25	0.96
FWS from PFL data	2.98	1.92	5.04	3.29	1.00
Reference Case	3.05	1.85	4.67	3.16	0.89
S3, Lower St. Dev.	3.05	1.68	5.17	3.23	1.01
S1, Lower St. Dev.	3.15	1.94	5.19	3.50	1.13
S2, Lower St. Dev.	3.16	1.93	5.13	3.43	1.02
S3, Higher St. Dev.	3.25	1.51	5.33	3.43	1.22
S1, Higher St. Dev.	3.26	1.93	5.17	3.45	1.07
Low Conf. DZ removed	3.54	2.17	5.25	3.63	1.01

Table 3-7. Cases sorted by descending median $Log_{10}(U_r)$. Results for a release at 2,020 AD.

Case	Median	5th percentile	95th percentile	Mean	Std deviation
10xSet_C	–2.81	–5.62	–1.51	–3.08	1.26
Un-correlated	–3.11	–5.78	–1.83	–3.36	1.17
S2, Higher St. Dev.	–3.15	–5.69	–1.55	–3.32	1.24
FWS from PFL data	–3.23	–5.70	–1.64	–3.37	1.20
Lower matrix porosity	–3.23	–5.70	–1.64	–3.37	1.20
S1, Lower St. Dev.	–3.23	–5.66	–1.57	–3.35	1.21
Overburden	–3.24	–5.72	–1.65	–3.38	1.20
S2, Lower St. Dev.	–3.25	–5.68	–1.73	–3.41	1.17
DFN realisation 2	–3.26	–5.85	–1.89	–3.44	1.17
S3, Lower St. Dev.	–3.27	–5.68	–1.54	–3.37	1.23
S1, Higher St. Dev.	–3.28	–5.61	–1.47	–3.32	1.25
S3, Higher St. Dev.	–3.30	–5.69	–1.50	–3.38	1.26
Correlated	–3.32	–5.76	–1.90	–3.48	1.12
Reference Case	–3.35	–5.81	–1.82	–3.50	1.18
Low Conf. DZ removed	–3.39	–5.79	–1.76	–3.56	1.18

Table 3-8. Cases sorted by ascending median $Log_{10}(F_r)$. Results for a release at 2,020 AD.

Case	Median	5th percentile	95th percentile	Mean	Std deviation
10xSet_C	5.54	4.50	8.93	5.85	1.25
Correlated	5.58	4.72	7.63	5.88	0.93
S2, Higher St. Dev.	5.59	3.87	8.01	5.75	1.21
Un-correlated	5.69	4.79	7.38	5.91	0.85
DFN realisation 2	5.76	4.76	7.65	5.98	0.96
Lower matrix porosity	5.82	4.77	7.40	5.97	0.87
FWS from PFL data	5.84	4.77	7.54	6.04	0.96
Overburden	5.84	4.77	7.42	5.94	0.81
S3, Lower St. Dev.	5.85	4.75	7.63	6.00	0.96
Reference Case	5.93	4.82	7.40	6.02	0.83
S2, Lower St. Dev.	5.96	4.89	7.65	6.14	0.95
S3, Higher St. Dev.	6.04	4.73	9.24	6.41	1.38
S1, Lower St. Dev.	6.05	4.73	7.74	6.21	1.04
S1, Higher St. Dev.	6.18	4.59	8.63	6.35	1.23
Low Conf. DZ removed	6.23	4.77	7.72	6.27	0.93

3.4.3 Sensitivity of salinity

Comparisons of salinities in KLX01–04 are shown in Figure 3-49 and Figure 3-50 for the reference Case and many of the variants to illustrate the sensitivity of the simulated hydro-geochemistry in the Laxemar subarea. These plots show that the salinity is mostly insensitive to the uncertainties considered. However, the case with high stochastic variability within the deterministic DZ's stands out as having a very poor prediction of salinity, with the Brine being flushed to a much greater depth than the other variants. Again, suggesting this case is not plausible. The variant with higher transmissivity in Set_C also has Brine at greater depth, suggesting the hydraulic conductivity may be unrealistically high.

3.5 Discussion

The reference case from the SDM report by /Hartley et al. 2006a/ has been utilised here to quantify SA performance measures based on particle tracking for a release from the canister positions at times in the past, present and future to study the evolution of discharge areas and performance measures over the current temperate climatic period, and to be used as an analogue for future temperate periods. The model uses an ECPM conceptual model, where hydraulic properties are based on upscaling a Hydro-DFN. The hydraulic conductivity in each finite-element is parameterised by a full tensor in order to represent anisotropy in the underlying fractures. The deterministic deformation zones that have been inferred from the interpreted site information are also incorporated. The simulations are transient and model the effects of shore-level displacement and changes in the salinity in the Baltic Sea on groundwater flow and hydro-geochemical mixing. The time period modelled is from 8,000 BC to 20,000 AD. At chosen release times, particles are released from the canister positions to calculate pathlines using the instantaneous velocity field at the chosen times. This gave ensemble statistics for performance measures as well as the spatial distribution of exit locations.

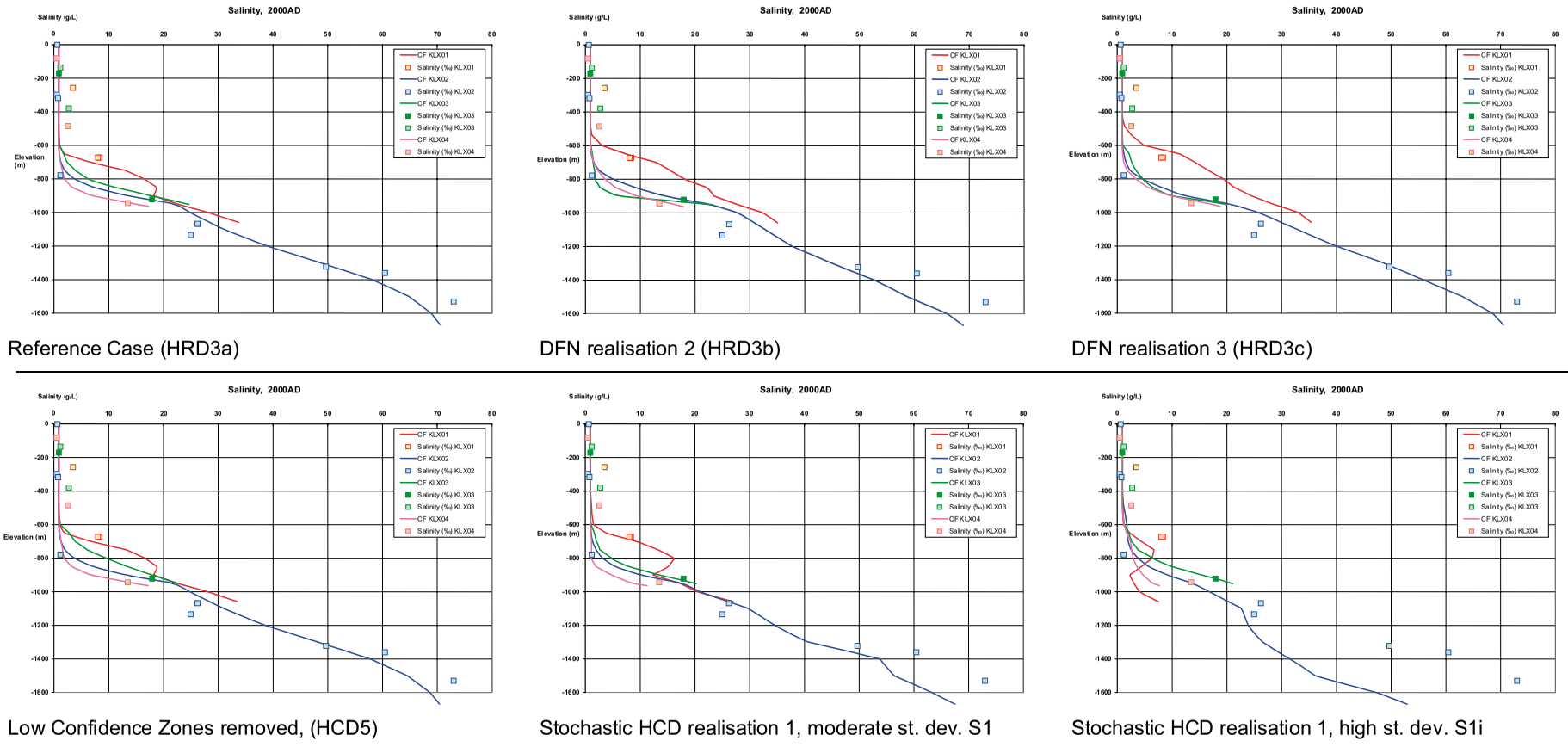

Figure 3-49. *Comparison of salinity in KLX01–04 between the Reference Case, DFN realisation 2 and 3, low confidence zones removed, and two stochastic cases.*

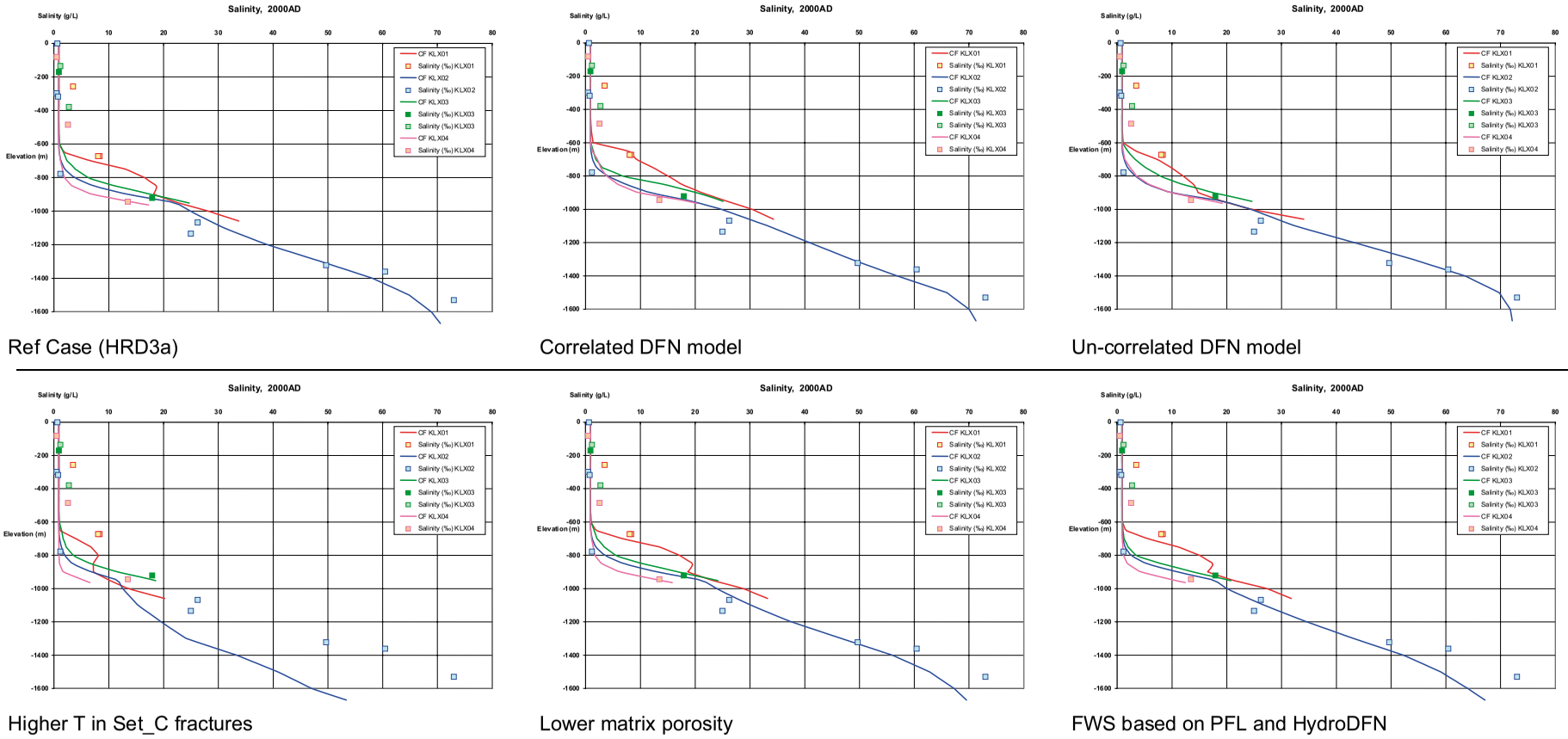

Figure 3-50. *Comparison of salinity in KLX01–04 between the Reference Case, cases with correlate and uncorrelated DFN models, a case with higher T in Set C, lower matrix porosity, and FWS based on PFL data.*

It was found that least favourable performance measures are found between about 2,000 BC and 1,000 BC. This time-frame coincides with that at which the coastline is directly above the starting positions. After the present-day, the performance measures are generally very constant. The only significant changes take place in the 20–30% of flow-paths that discharge at the shoreline which slowly retreats in the future. Based on the evolution of performance measures and exit locations, 6,000 BC, 2,000 BC, 2,020 AD and 6,000 AD were chosen as representative times to be used in the more detailed repository-scale modelling reported in Section 4.

A series of variants have been simulated to explore the sensitivity of the SA performance measures, exit locations and groundwater chemistry to various uncertainties that were highlighted in the SDM or were considered important for SA. One group of simulations were performed to study the sensitivity to the deterministic deformation zones, including cases with spatial variability within deformation zones, and with low confidence zones absent. Another group included variants based on variations in the Hydro-DFN model. A third group investigated sensitivities to transport parameters. Finally, the sensitivity to the hydraulic soil domain model was addressed. The variants are summarised in Table 3-5.

One variant that stood out has a higher transmissivity in the sub-vertical Set_C giving greater heterogeneity than the reference case since it gave the least favourable performance measures of the cases explored, although the predicted salinities for this case suggest it perhaps has implausibly high hydraulic conductivities. The variants with stochastic variability within the deterministic deformation zones gave a large spread in the results. Some performance measures in the simulations were worse than in the reference case, whereas the converse also occurred for these stochastic cases. However, when a large stochastic variability was used, unrealistic salinity profiles were predicted. Thus, less emphasis is put on this set of cases. More plausible variants are found when the standard deviation in transmissivity is decreased by subtracting 0.5 from std. $\log(T)$ to give values of std. $\log(T)$ around 1.0 or less. A variant with a correlated relationship between fracture transmissivity-size, which was used in the base case for Forsmark, resulted in slightly worse performance measures than the reference case with a semi-correlated model. Not surprisingly, the case with low confidence deterministic deformation zones removed gave improved performance measures.

In the cases where all deterministic deformation zones were used, about 3% of the start positions start within the HCD, but a clear effect could be observed by removing these low confidence zones. Consideration was also given to the difference in starting particles in the different hydraulic rock domains. The initial Darcy velocity in HRD(A) is significantly higher than HRD(D, E, M) and has less spread between the 25^{th} and 75^{th} percentiles. Similarly the F-factor has a median about 0.5 in log-space higher in HRD(D, E, M) than HRD(A). Considering how performance measures vary between tunnel locations, the shortest travel times occur in repository subareas 2 and 3, and the longest travel times are in the southern part of subarea 1, subareas 5 and 7.

4 Detailed repository-scale modelling and input to Safety Assessment (SA)

As described in Section 2.2.5, the SA methodology requires flow-paths to be calculated for three potential paths for radionuclides to leave the canister and enter the host rock: via a fracture adjacent to the deposition hole; through the EDZ around the base of the deposition tunnel, or via the tunnel itself. To quantify each of these paths it is necessary to perform detailed flow and transport calculations down to the scale of a metre or less around the repository. Hence, fine-scale models must be constructed, and these models must also be nested in some way to capture the larger scale flow and transport situation at a variety of release times.

The methodology followed is outlined schematically in Figure 2-11. Generally, the approach is to use a repository-scale DFN model to represent in detail the pathways around the deposition holes, and if this model is of insufficient volume to capture the full flow-path to the surface, then the path is continued in a larger regional-scale DFN model. In the repository-scale DFN model, a combined model is used to embed a CPM sub-model representation of the porous materials backfilling the deposition holes (bentonite) and tunnel system (mixed bentonite and crushed rock) within a DFN model of the surrounding rock as show in the example given in Figure 2-7. In the regional-scale DFN model, we consider a local-scale DFN model embedded within an ECPM representation of the fracture network and deformation zones on a regional-scale as show in the example given in Figure 2-6. The ECPM model grid and properties are identical to those used in Section 3. For both models, the embedded nesting technique described in Section 2.2.1 is used to ensure continuity of pressure, and conservation of mass flux across. In this second model, the repository is represented by adding equivalent fractures to represent the tunnel system, but this does not include the detail of individual deposition holes. These models require that boundary conditions be defined on all external surfaces by importing the fluid density and pressure from the ECPM regional-scale models described in Section 3.

For the repository-scale models, the repository is represented explicitly down to a resolution of a metre or less, and so the model domain must be limited for practical reasons. Hence the repository and surrounding bedrock were represented by four individual models, each of which covers between 1 and 3 main tunnels and their associated deposition tunnels with a vertical extent from –700 m to 0 m elevation. This means that the individual repository-scale model domains may not capture the entire length of all flow-paths. Therefore, once a particle reaches the boundary of the repository-scale model, the pathline is continued in the regional-scale DFN model.

For the regional-scale models, the repository is represented at a slightly lower resolution than the repository-scale models, and so larger DFN domains are possible. Here, a DFN sub-model of 4,100×3,200×1,000 m is used. The sub-model domain includes a representation of the entire repository tunnel and EDZ system and has been chosen large enough to include a large majority of particle exit locations at the surface. In the SR-Can study for Forsmark 1.2 /Hartley et al. 2006b/, the robustness of this approach was quantified and the sensitivity to nesting was tested by comparing results when a particle is continued in an ECPM regional-scale model after being first tracked to the boundary of a repository-scale DFN model against tracking an entire path within a regional-scale DFN model. The comparison indicated that exit locations were consistent between these two approaches.

The repository-scale DFN models, augmented by regional-scale DFN models to complete the flow-paths, provide a much better resolution of flow and transport than the ECPM regional-scale models described in Section 3, since the entire flow-path is calculated within a DFN concept that gives a more natural representation of quantities such as the F-factor. Also, paths are forced to follow the fracture connections within a network, whereas they tend to be less tortuous in an

ECPM model. For these reasons, DFN models rather than ECPM models are used to provide the performance measures required as input to SA calculations. The models described in this section represent a refinement of the regional-scale cases described in Section 3. Uncertainties need to be quantified for this series of models also. However, to limit the number of calculations, only those key variants identified in Section 3 are considered.

4.1 Combined DFN/CPM repository-scale model

We shall start by describing the DFN/CPM combined repository scale models, in which a DFN sub-model is used for the bedrock and a CPM sub-model for the repository. The stochastic nature of this model exhibits heterogeneities in the occurrence and magnitude of flow, which is consistent with field-tests and is expected around a repository.

For this model, for practical reasons it was necessary to split the repository into four blocks, each containing one to three main tunnels as shown in Figure 4-1. The overall repository has an area roughly 3 km by 2 km (see Figure 2-16), and it should be noted that it is non-coplanar since each deposition tunnel slopes down slightly toward its adjoining main tunnel. A relatively thick domain was used so that many particles could be tracked to the near-surface within the DFN sub-model. For each model, a domain approximately 1 km by 1 km by 700 m thick was used. The vertical extent is from $z = -700$ m to $z = 0$ m elevation, with the base of the deposition tunnels is at around $z = -520$ m on average. An elevation of 0 m for the top of the DFN-sub-model

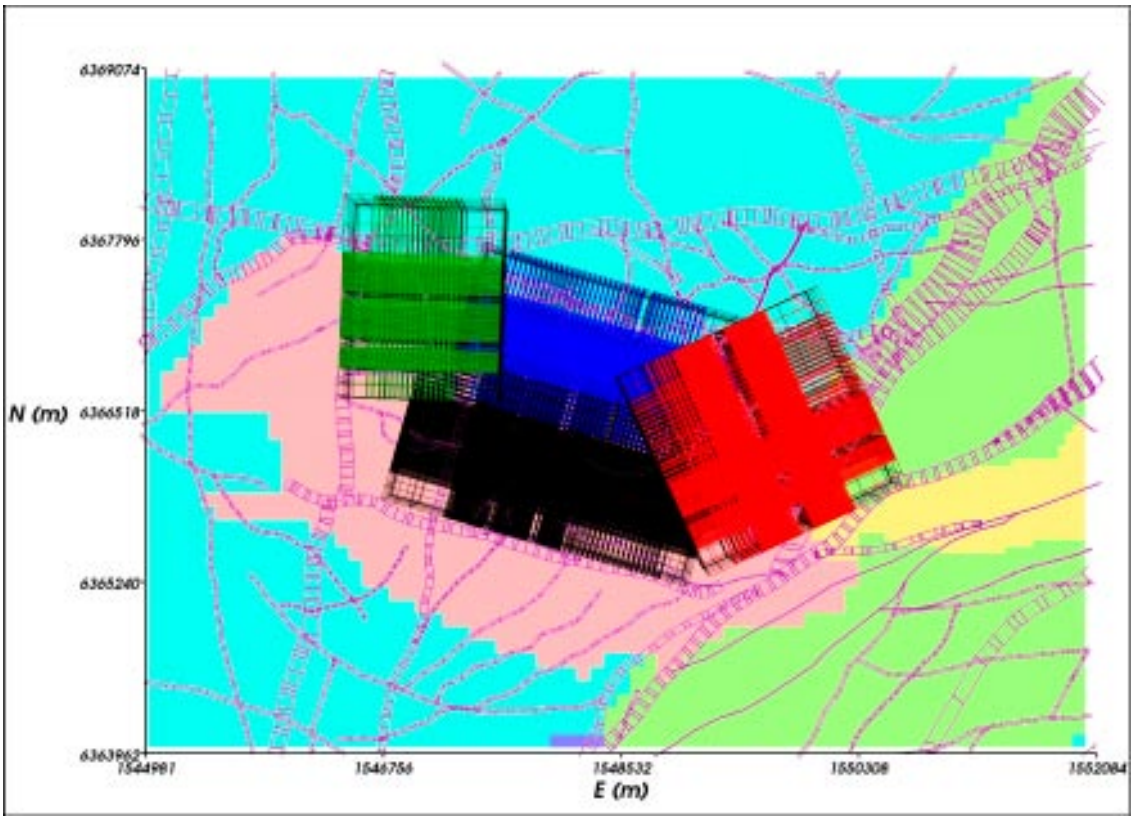

Figure 4-1. *The four repository-scale model grids to represent the repository areas numbered in Figure 2-16: Block 1 (area 1, green), block 2 (area 8, 9 and 10, red), block 3 (areas 2 and 4, blue), block 4 (areas 3, 5 and 7, black). The grids are superimposed on a horizontal slice through the HRD model at repository depth (z = –520 m): HRD(A) (blue-green), HRD(A2) (green), HRD(D,E,M) (pink), HRD(B,C) (orange). The HCD are also shown in purple on the section as defined by segment volumes.*

was chosen since it is near the base of the HSD layers in the regional-scale ECPM model which is an appropriate position from which to supply boundary conditions for the top surface. The bottom boundary was chosen at $z = -700$ m where typically salinity starts to increase providing a potential boundary to vertical flow. However, the boundary condition on the base is specified pressure and density, so particles may escape through this surface if flow is downwards. In these rare cases, particles are continued in the regional-scale model.

As shown in Figure 4-1, the four blocks overlap to keep the grid topology relatively simple. To calculate flow and transport for the whole repository, flow simulations were performed for each of the four blocks separately. Although there is an overlap, flow-paths were only calculated once for each deposition hole by only calculating flow-paths for those deposition tunnels that are associated with the main tunnels within the block, for each block.

For each block, a nesting procedure was used to set boundary conditions on the external surfaces of the block by interpolation from the corresponding regional-scale ECPM model at a selected time. The model set-up and numerical procedure is the same for each block and so we shall largely focus on block 3 as an example of the model set-up and results.

The division of rock domains used for the SDM reference case was retained as illustrated in Figure 4-2, and fractures were generated within each rock domain according to the appropriate Hydro-DFN model (see Section 2.3.2). A slight simplification was made in that the small volumes of rock domains HRD(B,C) and HRD(A2) were incorporated into HRD(A). Neither of these two domains is intersected by the repository. Using this as the base case, a number of variants as given in Table 4-1 were considered with different backfill, EDZ and fracture transmissivity and aperture parameters. For the case with increased backfill conductivity, an increase factor of 100 was used such that ithe hydraulic conductivity was elevated to 10^{-8} m/s, which is similar to the bulk property of the rock, and gives an effective transmissivity of order 10^{-7} m^2/s per unit tunnel width. For the EDZ, an increase factor of only 10 was used, since this gave a hydraulic conductivity of $3 \cdot 10^{-7}$ m/s and an effective transmissivity of 10^{-7} m^2/s per unit tunnel width, and hence should have a similar magnitude effect as the pessimistic backfill case. Slightly, different scenarios were considered for Forsmark due to the lower rock hydraulic conductivities at that site.

Table 4-1. List of cases modelled in the DFN/CPM repository-scale modelling.

Case name	Sensitivity	Properties	Description
HCD1P3_HRD3a_ddKhalf_ani_HSD1_BC3	Reference case	DFN – Semi-correlated *T*/*r*	SDM Reference Case
HCD1P3_HRD3a_ddKhalf_ani_HSD1_BC3_EDZ	Reference case + poor EDZ	DFN – Semi-correlated *T*/*r*	10 times higher conductivity in EDZ ($3 \cdot 10^{-7}$ m/s)
HCD1P3_HRD3a_ddKhalf_ani_HSD1_BC3_T	Reference case + poor tunnel	DFN – Semi-correlated *T*/*r*	100 times higher conductivity in tunnel backfill (10^{-8} m/s)
HCD1P3_HRD3a_ddKhalf_ani_cubic_HSD1_BC3	Reference case + cubic-law aperture	DFN – Semi-correlated T/r	Cubic law transport aperture
HCD1P3_HRD3a_ddKhalf_ani_S-C_HSD1_BC3	Reference case + DFN anisotropy	DFN – Semi-correlated T/r	Transmissivity for Set_C 10 times higher
HCD1P3_HRD4_ddKhalf_ani_HSD1_BC3	Reference case + correlated DFN	DFN – Correlated T/r	Correlated *T* model

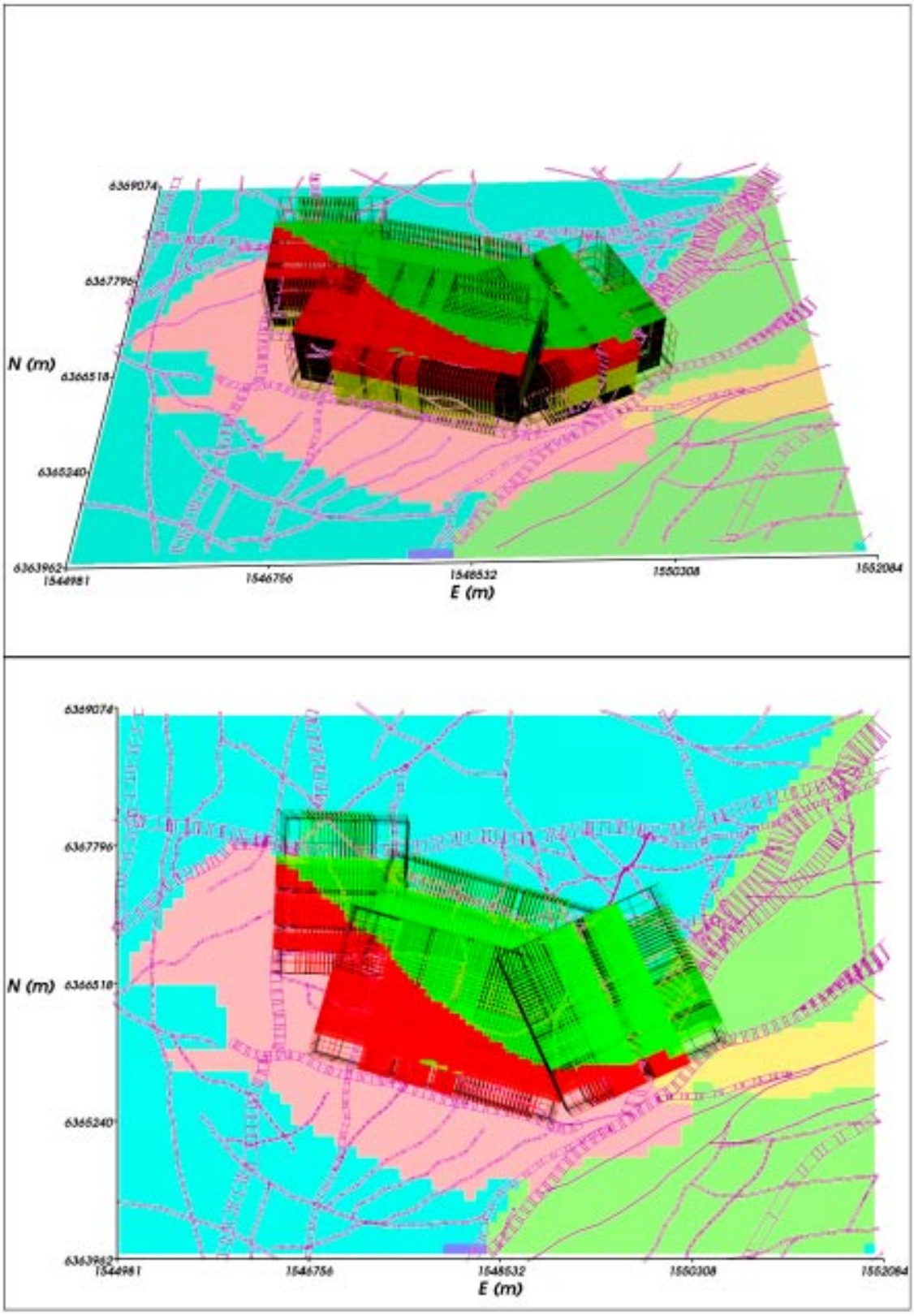

Figure 4-2. *The four repository-scale model grids, coloured by rock domain: HRD(A) (green), HRD(D,E,M) (red). The grids are superimposed on a horizontal slice through the HRD model at repository depth (z = –520 m): HRD(A) (blue-green), HRD(A2) (green), HRD(D,E,M) (pink), HRD(B,C) (orange). The HCD are also shown in purple on the section as defined by segment volumes. Top: oblique view. Bottom: Plan view.*

4.1.1 Model set-up and specification

An illustration of the model domain for block 3 is shown in Figure 4-3. Most of the domain, i.e. apart from the repository, is the DFN sub-model. The CPM sub-model is composed of just the transport tunnels, main tunnels, deposition tunnels and deposition holes as shown in Figure 4-4 with properties as given in Table 2-2. Figure 4-3 and Figure 4-4 show the finite-element grid used to discretise the tunnels. As can be seen, all structures are represented, but refinement is essentially the minimum that could be used with the grid size varying from about 1 m for the cross-section of deposition holes to about 10 m for the spacing along the transport tunnels. The ramp and shafts were added as conductive two-dimensional features with equivalent properties to provide a simplification to their geometry which would have been difficult to include explicitly in three-dimensions. Figure 4-4 also shows the representation of the EDZ as equivalent fractures that are positioned just beneath the base of each deposition tunnel and intersect the top of each deposition hole, providing an alternative potential pathway.

The DFN sub-model that surrounds the repository is shown in Figure 4-5. The fractures are derived from 3 sources: deterministic deformation zones imported from the geological model (shown in the lower part of Figure 4-5), stochastic fractures imported from the regional DFN model including fractures down to a radius of 14 m, additional stochastic fractures in the range 1–14 m radii. With reference to Section 2.3.3, the connected fracture intensity calculated for a truncation radius, r_{min}, of 0.5 m is about 0.2 m^2/m^3, which suggests a connected fracture spacing of about 5 m for r_{min} of 0.5 m. Since the height of the deposition hole is about 7 m, then a truncation radius of 1 m is an appropriate choice. However, because the network is heterogeneous, then it does not guarantee that every deposition hole will be intersected by a connected fracture. Reducing the minimum fracture length further is not feasible due to the size of model. However, neglecting the smallest fractures is considered reasonable since these are not only likely to have lower transmissivity, but they also have a lower probability of connecting to the network, and hence carry flow. The additional stochastic fractures were included throughout the model domain for fractures down to a radius of 3.4 m, but fractures of radii of 1 m to 3.4 m length were only generated in the volume around and between the deposition tunnels and at elevations z = –550 m to z = –490 m, i.e. 30 m above and below the repository.

For block 3, about 1.47 million fractures were generated in the model region. Some of these were subdivided to improve the discretisation of flow and transport giving a total of about 1.68 million fracture objects. Each fracture larger than 20 m length is sub-divided into 20 m sub-fractures (‘tessellated’). As part of the flow calculations, the first step was to remove isolated or dead-end fractures. Since the network is sparsely connected, as many as 0.6 million isolated and 0.3 million dead-end fractures are removed since they will not influence steady-state flow. This is a conservative assumption, since diffusion into dead-end fractures is a potential retardation process. The remaining connected network contains about 1.95 million degrees of freedom located at fracture intersections and in the CPM parts.

The connectivity of the network is illustrated in Figure 4-6 by showing a slice through the network at repository depth before and after removing unconnected parts of the network. The effect is dramatic and consistent with the study made in Section 2.3.3. The dense area of fracturing in the middle is where fractures of radius less than 3.4 m are generated around the deposition tunnels. Observe that more fractures are removed away from the repository as the tunnels actually create extra hydraulic connections that would not otherwise exist. Also, more fractures are removed from the southern part of the block which corresponds to hydraulic rock domain HRD(D, E, M). It is perhaps worth saying that the dead-end fractures removed are the ones where a fracture has only one connection with another fracture. It is then removed, and the algorithm is recursive in order to remove any sequences of dead-ends. However, dead-ends can occur as closed loops of fractures each connected to two or more other fractures but with only one way in/out of the loop, and these are not removed. Such closed loops may be a side-shoot of the main network or may only be connected to a section of tunnel. These were found to occur in the DFN models of Forsmark and caused some problems for particle-tracking. They also occur here at Laxemar.

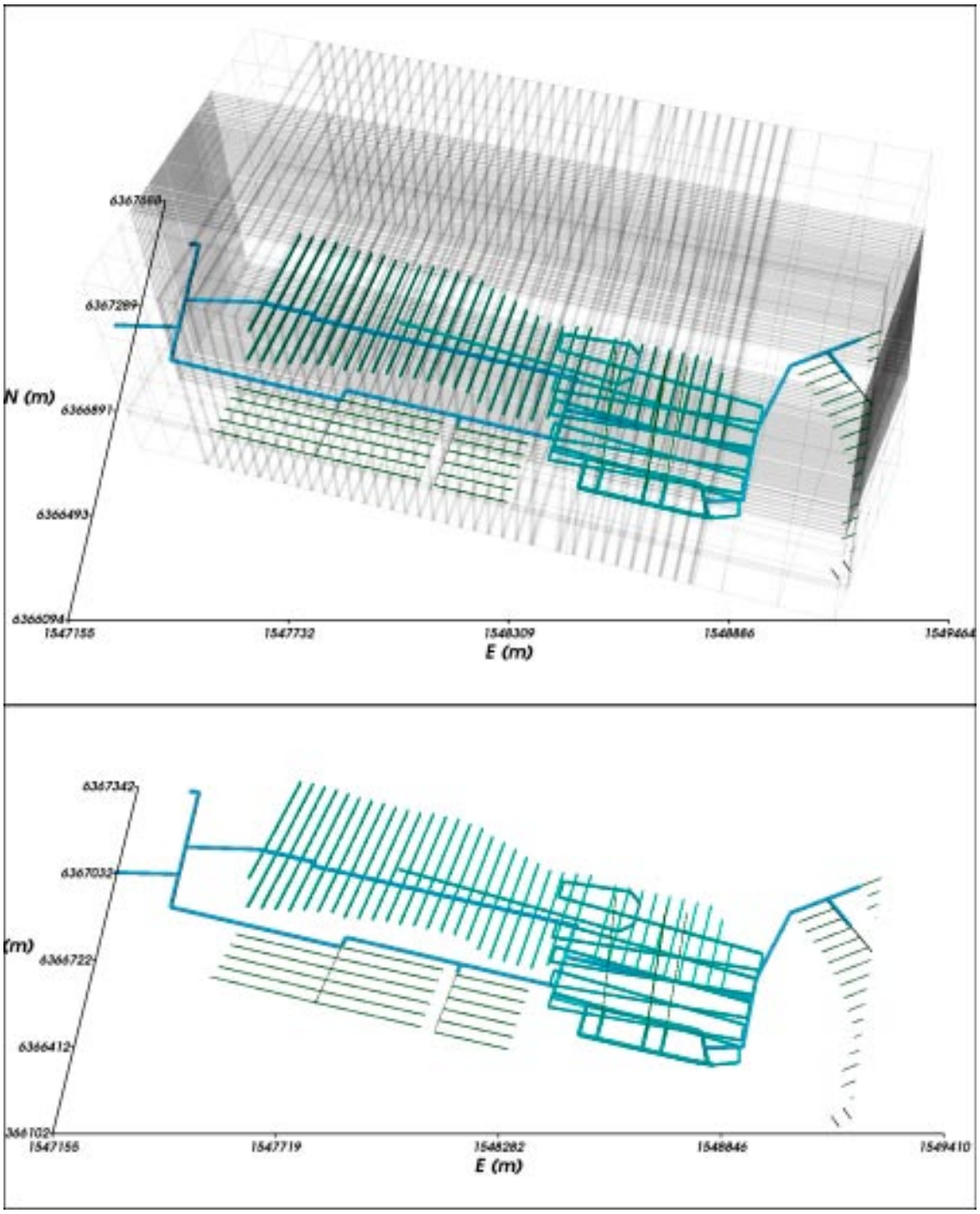

Figure 4-3. *Domain used for the combined repository-scale DFN model for block 3. Top: the outer grid shows the domain for the DFN sub-model. Inside of that, the repository structures are represented by a CPM sub-model. The spiral ramp in the forefront is actually represented by equivalent fractures. Bottom: representation of the repository, including the CPM sub-model and ramp represented by equivalent fractures.*

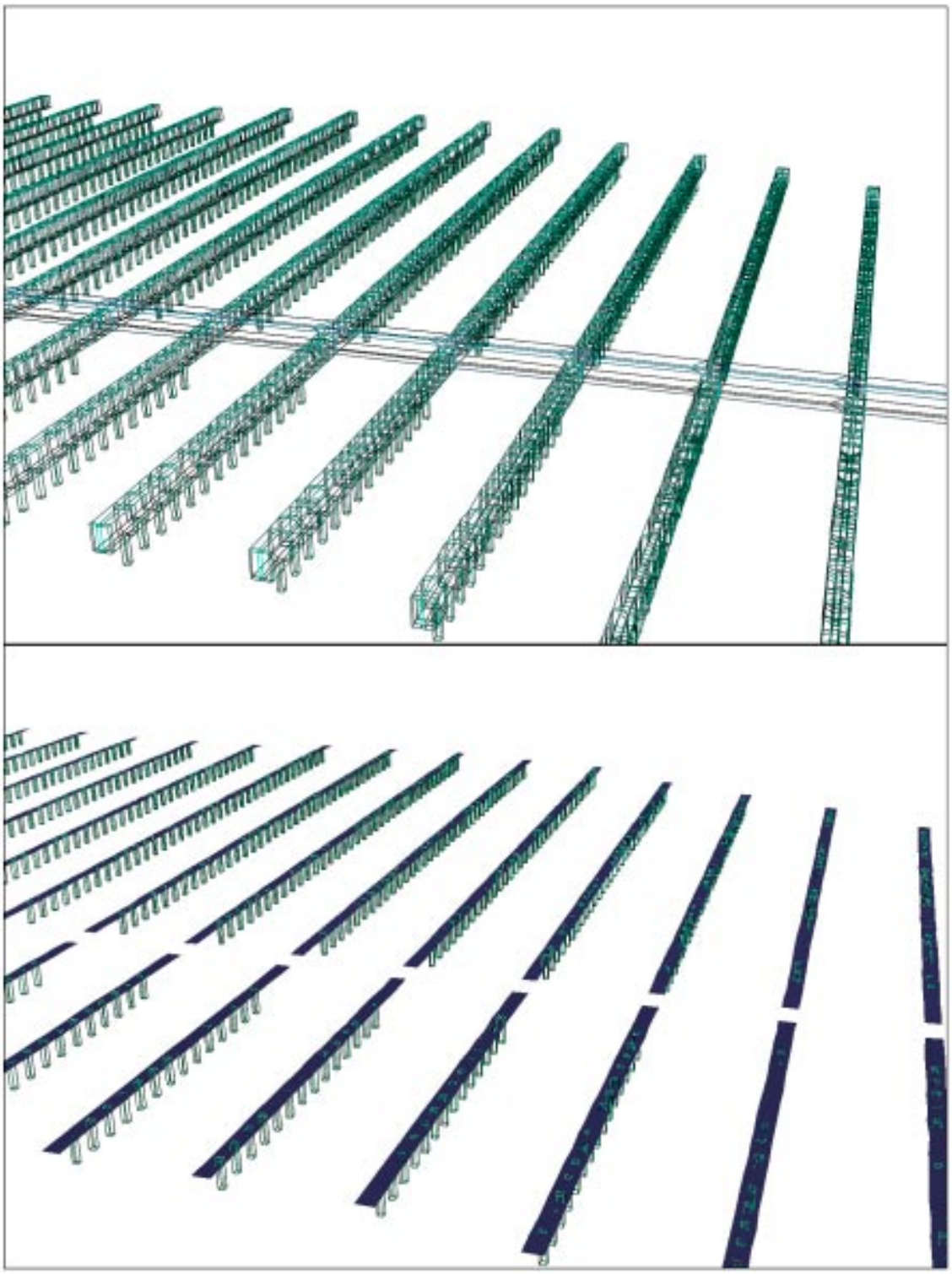

Figure 4-4. *Representation of repository structures as CPM sub-model within the combined DFN/CPM model for block 3. Top: close-up of finite-element grid for deposition tunnels and canisters. Bottom: deposition tunnels have been removed to show EDZ (represented by equivalent fractures) and canisters.*

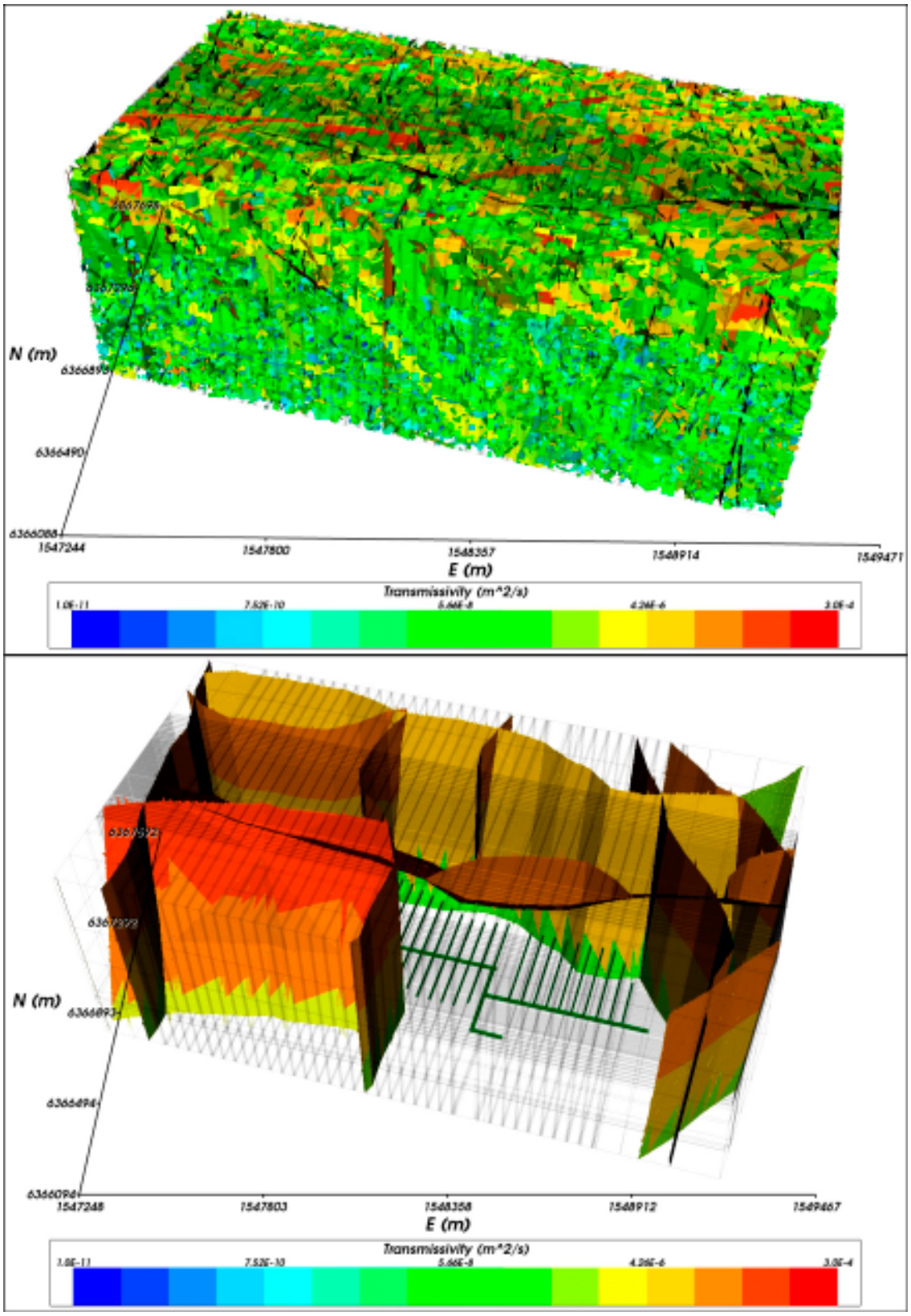

Figure 4-5. *Combined DFN/CPM reference case model of repository block 3. Top: DFN sub-model. Fractures are coloured by transmissivity. The larger fractures correspond to deterministic deformation zones from the geological model. The transmissivity model includes step changes at –200 m and –600 m. Bottom: deterministic deformation zones, coloured by transmissivity, and the repository representation.*

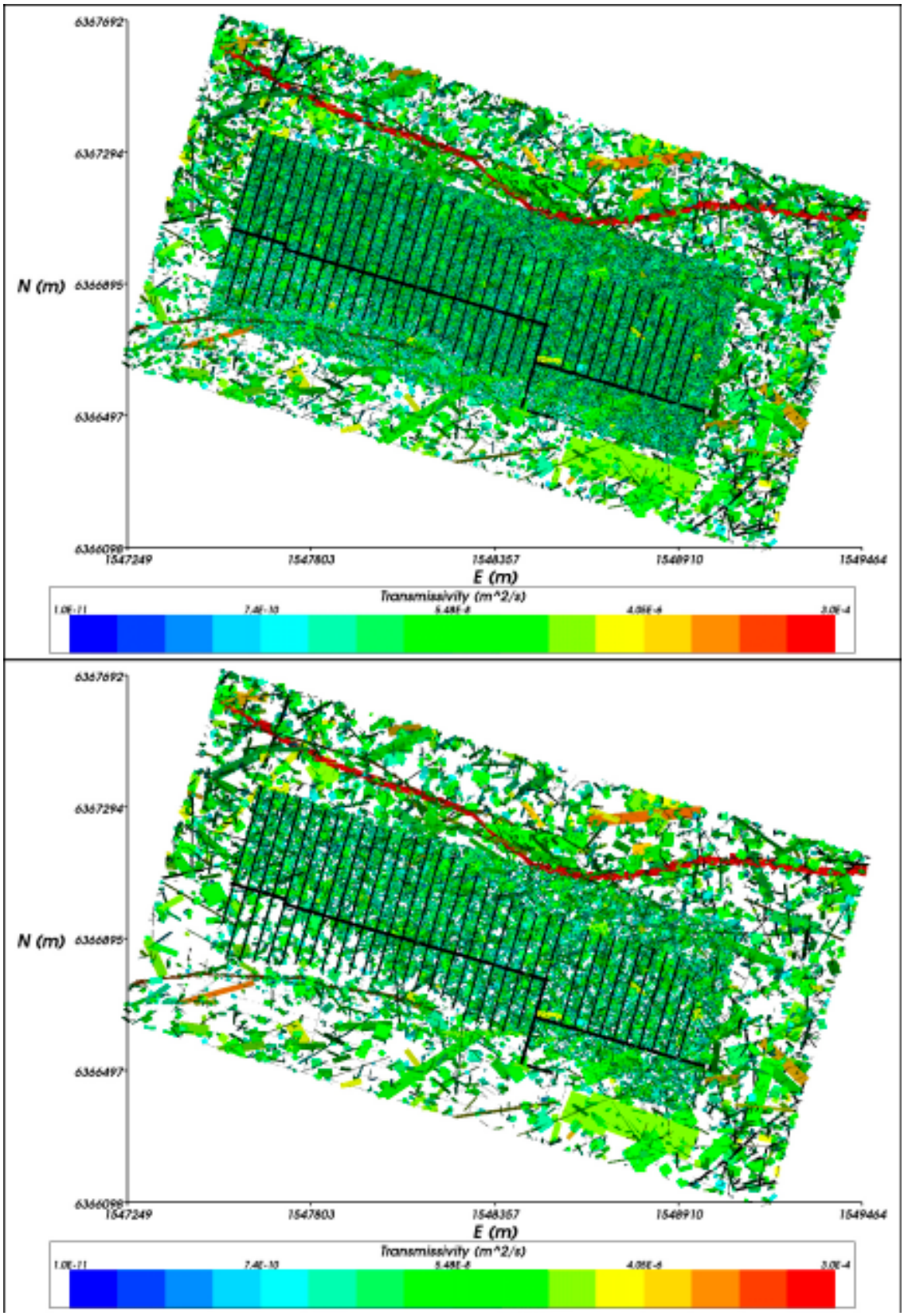

Figure 4-6. *A horizontal slice (z = –520 m) through the combined DFN/CPM reference case model of repository block 3. Fractures are coloured by transmissivity. The CPM part is the fishbone like structure in the middle. Top: all fractures generated with radial dimension greater than 3.4 m everywhere, and greater than 1 m in the centre around the tunnels. Bottom: connected fractures only.*

The boundary conditions for each combined model were obtained by interpolation of the residual pressure and groundwater density from the relevant regional-scale ECPM model (the ECPM reference case for the models shown here) at selected times. Again, the times selected were 6,000 BC, 2,000 BC, 2,020 AD and 6,000 AD (see Section 3.4.1). The residual pressure was held constant on the outer boundary of the DFN sub-model. At the interface between the two sub-models, extra internal conditions were enforced to ensure continuity of residual pressure and conservation of mass-flux across the interface between the CPM and DFN parts.

4.1.2 Variable-density flow calculations

Steady-state calculations of groundwater flow in the combined DFN/CPM models were performed at selected instances in time. The times chosen were 6,000 BC, 2,000 BC, 2,020 AD and 6,000 AD (see Section 3.4.1). The effects of variable groundwater density were taken into account in both regions using some new developments in CONNECTFLOW (Release 9.1). This allows a consistent flow-field to be calculated given a fixed spatial distribution of groundwater density. The distribution of density was obtained by interpolating the groundwater density calculated in the regional-scale ECPM model at a specified time on to each fracture intersection in the DFN sub-model, and on to each finite-element in the CPM sub-model. Figure 4-7 shows the density in the DFN at 2,020 AD. Roughly speaking, fluid density increases with depth and towards the coast. However, the increase only reaches a maximum of about 7 kg/m^3 at –700 m. Likewise, the residual pressure was also interpolated from the regional-scale model. In the flow calculations, groundwater density was held fixed throughout the whole domain, while residual pressure was only fixed as a boundary condition at the intersections of fractures with the external boundaries. There is also a condition of continuity in residual pressure at the interface between the DFN and CPM that represents the tunnels, etc. The steady-state residual pressure

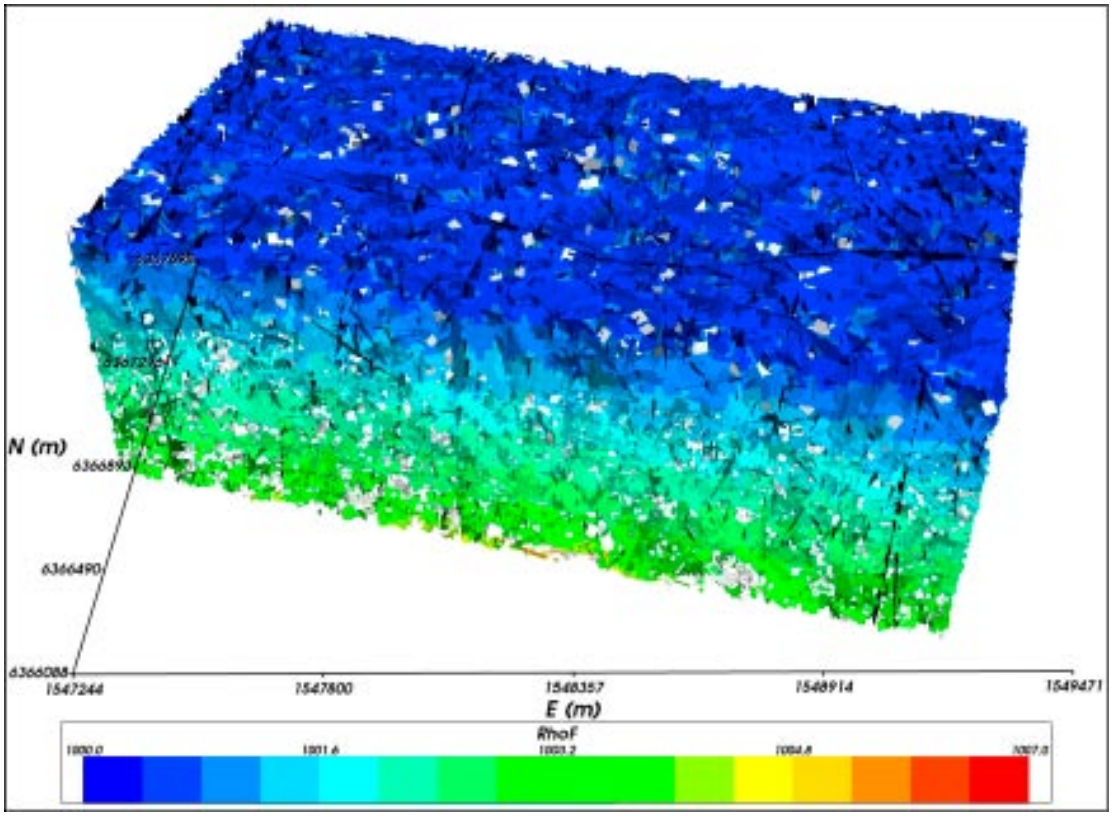

Figure 4-7. *Distribution of groundwater density used in the flow calculation at 2,020 AD in repository block 3 for the combined DFN/CPM reference case model. Fractures are coloured by fluid density (kg/m^3).*

consistent with the fluid density and fixed pressure boundary conditions was then calculated in the DFN model with the pressure degrees of freedom calculated at each fracture intersection. This methodology was verified in a simple situation using the Henry test case in the Forsmark SR-Can modelling /Hartley et al. 2006b/. The distribution of residual pressure calculated at 2,020 AD is shown in Figure 4-8 with the fractures above the repository removed to show the

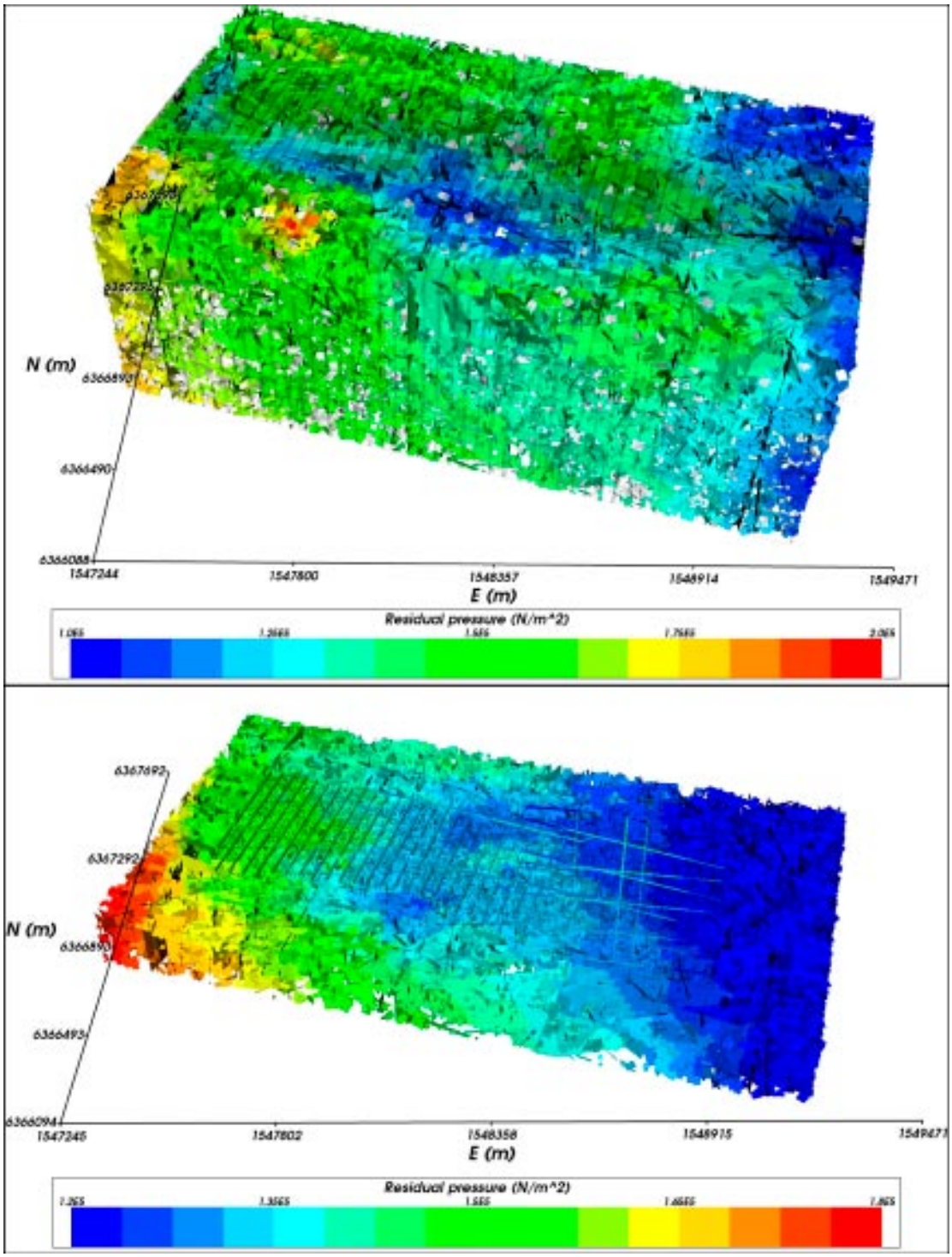

Figure 4-8. *Results of variable-density flow calculation at 2,020 AD in repository block 3 for the combined DFN/CPM reference case model. Fractures are coloured by residual pressure. Top: all fractures. Bottom: fractures above the repository at z = –520 m have been removed to show residual pressure around and including the CPM sub-model and ramp. Only connected fractures are shown in the lower plot.*

continuity of residual pressure through the DFN and CPM sub-models. A residual pressure of 10^4 N/m^2 equates to a head of about 1 m. Note: The equations solved for variable-density are conservation of mass-flux (density multiplied by Darcy velocity) rather than just conservation of flow as with the constant-density case. Also, the Darcy velocity has two components coming from the gradient of residual pressure and a buoyancy term in the vertical direction.

4.2 Combined ECPM/DFN regional-scale model

Although the repository-scale models described in Section 4.1 can be used to calculate flow-paths to a high resolution around the deposition holes, due to restrictions of model size, they cannot capture the full length of all paths. Therefore, to complete flow-paths for some particles more extensive models are required, and hence models with a DFN local-scale model embedded within a regional-scale ECPM were constructed. The approach was then to use the end points of paths obtained from modelling flow-paths in the repository-scale model as particle release points in these regional-scale models to continue the path to the biosphere. That is, particle trajectories were calculated in two legs: the first in the repository-scale models, the second in the regional-scale. Hence, the regional-scale models were used to augment transport calculations in the detailed repository-scale models described in Section 4.1.

A top-down approach to developing these models was followed. This involved starting with the regional-scale realistic case ECPM model, inserting a local-scale DFN sub-model with the corresponding parameters, and including a slightly idealised representation of the repository. The objective is to construct a single model that can capture particle tracks starting in the DFN sub-model and continuing through a regional-scale ECPM model. This was found to be tractable although some compromises were necessary, including truncation of the fracture size distribution (a lower limit of 8 m for radius was used), and the use of equivalent fractures instead of explicit volumes to represent the repository.

4.2.1 Model set-up and specification

The combined ECPM/DFN model consists of a continuum sub-model that is identical to the reference case described in Section 3, and an embedded local-scale DFN model that incorporates the repository. The top of the DFN model lies 50 m below the HSD surface layers (3 m thick) and has dimensions 4,100×3,200×1,000 m, encompassing the entire repository footprint. The DFN incorporates the deterministic DZ model and the regional-scale DFN that includes stochastic fractures with radial dimensions of 564 m down to 14 m. In addition, stochastic fractures were generated down to a radial dimension of 8 m. These stochastic fractures were specified according to the semi-correlated transmissivity model given in Section 2.3.2.

The combined model is illustrated in Figure 4-9 for the near-surface layer, which also includes a view of the model with deterministic DZ's superimposed. A close-up view of the DFN sub-model is shown in Figure 4-10. These figures show that there is strong heterogeneity in both the DFN and ECPM sub-models, and in HRD(A) large stochastic fractures contribute to relatively high equivalent hydraulic conductivities in the near-surface layer. In the local-scale DFN model, the deterministic deformation zones are modelled explicitly as planar features, and it may be observed that there is continuity in the representation across the interface between the two sub-models. A clearer view of this is provided by Figure 4-10 and Figure 4-11, which show the DFN model and the interface between the sub-models in closer detail. In the near-surface, outside of HRD(A2), the bedrock has a higher hydraulic conductivity and this, combined with the effect of using the semi-correlated transmissivity model, means that some of the areas of highest hydraulic conductivity in the ECPM model relate to large stochastic fractures as well as the deterministic DZ's.

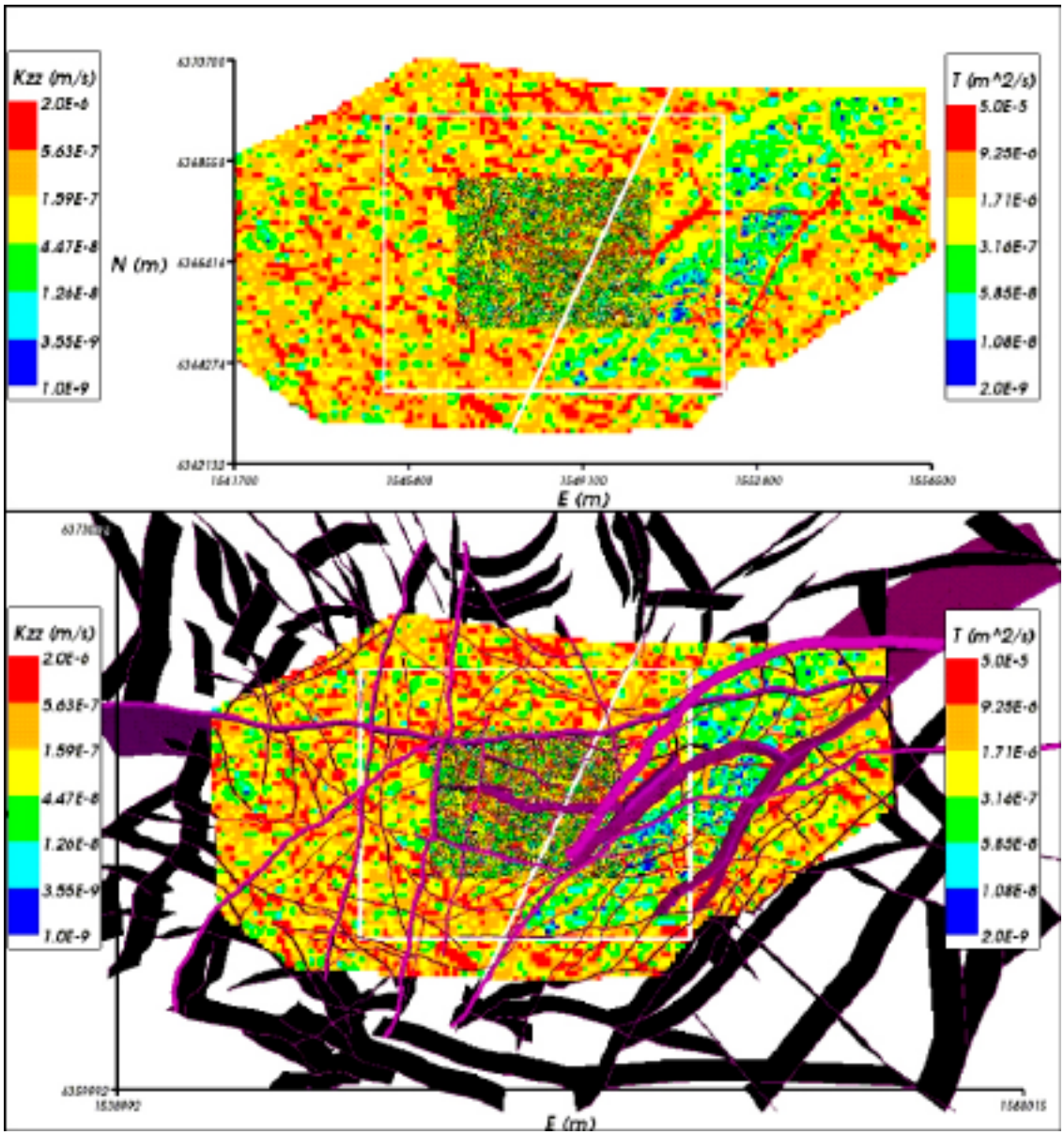

Figure 4-9. *Regional combined ECPM/DFN model with the top 53 m removed to show the central local-scale DFN sub-model. The ECPM model is coloured by vertical hydraulic conductivity (K_{zz}), the DFN model in the centre is coloured by fracture transmissivity, T. Bottom: with deterministic DZ geological model superimposed in purple. The white rectangle indicates the area used for the detailed views of Figure 4-10 and Figure 4-14. The diagonal white line indicates the position of the vertical cross-section illustrated in Figure 4-12 and Figure 4-13.*

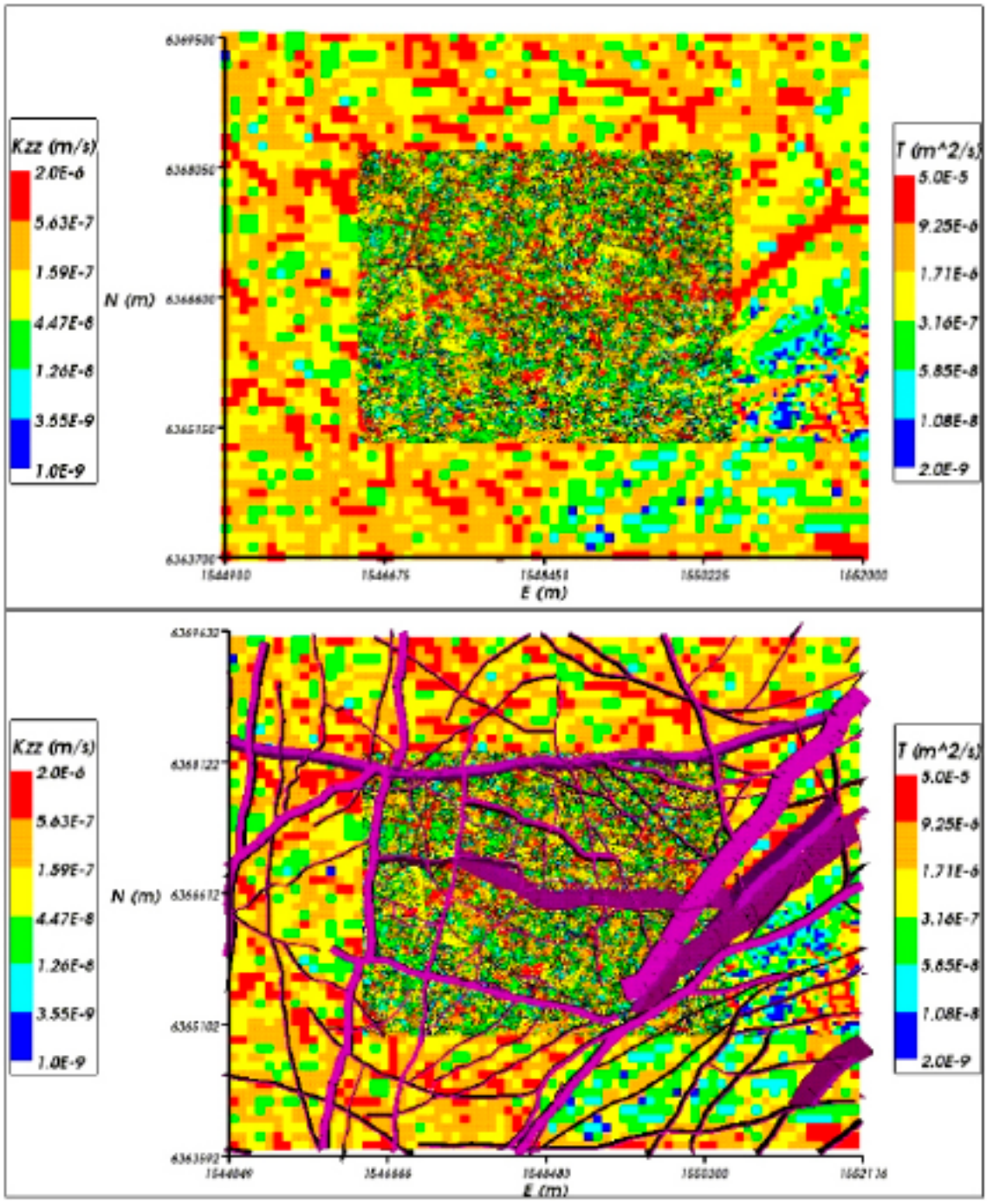

Figure 4-10. *Close-up view of the DFN sub-model within the regional combined ECPM/DFN model. The representation of the deterministic deformation zones in the DFN and their continuity into the surrounding ECPM is shown. The ECPM model is coloured by vertical hydraulic conductivity (Kzz), the DFN model in the centre is coloured by fracture transmissivity. Bottom: DFN model with deterministic DZ geological model superimposed in purple.*

As with the repository-scale models, the division of rock domains used for the SDM reference case was retained in the DFN sub-model. Therefore, it was possible to generate stochastic fractures within each rock domain according to the appropriate Hydro-DFN model (see Section 2.3.2). This is illustrated in Figure 4-11 for a horizontal slice at repository depth (z = –520 m) and in Figure 4-12 which shows a (SSW-NNE) vertical cross-section (of strike 25°) through the model, coloured by rock type. In Figure 4-13, the same section is shown,

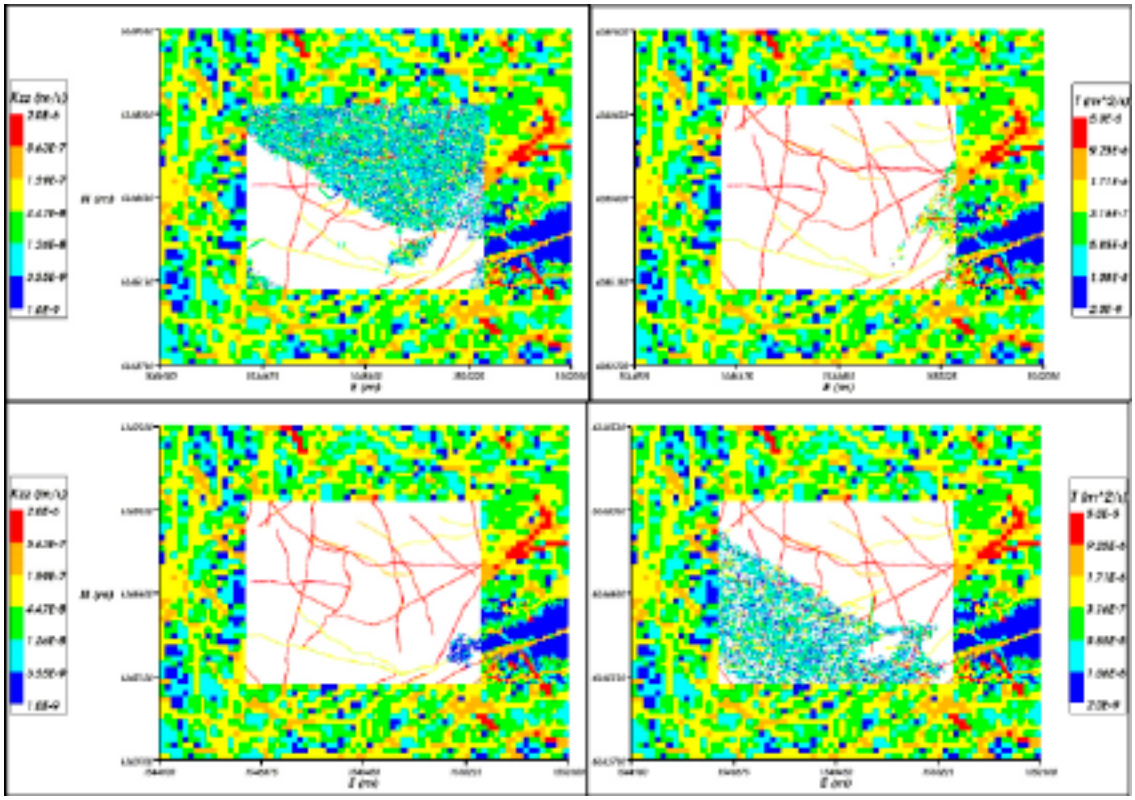

Figure 4-11. *Close-up view of the DFN sub-model for a horizontal slice through the regional combined ECPM/DFN model at repository depth (z = –520 m). Each plot shows the fractures generated within one rock domain. Top left: HRD(A); top right: HRD(A2); bottom left: HRD(B,C); bottom right: HRD(D,E,M). The ECPM model is coloured by vertical hydraulic conductivity (Kzz), and the DFN model is coloured by fracture transmissivity.*

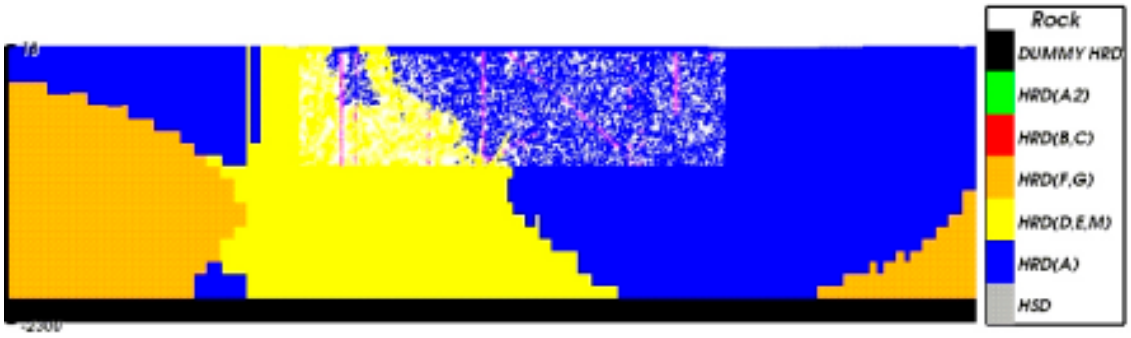

Figure 4-12. *A vertical slice through the combined ECPM/DFN regional model, cutting through the repository from SSW (left) to NNE (right). The ECPM and the stochastic DFN are coloured by rock type according to the legend. Deterministic deterministic DZ's are coloured purple in the DFN.*

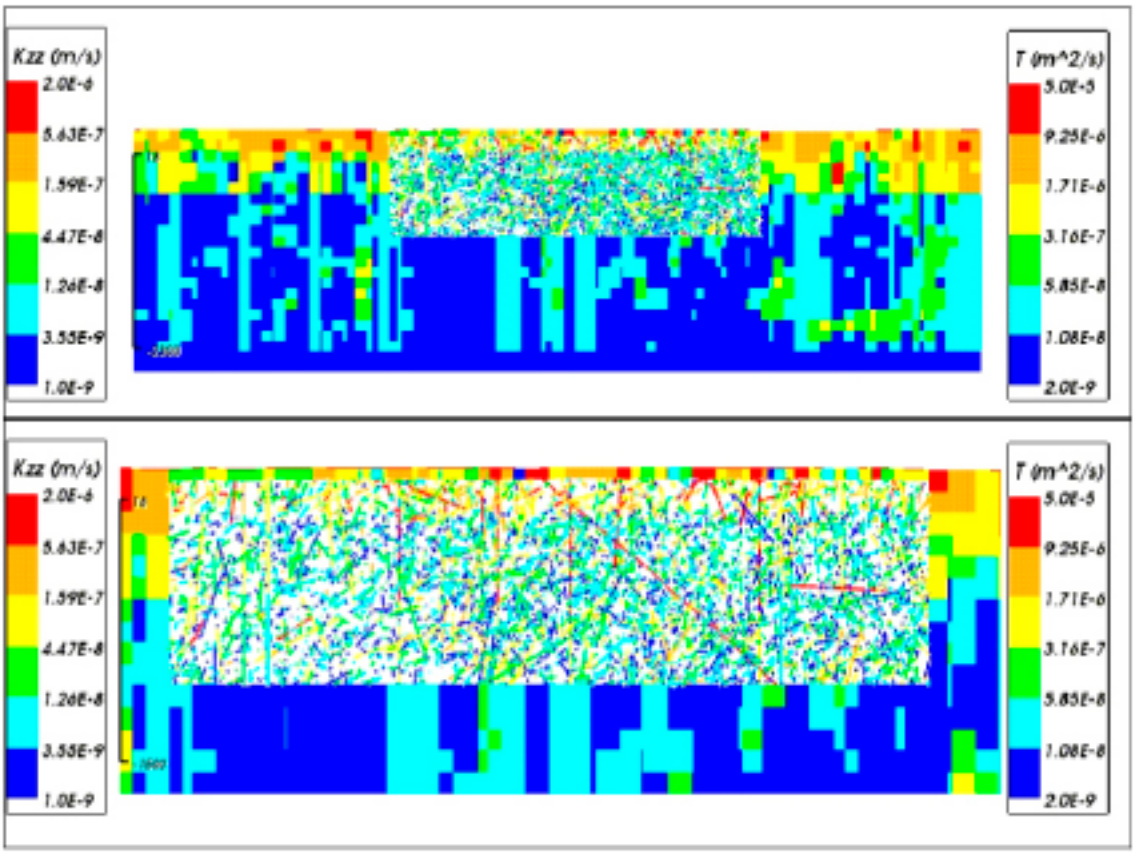

Figure 4-13. *A vertical slice through the combined ECPM/DFN regional model cutting through the repository from SSW (left) to NNE (right). Top: The whole ECPM and DFN model. Bottom: The area around the DFN only. The ECPM model is coloured by vertical hydraulic conductivity (K_{zz}), the DFN is coloured by transmissivity. The lower transmissivity of fractures below z = –200 m can also be seen.*

coloured by vertical hydraulic conductivity (ECPM model) and transmissivity (DFN model). The different fracture scales modelled may be seen in this figure. In addition, the lower fracture intensity in HRD(D,E,M) compared to that in HRD(A), and the lower transmissivity of fractures below an elevation of –200 m may be observed.

A horizontal cross-section through the model, Figure 4-14, shows the interface between the DFN and ECPM sub-models. The lower picture shows the detailed fracturing incorporated around the repository and the large variation in fracture scales that result from the power-law size distribution. This figure also shows how the repository is represented by low transmissivity fractures. All tunnels, shafts and the ramps were represented in this way in the regional-scale model.

Figure 4-15 (upper plot) shows in yet closer detail the individual fractures around some of the deposition tunnels. For individual tunnels in this repository block, up to five large fractures cut across adjacent tunnels on average, and many of the smaller fractures may not connect to the network (although 3D connectivity can be under-represented on 2D slices). Figure 4-15 also shows how the repository tunnels are included in the DFN region as vertical fractures. These ‘tunnel fractures’ are assigned an equivalent transmissivity to represent a backfilled tunnel of specified hydraulic conductivity and cross-sectional area, and they will exchange flow with the surrounding fracture network. Similarly, the EDZ was represented as horizontal fractures at the base of the tunnel, forming an inverted T-shape so as to ensure a connection between the tunnel and EDZ. Using this representation, it is possible if necessary to track particles that start from within the repository, initially through the fractures close to the repository and then on through the ECPM sub-model. Also, if there is no connected pathway through the fracture system around a particle release point, then the flow-path may enter the tunnel or EDZ, or both, where they carry more flow.

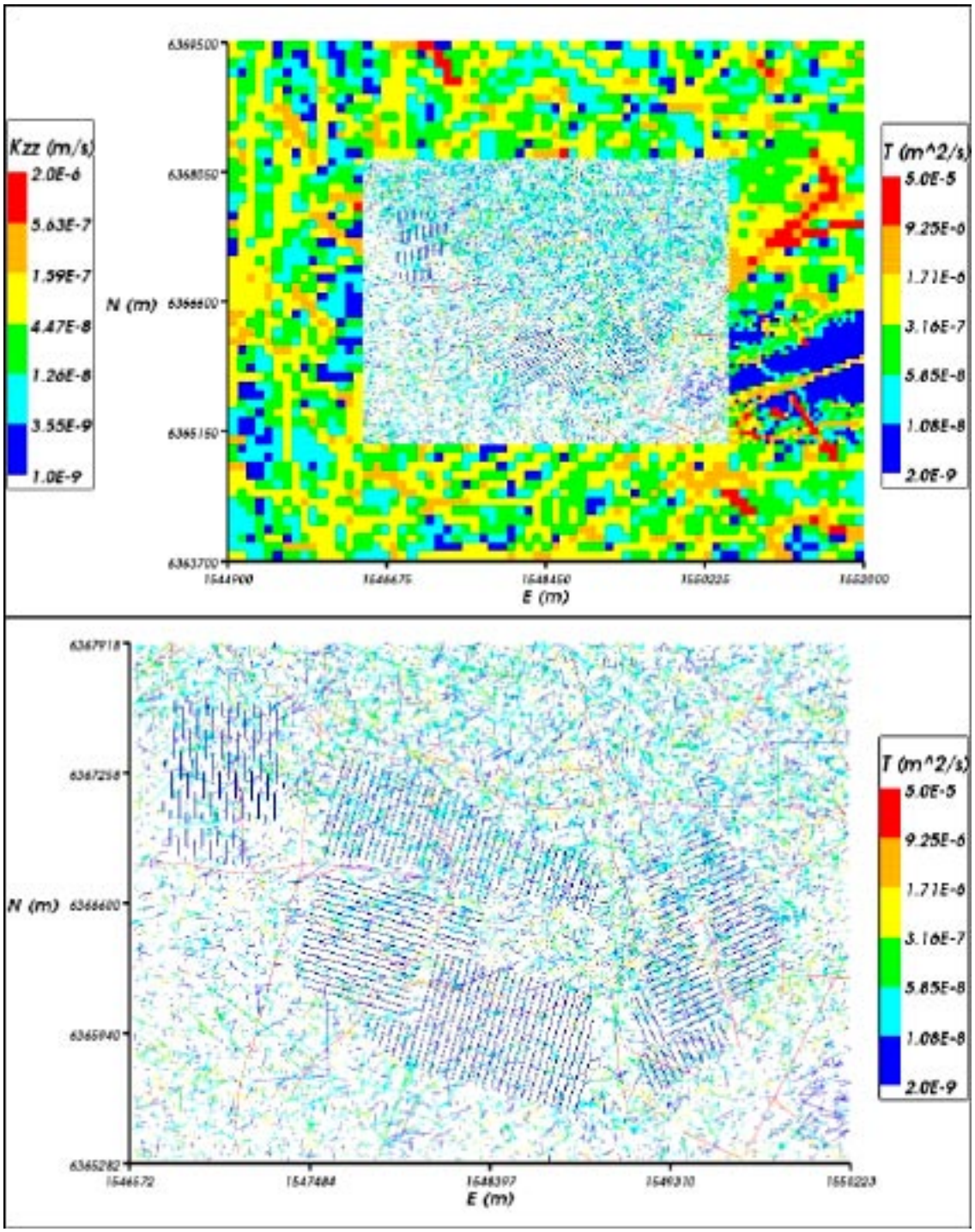

Figure 4-14. *The combined ECPM/DFN regional model at repository depth (z = –520 m): A horizontal slice at z = –520 m is taken through all components of the model except for the fractures representing the repository structures, which are plotted in 3D. The DFN area (top) and the repository area (bottom) are shown. The CPM model is coloured by vertical permeability (K_{zz}). For the DFN model, fractures are coloured by transmissivity.*

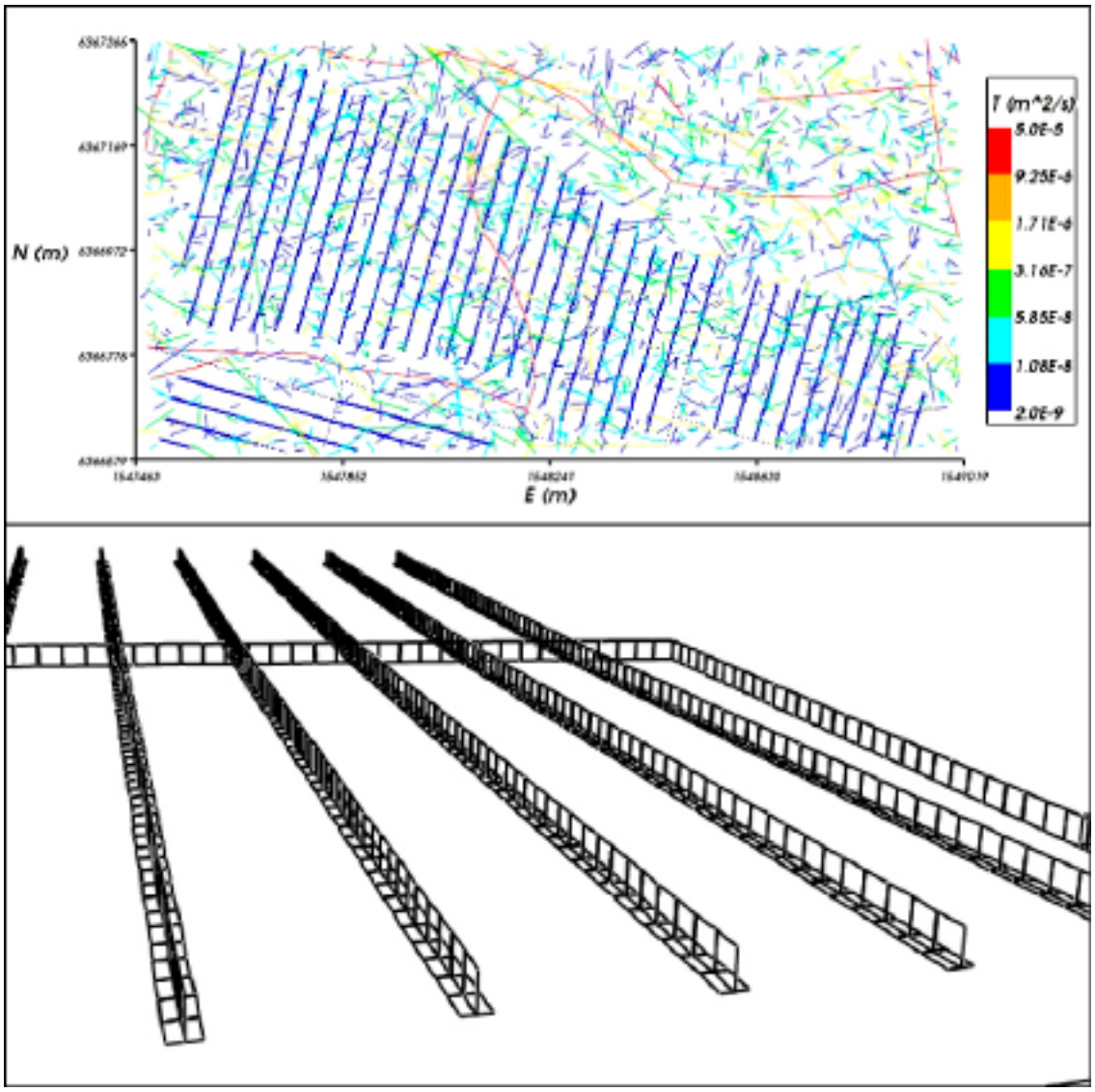

Figure 4-15. *Detailed view of the DFN model around the repository. Top: the fracturing around some of the deposition tunnels. A horizontal slice at z = –520 m is taken through all components of the model except for the fractures representing the repository structures, which are plotted in 3D. Fractures are coloured by transmissivity. Bottom: representation of tunnels and EDZ as equivalent fractures, discretised into 7.5 m long fracture sections.*

4.2.2 Variable-density flow calculations

Using an identical approach to the repository-scale model, the fluid density was interpolated from the realistic case ECPM model at 2,020 AD on to both sub-models, and then a self-consistent distribution of residual pressure and flow-field was computed. Continuity of fluid-density and residual pressure along with conservation of mass-flux was ensured at the interface between the two sub-models.

Figure 4-16 shows the consistent pressure distribution calculated in the ECPM/DFN model just below the HSD layers and on a horizontal slice at repository depth. For the slice, the continuity in pressure can be seen across the ECPM/DFN interface.

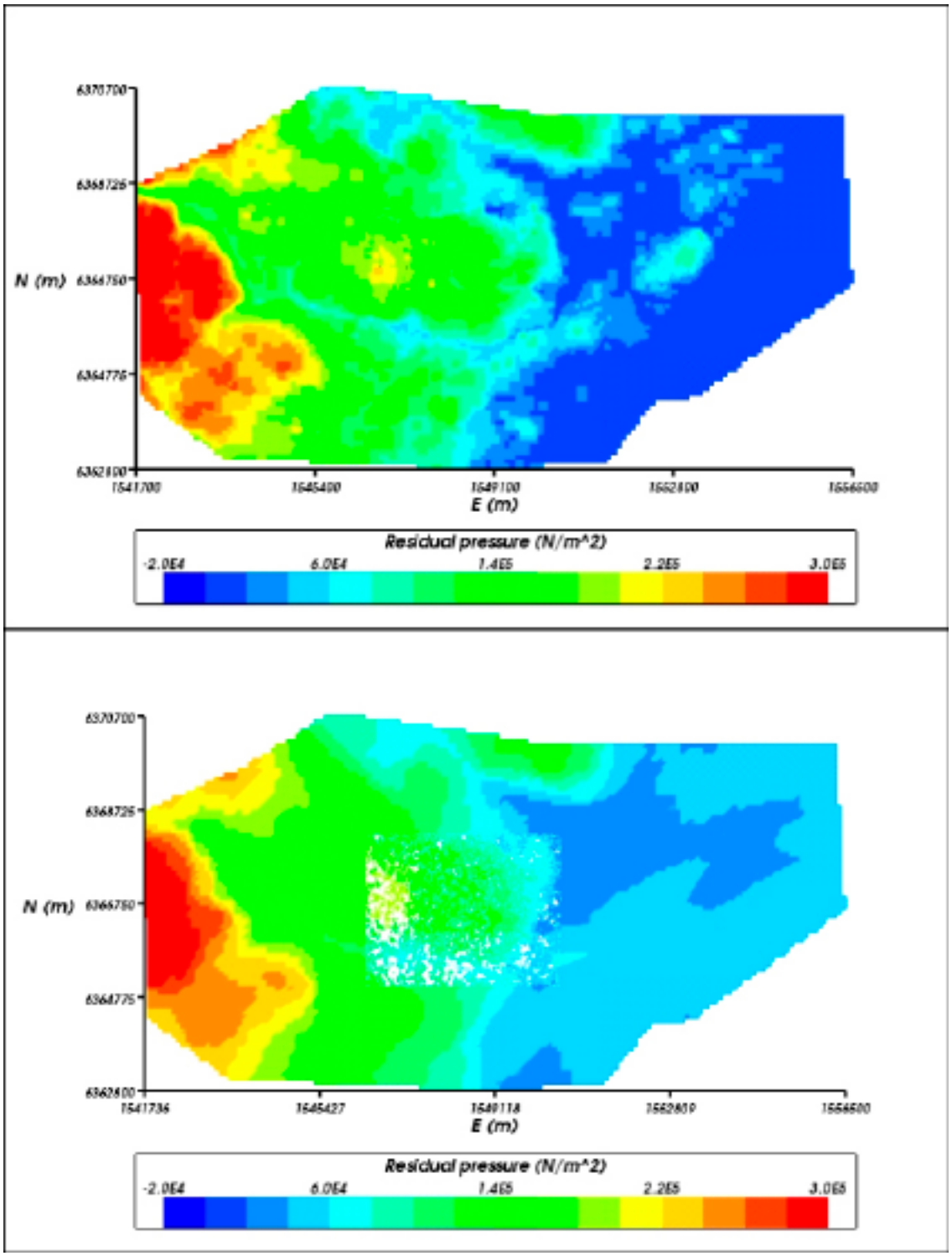

Figure 4-16. *Distribution of residual pressure in the combined regional ECPM/DFN model in plan view. Top: HSD layers removed. Bottom: horizontal slice at z = –520 m. The DFN sub-model is in the centre.*

The pressure and fluid density distributions for the DFN sub-model are illustrated in Figure 4-17. The fracture network, including all fractures, is shown although those coloured grey are not connected to the network. A significant rise in fluid density, 2% occurs around an elevation of –800 m to –700 m.

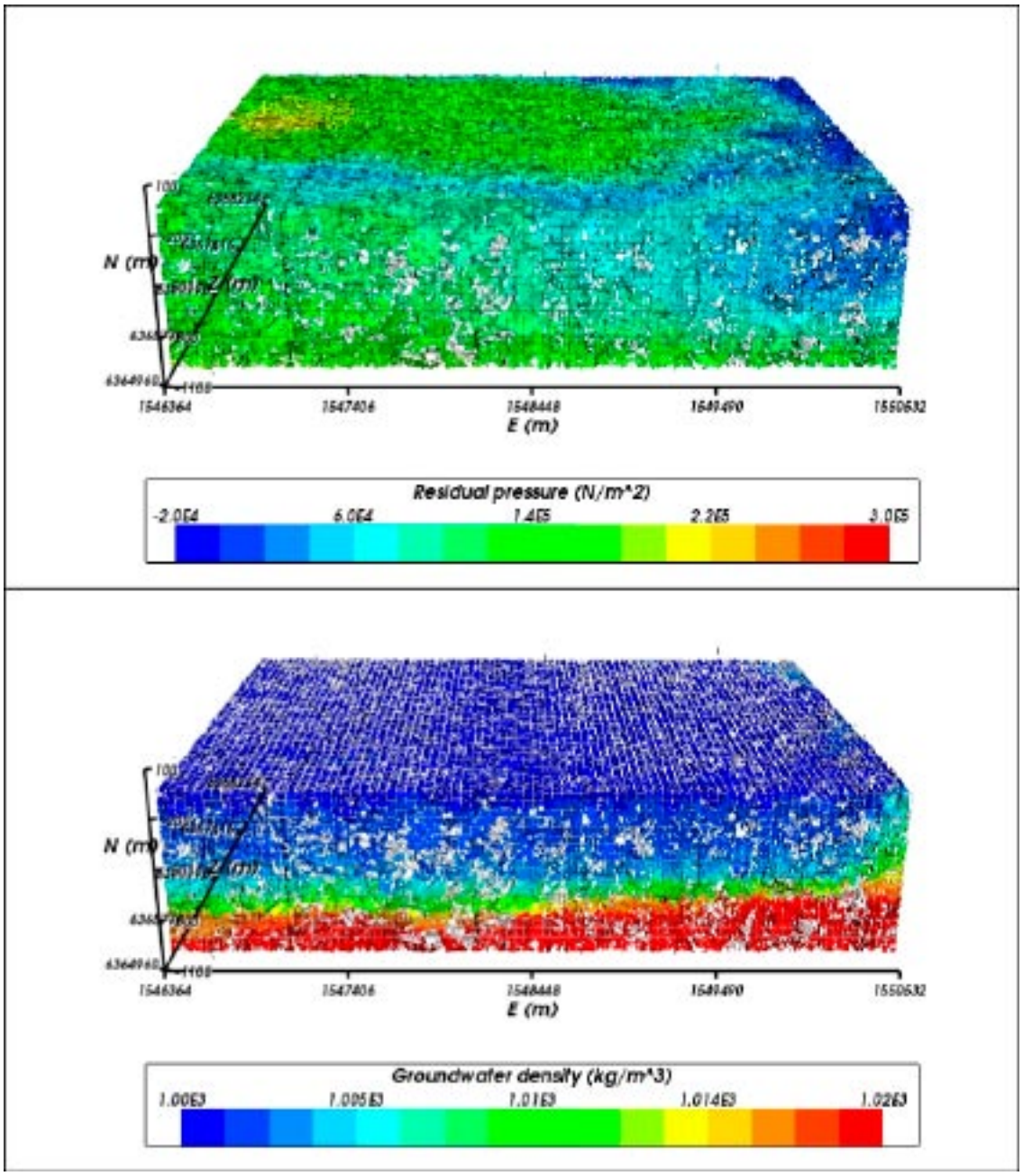

Figure 4-17. *The DFN sub-model of the combined regional ECPM/DFN model. Top: distribution of residual pressure. Bottom: distribution of fluid density. Fractures not connected to the network are coloured grey.*

Figure 4-18 and Figure 4-19 show a close-up view of the DFN on horizontal slices at $z = -150$ m and $z = -520$ m, with colouring to show the distributions of pressure and fluid density.

A close-up view of the pressure distribution around repository blocks 3 and 4 is given in Figure 4-20. This may be compared to the pressure distribution for the repository-scale model for repository block 3, shown in Figure 4-8.

By inspecting several horizontal slices through the combined model at different depths it was confirmed that the density and pressure are consistent at the ECPM/DFN interface.

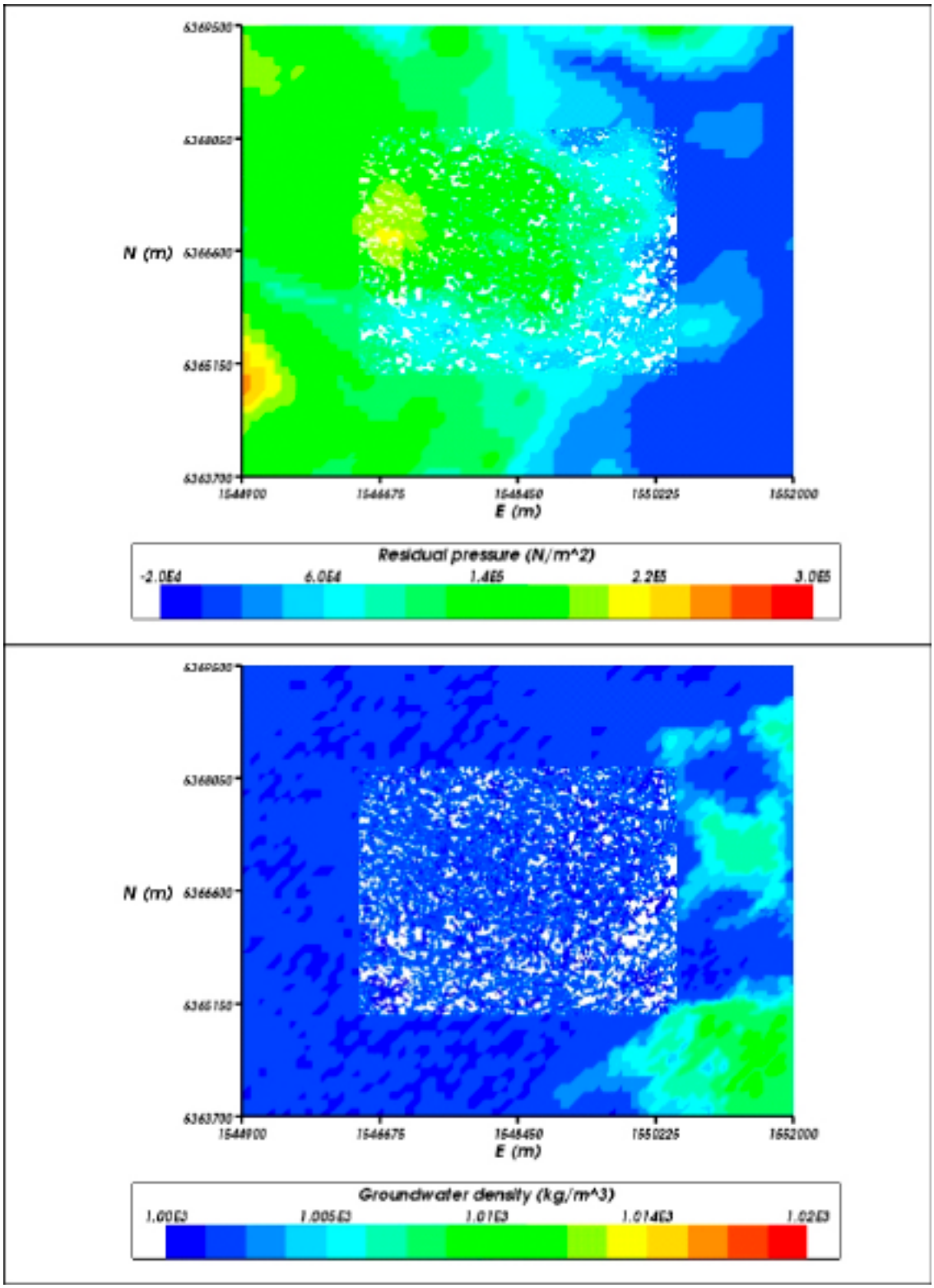

Figure 4-18. *Results of variable-density flow calculation at 2,020 AD for the combined ECPM/DFN model, close-up view of the DFN on a horizontal slice at z = –150 m. Top: distribution of residual pressure. Bottom: distribution of fluid density.*

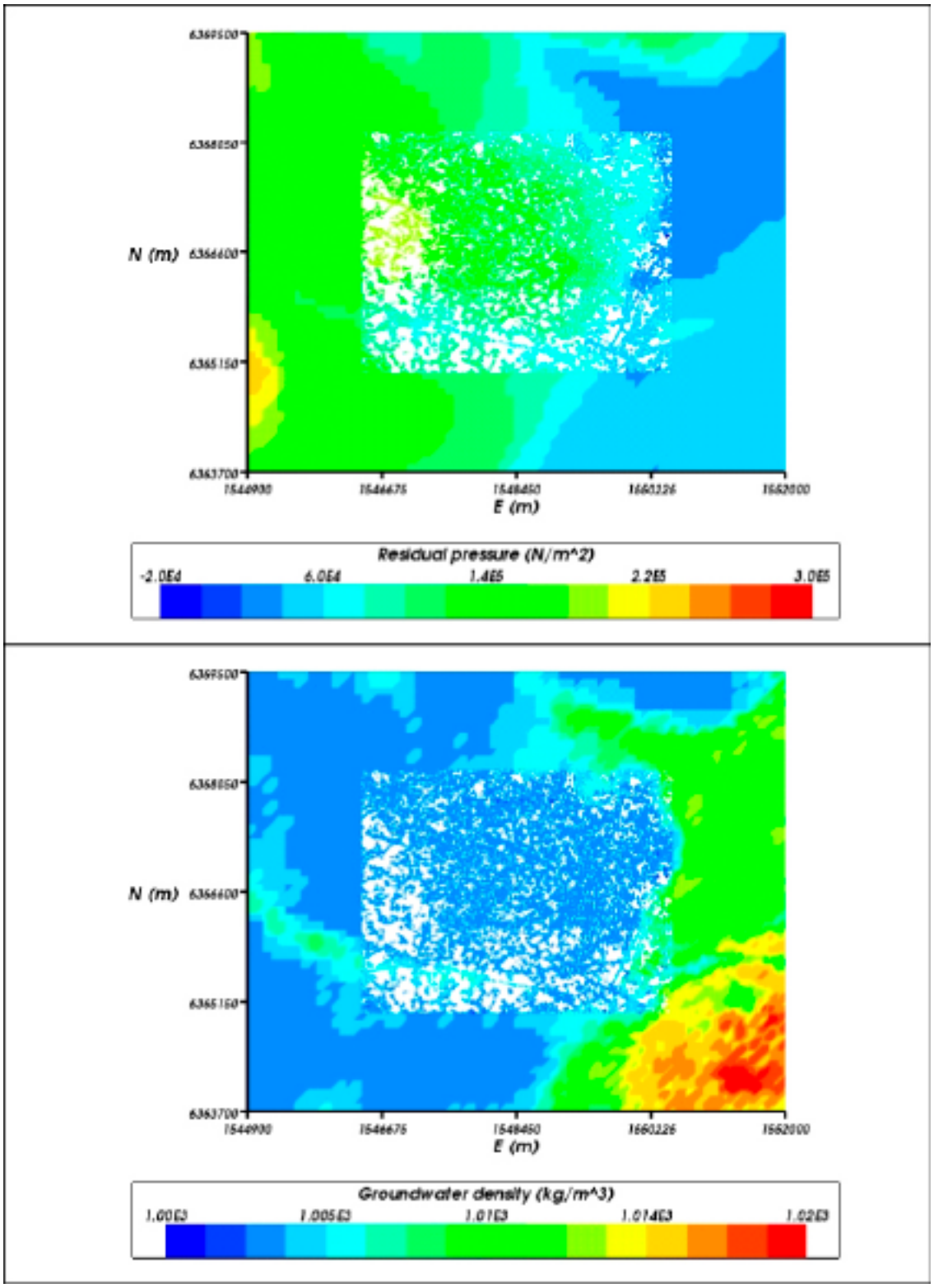

Figure 4-19. *Results of variable-density flow calculation at 2,020 AD for the combined ECPM/DFN model, close-up view of the DFN on a horizontal slice at z = –520 m. Top: Distribution of residual pressure. Bottom: Distribution of fluid density.*

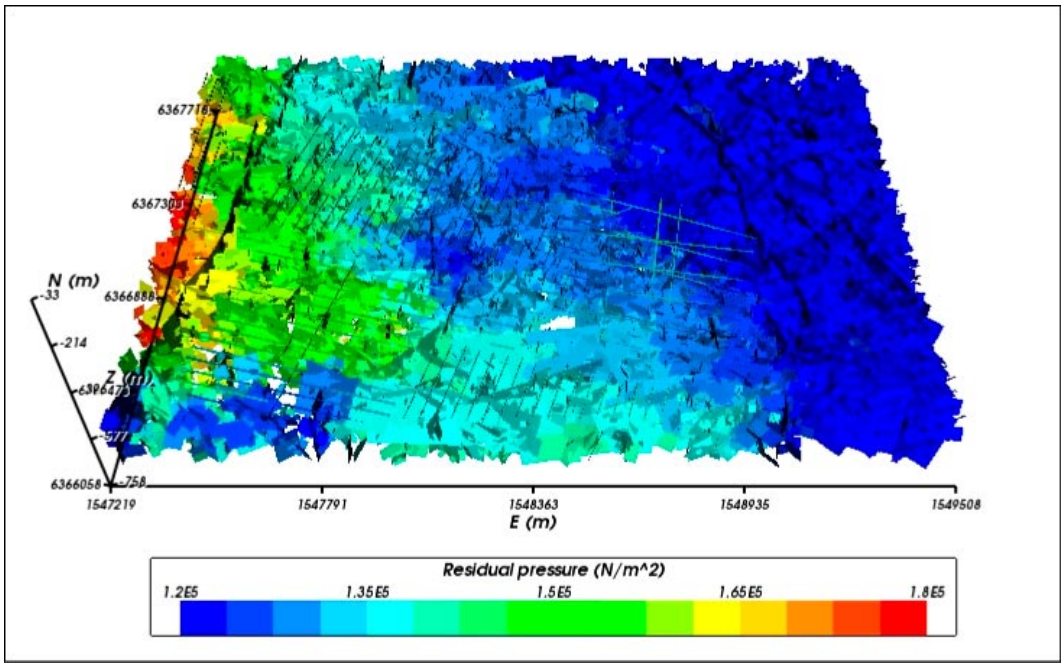

Figure 4-20. *Close-up view of residual pressure around repository blocks 3 and 4. The fractures representing repository structures are shown for all depths but other fractures above –520 m and below –700 m have been removed. Only connected fractures are shown. This may be compared with the residual pressure distribution for the repository-scale model for repository block 3, illustrated in Figure 4-8.*

4.3 Flow-paths

During the SR-Can study for Forsmark version 1.2 /Hartley et al. 2006b/, the algorithm in CONNECTFLOW for calculating particle-tracking through a DFN model was enhanced to support variable-density flow-fields.

The general approach involves moving particles between fracture intersections in a stochastic way. Successive particle destinations are selected by a random process that is weighted according to the fluxes between pairs of intersections. The fluxes are modified to account for buoyancy-driven flows.

As described in Section 2.2.5, three particles corresponding to three path types are released around each canister:

1. Path_Q1 in the fracture that intersects the deposition hole with the highest flux.
2. Path_Q2 in the EDZ fracture adjacent to the deposition hole.
3. Path_Q3 in the CPM tunnel 1 m directly above the deposition hole.

A total of 22,449 (3×7,483) particles are released, three for each deposition hole. Particles are first tracked until they reach the boundary of the repository-scale model. The approach allows particles to move from the DFN sub-model to the CPM sub-model, or vice versa, any number of times according to the flow-field and so particles may pass through one or more sections of tunnel (see Section 2.2.4). To compute a complete path from a canister to the surface, once the particle exits the repository-scale model, the particle is restarted in the regional-scale DFN flow-field (see Section 4.2) corresponding to the same release time.

The repository-scale model extends nearly to the surface, an elevation of 0 m, and at least a few hundred metres horizontally around the deposition tunnels comprising a repository block. Hence, paths are continued only a short distance in the regional-scale DFN model if they exit at the top of the repository-scale model. A relatively small number of particles exit at the vertical side or base of the repository-scale model. In this case, particles may have a significant part of their trajectory in the regional-scale DFN model. Also, there is a potential small jump in the particle trajectory as particles can only be restarted at the nearest node (fracture intersection) in the regional DFN. In either case, the performance measures are aggregated over the two legs of the trajectory in the repository-scale and regional-scale models. This is appropriate since both models use a DFN concept and have identical realisations of the fracture network down to a radius of 14 m.

Simulations of particle tracking in sparse heterogeneous networks can give rise to numerical issues due to the large variations in flow, bottlenecks and areas of near stagnant flow. These issues become particularly apparent when considering the release of particles in deposition holes, which as a consequence of the power-law fracture size concept, many holes are only intersected by small fractures that have low advective velocities, and are not connected to the main flow channels within the network. The Forsmark site /Hartley et al. 2006b/, was found to exhibit such characteristics. There many deposition holes were subject to either no flow, or flows that were so small, they were hard to resolve accurately in a numerical model. An illustration from Forsmark of the connected fracturing around some holes along 4–5 deposition tunnels is shown in Figure 4-21. It was found that flow-paths can get stuck if particles start in fractures or sections of tunnels with very small flows or in fractures with a very poor connection to the

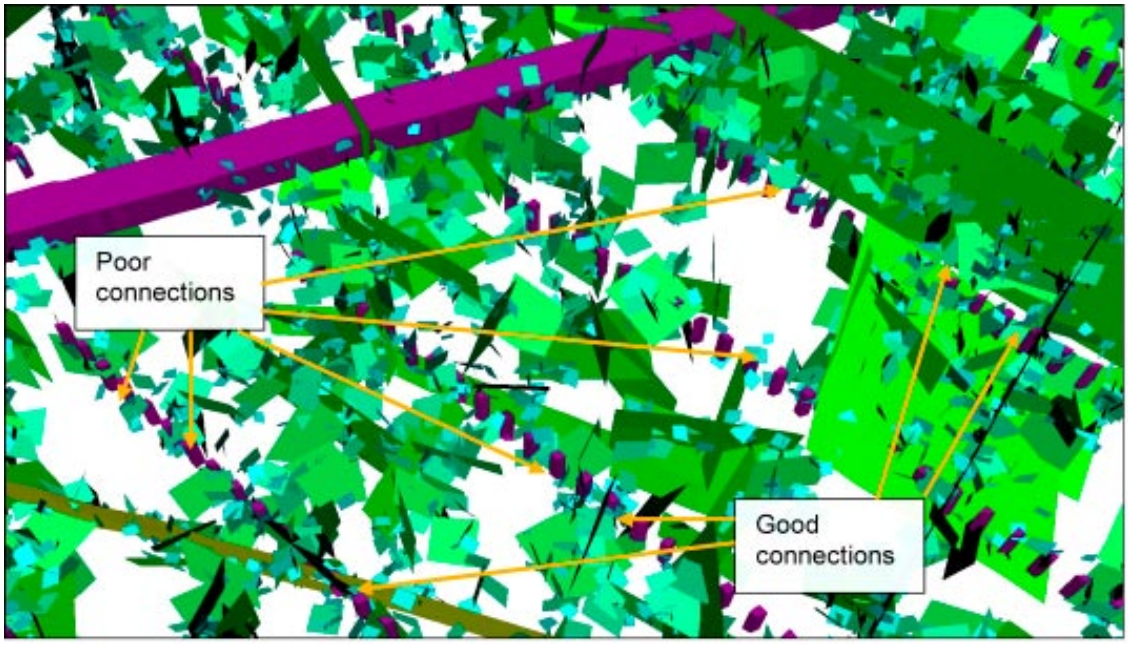

Figure 4-21. *Example of a connected fracture network surrounding canisters in a combined DFN/CPM model. The deposition holes and access tunnel are coloured purple, and the fractures are coloured by transmissivity. Only the connected fractures are shown.*

main flow channels These problems are less prevalent at Laxemar due to the increased connectivity, at least in rock domain HRD(A) where about 71% of deposition holes are intersected by a fracture which has an advective flow connection to the surface. However, the more sparsely fractured HRD(D,E,M) rock domain has only about 35% of deposition holes intersected by fractures with an advective flow connection to the surface.

Figure 4-22 shows particles released in block 3 at 2,020 AD. The particle-tracks are shown together with the exit locations on the top surface for the Path-Q1 release points (i.e. a release in a fracture adjacent to the deposition hole). Here, both legs of the particle path in the repository- and regional-scales are shown in different colours. It should be noted that where there is no fracture adjacent to the deposition hole in the repository-scale, the particle is started from the nearest connected fracture in regional-scale DFN, but these particles marked so to avoid using them in the performance measures. Flow-paths are only calculated for these locations to give an approximate indication of the discharge point that would have been calculated for these deposition holes, were a connected fracture to have intersected them, since in a different DFN realisation they may be intersected by a fracture. For this block, a significant proportion of particles exit the eastern vertical side of the repository block, giving some longer paths than were found in the other three blocks. The reason is the presence of the extensive zone ZSMEW007A that outcrops in the south of block 3 and gently dips NNE (see Figure 4-5: lower plot), which provides a shallow but long horizontal flow-path running west to east. This is interesting since it suggests major sub-horizontal deformation zones could have a significant positive impact on radionuclide transport making flow-paths longer, whereas sub-vertical deformation zones tend to have the negative impact of shortening flow-paths. Although the fractures are not shown in Figure 4-22, it can be seen the particles tend to align along linear features that are associated with either the deterministic DZ's or large stochastic fractures. Generally, if a particle can enter the connected network, then it tends to focus rapidly on the larger fractures, most notably the deterministic deformation zones, but also the large stochastic fractures greater than about 50 m in length.

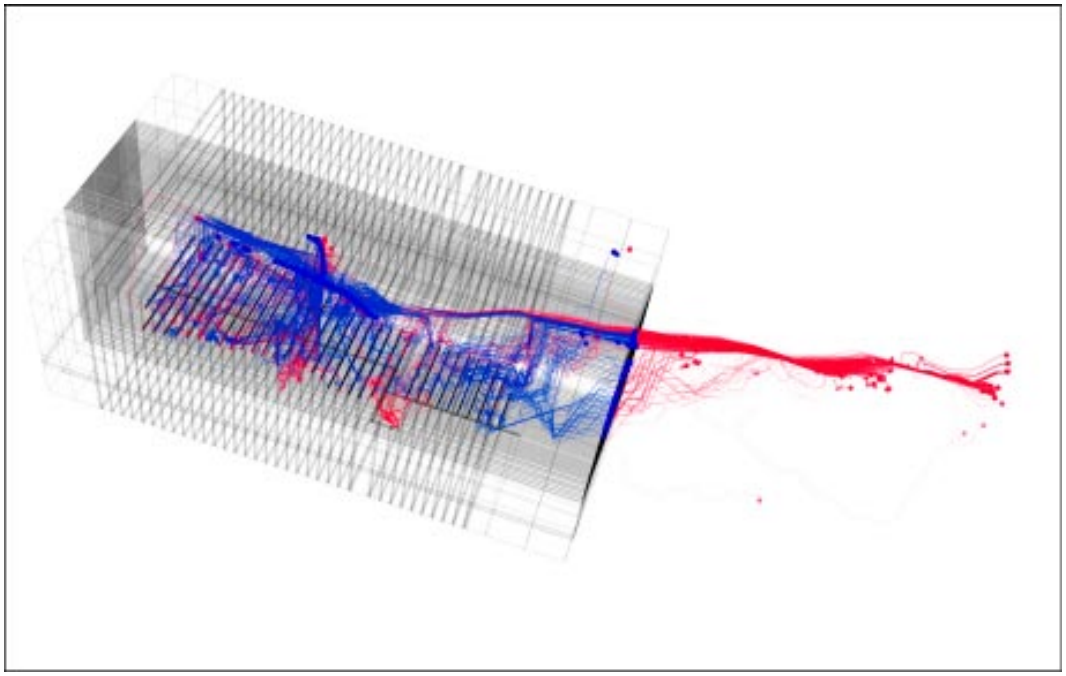

Figure 4-22. *Flow-paths in the variable-density flow through the combined DFN/CPM model of repository block 3 for a release at 2,020 AD and Path-Q1 (a fracture adjacent to the deposition hole). The first leg of the path in the repository-scale model is coloured blue and the exit location on the surface of this model is shown as a blue point. The second leg in the regional-scale DFN is coloured red and the exit location is shown as a red point.*

Considering all 7,483 particles, Figure 4-23 amalgamates the flow-paths calculated within the 4 repository-scale blocks into a single plot. The exit locations where the particles reach the boundary of the relevant repository block are also shown. These cluster along a number of lines. Mostly these correspond to deterministic DZ's or large stochastic fractures, but some just represent where particles exit the vertical sides of one of the blocks. This is only a significant effect for some particles in block 3. One clear characteristic of this overall picture of path trajectories is the greater dispersion of paths in the northern and eastern parts of the repository which correspond with rock domain HRD(A) compared with the southern part where particles concentrate on a small number of discrete conduits in rock domain HRD(D, E, M). The cause is the difference in fracture connectivity. In HRD(A), the network is relatively connected, so particles tend to be dispersed through the many connections through the network, while in HRD(D, E, M), particles tend to follow the tunnel or EDZ before they find a connection to a handful of deformation zones or large stochastic fractures that provide the only connections to the surface. To illustrate this behaviour more, Figure 4-24 shows close-ups of particle paths in the two rock domains. The fractures themselves are not shown in these plots, because it would become too cluttered. However, where particles converge on lines or inclined planes, then they correspond to large fractures. In HRD(A) it is seen that particles tend to follow the tunnels only for a short distance, usually finding a fracture path toward a large deformation zone in the north east that dips south-west toward the repository. For HRD(D, E, M), the particles mostly follow the tunnels or EDZ and only escape via 3 or 4 large fractures. Given this difference in the characteristics of the paths, it is important to assess the performance measures according to the rock domain in which deposition holes are located. Also, in HRD(D, E, M) there is likely to be more difference between the comparison on flow-paths predicted by a DFN model and a continuum porous medium model even when it is supposed to be an equivalent representation. This is because in the DFN model paths are funnelled into a few vertical upward paths in large fractures due to the low fracture intensity and consequent sparsity of long horizontal connections through the network, while an ECPM may allow horizontal trajectories albeit at low velocities. Hence, one might expect to see shorter flow-paths in the southern part of the repository than were predicted in Section 3.

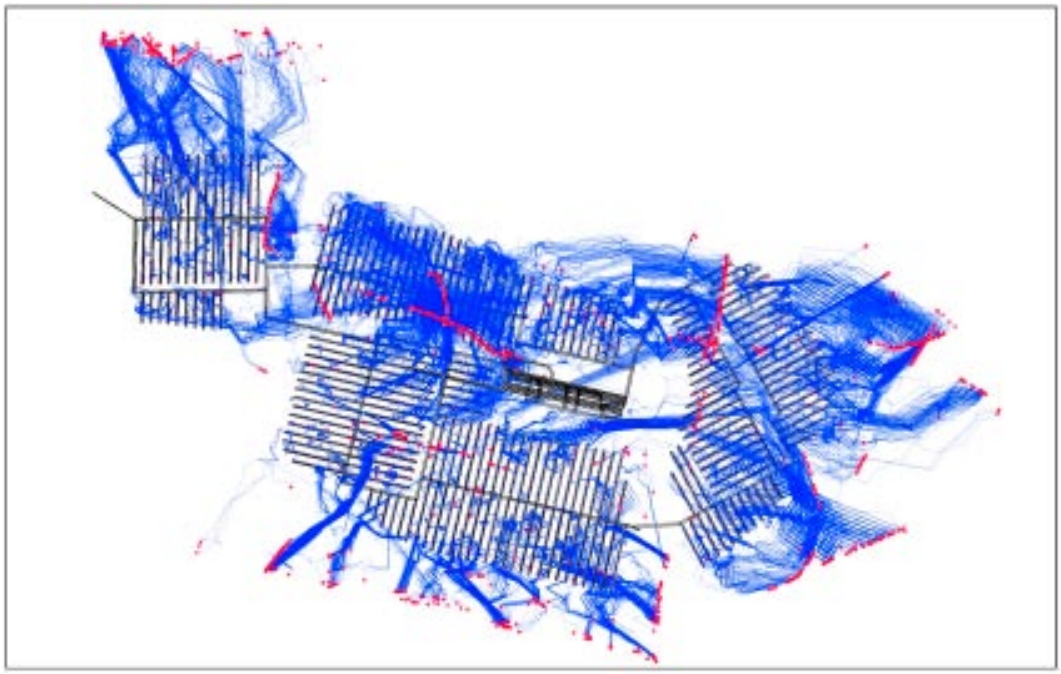

Figure 4-23. *Flow-paths for all 4 repository-scale blocks for a release at 2,020 AD. Only the leg of the flow-paths within the repository-scale models are shown here. The path trajectories are shown in blue, and points where the particles exit the relevant repository-scale model block are coloured red.*

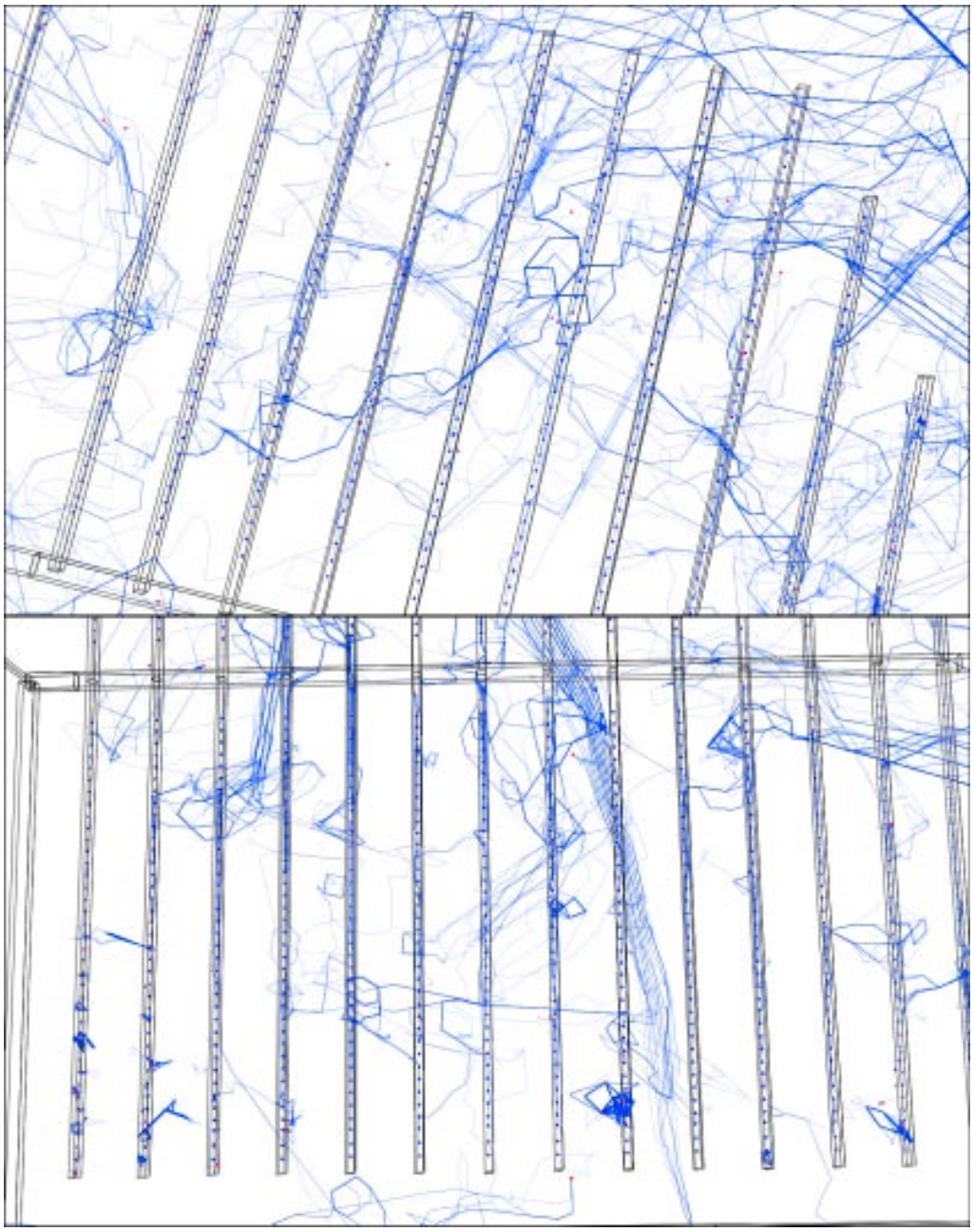

Figure 4-24. *Example close-ups of particle tracks through the repository-scale models for a release at 2,020 AD. Particle paths are coloured in blue and made semi-transparent, so that paths followed by several particles are drawn more heavily than ones followed by a single particle. The particle paths are stochastic, and hence particles may follow several different paths through the same fracture depending on the distribution of flow in the plane leading to the network dispersion seen in these plots. Top: particles released in part of block 3 within rock domain HRD(A). Bottom: particles released in block 4 in rock domain HRD(D, E, M).*

The exit locations on the surface for the amalgamated repository- and regional-scale models at the reference release times of 6,000 BC, 2,000 BC, 2,020 AD and 6,000 AD are shown in Figure 4-25 based on the Path-Q1 release point. At 2,020 AD, 99.5% of exit locations are within the DFN sub-model of the combined regional-scale model. Only 0.5% of particles continue into the ECPM representation. Hence, the vast majority of particle tracks are captured accurately by the DFN model and for those that are not, the majority of the path is inside the DFN sub-model. The plots in Figure 4-25 may be compared with the corresponding plots for the regional ECPM model in Figure 3-10, Figure 3-11 and Figure 3-14.

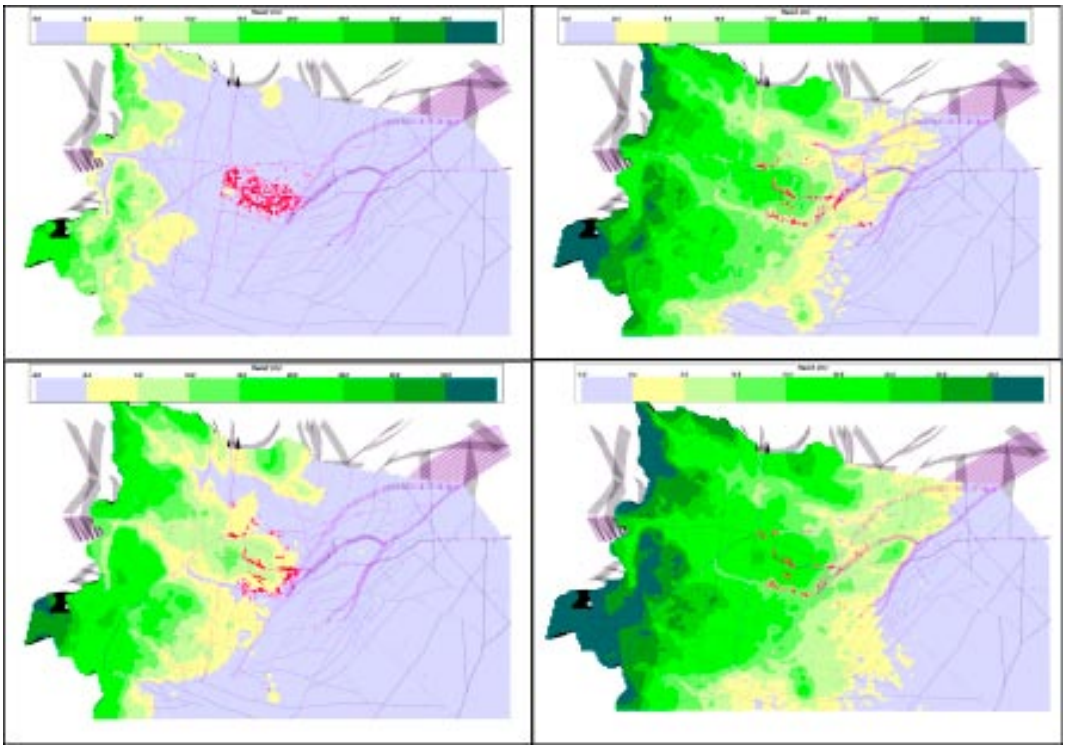

Figure 4-25. *Particle exit locations of particle tracks for release point Path-Q1 in the amalgamated repository- and regional-scale DFN models. The background colours show groundwater head and deterministic deformation zones. Top left: release at 6,000 BC; Bottom-left: release at 2,000 BC; Top right: release at 2,020 AD; Bottom right: release at 6,000 AD.*

For the Path-Q1 release point, it is important to note that only 52% of deposition holes are connected by a conductive fracture via the fracture network to the surface. This is because the fracture network is sparsely connected, especially in rock domain HRD(D,E, M) and because of the stochastic nature of the DFN, the fracture geometry and flow characteristics are highly spatially variable. Table 4-2 summarises the situation for paths Q1, Q2 and Q3 at release time 2,020 AD. For Q1, particles are released in the fracture abutting the deposition hole with the highest Darcy velocity. Although nearly all canisters are intersected by a fracture, many of these fractures are either unconnected and therefore have no flow, or are connected to a closed loop of fractures that has essentially no flow. Overall, about 34% of canisters are not intersected by a connected fracture, and a further 11% are in areas of stagnant flow without a connected path away from the canister. Only about 3% of particles become stuck due to mass balance problems in the numerical solution. This leaves about 52% of canisters that have Q1 paths to the surface. Of these, only about 47% of canisters are intersected by a connected fracture above the PFL detection limit of around 10^{-9} m^2/s. For the releases in the EDZ and the tunnel, Q2 and Q3,

Table 4-2. Summary of the particle tracking results for the amalgamated repository- and regional-scale DFN models released at 2,020 AD. For each of the 7,483 canister positions, paths Q1, Q2 and Q3 are computed.

Particles/canisters [%]	Q1 All	HRD(A)	HRD(D,E, M)	Q2	Q3
Fracture with T > 10^{-9} m^2/s	47%	63%	31	N/A	N/A
No connected fracture	34%	13%	48%	N/A	N/A
Particles that reach surface	52%	74%	40%	81%	84%
Stagnant flow	11%	10%	10%	15%	11%
Mass balance problems	3%	3%	2%	4%	5%

about 10% of particles remain close to the repository due to stagnant flow, and over 80% make it to the surface of the model. The reason there are areas of stagnant flow in the tunnel and EDZ is that the end of each deposition tunnel opposite the main tunnel is essentially a dead-end. That is, to get advection along or out of the tunnel there must be a head gradient along it which requires that at least two moderate to large water-bearing fractures intersects the tunnel, and the portion outside of these connections is subject to stagnant flow conditions. Figure 4-26 demonstrates that the deposition holes for which particles do not reach the surface correlate well with areas of the tunnel in where the Darcy velocity is very low. This shows that tunnel sections with very low Darcy velocity around 10^{-6} m/year, or less, tend to correspond very well with areas where Path-Q3 particles do not reach the surface. This is likely to be due to problems in resolving groundwater flow accurately with numerical models in these areas where the flows are

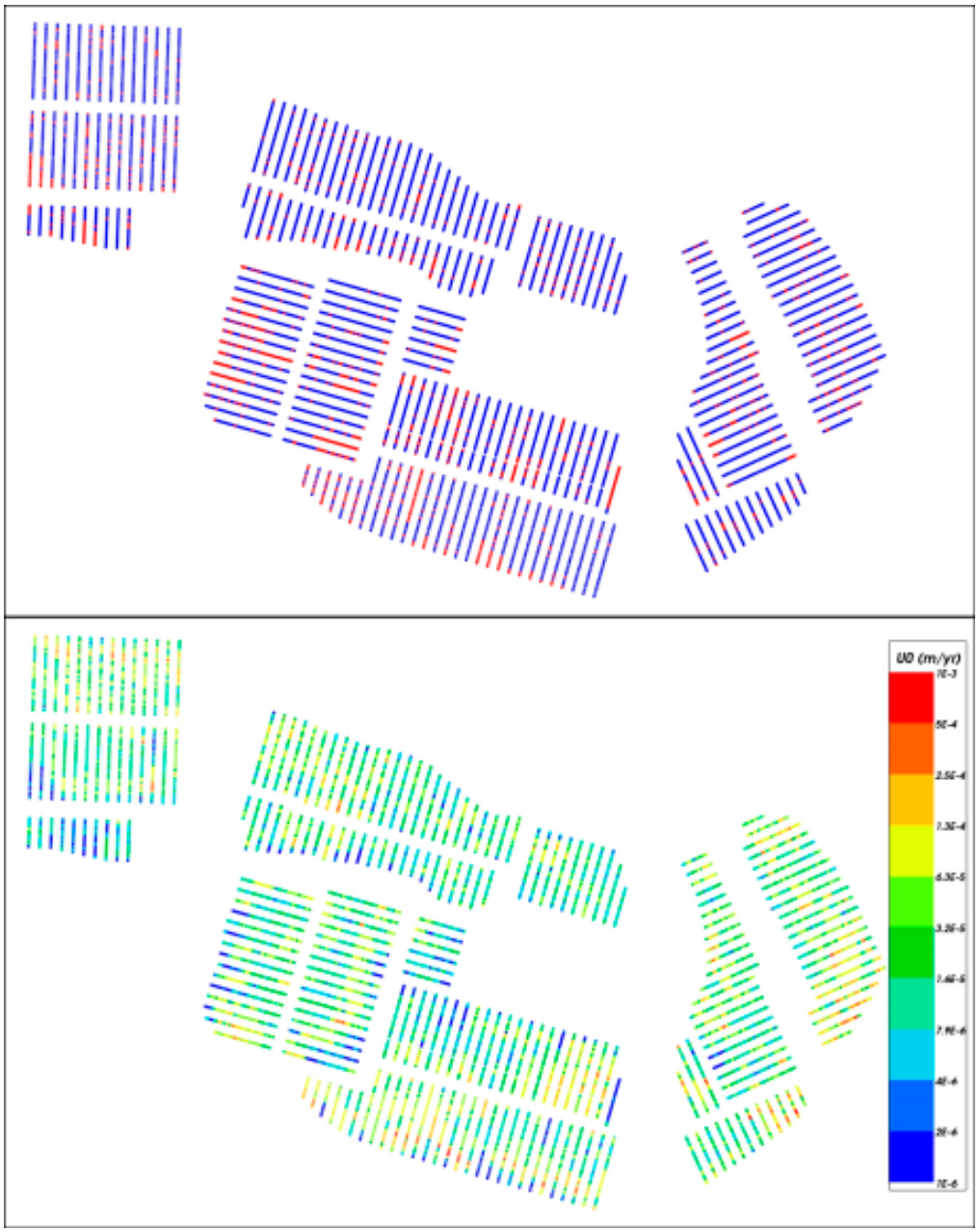

Figure 4-26. *Correlation between particle fate and Darcy velocity in the tunnel at particle start locations for the Path-Q3 release in the amalgamated repository- and regional-scale DFN models released at 2,020 AD. Top: deposition holes coloured blue correspond to where the flow-path reached the surface, while those coloured red became stuck in the fracture network. Bottom: Darcy velocity in the tunnel.*

so small. Also, it is worth observing that these deposition holes tend to be grouped around the ends of tunnels, and are more frequent in rock domain HRD(D, E, M) in the south and west of the repository. Considering the individual rock domains, HRD(A) has 74% of deposition holes with an advective Q1 path to the surface via an adjoining fracture, while HRD(D, E, M) has only 40%.

For release time 2,020 AD, the distribution of F-factors at particle release and exit locations (on the top surface) for each of the paths Q1, Q2 and Q3, is shown in Figure 4-27. There are less

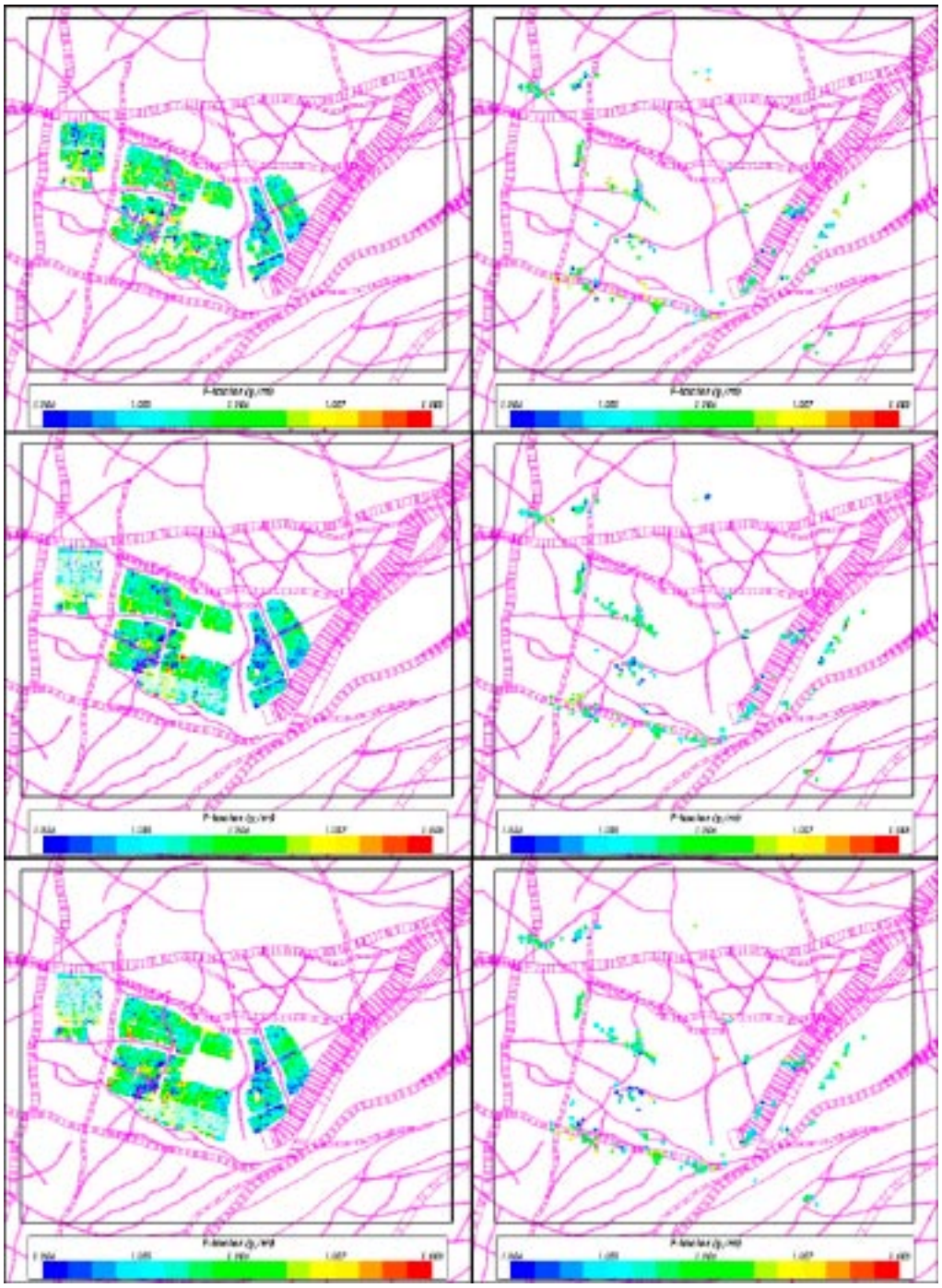

Figure 4-27. *Distribution of $\log_{10}(F_r)$ at 7,483 particle release (left) and exit (right) locations for the amalgamated repository- and regional-scale DFN model at release time 2,020 AD and for path-Q1, path-Q2 and path-Q3 (top to bottom). A horizontal slice through the HCD's at z = –520 m is also shown (purple). The black rectangle indicates the maximum extent of exit locations for all release times.*

exit locations for path Q1 than for the two other paths. This is because for Path-Q1 there is not always a connected fracture in which to start the particle. Otherwise, the distribution of exit locations and their F-factors at release time 2,020 AD is similar for paths Q1, Q2 and Q3. Many of the low values of F-factor correspond to intersection with low confidence deterministic DZ's.

Figure 4-28 shows the distribution of F-factors for path-Q1 at particle release locations for release times 6,000 BC, 2,000 BC, 2,020 AD, and 6,000 AD. A clear observation is that the distributions for the three later times are quite similar. There are a number of small F-factors, up to about 10^4 y/m, with a clear correlation to the proximity to either a deterministic deformation zone or a large stochastic fracture. Small F-factors are slightly more prevalent in the eastern part of the repository, but there are many localised variations that just depend on the localised fracturing. These observations confirm that flow is very heterogeneous and mostly localised.

Figure 4-29 shows the distribution of F-factors for path-Q1 at the exit points of the particles (on the top surface). This shows that the release is more localised in comparison to that predicted by the regional-scale ECPM modelling (see Section 3.2). At 6,000 BC, all particles appear almost

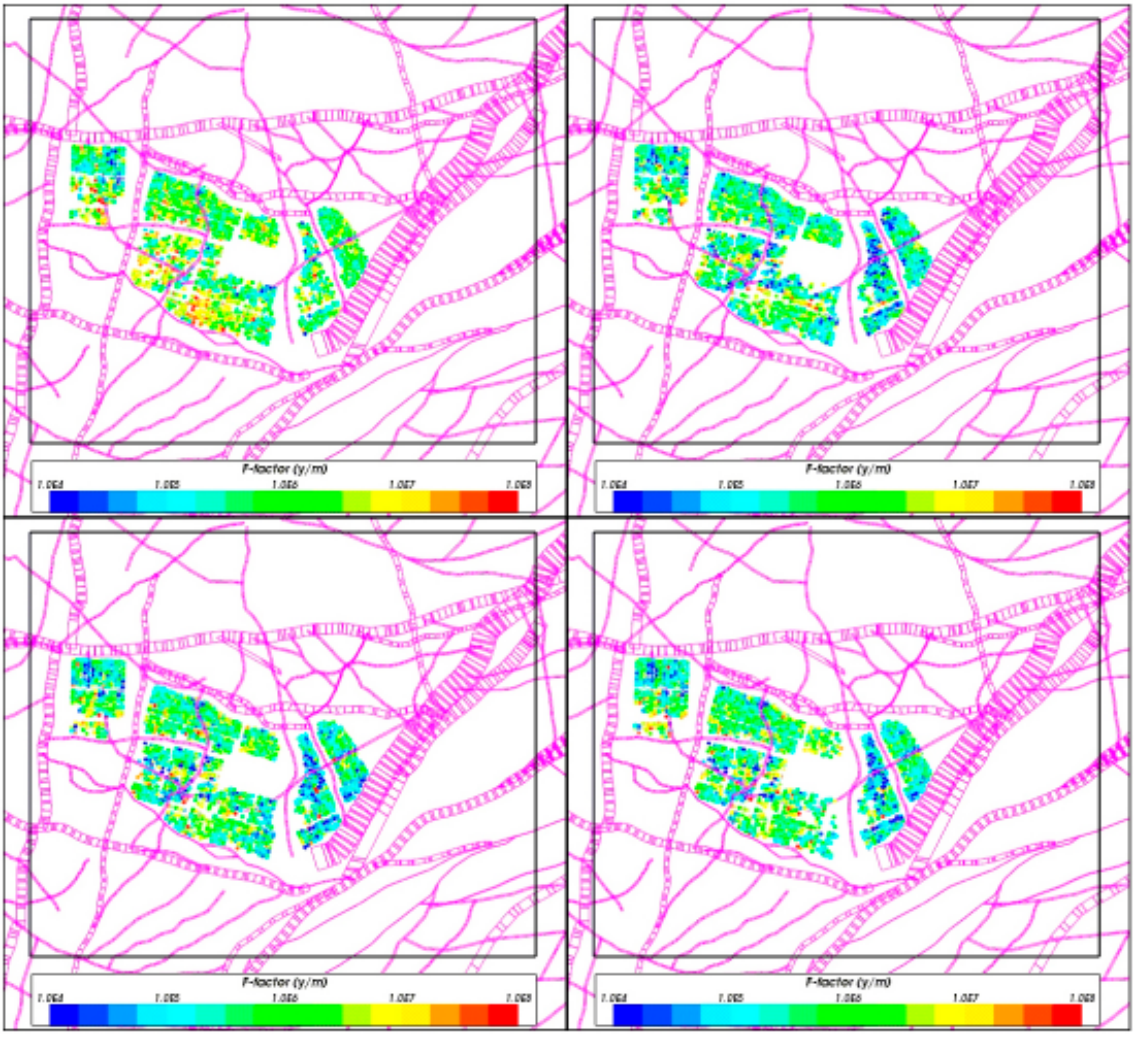

Figure 4-28. *Distribution of $\log_{10}(F_r)$ at 7,483 particle release locations for path-Q1 in the amalgamated repository- and regional-scale DFN model at release times: 6,000 BC (top left), 2,000 BC (top right), 2,020 AD (bottom left) and 6,000 AD (bottom right). A horizontal slice through the HCD's at z = –520 m is also shown (purple). The black rectangle indicates the maximum extent of exit locations for all release times.*

vertically above the repository and the path-lengths are between about 560 m and 18,000 m with a median of about 1,200 m. At 2,000 BC, the median path-length is about the same as that at 6,000 BC, the minimum path-length is slightly higher at about 590 m, and the maximum path-length is shorter at 13,000 m. For the two later release times, the minimum and median path-lengths, at around 600 m and 1,500 m respectively, are slightly longer than those at the earlier release times.

The travel-times in the rock, t_r, for path-Q1 are plotted at the particle release points for each of the four reference release times in Figure 4-30. A comparison of these plots shows that the travel-times are longer for 6,000 BC than for the later release times, and at 2,000 BC there are more particles with short travel-times (less than 10 years) than at the other three release times. For all release times, canister positions in subareas 9 and 7 of the repository (see Figure 2-16) have the longest travel-times, and canisters positions in subareas 2, 8, and 9 have the shortest travel-times. There is also a small area on the east of repository subarea 1 that has canister positions with relatively short travel-times.

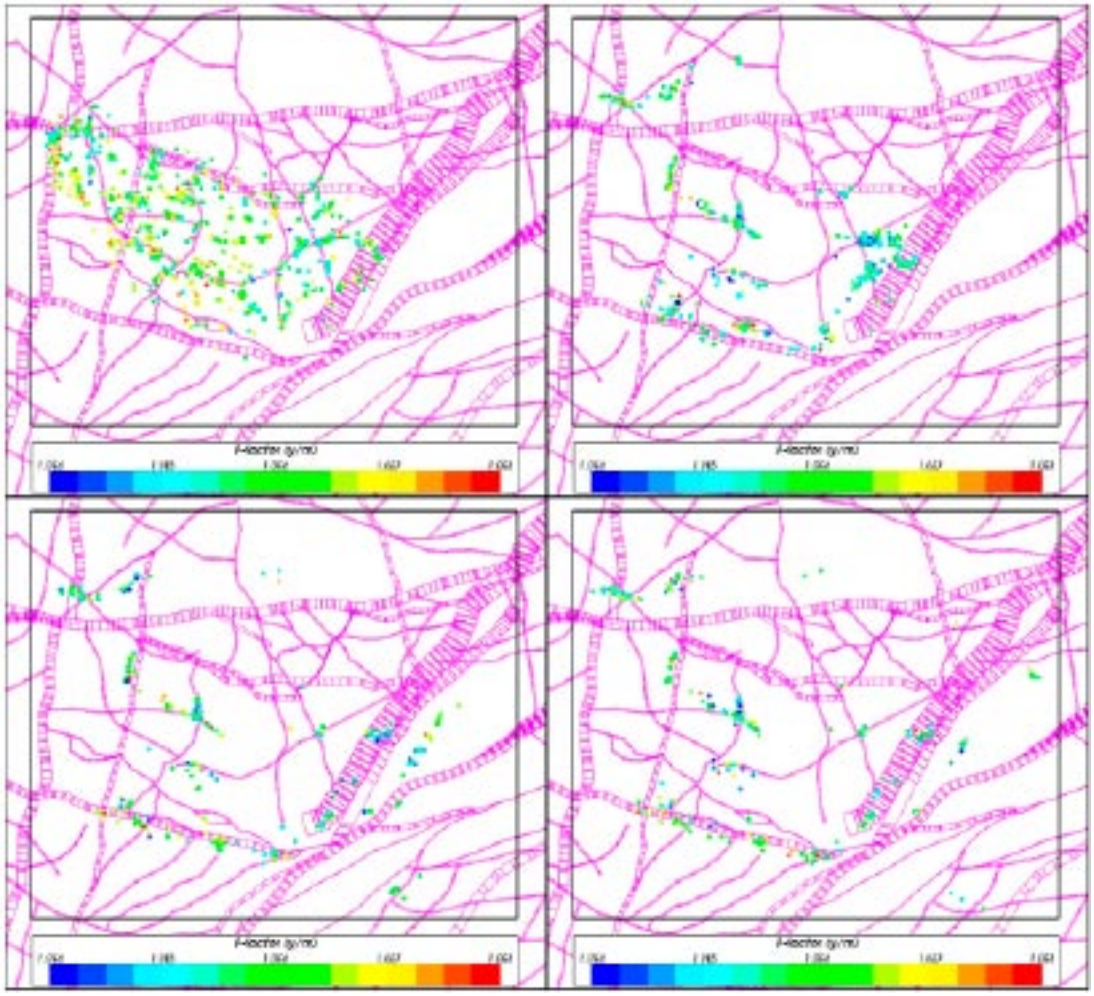

Figure 4-29. *Distribution of $\log_{10}(F_r)$ at particle exit locations for path-Q1 in the amalgamated repository- and regional-scale DFN model at release times: 6,000 BC (top left), 2,000 BC (top right), 2,020 AD (bottom left) and 6,000 AD (bottom right). A horizontal slice through the HCD's at z = –520 m is also shown (purple). The black rectangle indicates the maximum extent of exit locations for all release times.*

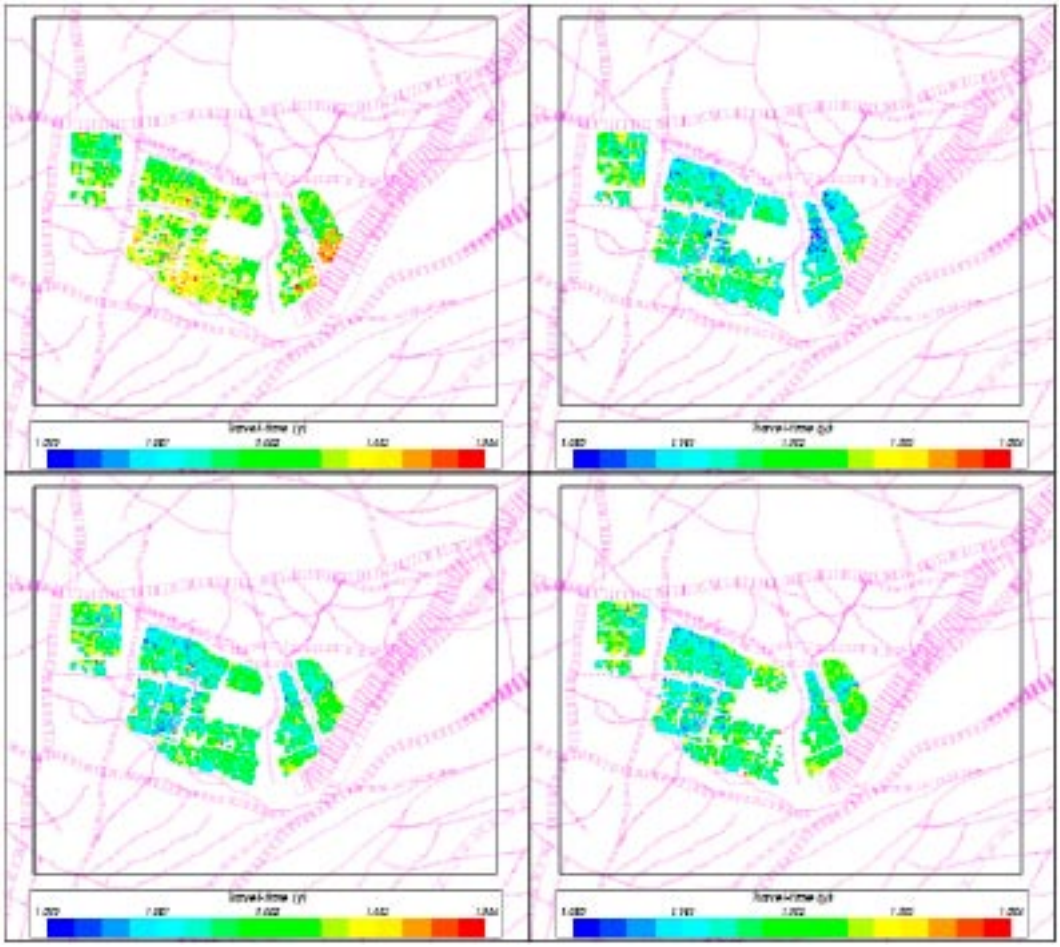

Figure 4-30. *Distribution of $\log_{10}(t_r)$ at 7,483 particle release locations for path-Q1 in the amalgamated repository- and regional-scale DFN model at release times: 6,000 BC (top left), 2,000 BC (top right), 2,020 AD (bottom left) and 6,000 AD (bottom right). A horizontal slice through the HCD's at z = –520 m is also shown (purple). The black rectangle indicates the maximum extent of exit locations for all release times*

4.4 Performance measures (PM's)

For each of the reference release times, 6,000 BC, 2,000 BC, 2,020 AD and 6,000 AD, and for each of the paths Q1, Q2, and Q3, travel-times, initial Darcy velocities, path-lengths, and F-factors for the paths followed by the 7,483 particles released in the repository were obtained. These data were plotted as histograms and cumulative distribution plots to allow comparisons to be made between the PM's for paths Q1, Q2, and Q3, and between the PM's for different release times. In addition, for each path, a record was kept of the hydraulic domain and the repository tunnel within which the particle was released. This allowed comparisons to be made between the PM's for different hydraulic domains and between the PM's for different areas of the repository.

4.4.1 Q-equivalent (*Qeq*) for input to near-field model (COMP23)

The near-field code COMP23 calculates the non-stationary nuclide transport in the near-field of a repository. The system is divided in to compartments, where the only restriction is that a compartment is formed of the same material. The model, which is a very coarsely discretised Integrated Finite Difference Model, embeds analytical solutions at locations where other models require a very fine discretisation such as entrances and exits from small holes and fractures.

In the repository, radionuclides leaking out through a small hole in the canister wall diffuse into the bentonite buffer and may then migrate through various pathways into the flowing water in rock fractures. The pathways are illustrated in Figure 2-15.

For compartments in contact with water flowing in fractures in the rock, the diffusive transport is determined by an equivalent flow-rate, *Qeq* [m^3/yr]. This parameter is a fictitious flow-rate of water that carries a concentration equal to that at the compartment interface. It has been derived by solving the equations for diffusional transport to the passing water by using boundary layer theory /Neretnieks 1979/. The value of *Qeq* is dependent on the geometry of the contact area, the water flux, the flow porosity or fracture aperture and the diffusivity. As part of the SR-97 assessment formulae were derived for a CPM model /Moreno and Gylling 1998/. The formulae are different for a DFN model as detailed below for the three pathways.

Q-equivalent release into fractured rock for the nested model (Q1)

Path Q1 considers release of radionuclides into the fractured rock surrounding the deposition hole, and hence the particle starts within a fracture that intersects the wall of the deposition hole. Several fractures may intersect the canister. For reasons of making a conservative assumption, the flux into all fractures that intersect the canister and contribute to advective flow away from the canister are included in the calculation of *Qeq*. That is, an effective flow-rate is calculated for all fractures that cut deposition hole and are connected to at least one other fracture. These effective flow-rates are summed for the deposition hole to give the total *Qeq*. The equivalent groundwater flow rate for Q_{eq1} can be written as:

$$Q_{eq1} = \sum_f \left(2\frac{Q_f}{\sqrt{a_f}} \sqrt{\frac{4D_w t_{wf}}{\pi}} \right), \text{ where } t_{w,f} = \frac{L_f \cdot e_{t,f}}{Q_f / \sqrt{a_f}} \qquad \text{Equation (4-1)}$$

If there are several fractures intersecting a single deposition hole, then a conservative approach to calculate the equivalent groundwater flow-rate requires the flow to be summed across all the fractures. Hence, the equivalent Darcy velocity, U_{r1}, for all fractures intersecting the deposition hole is:

$$U_{r1} = \frac{1}{w_c} \sum_f \frac{Q_f}{\sqrt{a_f}} \qquad \text{Equation (4-2)}$$

where:

D_w is the diffusivity in water, [m^2/yr].

$t_{w,f}$ is the time the water is in contact with the deposition hole within each fracture, [yr].

L_f is the length of the fracture intersection with the wall of the deposition hole, [m].

U_{r1} is the average initial Darcy velocity in the fracture system averaged over the rock volume adjacent to the canister (water flux) [m/yr].

Q_f is the volumetric flux in the fracture adjacent to the deposition hole [m^3/yr].

$e_{t,f}$ is the transport aperture of the fracture adjacent to the deposition hole [m].

a_f is the area of the fracture plane intersecting the hole [m^2].

w_c is the canister height [m].

Here, D_w was set to 0.0316 m^2/yr, and w_c was set to 5 m. All other values were determined in the DFN flow simulations.

Potentially a damaged zone may form due to spalling in the rock wall in the deposition hole for waste canisters. The zone can have higher conductivity and porosity than the intact rock. I which case, water will be drawn into the damaged zone from fractures that intersect the deposition hole. The water can attain a longer residence time in contact with the buffer in the hole than would otherwise be the case when only the thin fracture contacts the buffer. This may lead to a higher exchange of solutes between the flowing water and the pore water in the buffer /Neretnieks 2006/. The implications of such an effect are quantified for the reference case in Appendix D.1.

Q-equivalent release into the EDZ

Path Q2 considers the release of radionuclides into the EDZ. Here the particles are released within a fracture used to represent the EDZ that surrounds the top of the deposition hole. The equivalent groundwater flow-rate, Qeq_2, is calculated from the flow in the EDZ fracture that cuts deposition hole and are connected to at least one other fracture. These effective flow-rates are summed for the deposition hole to give the total Qeq. The equivalent groundwater flow-rate, Q_{eq2}, can be written as:

$$U_{r1} = \frac{1}{w_c} \sum_f \frac{Q_f}{\sqrt{a_f}}. \qquad \text{Equation (4-3)}$$

The equivalent Darcy velocity, U_{r2}, for flow in the EDZ is:

$$U_{r2} = \frac{Q_E}{w_E \sqrt{a_E}} \qquad \text{Equation (4-4)}$$

where:

L is the half circumference of the deposition hole, [m].

U_{r2} is the average initial Darcy velocity in the EDZ fracture averaged over the fracture cross-sectional area [m/yr].

Q_E is the volumetric flux in the EDZ fracture between each deposition hole [m^3/yr].

ε_E is the EDZ porosity [m].

a_E is the horizontal area of the EDZ between each deposition hole [m^2].

w_E is the EDZ thickness [m].

Here, L_E was set to 2.8 m, w_E was set to 0.3 m, and ε_E was set to 10^{-4}. All other values were determined in the DFN flow simulations.

Q-equivalent release into the tunnel

Path Q3 considers the release of radionuclides into a fracture that intersects the tunnel. It is assumed that diffusive equilibrium of radionuclides is achieved in the tunnel backfill and diffusion takes place into the water flowing in fractures surrounding the tunnel. Hence, an equivalent flow-rate, Qeq_3, is required for advective flow in the first fracture encountered along the path after a particle is released in the tunnel backfill above the deposition hole. The equivalent groundwater flow-rate, Qeq_3 is calculated from the flow-rate in the first fracture the particle enters after leaving the tunnel. The equivalent groundwater flow-rate, Q_{eq3}, can be written as:

$$U_{r2} = \frac{Q_E}{w_E \sqrt{a_E}}. \qquad \text{Equation (4-5)}$$

The equivalent Darcy velocity, U_{r3}, for flow in the EDZ is:

$$U_{r3} = \frac{Q_f}{w_T \sqrt{a_f}} \qquad \text{Equation (4-6)}$$

where:

L_f is the length of the fracture intersection with the wall of the tunnel [m].

U_{r3} is the Darcy velocity in the fracture averaged over the fracture cross-sectional area [m/yr].

Q_f is the volumetric flux in the fracture adjacent to the tunnel [m^3/yr].

w_T is the fracture width intersecting the tunnel [m].

a_f is the area of the fracture plane intersecting the tunnel [m^2].

$e_{t,f}$ is the transport aperture of the fracture intersecting the tunnel [m].

Here, L_f was set to 7 m, w_f was set to 2.5 m. All other values were determined in the DFN flow simulations.

The formulae above are based on an assumption that transport in the tunnel is predominantly due to diffusion. If, significant advective flow takes place within the tunnel backfill, then an extra term should be evaluated in calculating *Qeq3*. The implications of advective flow in the tunnel backfill are quantified in Appendix D.2.

4.4.2 Reference case

For each of the four release times, the PM's obtained for the three different paths Q1, Q2, and Q3 were compared. As expected, for travel-time and F-factor in the rock, t_r and F_r respectively, the distributions are similar for the different paths Q1, Q2, and Q3. However, since the corresponding particles are released in different materials, the distributions of initial Darcy velocity U_r are significantly different. This is illustrated by cumulative distribution plots of t_r, U_r and F_r in Figure 4-31. The curves shown are normalised with respect to the total number of deposition holes; the offset to the left corresponds to deposition holes with zero flow. The offset to the right indicates the fraction of flow paths which do not find a complete path through the geosphere. Thus, the curves represent the fraction of deposition holes which simultaneously have a flow greater than zero and have flow paths which exit the geosphere. For example, for Q1 more than 30% of deposition holes are not intersected by a fracture bearing advective flow and more than 10% of particles that start from the deposition hole do not find a pathway to the surface. The offset on the left is a legitimate result of a low intensity of connected fractures around the deposition holes, especially in rock domain HRD(D, E, M). The offset on the right is more of a numerical artefact of the difficulty in tracking particles through sparse heterogeneous networks. It is expected that these numerical effects will be largely resolved in time for SR-Site.

For each of these PM's, the cumulative distribution for each of the paths Q1, Q2, and Q3 is plotted for release time 2,020 AD. For U_r, the values of U_{r1}, U_{r2} and U_{r3} are plotted. The F-factor is very slightly higher in Path-Q1 probably due to extra residence in the first fractures in which the particles are released, whereas the first part of paths Q2 and Q3 are in the EDZ and tunnel where no F-factor is calculated. Due to the variability in connectivity and transmissivity of fractures intersecting the deposition holes, there is much greater heterogeneity in the initial velocity for Q1 than the other paths. The median equivalent Darcy velocity is highest in the EDZ, and least in the tunnel. In Log10-space, the median travel-time is 1.77, the median initial Darcy velocity is –3.67, the median path-length is 3.17, and the median F-factor is 5.66 for the Q1 path for a release at 2,020 AD. Comparing with the ECPM model PM's, the median initial velocities and F-factors from the upscaled DFN are very similar, but the travel-time here is much shorter. Presumably this is because flow-paths see much less of the fracture pore space than the total connected fracture pore space. That is, in a DFN model the travel time will depend only on the transport aperture of fracture accessed by flow-paths, while in the ECPM model, the travel time is based on the equivalent porosity of all fractures within each finite-element through which a pathline passes.

The distributions of path-length in the rock, L_r, are also similar for the three different paths Q1, Q2, and Q3. This is illustrated in Figure 4-32 by a cumulative distribution plot of path-length for release time 2,020 AD. There is a distinctive long tail in the distribution after the 70th percentile which corresponds to longer flow-paths that discharge along the shoreline. Hence, about 70% of release positions have short flow-paths that discharge above the site area with path-lengths less than about 1,500 m which have little sensitivity to future shoreline movements, whereas about 30% of particles have longer paths that are more sensitive to the shoreline evolution. For path Q1 at 2,020 AD, the cumulative distributions of L_r for particles released in the three hydraulic rock domains, HCD, HRD(A) and HRD(D,E,M), are plotted in Figure 4-33. The following observations are made: irrespective of where particles are released, path-lengths range from a few hundred metres up to about 3-4 km; particles released in the HCD have a shorter median path-length than those released in the HRD, and particles released in HRD(A) have a shorter median path-length than those released in HRD(D,E,M). These observations are true for all release times and all paths Q1, Q2, and Q3. The longer paths in HRD(D,E,M) are thought to be a consequence of particles having to travel further within the poorly connected fracture network to find a good vertical connection to the top surface.

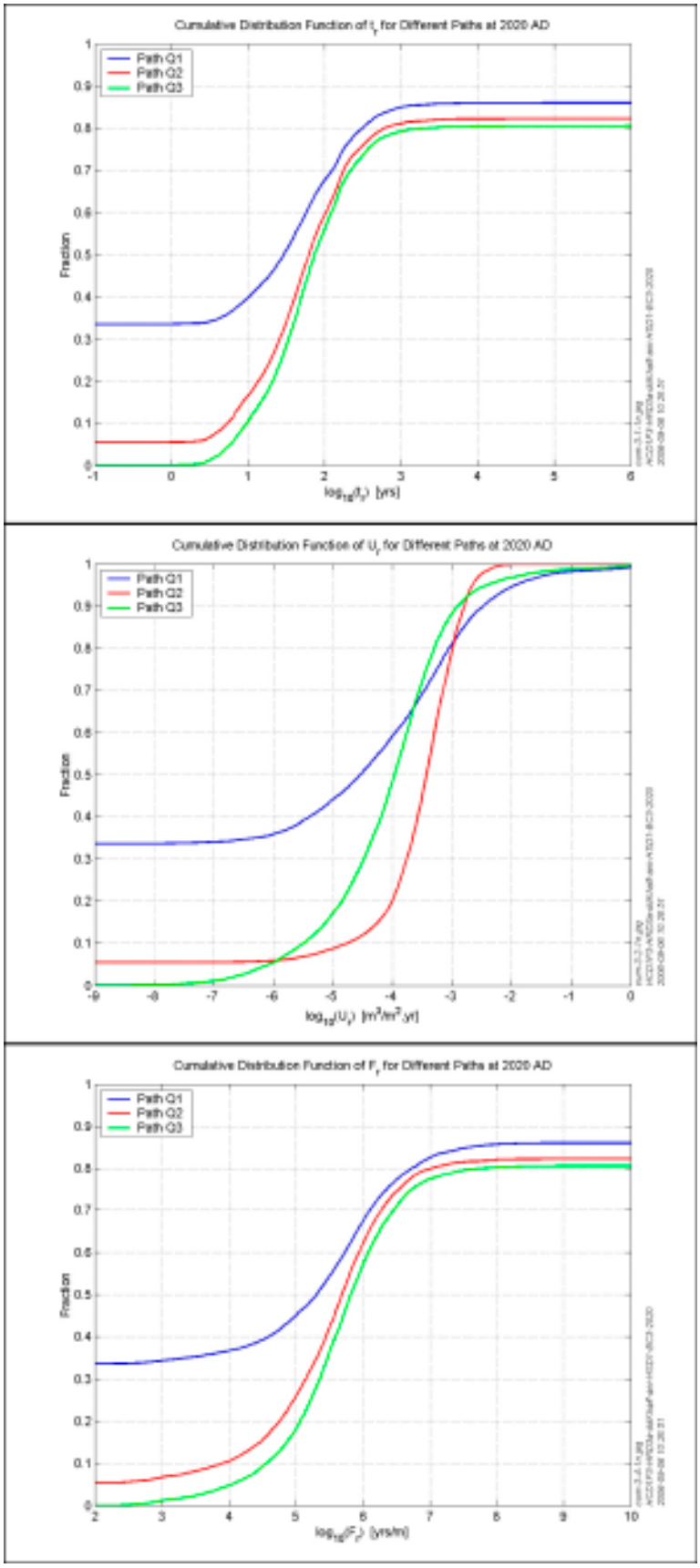

Figure 4-31. *Cumulative distribution plots for the PM's t_r (top) and U_r (middle), F_r (bottom) for paths Q1, Q2, and Q3 in the amalgamated repository-scale and regional-scale DFN models with 7,483 particles released at time 2,020 AD.*

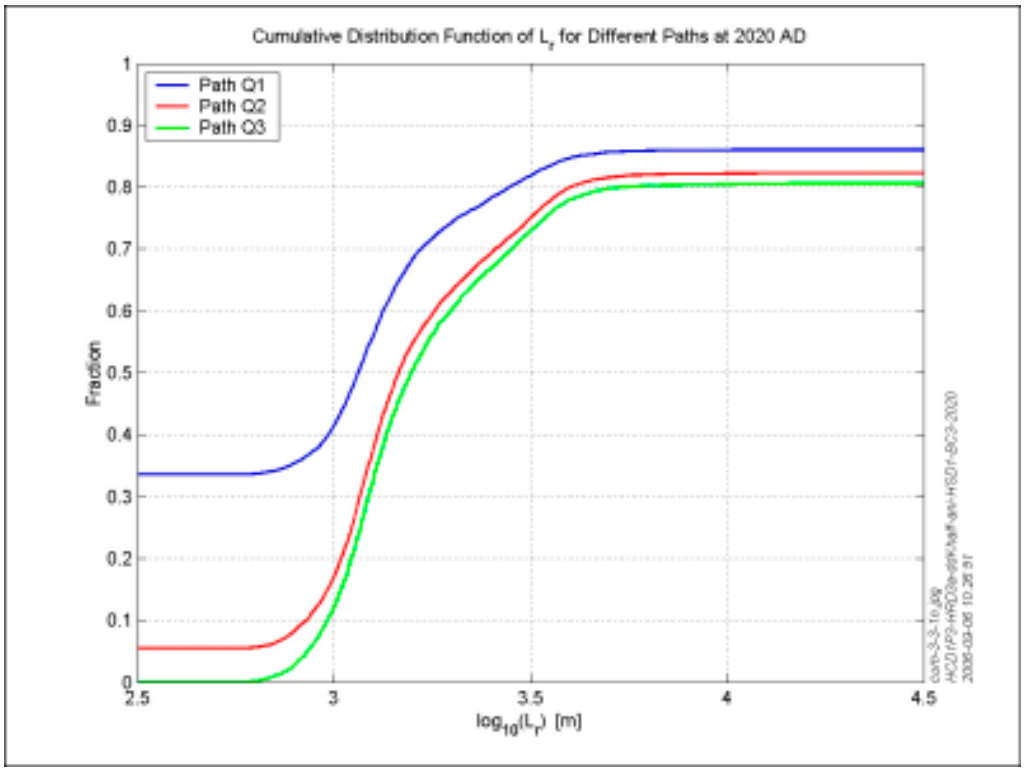

Figure 4-32. *Cumulative distribution plot for path-length in the rock L_r for paths Q1, Q2, and Q3 in the amalgamated repository-scale and regional-scale DFN models with 7,483 particles released at time 2,020 AD.*

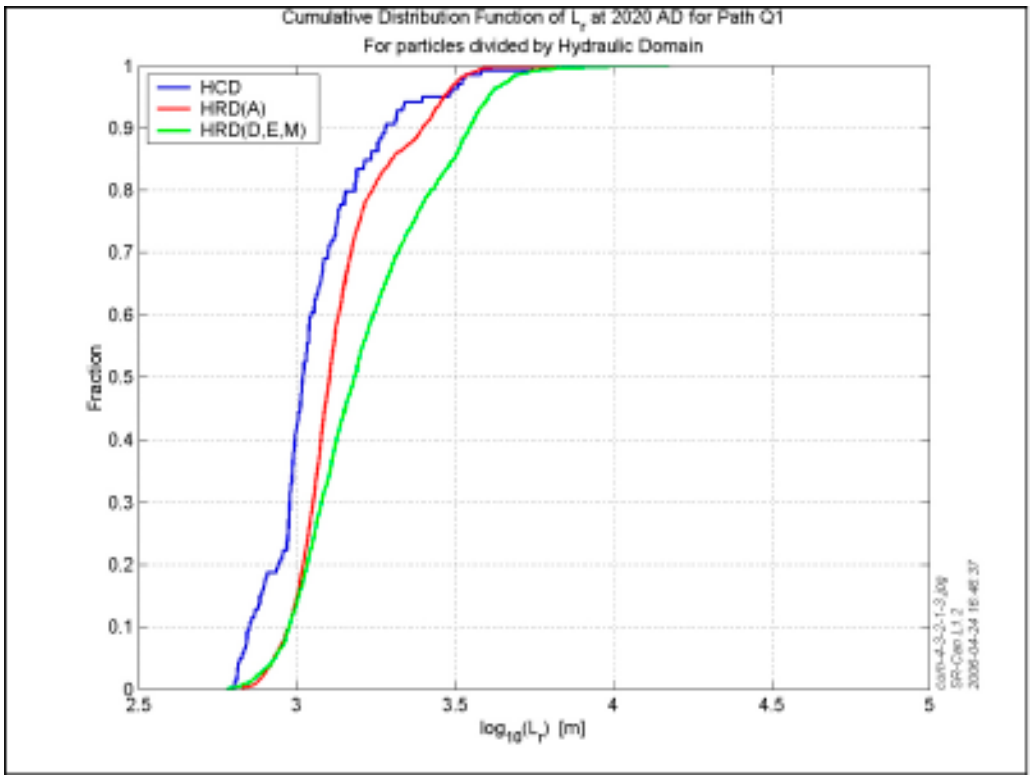

Figure 4-33. *Cumulative distribution plots for path-length in the rock, L_r, for path Q1 in the amalgamated repository-scale and regional-scale DFN models with particles released at 2,020 AD. Here, the total fraction for each rock domain is normalised to 1.*

The path-lengths in the tunnel (Figure 4-34) and in the EDZ (Figure 4-35) indicate a range from less than a metre to about 300 m. For L_T, the distributions for paths Q1 and Q2 are similar, and the median values of the distributions for paths Q1, Q2, and Q3 are all around 10 m, but the path-length in the tunnel is slightly higher for path Q3. The 95th percentile for L_T is only about 70 m. For L_{EDZ}, the distributions for paths Q1, Q2, and Q3 are similar, with median values of around 30 m. The 95th percentile for L_{EDZ} is higher at about 120 m. This suggests that both tunnel and EDZ play their parts as groundwater pathways, but the EDZ has a greater effect in the reference case.

The PM's obtained for different release times were also compared. Key observations are discussed below, using plots of the PM distributions for path Q1 as illustrations.

The travel-time in the rock, t_r, is shown as a histogram for each of the four representative times in Figure 4-36. The corresponding cumulative distribution plots are shown in Figure 4-37. The travel-time varies between about 1 year and 10,000 years. At release time 6,000 BC, the median value is about 240 years. This decreases to about 30 years at release time 2,000 BC, and then increases slightly to about 60 years for 2,020 AD and 6,000 AD. The t_r distributions for the three later release times are flatter than that for release time 6,000 BC and the 5th percentiles are about 4–6 years.

The F-factor in the rock, F_r, is shown as a histogram for each of the four representative times in Figure 4-38. The corresponding cumulative distribution plots are shown in Figure 4-39. Although the shapes of the F-factor distributions are similar for all four release times, the distribution at 6,000 BC has a shorter tail at the lower end of the F_r scale and a higher median of $1.3 \cdot 10^6$ y/m compared to the three later release times, which have median values of about $5 \cdot 10^5$ y/m. Correspondingly, the median of the initial Darcy velocity in the rock, U_r, distribution is lower for 6,000 BC than for the three later release times, as shown by the cumulative distribution plot in Figure 4-40. A clear observation is that the distributions for the three later times are quite similar, suggesting much less sensitivity to the position of the shoreline than in the regional-scale ECPM model – compare with Figure 3-25 to Figure 3-27.

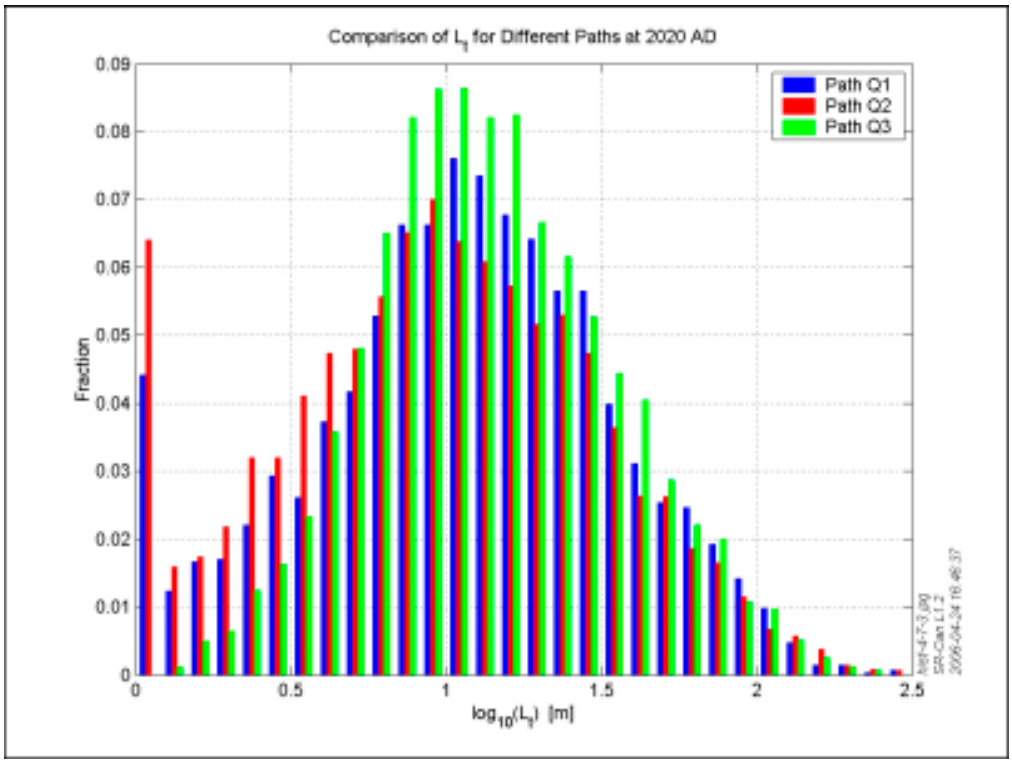

Figure 4-34. *Histograms of path-length in the tunnel, L_t, for the paths Q1, Q2 and Q3 followed by particles released in the amalgamated repository-scale and regional-scale DFN models at time 2,020 AD.*

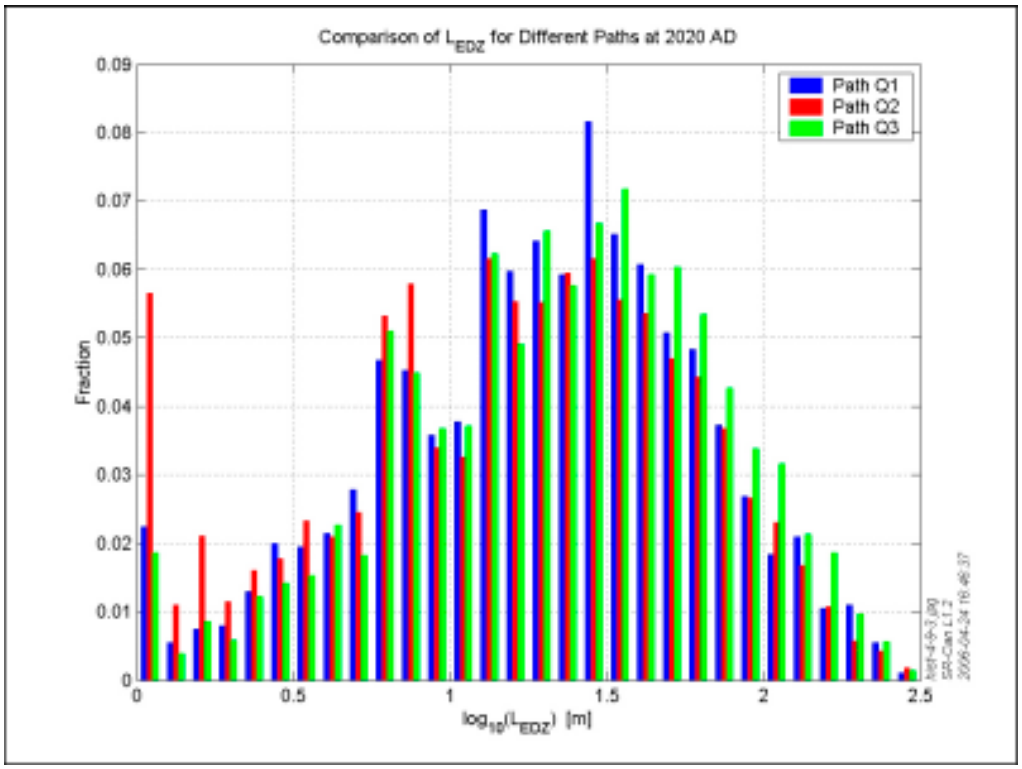

Figure 4-35. *Histograms of path-length in the EDZ , L_{EDZ},for the paths Q1, Q2 and Q3 followed by particles released in the amalgamated repository-scale and regional-scale DFN models at time 2,020 AD.*

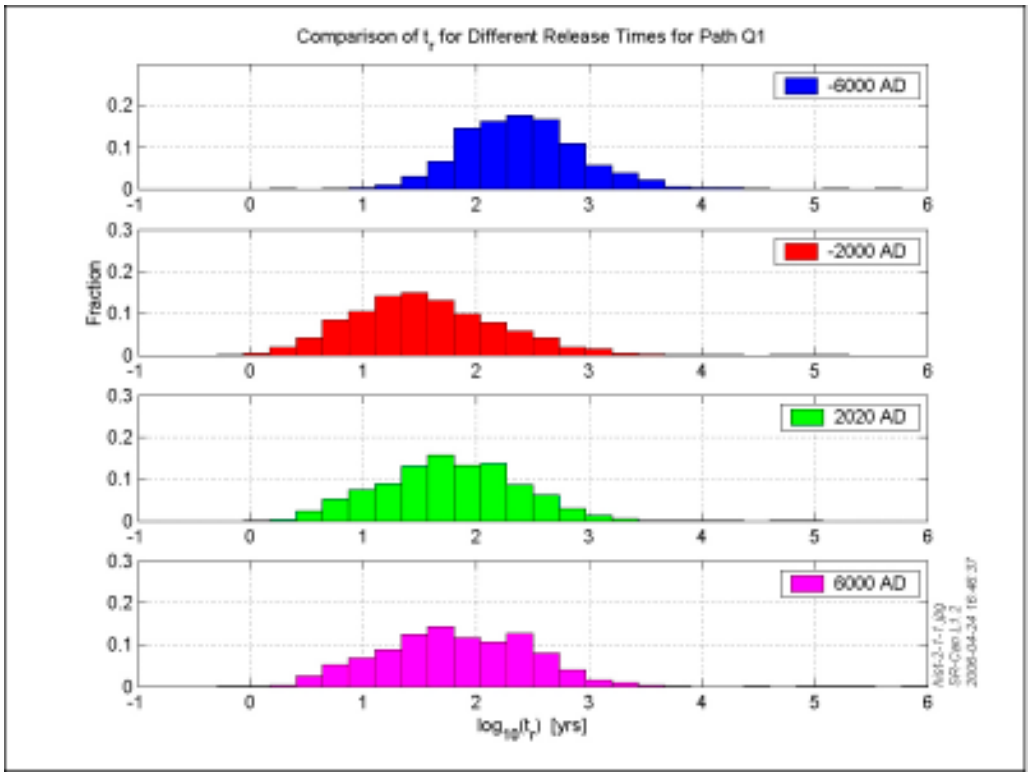

Figure 4-36. *Histograms of the travel-time in the rock, t_r, for the amalgamated repository-scale and regional-scale DFN models with 7,483 particles released at times 6,000 BC, 2,000 BC, 2,020 AD, and 6,000 AD.*

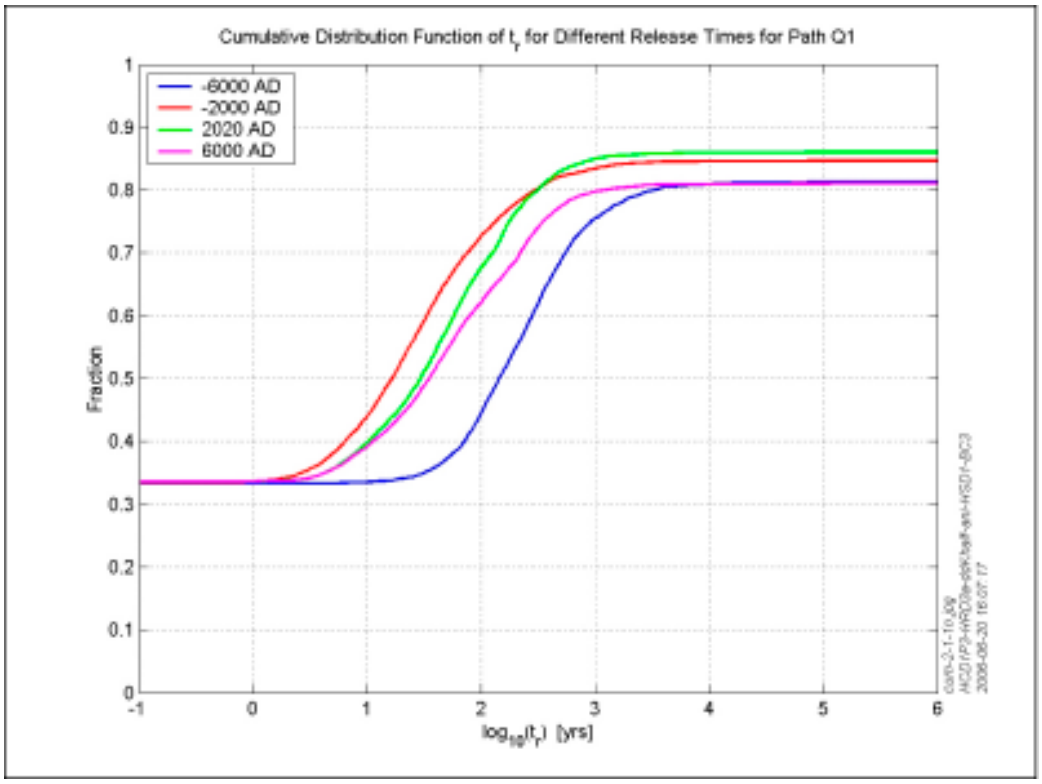

Figure 4-37. *Cumulative distribution plots of travel-time in the rock, t_r, for the amalgamated repository-scale and regional-scale DFN models with 7,483 particles released at times 6,000 BC, 2,000 BC, 2,020 AD, and 6,000 AD.*

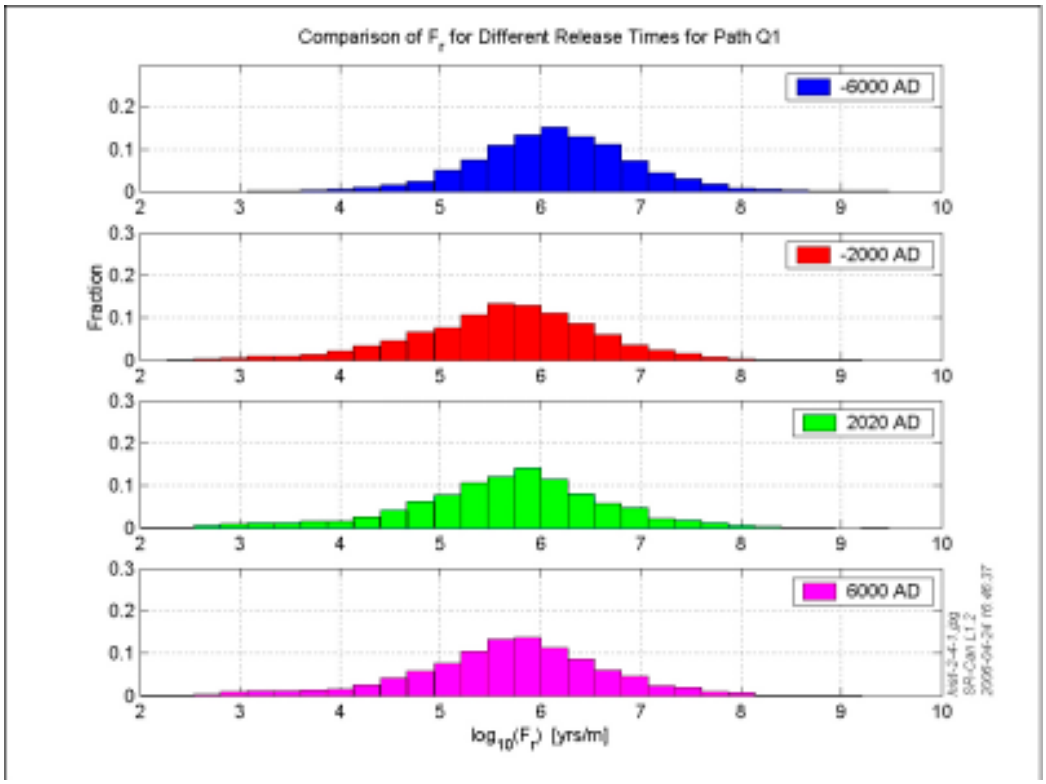

Figure 4-38. *Histograms of the F-factor in the rock, F_r, for the amalgamated repository-scale and regional-scale DFN models with 7,483 particles released at times 6,000 BC, 2,000 BC, 2,020 AD, and 6,000 AD.*

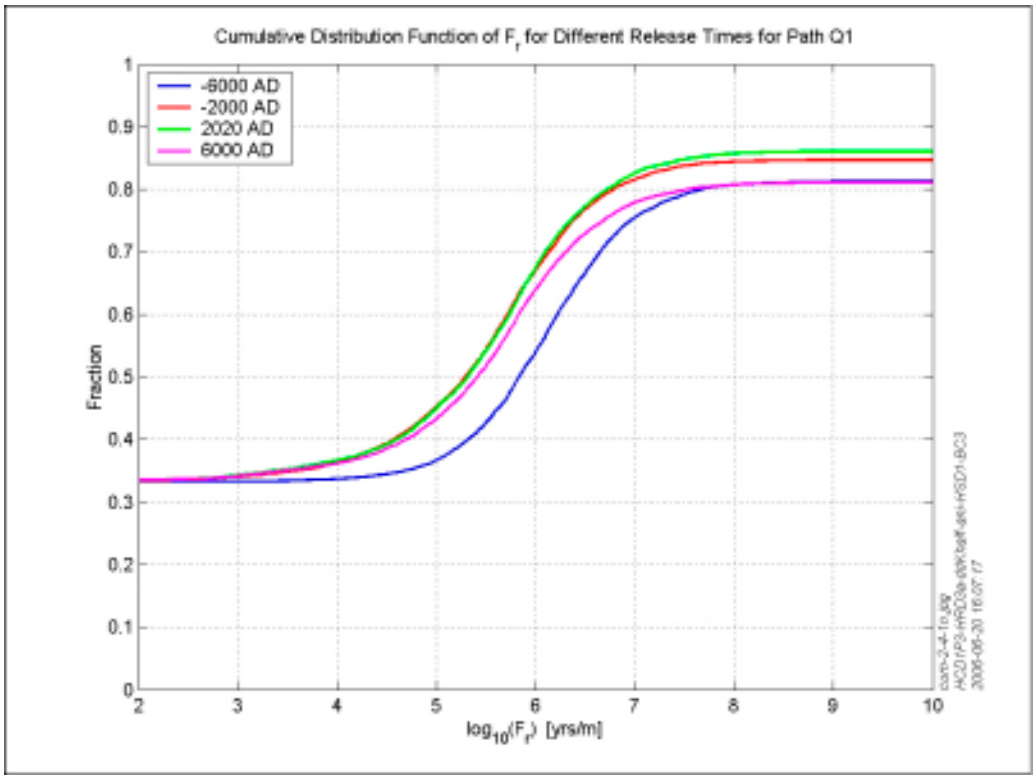

Figure 4-39. *Cumulative distribution plots of F_r for path Q1 in the amalgamated repository-scale and regional-scale DFN models with 7,483 particles released at times 6,000 BC, 2,000 BC, 2,020 AD, and 6,000 AD.*

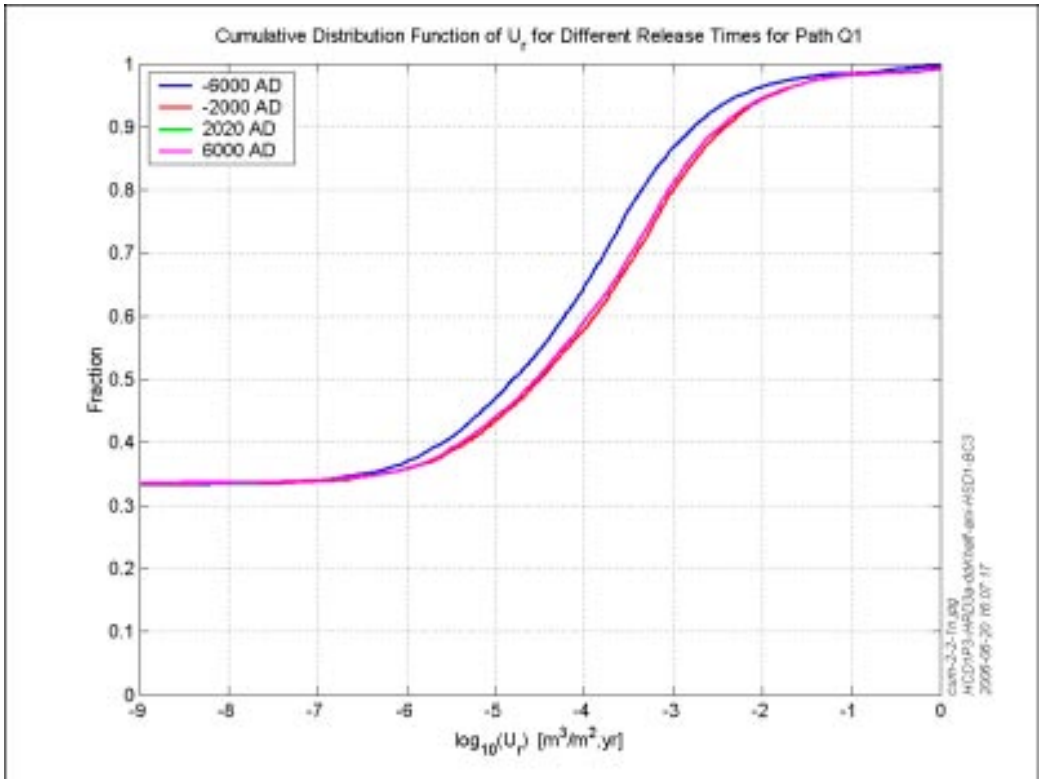

Figure 4-40. *Cumulative distribution plots of U_r for path Q1 in the amalgamated repository-scale and regional-scale DFN models with 7,483 particles released at times 6,000 BC, 2,000 BC, 2,020 AD, and 6,000 AD.*

Path-lengths for all four release times range from a 5th percentile of about 800 m to a 95th percentile of around 3,000 m with a median of around 1,000 m. The path-lengths distributions are less sensitive to the shoreline evolution than for ECPM, even in terms of the 75th–95th percentiles.

A comparison of the PM statistics compiled for the release of particles from the three different hydraulic domains, HCD, HRD(A), and HRD(D,E,M), was performed. The findings are discussed below.

Cumulative distribution plots of travel-time in the rock, t_r, for the Q1 path followed by particles released in the HCD, HRD(A) and HRD(D,E,M), for the four release times are given in Figure 4-41. Comparisons of distributions of travel-time in the rock, t_r, for the different hydraulic rock domains indicate that at release times 6,000 BC and 2,000 BC, particles released in the different hydraulic domains have distributions of similar shape. However, particles released in the HCD have slightly shorter median travel-times compared to those for particles released in HRD(A), which have shorter median travel-times than those for particles released in HRD(D,E,M). For example, at 6,000 BC for path-Q1, the median travel-time for release in the HCD is 130 years, compared to 180 years for release in HRD(A), and 333 years for HRD(D,E,M). At later release times, median travel-times for particles released in the HCD are significantly shorter than those for particles released in the HRD and median travel-times for the two rock domains are closer to each other. For example, at 2,020 AD for path Q1, the

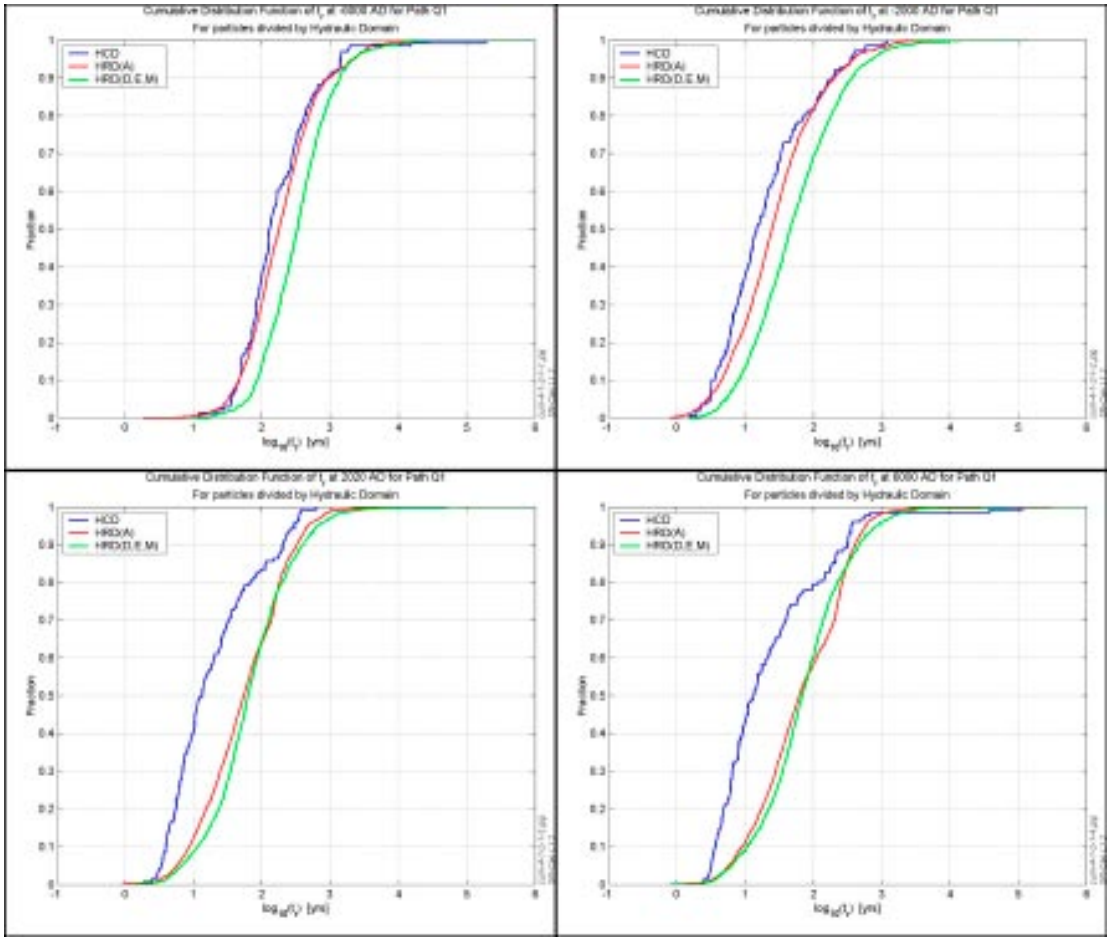

Figure 4-41. *Cumulative distribution plots for travel-time in the rock, t_r, for path Q1 in the amalgamated repository- and regional-scale DFN models with 7,483 particles released at times 6,000 BC, 2,000 BC, 2,020 AD, and 6,000 AD. The total fraction for each rock domain is normalised to 1.*

median travel-time for release in the HCD is 13 years, compared to 55 years for release in HRD(A), and 63 years for HRD(D,E,M). The results would suggest that the hydraulic gradient in the HCD increases after 2,000 BC giving faster travel times.

For all release times, the median F-factor for releases in the HCD is lower than that corresponding to releases in the HRD, and the median F-factor for a release in HRD(A) is lower than that for a release in HRD(D,E,M).

The initial Darcy velocity distributions differ for the paths Q1, Q2, and Q3, as illustrated for release time 2,020 AD in Figure 4-31. For path Q1, and for all release times, the median U_r values for HRD(A) and HCD are similar to each other and higher than that for HRD(D,E,M). For example, for 2,020 AD, the median for HRD(A) is $3.92 \cdot 10^{-4}$ m/y, for the HCD is $5.42 \cdot 10^{-4}$ m/y, and for HRD(D,E,M) is $1.14 \cdot 10^{-4}$ m/y. A similar pattern is observed for all release times for path Q2, although for this path, the distributions for the different hydraulic rock domains are more similar to each other than for path Q1, particularly for the two later release times. For path Q3, the initial Darcy velocity distributions for HRD(A) and HRD(D,E,M) are very similar to each other, but the median value for particles released in the HCD is significantly higher.

Considering the dependence of PM's on the deposition tunnel to which each canister position belongs, the travel-times for the Q1 paths grouped by deposition tunnel are plotted as box plots in Figure 4-42 for release times 6,000 BC and 2,000 BC, and Figure 4-43 for release times 2,020 AD and 6,000 AD. In these box plots, for each tunnel a vertical black line joining the 5th and 95th percentile values for travel-time is plotted, a blue rectangle of arbitrary fixed width is plotted between the 25th and 75th percentile values, and the median is plotted as a single red point. The boxes are necessarily very thin to fit on all deposition tunnels. The repository tunnels are numbered as indicated in Figure 3-35. These plots can be used in conjunction with the plots in Figure 4-30 of the distribution of $\log_{10}(t_r)$ at particle release locations to identify areas of the repository associated with pathlines with the longest and shortest travel-times.

A comparison of the plots for different release times in Figure 4-41 and Figure 4-42 shows that median travel times are in general longer for 6,000 BC than for the three later times. Figure 4-42 shows that at 6,000 BC, tunnels in the southern end of repository subarea 8 have the longest median travel-times and relatively long 95th percentile travel-times. Several tunnels in repository subareas 10 in the south-east and tunnels on the southern side of subarea 7 in the south also have relatively long median travel-times. Tunnels 310 and 322 have median travel-times amongst the highest and relatively high 95th percentile values. The tunnels with the shortest median and 5th percentile travel-times are in subareas 8 and 9, and the northern side of subarea 1. Comparison with the other box plots in Figure 4-42 and Figure 4-43 indicates that at the later release times, there is more variability in the median travel-time between adjacent tunnels compared to release time 6,000 BC. Still, shorter median travel times are found in parts of subareas 2, 3, 5, 8 and 9. All of which correspond with HRD(A). It should also be noted that there is much less variation between tunnels in the DFN model than for the ECPM model in Figure 3-36 and Figure 3-37.

At release time 2,000 BC, the longest median travel-times are for tunnel 502 and several tunnels in the southern part of subarea 1, and as for release time 6,000 BC, the shortest median and 5th percentile travel-times are for tunnels in subarea 8. For all release times, the median travel-time for tunnel 502 is significantly longer than that for adjacent tunnels, and the spread of the travel-time distribution is smaller.

For the two later release times, 2,020 AD and 6,000 AD, the median and 5th percentile travel-times in subarea 8 are again amongst the shortest. However, the tunnels with the shortest median travel-times are in the eastern side of subarea 3. In both cases, several tunnels in southern parts of subareas 1, 8, 9 and in subarea 10 have amongst the longest median travel-times.

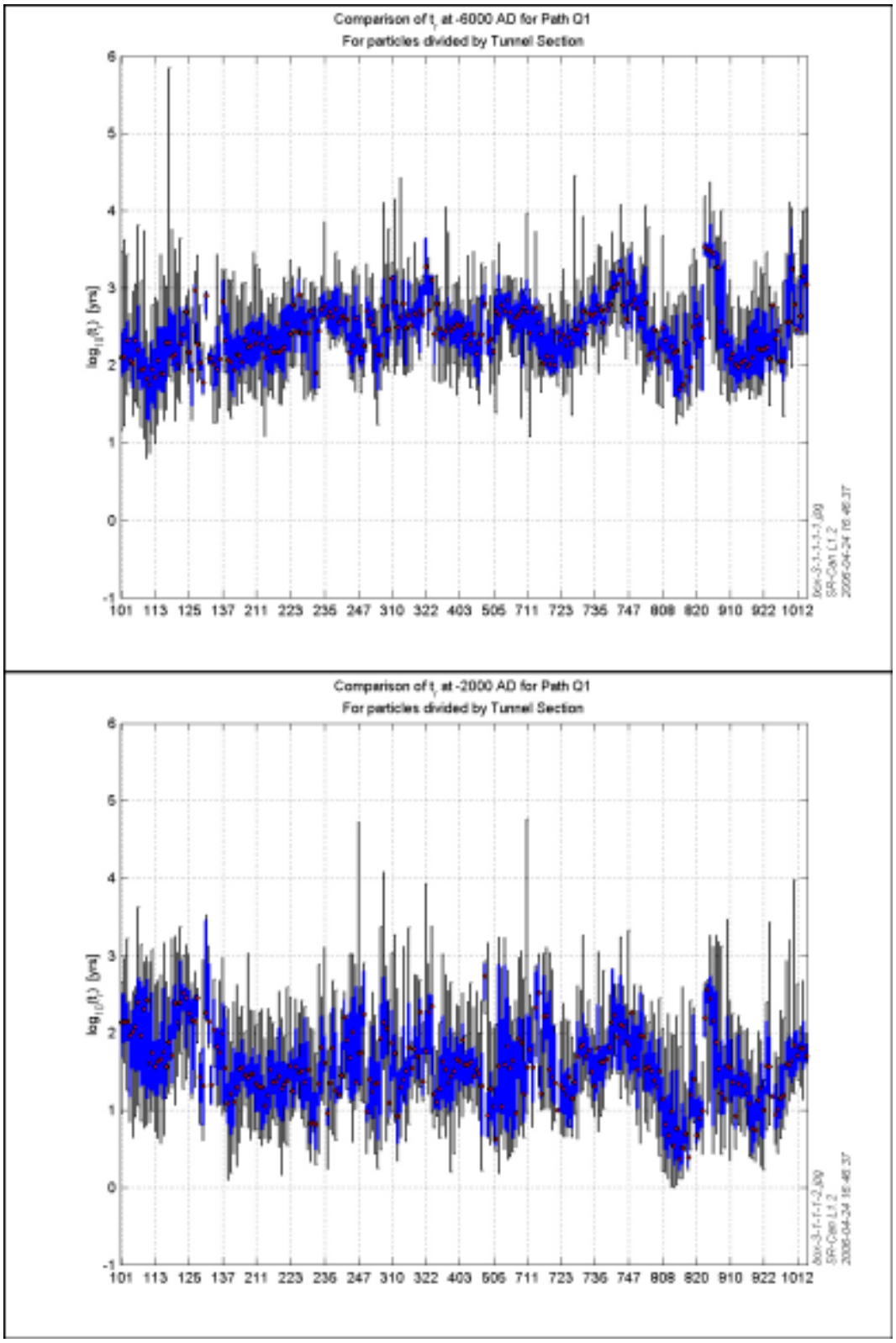

Figure 4-42. *Box plots of travel-time in the rock for the path Q1 followed by 7,483 particles released in the amalgamated repository-scale and regional-scale DFN models at release times 6,000 BC (top) and 2,000 BC (bottom).*

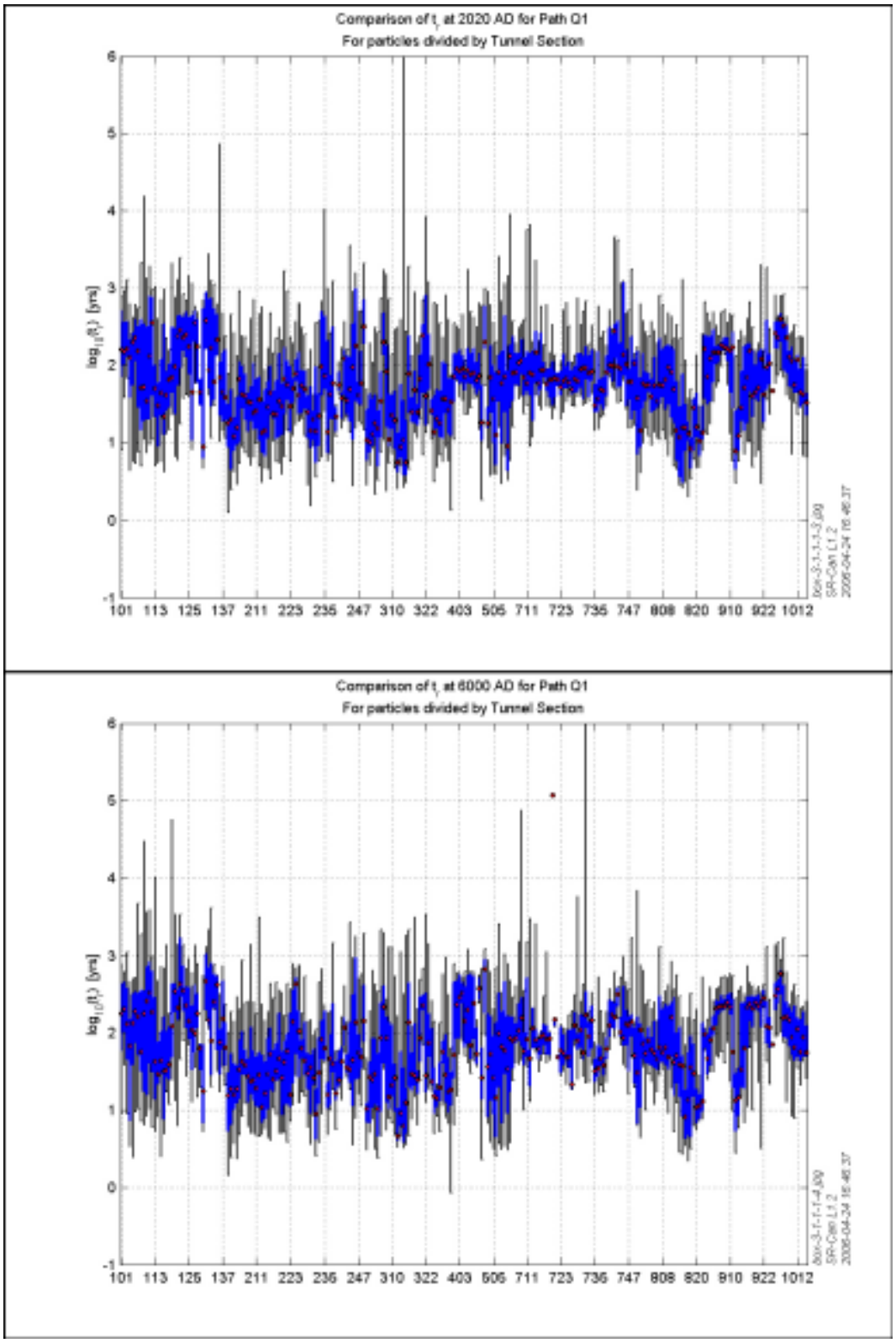

Figure 4-43. *Box plots of travel-time in the rock for the path Q1 followed by 7,483 particles released in the amalgamated repository-scale and regional-scale DFN models at release times 2,020 AD (top) and 6,000 AD (bottom).*

Figure 4-44 shows box plots for initial Darcy velocity for Path Q1 at release time 2,020 AD. This shows that the variability within a tunnel is far greater than the variability between tunnels. The box plots for F-factor reveals more variability between tunnels. Low median F-factors are distributed in subareas 3, 5, 8 and 10.

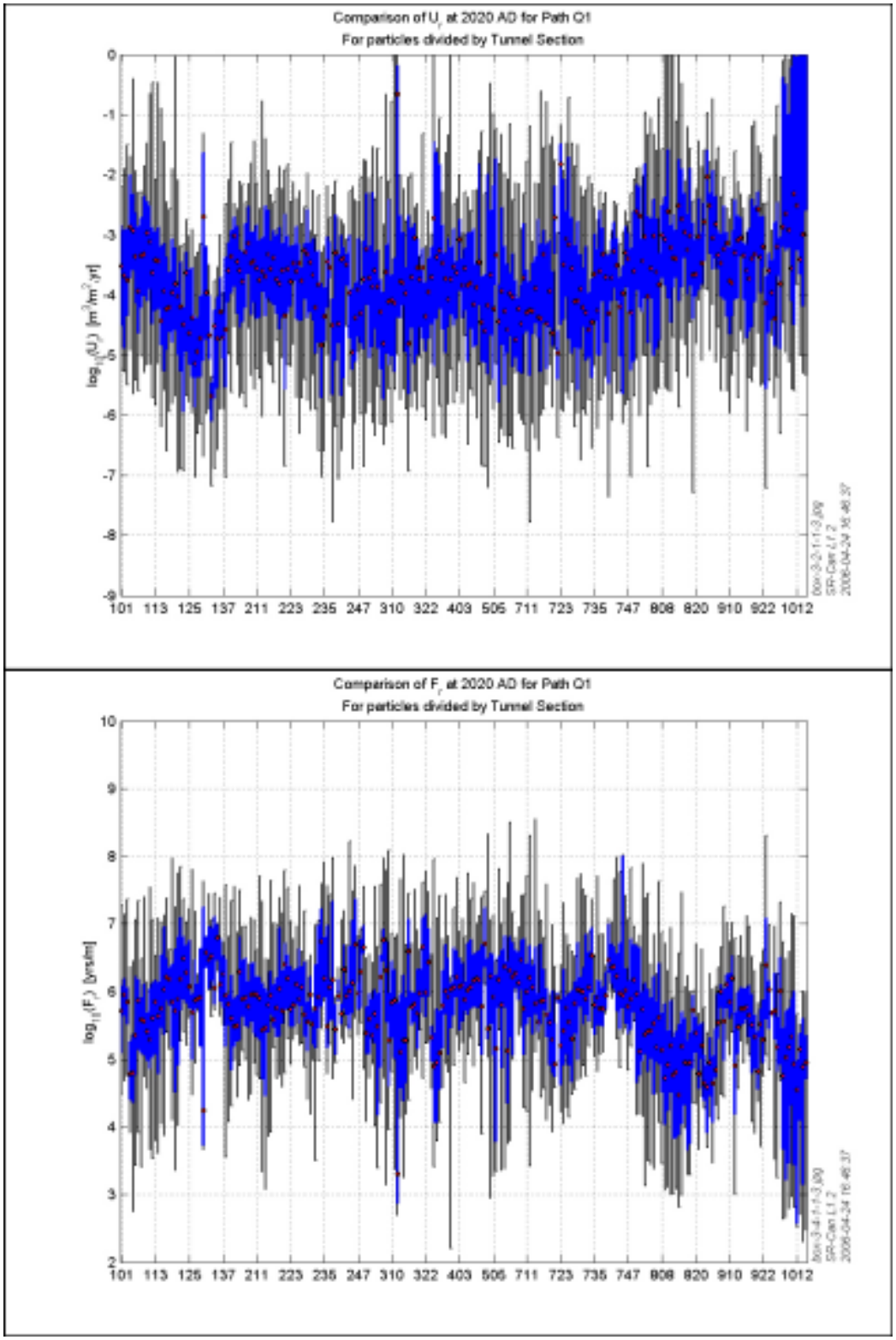

Figure 4-44. *Box plots of U_r (top) and F_r (bottom) in the rock for the path Q1 followed by 7,483 particles released in the amalgamated repository-scale and regional-scale DFN models at 2,020 AD.*

4.5 Variant case: cubic-law transport aperture

This case uses a cubic-law relationship between fracture transport aperture and transmissivity. This change will only affect the travel-time and *Qeq*. Cumulative distribution plots of travel-time for path Q1, path Q2, and path Q3 at release time 2,020 AD are given in Figure 4-45. Compared to the reference case, the median travel-times are slightly shorter. For example, the median travel-time for path-Q1 at 2,020 AD is 57 years for the reference case, and 35 years for the cubic-law transport aperture variant case.

4.6 Variant case: enhanced EDZ

This case has a ten times higher hydraulic conductivity in the EDZ than for the reference case, i.e. $3 \cdot 10^{-7}$ m/s. Cumulative distribution plots of travel-time, initial Darcy velocity and F-factor for path Q1, path Q2, and path Q3 at release time 2,020 AD are given in Figure 4-46. These may be compared to those for the reference case, given in Figure 4-31. The travel-time distributions for this variant are very similar to those for the reference case. For example, the median travel-time for path Q1 at 2,020 AD is 57 years for the reference case, and 51 years for the enhanced EDZ variant case. For the initial Darcy velocity, the distributions obtained for path Q1 from the reference case ($2.5 \cdot 10^{-4}$ m/y) and from this variant case ($2.8 \cdot 10^{-4}$ m/y) are similar. However, for the initial Darcy velocity for the other two paths, path Q2 and path-Q3, the median values ($2.5 \cdot 10^{-3}$ m/y and $2.9 \cdot 10^{-4}$ m/y respectively) are higher compared to the reference case ($4.0 \cdot 10^{-4}$ m/y and $1.1 \cdot 10^{-4}$ m/y respectively) and the path Q2 distribution is now similar to the path Q1 distribution. Cumulative distribution plots of F-factor can be compared with the corresponding figure for the reference case, Figure 4-31, shows that the F-factor distribution is not very sensitive to the increase in conductivity of the EDZ.

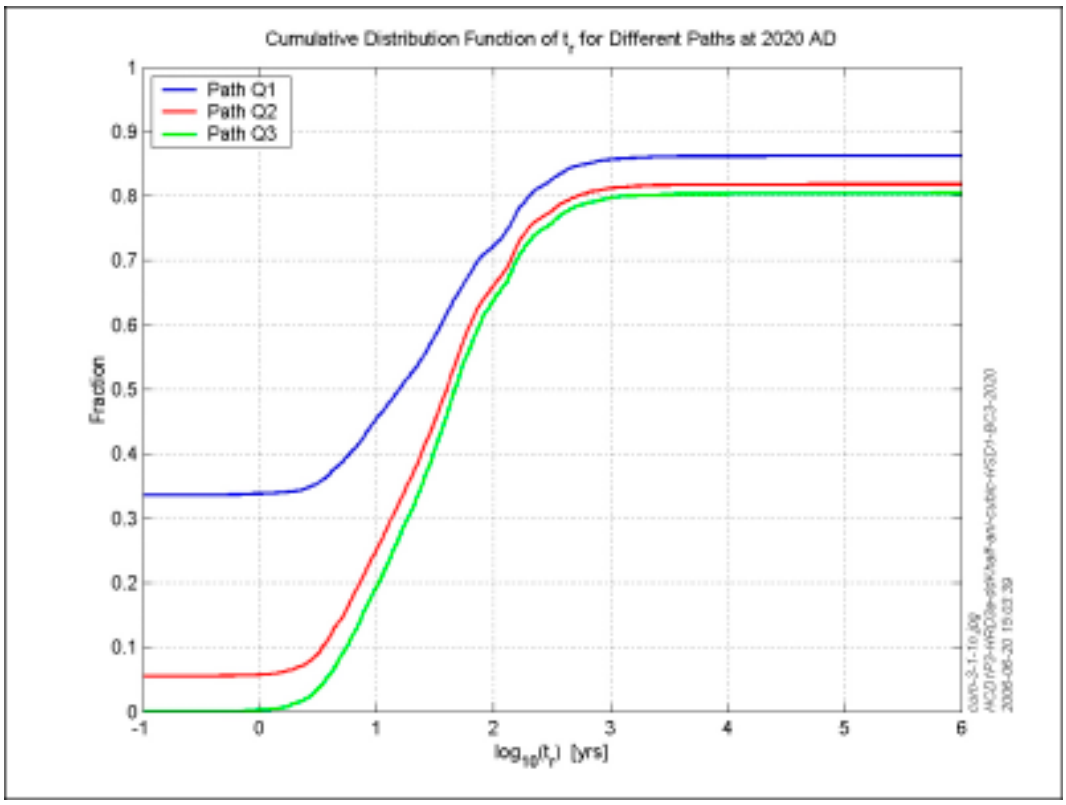

Figure 4-45. *Cumulative distribution plots of travel-time in the rock, t_r, for paths Q1, Q2 and Q3 in the cubic-law transport aperture variant of the amalgamated repository-scale and regional-scale DFN models with 7,483 particles released at time 2,020 AD.*

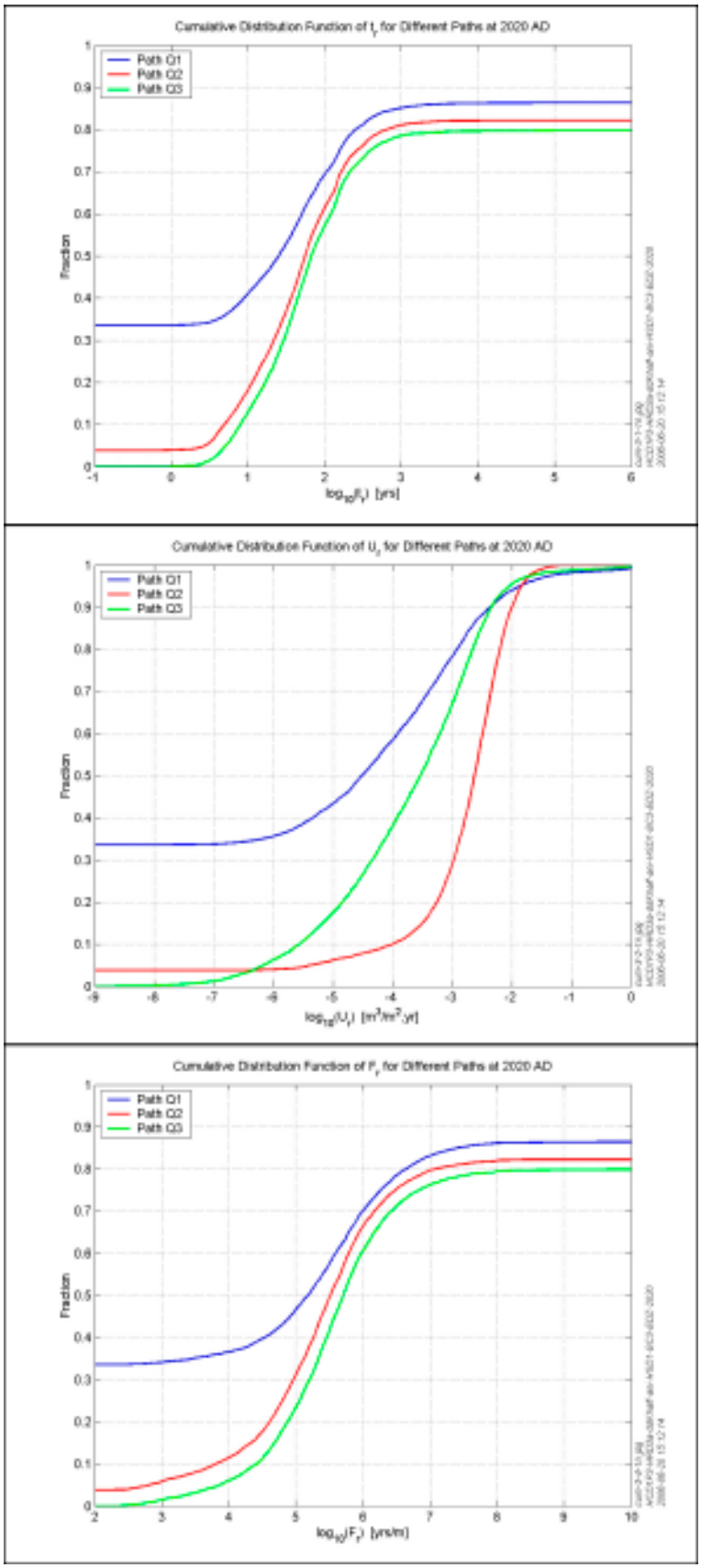

Figure 4-46. *Cumulative distribution plots of travel-time, initial Darcy velocity, and F-factor, in the rock, for paths Q1, Q2 and Q3 in the enhanced EDZ variant of the amalgamated repository-scale and regional-scale DFN models with 7,483 particles released at time 2,020 AD.*

Plots for path-length distribution are given in Figure 4-47 to Figure 4-49. Comparison with the corresponding plots for the reference case in Figure 4-32 to Figure 4-35 shows that for this variant case, the median of the path-length in the tunnel is slightly higher for all paths Q1, Q2,

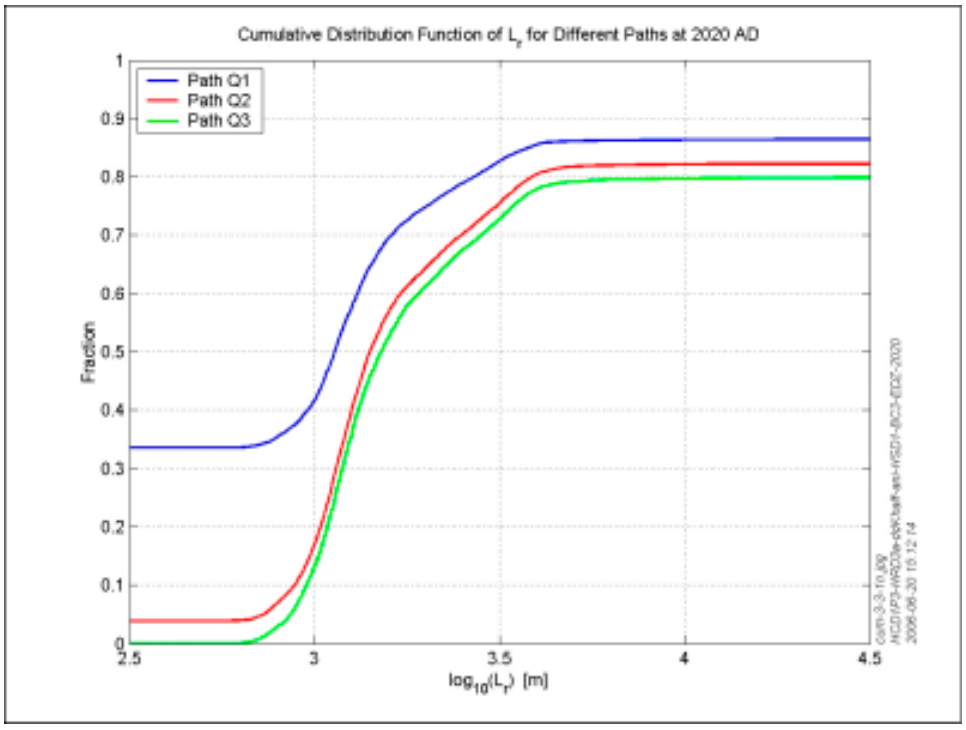

Figure 4-47. *Cumulative distribution plot of path-length in the rock, L_r, for paths Q1, Q2 and Q3 in the enhanced EDZ variant of the amalgamated repository-scale and regional-scale DFN models with 7,483 particles released at time 2,020 AD.*

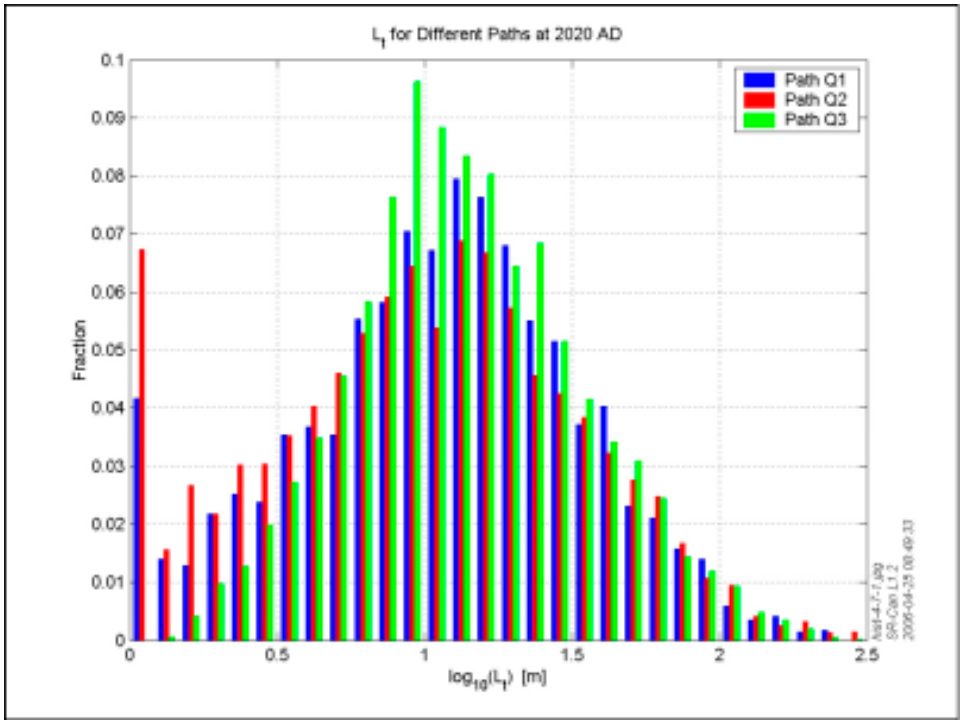

Figure 4-48. *Histograms of path-length in the tunnel, L_t, for paths Q1, Q2 and Q3 in the enhanced EDZ variant of the amalgamated repository-scale and regional-scale DFN models with 7,483 particles released at time 2,020 AD.*

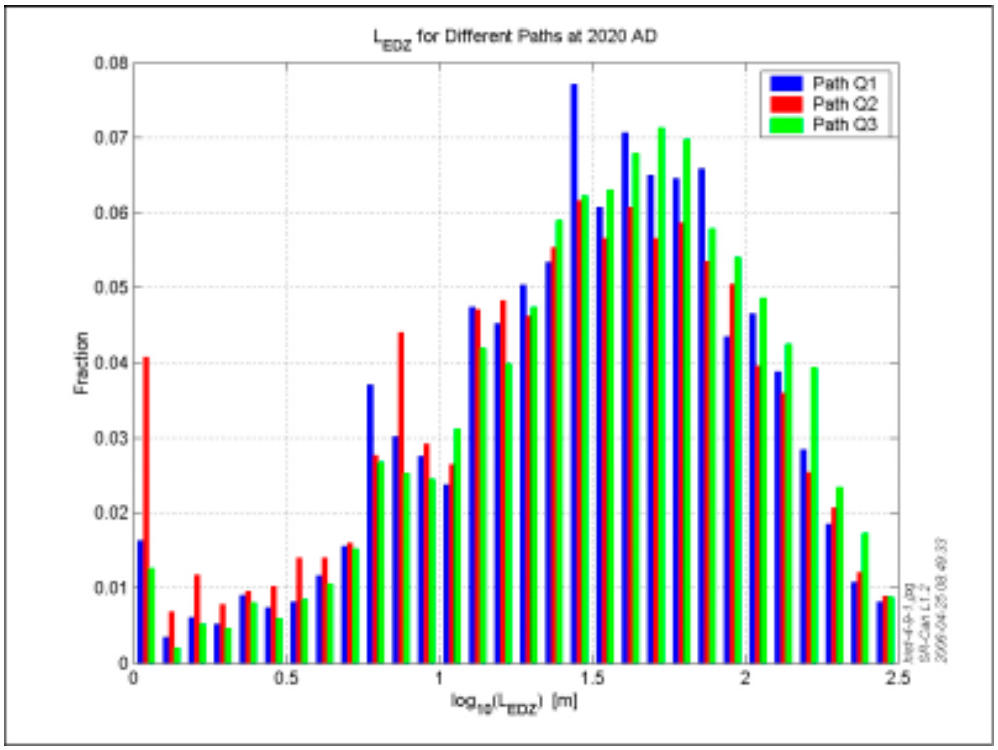

Figure 4-49. *Histograms of path-length in the EDZ, L_{EDZ}, for paths Q1, Q2 and Q3 in the enhanced EDZ variant of the amalgamated repository-scale and regional-scale DFN models with 7,483 particles released at time 2,020 AD.*

and Q3 than in the reference case. For path-lengths in the EDZ, the median is slightly higher for paths Q2 and Q3. Comparing the tables of statistics in Appendix C shows that the median and maximum path-lengths in the EDZ are also slightly longer for this variant case.

4.7 Variant case: degraded backfill in tunnel

This case uses a hundred times higher hydraulic conductivity in the tunnel backfill than the reference case, i.e. 10^{-8} m/s. Cumulative distribution plots for travel-time, initial Darcy velocity and F-factor are given in Figure 4-50. These plots may be compared with those for the reference case (Figure 4-31). The corresponding tables of statistics given in Appendix C for the reference case and for this variant case may also be compared. These comparisons show that for the mean and median values, the travel-times in the rock are slightly shorter for this variant because particles tend to have longer paths in the tunnel, and the Darcy velocities for path Q1 and path Q3 are slightly higher, and F-factors are lower for all three path types by 0.1–0.2 in median, log-space.

Plots for path-length distribution are given in Figure 4-51 to Figure 4-53. Comparison with the corresponding plots for the reference case in Figure 4-32 to Figure 4-35 shows that for this variant case, the median of the path-length in the tunnel is higher for all paths Q1, Q2, and Q3 than in the reference case. From the tables of statistics in Appendix C, the median path-length in the tunnel for this variant is longer than that for the reference case by a factor of just over 2, for example, for path-Q1 the median path-length in the tunnel for the reference case is 12 m, compared to 25 m for the variant case. Thus, even for this pessimistic case for tunnel backfill properties, the tunnel does not have a large effect on SA performance measures.

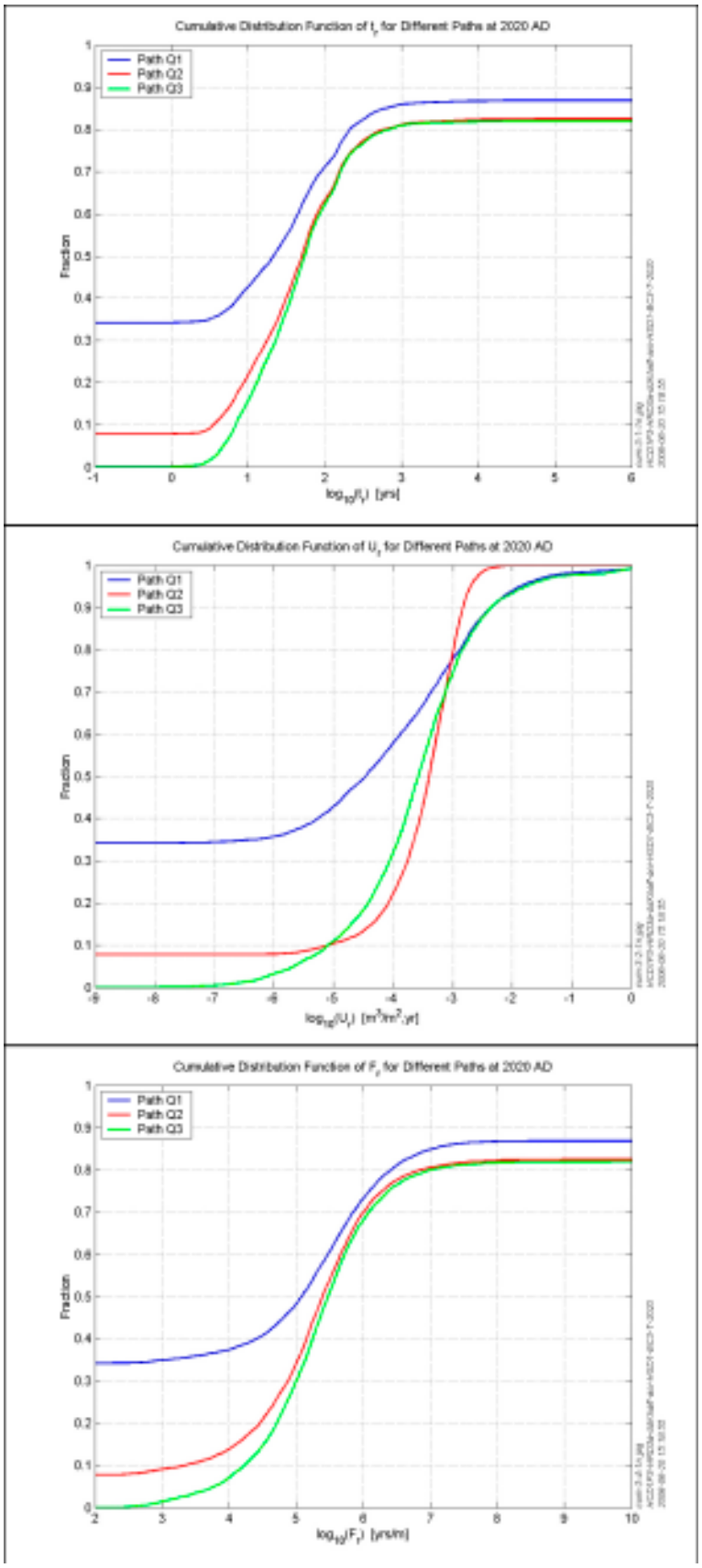

Figure 4-50. *Cumulative distribution plots of travel-time, initial Darcy velocity and F-factor in the rock for paths Q1, Q2 and Q3 in the degraded tunnel variant of the amalgamated repository-scale and regional-scale DFN models with 7,483 particles released at time 2,020 AD.*

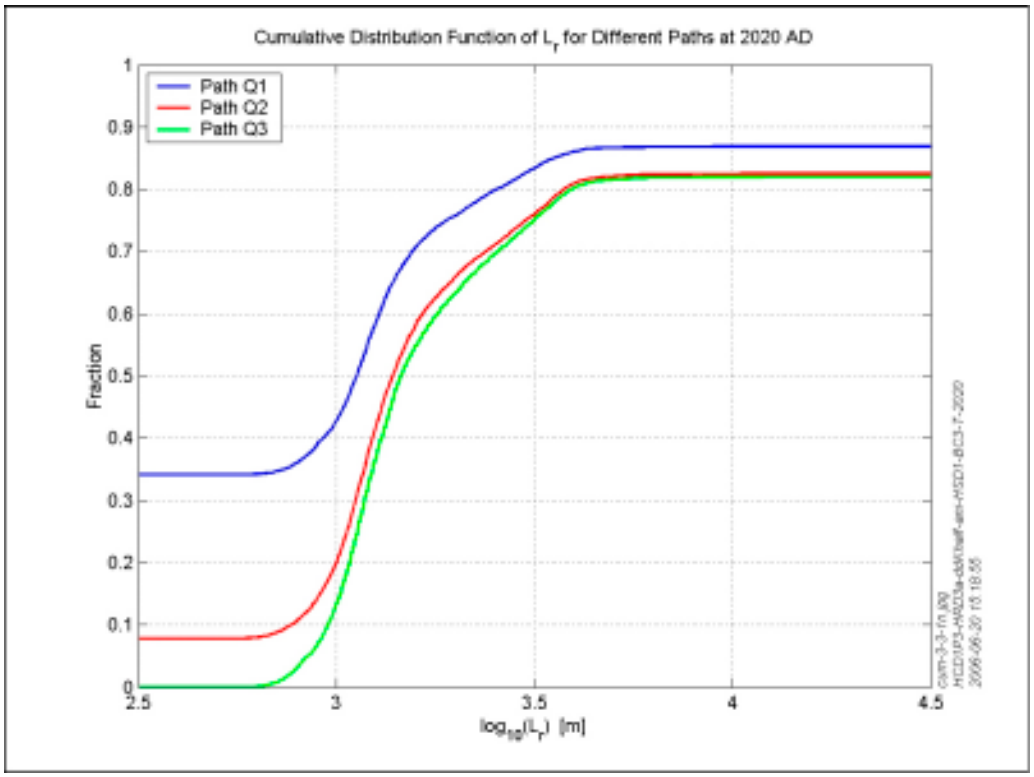

Figure 4-51. *Cumulative distribution plot of path-length in the rock, L_r, for paths Q1, Q2 and Q3 in the degraded tunnel variant amalgamated repository-scale and regional-scale DFN models with 7,483 particles released at time 2,020 AD.*

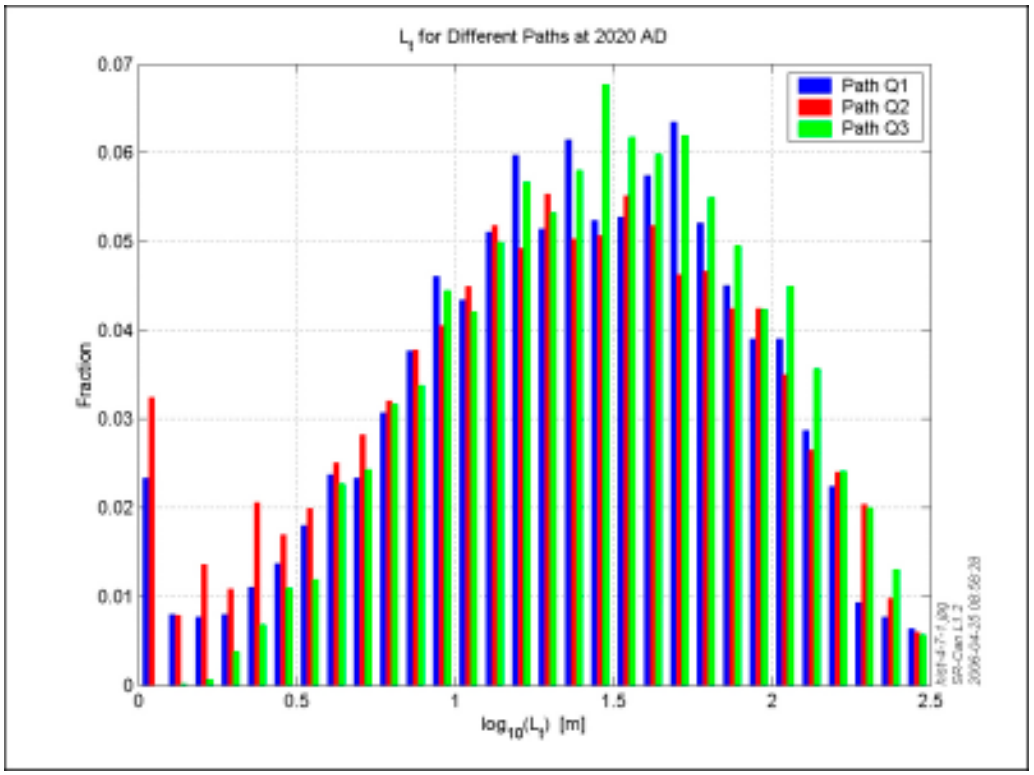

Figure 4-52. *Histograms of path-length in the tunnel, L_t, for paths Q1, Q2 and Q3 in the degraded tunnel variant of the amalgamated repository-scale and regional-scale DFN models with 7,483 particles released at time 2,020 AD.*

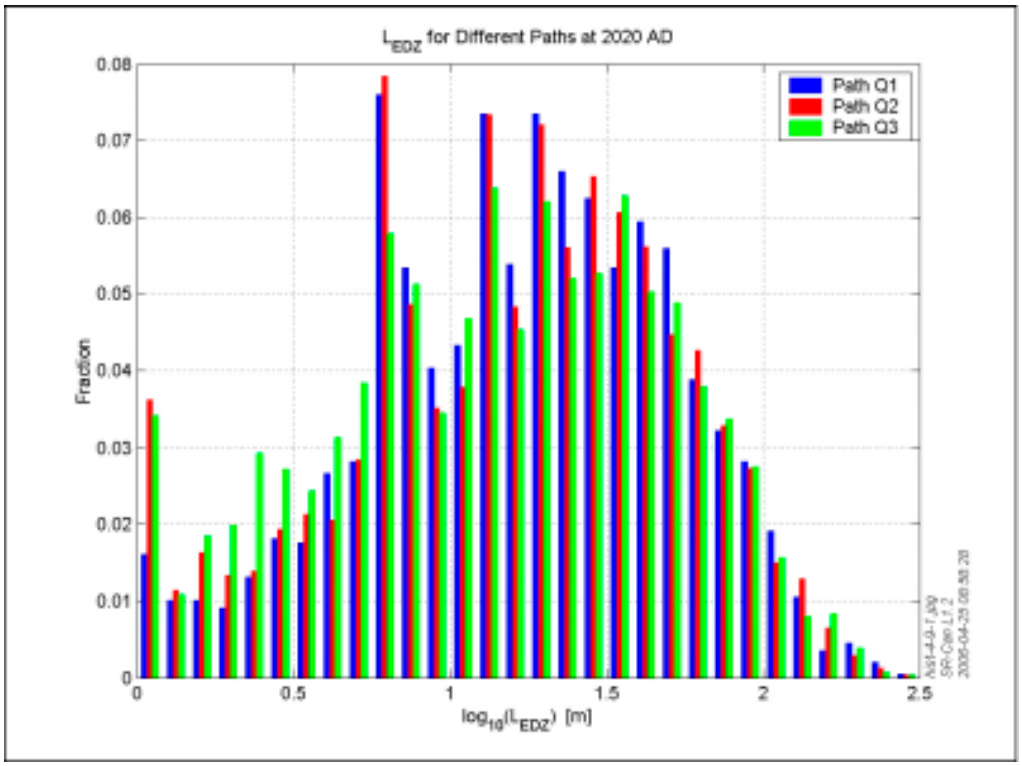

Figure 4-53. *Histograms of path-length in the EDZ, L_{EDZ}, for paths Q1, Q2 and Q3 in the degraded tunnel variant of the amalgamated repository-scale and regional-scale DFN models with 7,483 particles released at time 2,020 AD.*

4.8 Variant case: DFN anisotropy

In this case tens time higher transmissivity is assigned to the sub-vertical Set_C oriented parallel to the maximum horizontal stress. This case was identified as the least favourable of the sensitivities considered in the ECPM modelling, see Section 3.4.2. However, it is perhaps overly pessimistic, since the predicted salinity profile in Section 3.4.3 at depth in the Laxemar subarea is much deeper than field data would suggest, which points to the model variant having too high a hydraulic conductivity. The PM's for this case are shown in Figure 4-54. Median travel times are slightly shorter e.g. pathQ1 $\log(t_r)$ is 1.69 compared to 1.77 for the reference case. Initial velocities are about 0.2 higher, and F-factor statistics are about 0.2 lower in log-space.

4.9 Variant case: correlated transmissivity model

The performance measure statistics for this variant case are very similar to those for the reference case as can be seen in Appendix C. The statistics only change by 0.1 in log-space.

4.10 Deposition hole rejection criteria

All the statistics given in the above sections are based on an ensemble over all 7,483 deposition hole locations. However, in practice some deposition holes will not be excavated to avoid areas that may have an adverse effect on repository performance. Such a decision will be based on two main criteria. The first is that a deposition hole will not be constructed directly beneath a fracture sufficiently large to cross-cut the full perimeter of the deposition tunnel face. This full perimeter intersection (FPC) criterion is to avoid large sub-vertical fractures that have a higher

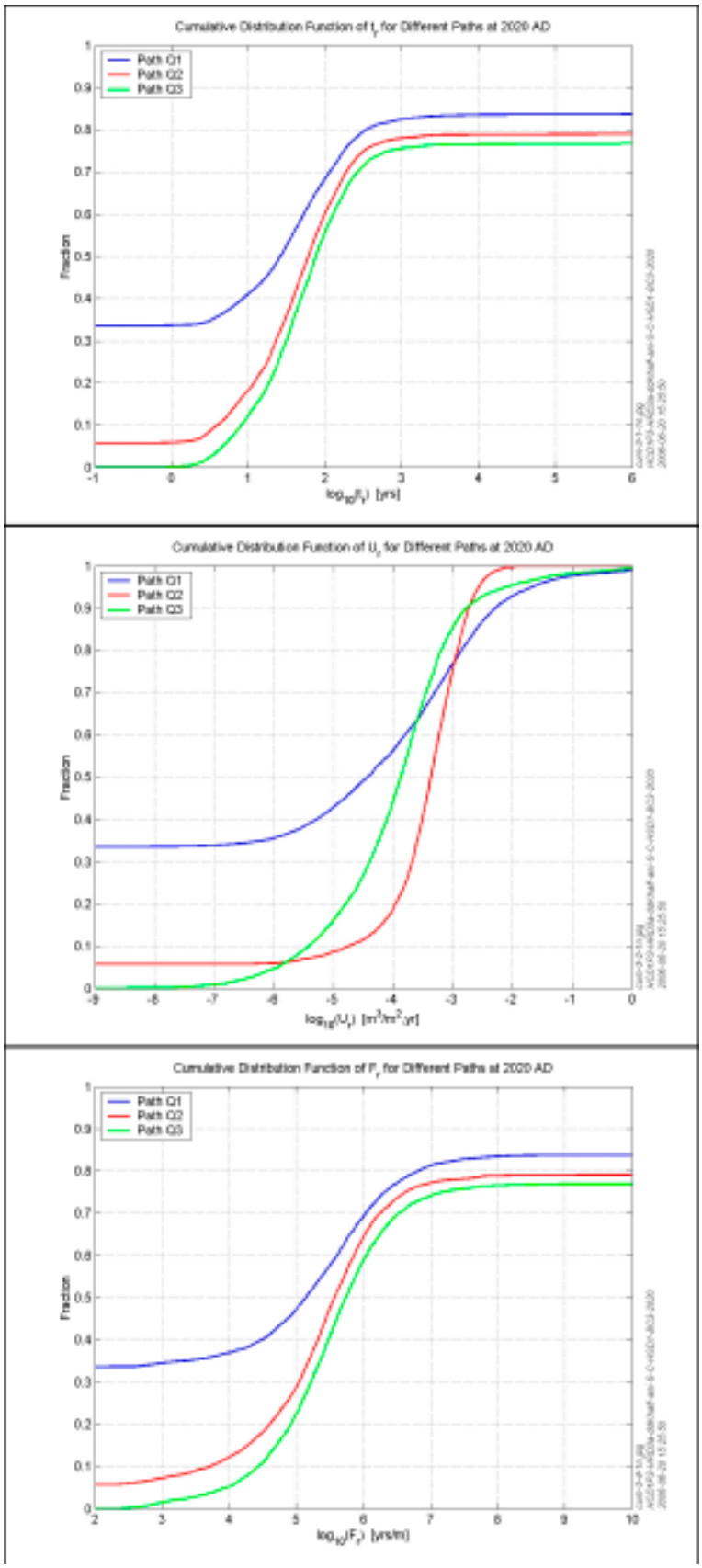

Figure 4-54. *Cumulative distribution plots of travel-time, initial Darcy velocity and F-factor in the rock for paths Q1, Q2 and Q3 in the Set_C anisotropy variant of the amalgamated repository-scale and regional-scale DFN models with 7,483 particles released at time 2,020 AD.*

probability of carrying relatively large groundwater flows. If the location passes this first criterion, then a probe hole will be drilled to check whether there is a transmissive sub-horizontal fracture intersecting the trajectory of the deposition hole based on some type of hydraulic test in the probe hole. This deposition hole screening process is likely to eliminate many of the less favourable locations, and hence improve repository performance. The impact may be quantified by simulating this process using the repository-scale DFN models developed in this section.

An algorithm was used to post-process the DFN models and create three extra columns in the performance measures for each deposition hole location. The first column records whether a fracture that cuts the deposition hole also cross-cuts all four sides of the deposition tunnel above. The second column gives the linear side length of the largest fracture intersecting the deposition hole, and the final column gives the transmissivity of the most transmissive fractures intersecting the deposition hole. Here, the deposition tunnel is approximated as having a square cross-section.

In more detail, the algorithm is implemented as follows:

a) Loop over all the deposition holes.

b) For each deposition hole, firstly identify the corresponding deposition tunnel and second determine all the fractures that intersect the hole.

c) For each fracture that intersects the deposition hole determine:
   1) Is the fracture a deterministic deformation zone? If "Yes", write a "2" in the first column of the output file and "1000.0" (a generic length) in the second column.
   2) Is the fracture associated with the EDZ? If "Yes", skip the fracture. In particular, do not include the fracture when determining the maximum fracture size for fractures that intersect the deposition hole.

3) The fracture properties. Since the centre and edge vectors of the rectangular fracture plane are require to calculate whether the fracture intersects the full perimeter of the tunnel, and the length and transmissivity are also of interest.

d) Does the fracture cross-cut the deposition tunnel? If at least one of the fractures intersecting the deposition hole cross-cuts the deposition tunnel, then the deposition hole is marked as failing the full perimeter criterion (FPC).

e) Calculate the linear length of the largest fracture intersecting the deposition hole. This is set to zero if no fractures intersect the deposition hole.

f) Calculate the transmissivity of the most transmissive fracture intersecting the deposition hole.

The FPC, fracture length, and fracture transmissivity values derived for each deposition hole are used to with the performance assessment to simulate engineering criteria used to reject deposition holes and assess how this process impacts on risk. Two criteria were considered. The first is based on FPC only, and the second is based on both FPC and whether the transmissivity is greater than 10^{-6} m^2/s.

The results of applying the deposition hole rejection criteria are presented in Table 4-3 below in terms of remaining deposition hole positions.

In the table it is seen that the FPC criterion for both correlation cases results in more deposition locations being removed than using the only the hydraulic condition $T > 10^{-6}$ m^2/s criterion. A lower threshold of $T > 10^{-7}$ m^2/s results in comparable or more locations being removed than using the FPC alone. Furthermore, combining the FPC and $T > 10^{-6}$ m^2/s criterion has a minor effect relative to using the FPC criterion alone. If lower transmissivity thresholds are used, these dominate the screening and the FPC has a minor effect on the number of rejected deposition locations.

Table 4-3. Calculated percentage of remaining deposition positions using various rejection criteria. The total number of deposition holes is 7,483.

Rejection criterion	Remaining percentage of deposition holes after rejection criteria [%]							
	Excluding only deposition holes intersected by low confidence zones	FPC	T > 10^{-6} m²/s	T > 10^{-7} m²/s	T > 10^{-8} m²/s	FPC and T > 10^{-6} m²/s	FPC and T > 10^{-7} m²/s	FPC and T > 10^{-8} m²/s
Base case DFN (semi-correlated)	99.8	90	96	78	46	88	74	45
DFN with fully correlated (T vs. r)	99.8	90	97	91	62	89	86	61

Applying the FPC criterion or combined FPC and $T > 10^{-6}$ m²/s criterion results in somewhat shifted Q_{eq} and F-factor distributions for the Q1 path as shown for Laxemar conditions in Figure 4-55 and Figure 4-56 below. Specifically, the Q_{eq} distribution shows that the highest flow rates are removed from the distribution, whereas the F distribution shows a shift to higher values by slightly less than half a unit in log space. The difference between applying the FPC criterion alone or in combination with the $T > 10^{-6}$ m²/s criterion has a minor effect as indicated already by Table 4-3. Hence, based on the current fracture model, the FPC criterion seems to be a sufficient test for screening out the worst deposition hole locations.

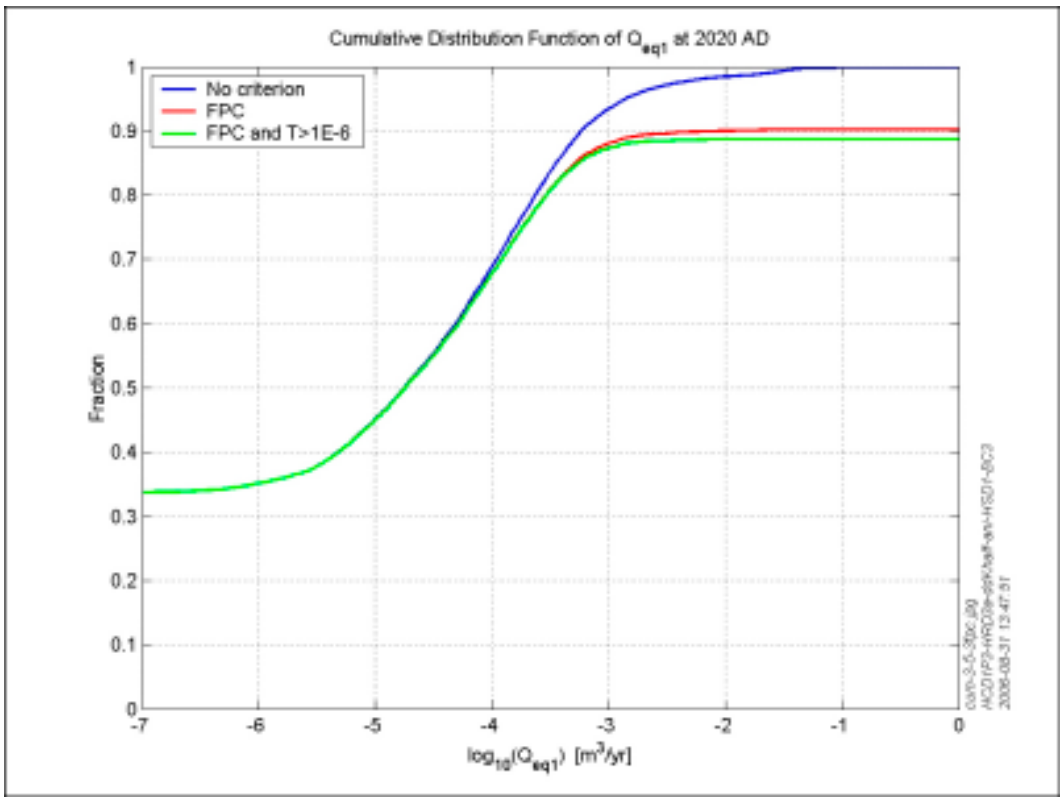

Figure 4-55. *Comparison of cumulative distribution plots of Qeq for path Q1 in the amalgamated Laxemar repository and regional-scale models with 7,483 particles released at time 2,020 AD based on different deposition hole rejection criteria.*

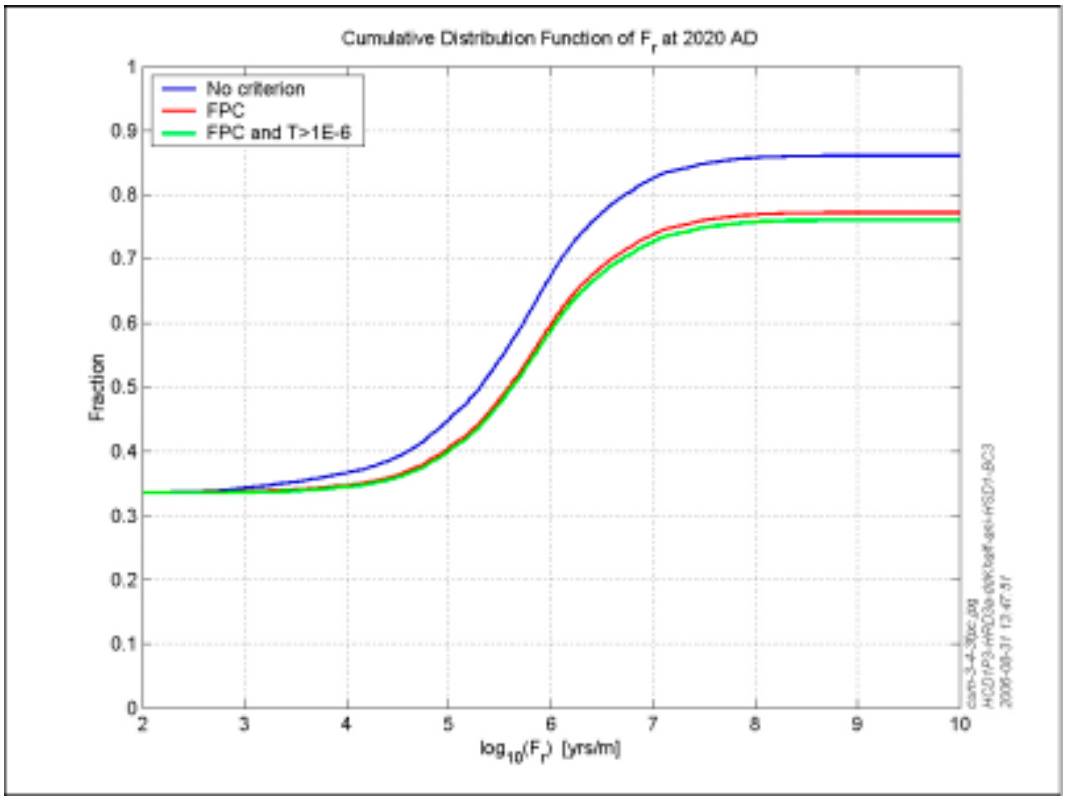

Figure 4-56. *Comparison of cumulative distribution plots of F_r for path Q1 in the amalgamated Laxemar repository and regional-scale models with 7,483 particles released at time 2,020 AD based on different deposition hole rejection criteria.*

4.11 Discussion

Detailed repository-scale models have been used to derive near-field and far-field performance measures for input to SA calculations. A DFN conceptual model has been applied to represent the entire repository and flow in the bedrock around each deposition hole down to the scale of a few metres or less. As an advance on the methodology used in the interim SR-Can assessment, variable-density flow calculations have been implemented in DFN models so that the effects of buoyancy-driven flow due to the presence of salinity are represented consistently within both DFN and ECPM models of the site. Since the SA calculations use a stream-tube concept for the far-field modelling in FARF31, groundwater flow and flow-paths are calculated at an appropriate series of representative times with boundary conditions and the salinity distribution being interpolated on to the steady-sate repository-scale models from ECPM transient regional-scale coupled groundwater flow and salt transport models based on a consistent underlying DFN.

The use of a DFN conceptual model offers a number advantages in calculating SA performance measures compared to the ECPM model used in Section 3. Firstly, the potential retention due to sorption and RMD, as quantified by the F-factor, is represented in a more natural way since the fracture surface contact area is recorded explicitly along flow-paths. Secondly, heterogeneity in the bedrock properties due to variability in fracture properties and spatial distribution can be captured in detail within a DFN model. Also, since the bedrock is relatively sparsely connected, characteristics of flow and transport such as restricted connectivity and focussing of flow into repository structures or large deformation zones can be represented realistically, while continuum models need to homogenise flow much more.

In terms of the SA performance measures for a release at 2,020 AD, the DFN model predicts travels times with a median about 60 years; initial velocity has a median around $2 \cdot 10^{-4}$ m/y with a standard deviation of 1.3 orders of magnitude in log space; the F-factor has a median of $5.4 \cdot 10^{5}$ y/m with a standard deviation of about 1.0 in log-space. At later times in the future, the performance measures are very similar. At 2,000 BC the performance measures are less favourable with a median travel time of 32 years, median initial velocity of $3 \cdot 10^{-4}$ m/y and an F-factor of $4.8 \cdot 10^{5}$ y/m. At 6,000 BC when the site is covered by a shallow sea, the performance measures are the best.

Particles are released from three points around each canister position to provide equivalent flow rates for the near-field (COMP23) SA models, and transport statistics along the pathway to the surface for input to far-field (FAR31) SA models. The release points give the three paths: Q1, a release in a fracture abutting the deposition hole; Q2, a release point in the EDZ at the top of the deposition hole; Q3, a release in the tunnel above the canister.

The DFN is sparsely connected, especially in hydraulic rock domain HRD(D, E, M), and so there is not always an advective pathway through a fracture that intersects the deposition holes via the fracture network to the surface. Overall, about 34% of deposition holes are not intersected by a connected fracture, and a further 11% are in areas of stagnant flow without a connected path away from the canister. Only about 3% of particles become stuck due to mass balance problems in the numerical solution. This leaves about 52% of deposition holes that have a Q1 path, i.e. a path to the surface via an intersecting fracture. Of these, only about 47% of canisters are intersected by a connected fracture above the PFL detection limit of around 10^{-9} m^2/s. For the releases in the EDZ and the tunnel, Q2 and Q3, about 10% of particles remain close to the repository due to stagnant flow, and over 80% make it to the surface of the model. The reason there are areas of stagnant flow in the tunnel and EDZ is that the end of each deposition tunnel opposite the main tunnel is essentially a dead-end. That is, to get advection along or out of the tunnel there must be a head gradient along it, which requires that at least two moderate to large water-bearing fractures intersect the tunnel, and the portion outside of these connections is subject to stagnant flow conditions. Travel-time and F-factor are almost identical for each of the release points around the canister, which suggests that the flow-path is the same for each release point and that flow does not diverge down different flow conduits around the repository. Considering the individual rock domains, HRD(A) has 74% of deposition holes with an advective Q1 path to the surface via an adjoining fracture, while HRD(D, E, M) has only 40%.

Generally flow-paths tend to be focussed toward the deterministic deformation zones and the larger stochastic fractures since these are more connected, have higher transmissivity, and hence carry more flow. Typically, there are few long horizontal flow-paths that discharge away from the site area. This is due to the limited horizontal connectivity and geometry of the fracture network. One exception is the gently northward dipping and extensive zone ZSMEW007A that outcrops in the centre of the repository, which provides a shallow but long horizontal flow-path running west to east. This is interesting since it suggests major sub-horizontal deformation zones could have a significant positive impact on radionuclide transport making flow-paths longer, whereas sub-vertical deformation zones tend to have the negative impact of shortening flow-paths. One clear characteristic of this overall picture of path trajectories is the greater dispersion of paths in the northern and eastern parts of the repository which correspond with rock domain HRD(A) compared with the southern part where particles concentrate on a small number of discrete conduits in rock domain HRD(D, E, M). The cause is the difference in fracture connectivity. In HRD(A) the network is relatively connected, so particles tend to be dispersed through the many connections through the network, while in HRD(D, E, M), particles tend to follow the tunnel or EDZ before they find a connection to a handful of deformation zones or large stochastic fractures that provide the only connections to the surface.

Particles are released in three hydraulic rock domains: HRD(A) in the north and east of the repository, HRD(D, E, M) in the south and west, and 3% in low confidence HCD. Comparing performance measures for these 3 different rock domains, travel-time in the rock indicates that at release times 6,000 BC and 2,000 BC, particles released in the different hydraulic domains have distributions of similar shape. However, particles released in the HCD have slightly shorter median travel-times compared to those for particles released in HRD(A), which have shorter median travel-times than those for particles released in HRD(D,E,M). For example, at 6,000 BC for path Q1, the median travel-time for release in the HCD is 130 years, compared to 180 years for release in HRD(A), and 333 years for HRD(D,E,M). At later release times, median travel-times for particles released in the HCD are significantly shorter than those for particles released in the HRD and median travel-times for the two rock domains are closer to each other. For example, at 2,020 AD for path Q1, the median travel-time for release in the HCD is 13 years, compared to 55 years for release in HRD(A), and 63 years for HRD(D,E,M). The results would suggest that the hydraulic gradient in the HCD increases after 2,000 BC giving faster travel times. For all release times, the median F-factor for releases in the HCD is lower than that corresponding to releases in the HRD, and the median F-factor for a release in HRD(A) is lower than that for a release in HRD(D,E,M).

Sensitivities to the tunnel and EDZ properties have been considered as well as the relationship used between fracture transmissivity and size. The sensitivity of the performance measures in the rock to backfill and EDZ properties is relatively small since the results suggest that flow-paths are not channelled sufficiently by the repository for it to form a complete groundwater pathway to the surface. This is because the larger fractures and deformation zones although sparsely distributed within the candidate area, still have a much higher groundwater flow capacity than the repository. Even in the pessimistic variants the 90th percentile for the distance in the EDZ or tunnel is about 100 m, so at worst it only provides a short-cut from the deposition hole to the fracture system about 1 tunnels length away. This suggests flow tends to be limited by what the fracture system can supply and paths have to leave the tunnel or EDZ after a relatively short distance to find a flow-path to the surface through the fracture network.

The variant cases for the DFN using a higher transmissivity in Set_C and correlated fracture transmissivity-size relationship also indicate the performance measures are relatively insensitive to these uncertainties.

For the current fracture model, avoiding locations where fractures intersect the full perimeter of a tunnel seems to be a sufficient test for screening out the worst deposition hole locations without having to perform flow tests of fracture transmissivity in deposition pilot holes.

5 Gas migration and its effects on groundwater flow

Gas is expected to be produced from corrosion of the iron insert in any copper canister that allows ingress of water through a breach in the copper shell as a result of damage or a manufacturing defect. To escape, the gas will need to pass through the bentonite buffer around the copper canister without damaging the properties of the buffer as a barrier to groundwater flow and the transport of radionuclides. Such damage might be caused by an excessive build up of gas pressure, but current expectations are that the gas will escape satisfactorily through the buffer.

Gas escaping from the buffer will then migrate through the geosphere. The potential gas migration through the geosphere, and any consequences it might have for a repository at Laxemar, are addressed in this section and contribute to the wider SR-Can assessment. As the work will be of a different nature to the geosphere groundwater flow and transport calculations, for example in not being so amenable to large-scale numerical modelling, this work is carried out as a more or less separate activity from the main groundwater flow and transport calculations, although it does draw on the data used in those calculations and on some of their results as described in Sections 3 to 4.

A comparable simple gas assessment was carried out for an earlier stage of the development of the SKB copper canister concept for the disposal of spent fuel. This work was reported in SKB TR 93-31 /Wikramaratna et al. 1993/ but is now more than a decade old. The intention of the current work is to update and extend this earlier work to bring it into line with current requirements and with data specific to Laxemar. In particular:

a) Understanding of gas flow has developed over the last ten years, and it is appropriate to consider how this might affect the performance safety assessment.

b) The data has improved over the last ten years. In particular, there are better measurements of the canister corrosion rates /Smart 2001/, there has been an improved canister assessment /Bond et al. 1997/, and there are now site-specific hydrogeological data which can be taken into account e.g. /SKB 2005/ and /SKB 2006a/. The current conceptual model of flow in DFN's used in SR-Can is also different from that used in /Wikramaratna et al. 1993/; the current concept is of flow through fracture planes, the previous model was of flow along fracture intersections.

c) Additional issues not discussed in SKB TR 93-31 /Wikramaratna et al. 1993/ have been identified for consideration in the SR-Can assessment. These are the possible effects of free gas in the geosphere on groundwater flow and radionuclide transport.

The following four subsections address the following issues:

a) The sources and amounts of gas that might be generated or be present in the repository or host rock.

b) The characteristics of the flow and transport of gas through the geosphere.

c) Assessment of any implications that geosphere gas transport might have for groundwater flow and the transport of dissolved radionuclides.

A summary of the conclusions reached is provided in Section 5.5.

5.1 Sources and amount of gas

Although the primary objective of the work described in this section, Section 5, is the characterisation of gas flow through the geosphere and its effects, a prerequisite for this is an understanding of the rates of gas production that could come from the wastes, and of any other sources of gas that might be present. Gas generation is expected to result predominantly from the anaerobic corrosion of the cast iron insert in the copper canister to release hydrogen. This requires the presence of a breach in the canister, but it also depends on the availability of water. The extent to which the rate of the corrosion process may be limited by the availability of water needs to be considered, and therefore is assessed here. It is possible that some gas will be trapped in the repository at repository closure and that sources of natural gas may exist. The potential volumes of such gases in relation to the volumes that might arise from corrosion in a canister are briefly reviewed, and any implications of their presence noted.

Other sources of gas from the spent fuel wastes have been previously assessed to be insignificant from the point of view of radiological hazard and the volume of gas involved (e.g. helium from radioactive decay and ^{14}C from the fuel itself and from the Zircaloy cladding), and are not reassessed here.

5.1.1 Gas generation from corrosion in canisters

The scenario that will lead to generation of gas from a waste canister is envisaged to be one in which a small defect present in a canister allows ingress of groundwater into the canister, resulting in generation of hydrogen from the anaerobic corrosion of the cast iron insert in the canister. An upper limit to the rate of gas generation may be derived by assuming that water is freely available to the corroding iron surface, in which case the gas generation rate is determined by the iron surface area and the corrosion rate (which may in principle vary with time and groundwater chemistry). However, water availability may be limited by the rate at which it can be supplied by transport through the breach, the bentonite buffer, the host rock, and repository features such as the tunnel and engineering damaged zone (EDZ).

Availability of water is also likely to be affected in a complex way by the build up of gas pressure in the canister as a result of gas production (and possibly water ingress), and by the formation of corrosion product. Gas pressure build up will oppose the advective flow of water into the canister, which would cease once the gas pressure reached the local hydrostatic pressure. Thereafter, any water flow into the container would be gas phase diffusion of water vapour. The precise behaviour could be complex, with a number of factors affecting the evolution of the system:

a) any free water present may be forced from the hole in the copper shell by a build up of gas pressure, the extent to which this could occur depending on the position of the breach and whether any free water was present in the canister as a result of water ingress (significant quantities of free water should only be present if, for a time at least, the flow rate of water into the canister is greater than the rate of water consumption by the corrosion reaction),

b) the nature and position of any open connection between the inside (channels for the fuel assemblies) and the outside (annular space between the insert and the copper shell) of the iron insert will affect the access of water to the inside iron surfaces,

c) anaerobic corrosion of iron, to produce magnetite, results in an increase in the volume of solid, and this expansion could close up the space between the iron insert and the copper shell, particularly around the breach in the copper shell, restricting the movement of water or water vapour within the canister.

These issues were considered in detail in SKB TR 93-31 /Wikramaratna et al. 1993/ and in SKB TR 97-19 /Bond et al. 1997/, and the detailed analysis provided is not repeated here, but the overall conclusions are reviewed in relation to the current situation. Note that it is assumed that only a small proportion of the canisters in the repository are breached at any particular time,

so that the time scale for gas release only needs to be considered in relation to the particular canister not the repository as a whole (except for possible effects on radionuclide transport).

An upper bound to the gas generation rate per breached canister is obtained by assuming that water is freely available. The cast iron insert is cylindrical in external shape, and has the dimensions shown in Table 5-1 /SKB 2004d, 1999/, where the dimensions of the channels for fuel assemblies are for BWR fuel (see Figure 5-1). Since canisters for BWR fuel are more numerous and have a larger iron/steel surface area than for containers for PWR fuel, only canisters for BWR fuel are considered here. The arguments are immediately transferable to canisters for PWR fuel, but the potential gas generation rates will be slightly reduced if controlled by the surface area of the cast iron insert (and water penetrates to the channels containing the fuel assemblies).

Table 5-1. Dimensions of iron insert in copper fuel canister for BWR Fuel.

Dimension	Value	Unit
External diameter	949	mm
External height	4,573	mm
Side of square channel for fuel assembly	160	mm
Length of channel for fuel assembly	4,470	mm
Number of channels for fuel assemblies	12	–

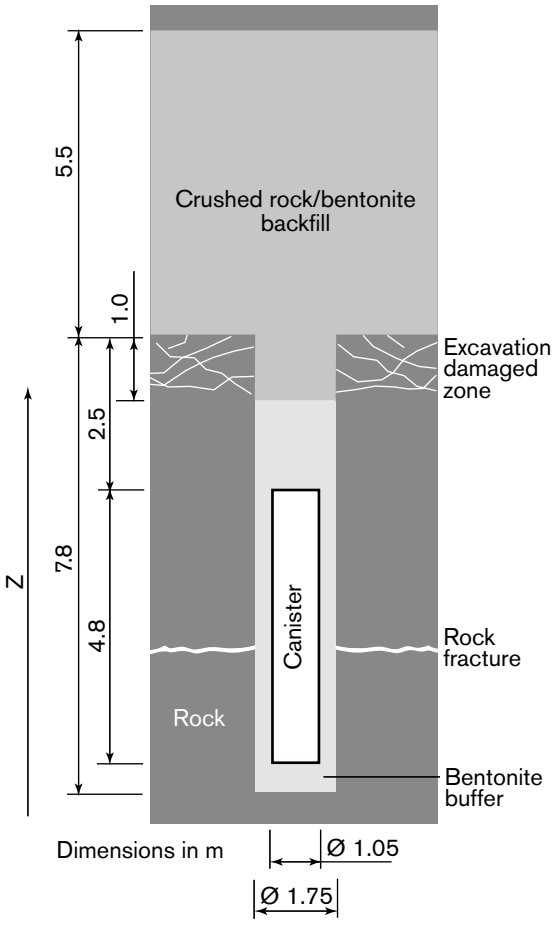

Figure 5-1. *A canister is shown in a deposition hole with surrounding bentonite buffer.*

From the figures shown in Table 5-1, it follows that the internal[2] and external areas of the cast iron insert are 35.7 and 15.1 m^2, giving a total surface area of 50.8 m^2. The best long-term estimate of the corrosion rate of mild steel is given in /Smart 2001/ as 0.1 μm y^{-1} (see also /SKB 2004a/), with a possible uncertainty of an order of magnitude in either direction. At 50°C, the corrosion rate for cast iron is somewhat lower than that of carbon steel[3]. Taking the density and molar mass of the iron insert to be those of pure iron, and taking the anaerobic corrosion of iron to occur as in the following equation:

$$3Fe + 4H_2O \rightarrow 4H_2 + Fe_3O_4 \,, \qquad \text{Equation (5-1)}$$

the gas generation rate from corrosion over the total surface area of the iron insert is $2.1 \cdot 10^{-2}$ m^3 y^{-1} at STP[4]. The corresponding rate of consumption of water is $1.7 \cdot 10^{-5}$ m^3 y^{-1}, taking the density of water to be 999.5 kg m^{-3} at 12°C /Lide 1994/, the ambient temperature given in /SKB 2004c/ for the repository depth and assumed throughout in this section. The assumption that water can reach the fuel assembly channels is consistent with the conservative assumptions made for water-borne radionuclide transport in the canister defect scenario, since unless water does reach the fuel assemblies, no such radionuclide transport can occur.

Whether or not corrosion can occur at the best estimate rate of 0.1 μm y^{-1} depends therefore on whether water can reach the iron and steel surfaces at a rate of $1.7 \cdot 10^{-5}$ m^3 y^{-1}. This will depend on the rate at which water can pass through the bentonite buffer and be supplied by the fracture network connected to the outer surface of the buffer.

As discussed in /Wikramaratna et al. 1993/, advection of liquid water through the bentonite to a small hole or crack in the canister will be largely controlled by the size of the hole and the behaviour close to the orifice, where most of the pressure gradient driving the water flow will be concentrated. It is suggested in /SKB 1999/ that the maximum size of a defect that would escape detection during canister inspection would be 1 mm^2, although this could enlarge with time after disposal. The saturated bentonite buffer annulus between the canister and the rock wall of the deposition hole is 0.35 m thick. Following /Wikramaratna et al. 1993/, the water flow rate through the orifice is obtained by considering flow through a hemispherical shell with an inner radius equal to the radius of the defect (considered as a circular hole), and an outer radius equal to the thickness of the bentonite buffer (see Figure 5-2). The flow rate, Q_w [m^3 s^{-1}] of water through the hole is given by:

$$Q_w = 2\pi K \frac{r_i}{1 - \frac{r_i}{r_o}} \frac{p_o - p_i}{\rho_w g} \qquad \text{Equation (5-2)}$$

where

K is the hydraulic conductivity of the bentonite [m s^{-1}],
r_i is the inner radius of the hemispherical shell [m],
r_o is the outer radius of the hemispherical shell [m],
p_o is the water pressure on the outer boundary [Pa],
p_i is the water pressure on the inner boundary [Pa],
ρ_w is the density of the water [kg m^{-3}],
g is the acceleration due to gravity [m s^{-2}].

[2] In calculating the inner surface area, it is assumed that the whole of the bottom surface of the lid to the insert and the facing surface of the insert (minus the gaps for the channels) are accessible to water. This is consistent with the assumption that radionuclides can diffuse from the fuel when water access to the insert is achieved, although it is possible that corrosion product will seal the gaps between the lid and the body of the insert.

[3] Note that, although the insert is largely cast iron, the fuel assembly channels are lined with carbon steel as part of the fabrication process.

[4] Standard temperature and pressure of 0°C and 1 atmosphere (101,325 Pa) pressure.

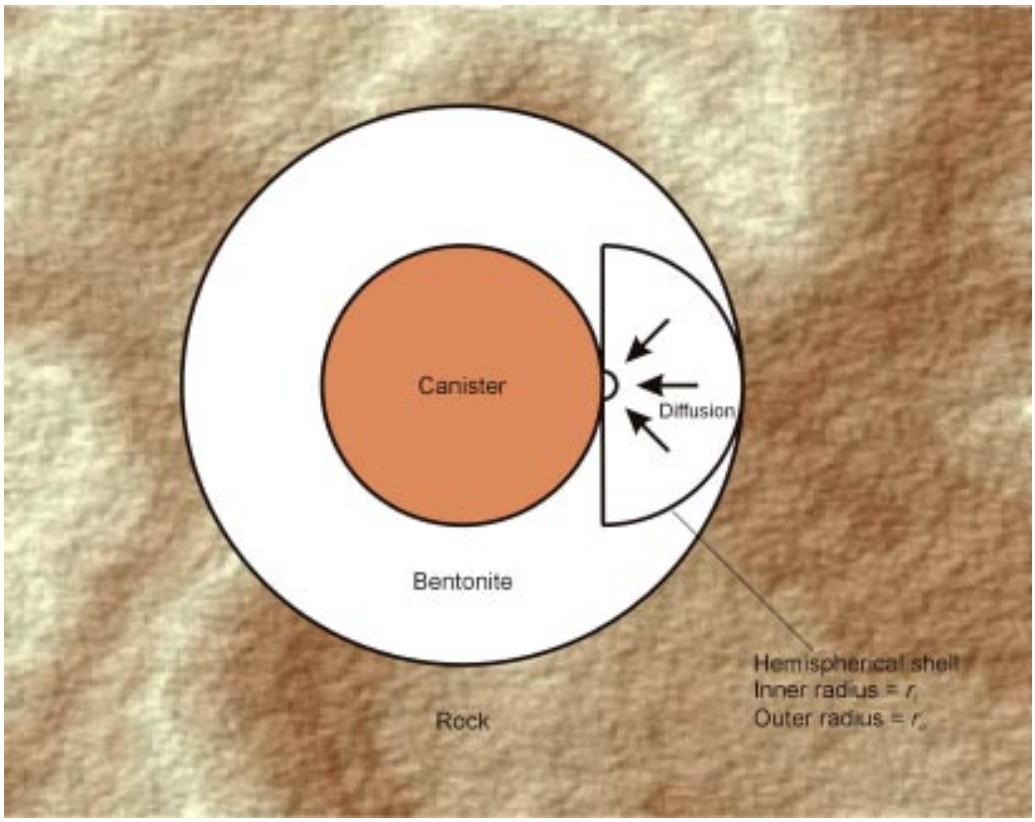

Figure 5-2. *A schematic diagram (in plan view) shows spherical diffusion through the bentonite buffer to a defect in the canister.*

The hydraulic conductivity for saturated bentonite at the reference dry density of 1.59 kg m^{-3} /SKB 2004c/ is less than 10^{-13} m s^{-1} /Börgesson et al. 1995, Börgesson et al. 1996/, and is consistent with the design requirement /SKB 2004b/ that the hydraulic conductivity be less than 10^{-12} m s^{-1}. The canisters are expected to be placed at a depth of slightly more than 520 m, at which depth the hydrostatic pressure would be about 5.1 MPa (this is calculated assuming the density of the groundwater is that of pure water at 12°C; in practice the density of the water and hence the hydrostatic pressure would be somewhat higher because of the salinity of the groundwater). Initially the gas pressure in the canister would be about 0.1 MPa (approximately atmospheric pressure). Taking the inner radius to be that of a circular hole of area 1 mm^2 (0.56 mm radius) and the external radius to be 0.35 m, the water flow rate through the defect would be $5.71 \cdot 10^{-6}$ m^3 y^{-1}, assuming a bentonite permeability of 10^{-13} m s^{-1}. This is about 33% of the inflow rate required to sustain corrosion at 0.1 µm y^{-1} over the whole surface area of the iron insert. It is possible that a defect in a canister could have an effective radius greater than 0.56 mm. Radii of 1 and 1.5 mm are considered in reference /SKB 2004a/, with the recognition that these are rather large values. Such an increase in radius would not be quite sufficient to provide enough water to support the corrosion rate over the whole surface of the metal insert. As indicated in the introduction to this subsection, there are other factors that will tend to reduce water ingress.

Water availability may be limited by the capacity of the host geology to supply water at a sufficiently high rate. The repository at Laxemar is designed to straddle two rock domains (see Section 3). The south-western part of the repository will be in a low permeability domain HRD(D, E, M), while the rest will be in a high permeability domain HRD(A). Clearly, water availability would be expected to be less of an issue for those deposition holes sited in the high permeability rock domain HRD(A). The calculated capacity of the host geology to supply the required groundwater to support unconstrained corrosion depends somewhat on the computational model assumed.

Using the DFN "base case", groundwater flow calculations for the Darcy velocities[5] adjacent to those deposition holes intersected by at least one flowing fracture give a geometric mean value of $1.2 \cdot 10^{-4}$ m y^{-1} in HRD(D, E, M) and $3.3 \cdot 10^{-4}$ m y^{-1} in HRD(A) (these are the values from the calculation at 2,020, although the values at different times were similar). The Darcy velocity required to support corrosion at the experimentally observed rate over all the iron surfaces, assuming the groundwater flows through a circular area of radius 0.35 m, is $4.5 \cdot 10^{-5}$ m y^{-1}. The calculated mean Darcy velocity, even in the low permeability rock domain HRD(D, E, M), is more than 2.7 times this value. However, the variability of the Darcy velocities between different deposition holes is significant. In rock domain HRD(D, E, M), only 52% of the deposition holes are intersected by a flowing fracture (87% in HRD(A)), and the Darcy velocities obtained from the DFN "base case" model are sufficient to support unrestricted corrosion at the deposition holes for less than 32% of the deposition holes (69% in HRD(A)).

At long times, when any defect has enlarged or some other damage to the canister may have occurred, groundwater flow from a larger area than for a small defect may converge towards the aperture in the canister, in which case the groundwater flow rate will place less restriction on the gas generation rate.

Although these estimates based on calculated Darcy velocities only provide a rough measure of the effect of groundwater flow in the host rock on water availability, they do indicate that the geosphere, at least for some deposition holes, would provide a further significant restriction on water availability. Some deposition holes will have a significant conducting feature intersecting the deposition hole close to the defect; for many of these there will be an adequate supply of groundwater to support the corrosion. Others will not be intersected by a flowing fracture, and for these the groundwater flow towards the canister defect is likely to be very small. Others still may be intersected by a flowing feature but the intersection could be some distance from the defect in the canister; in these cases, groundwater would have to flow for a significant linear distance through the bentonite buffer, perhaps from the backfilled access tunnel or the damage zone surrounding this, and this would restrict availability of water from the host rock. Because of the likely variability in local groundwater flows, no reliance is placed on restricted groundwater flow through the geosphere in assessing the effects of water availability in controlling gas production from corrosion.

The conclusion of the above is that, while the defect in the canister is limited to a small hole, corrosion over the whole surface area of the iron insert cannot occur at a rate more than the best estimate value about 0.1 μm y^{-1} because of controls on the advective flux of water through the bentonite buffer. Additionally, constraints provided by the geosphere on groundwater flow are likely to restrict the effective corrosion rate (i.e. taken to occur over the whole surface of the iron insert) to a value less than this for a significant fraction of the deposition holes. In addition, the corrosion rate will slow as an opposing gas pressure builds up in the canister. An indication of the time-scale over which the pressure builds up and the water influx rate reduces can be obtained if it is assumed that the gas production rate is limited by water supply (i.e. the gas generation rate is determined by the water inflow rate, all the inflowing water being converted to hydrogen).

Using Equations (5-1) and (5-2), the change of pressure in the canister is given by:

$$\frac{dp_i(t)}{dt} = 2\pi K \frac{r_i}{1-\frac{r_i}{r_o}} \frac{p_o - p_i(t)}{\rho_w g} \frac{R\Theta}{V} \zeta_w = \alpha \left[p_o - p_i(t)\right] \qquad \text{Equation (5-3)}$$

where

[5] The Darcy velocity has been estimated as $q = \frac{1}{h}\sum_f \frac{Q_f}{\sqrt{A_f}}$, where h is the height of the deposition hole, Qf is the flow between intersections of the fracture, Af is the area of the fracture, and the sum is over the fractures intersecting a deposition hole.

R is the Universal Gas Constant [8.3145 J mol^{-1}K^{-1}],

Θ is the absolute temperature in the canister [K],

V is the void volume in the canister when filled with fuel and sealed,

ζ_w is the molar density of water [mol m^{-3}],

$$\alpha = 2\pi K \frac{r_i}{1-\frac{r_i}{r_o}} \frac{R\Theta}{\rho_w g V} \zeta_w.$$

Integrating Equation (5-3) gives:

$$p_i(t) = p_o - [p_o - p_i(t=0)]e^{-at} \qquad \text{Equation (5-4)}$$

and the gas production rate, Q_g [m^3 s^{-1} at STP], as a function of time becomes:

$$Q_g = 2\pi K \frac{r_i}{1-\frac{r_i}{r_o}} \frac{p_o - p_i(t)}{\rho_w g} \zeta_w \frac{R\Theta_s}{p_s} \qquad \text{Equation (5-5)}$$

where

Θ_s is standard temperature (0°C),

p_s is standard pressure (101,325 Pa).

The void volume, V, in the canister is taken to be 1 m^3. This is as assumed in /SKB 2004b/. The volume calculated from the canister geometry without allowing for the presence of the fuel assemblies would be 1.39 m^3, so a void volume of 1 m^3 seems reasonable when account is taken of these.

Figure 5-3 shows the variation of canister pressure and gas generation rate calculated on the basis of the above assumptions.

The figure shows that the canister gas pressure would increase sufficiently to reduce the water ingress rate and hence the potential gas generation rate significantly after 1,000 years, reducing the latter by almost an order of magnitude after about 15,000 years. At some point the advective flux of water into the canister will have diminished to such an extent that the diffusion of water vapour into the canister will become the main water supply mechanism. This is discussed in some detail using numerical models in /Bond et al. 1997/ but it is possible to derive an upper

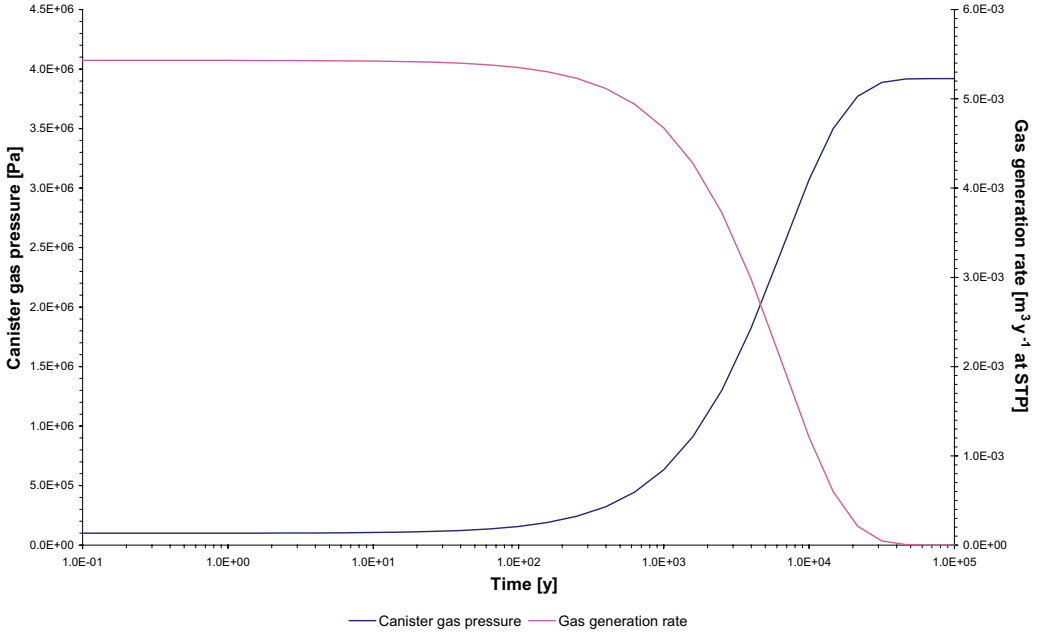

Figure 5-3. *Variation of canister gas pressure and gas generation rate as gas accumulates in canister.*

bound to the potential diffusive flux by considering diffusion just through the defect in the copper canister. If this is modelled as a channel of uniform cross-section, then the diffusive flux, Q_v [mol s^{-1}] of water vapour can be estimated as

$$Q_v = AD_v \frac{1}{L}\frac{p_v}{R\Theta} \qquad \text{Equation (5-6)}$$

where

A is the area of the defect channel in the copper overpack [m^2],

D_v is the diffusion coefficient for water vapour in hydrogen [$m^2 s^{-1}$],

L is the thickness of the copper overpack [m],

p_v is the saturated water vapour pressure under the ambient conditions [Pa].

It is assumed that diffusion away from the inside end of the defect channel is much faster than diffusion through the channel itself so that the concentration of water vapour at the end of the channel can be taken as zero. This may not be the case, in particular because of the build up of magnetite corrosion product in the annulus between the iron insert and the copper overpack, especially close to the defect, but this assumption provides an upper bound to the diffusive flux (compare with /Bond et al. 1997/). As noted above, the area of the defect is taken to be 1 mm^2. The thickness of the copper canister is 50 mm, which gives the length of the path for diffusion. An upper bound to the diffusion coefficient at atmospheric pressure is estimated to be 10^{-4} $m^2 s^{-1}$, on the basis of comparison with values for comparable binary gas mixtures (e.g. in /Lide et al. 1994/). Since gas-phase diffusion coefficients are inversely proportional to pressure, the diffusion coefficient at hydrostatic pressure, when the gas pressure has built up to this value in the canister, would be $2.0 \cdot 10^{-6}$ $m^2 s^{-1}$. The saturated vapour pressure for water at 12°C is 1.411 kPa /Lide et al. 1994/.

The above assumptions and data values give a diffusive flux of water vapour through the defect channel of $1.3 \cdot 10^{-8}$ m^3 y^{-1} of liquid water equivalent, which would produce $1.7 \cdot 10^{-5}$ m^3 y^{-1} at STP of gas. This is less than 0.1% of the rate of gas generation produced by corrosion at 0.1 µm y^{-1} over all the surfaces of the cast ion insert. From Figure 5-3 it can be seen that it would be more than 40,000 years before water availability became controlled by vapour diffusion through the defect rather than by advection through the bentonite buffer.

When the corrosion is controlled by vapour diffusion, the pressure would continue to rise, but at most at a rate of 1.8 Pa y^{-1}. What the effect would be depends on the properties of the bentonite buffer. The bentonite would not be expected to deform around the defect until the gas pressure reached the stress exerted by the bentonite. The swelling pressure of the saturated bentonite is estimated to be in the range 5.8–13 MPa /SKB 2004a/, so when the hydrostatic pressure of about 5 MPa is added to this the stress in the buffer will be in the approximate range of 11–18 MPa. To reach a pressure of, say, 15 MPa, at a rate of increase from hydrostatic of 1.8 Pa y^{-1} would take a further $5.6 \cdot 10^6$ years after the time at which the gas pressure reaches that of the ambient water pressure. Whether this would result in the gas creating a gas-filled gap between the canister and the buffer from which the gas could diffuse, or whether it deformed the bentonite around the defect, ultimately creating a gas pathway through the bentonite, depends on the behaviour of the bentonite buffer, which is beyond the scope of this study. However, some comments on potential gas transport mechanisms through the bentonite are provided in Section 5.2 as background to discussion of gas transport through the geosphere. /Wikramaratna et al. 1993/ considered various scenarios for the diffusion of dissolved hydrogen through the buffer from the canister. The results obtained indicated that diffusion of dissolved hydrogen from the defect itself through the bentonite would not be sufficient to remove hydrogen from the canister at the rate at which it is generated, but if the gas formed a gap between the bentonite and the canister then the much increased area over which diffusion would occur could allow the gas to diffuse through the bentonite at the rate at which it is generated once the generation rate is controlled by diffusion of water vapour into the canister. This depends on the groundwater being able to transport the dissolved gas away from the outer surface of the bentonite sufficiently quickly. These conclusions are further examined in Section 5.2.

Table 5-2 provides a summary of gas generation rates obtained when this is controlled by different processes, together with the corresponding water consumption rate.

Table 5-2. Summary of gas generation and equivalent water consumption rates corresponding to different controlling processes.

Controlling process	Gas generation rate ($m^3\ y^{-1}$ at STP)	Equivalent water consumption rate ($m^3\ y^{-1}$)
Corrosion at 0.1 μm y^{-1} on all insert surfaces	$2.1 \cdot 10^{-2}$	$1.7 \cdot 10^{-5}$
Water advection through bentonite buffer	$7.1 \cdot 10^{-3}$	$5.7 \cdot 10^{-6}$
Water vapour diffusion through defect in copper	$1.7 \cdot 10^{-5}$	$1.3 \cdot 10^{-8}$
Mean groundwater flow at deposition hole†	$1.0 \cdot 10^{-1}$	$8.2 \cdot 10^{-5}$

† This is the mean groundwater flow from the DFN "base case" for those deposition holes intersected by a flowing fracture. Note that this groundwater flow is sufficient to support unrestricted corrosion.

Where comparisons are possible, these gas generation rates are similar to those presented in the SR-97 assessment /SKB 1999/, with some small differences due to differences in assumptions (for example, in the area of iron surface potentially subject to corrosion).

The constraints of water supply mean that the maximum potential rate of gas production from corrosion is unlikely to be realised. Corrosion is also likely to be constrained by issues such as the accessibility of the entire iron surface because of lack of connection between the inner and outer surfaces and because of the build up of corrosion product. Build up of gas pressure in the canister will further restrict water inflow and reduce the gas generation rate, so that in the medium term the rate of gas production will drop substantially, and only be sustained by water vapour diffusion. The value of the gas generation rate given for this regime in Table 5-2 is probably an over estimate because it neglects any impediments to diffusion of the water vapour within the canister.

Figure 5-4 shows the cumulative gas production corresponding to the gas generation rate shown in Figure 5-3. It also shows the growth of the metal surface due to the replacement of iron by less dense magnetite (density about 5,200 kg m^{-3}), assuming corrosion occurs uniformly across all iron surfaces (these two curves are clearly rescaled versions of each other). With this

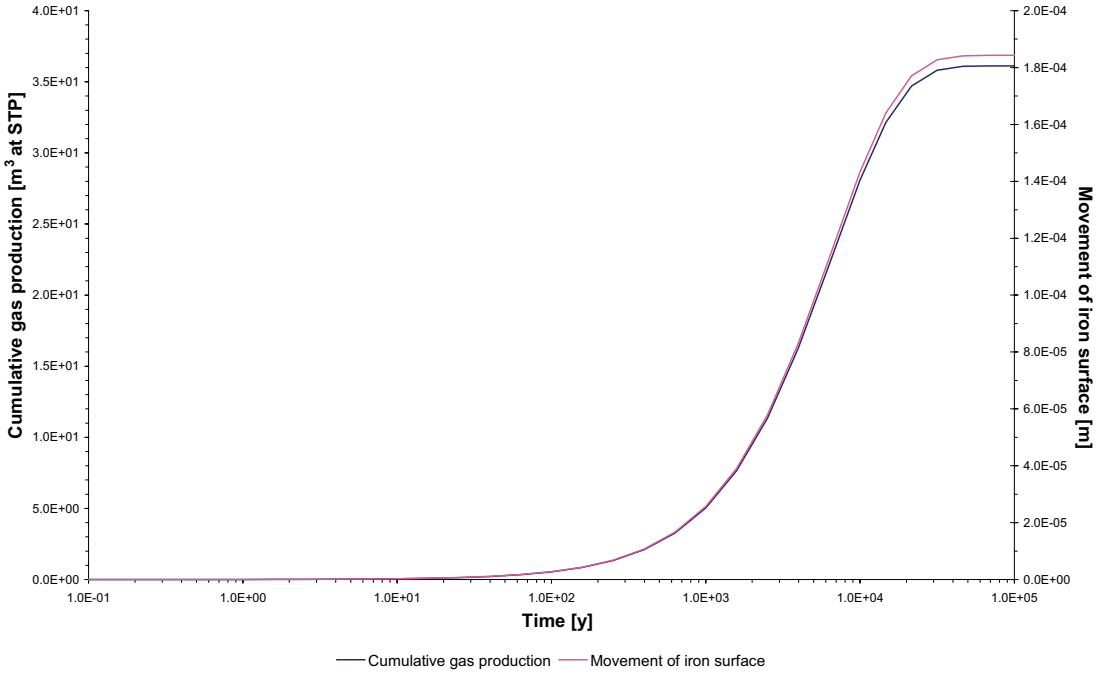

Figure 5-4. *Cumulative gas production and growth of corroding metal surface for corrosion controlled by liquid phase water supply.*

magnetite density, the iron undergoes an expansion by a factor of about 2.09 as a result of corrosion to produce magnetite. With corrosion controlled by advection of water through the buffer, the magnetite corrosion product is never sufficient to fill the 1 mm wide gap between the cast iron insert and the copper overpack (but water supply by diffusion would be expected eventually to allow corrosion to close the gap). In practice, corrosion is likely to occur more rapidly closer to the defect through which the water enters the canister than at more distant locations. Even here, if corrosion occurs at a rate of 0.1 μm y^{-1}, unrestricted by water availability, it would take 10,000 years to completely block the gap.

At the corrosion rate of 0.1 μm y^{-1}, the cast iron insert would be expected to last at least 250,000 years. Over this length of time, the possibility must be envisaged that any defect in the canister may have become enlarged or some copper overpacks may have failed in some other more drastic way, allowing less restricted access to the iron insert by groundwater. At this point corrosion may occur at a rate unrestricted by the engineered barriers, although the passivation of the metal by thick magnetite layers would tend to keep the corrosion rate at the lower end of the measured values.

The effect of corrosion of the iron insert caused by water ingress on canister integrity was examined in detail by /Bond et al. 1997/. They found that the build-up of corrosion product would initially be localised around the defect because of the effect of the build-up of corrosion product in restricting diffusion of water vapour in the annulus between the insert and the copper overpack. This localised corrosion would eventually, after ~ 200,000 years, lead to the failure of the copper canister around the defect producing a larger hole in the canister, estimated to have an area of 0.01 m^2. Beyond this time water availability is assumed not to limit the corrosion (much of the iron would still remain at this time because of the way corrosion was restricted prior to canister failure). Note that after 100,000 years the radiotoxicity of the fuel is estimated to have declined to about that of the uranium ore mined to produce the fuel, and remains at about that level thereafter /SKB 1999/. After ~ 400,000 years further corrosion would force the lid from the copper canister. For the transport of radionuclides from a defective canister in the groundwater, it is cautiously assumed that appearance of the larger hole (0.01 m^2) in the canister occurs after 20,000 years, and that after this the canister itself no longer contributes to the containment.

For the purpose of assessing gas migration through the geosphere, it would be reasonable to assume that an upper bound to the gas generation rate is that resulting from unrestricted corrosion ($2.1 \cdot 10^{-2}$ m^3 y^{-1} at STP). The rate is likely to drop to a value at least an order of magnitude less than this over a period of 15,000 years, and remain low until greater disruption of the canister occurs to allow more water ingress, at which point, which is estimated to occur after ~ 200,000 years, the gas production rate is likely to be similar to that resulting from unrestricted corrosion.

Figure 5-5 provides an indication of the rate of gas production and the cumulative gas production for the extended period covered by these scenarios: corrosion limited by advected supply of water; followed by corrosion limited by diffusion of water vapour; and finally corrosion not limited by water availability. Two cases are shown: the first with the extensive canister failure at 20,000 years and the second with this failure at 200,000 years. The cumulative gas production is limited by the mass of cast iron present, so that the most gas that can be produced is $5.9 \cdot 10^3$ m^3 at STP. No account is taken of the change in the surface area of the iron as it corrodes in producing Figure 5-5.

5.1.2 Gas trapped in repository

Gas will be trapped in the repository when it is closed. This gas will be in the pore space of the unsaturated bentonite buffer blocks placed around the canisters; in the slots between the buffer and the rock walls of the deposition holes and the canister, and in the pore spaces and voids of the backfilled tunnel. Gas in these spaces may be regarded as “in communication” with the

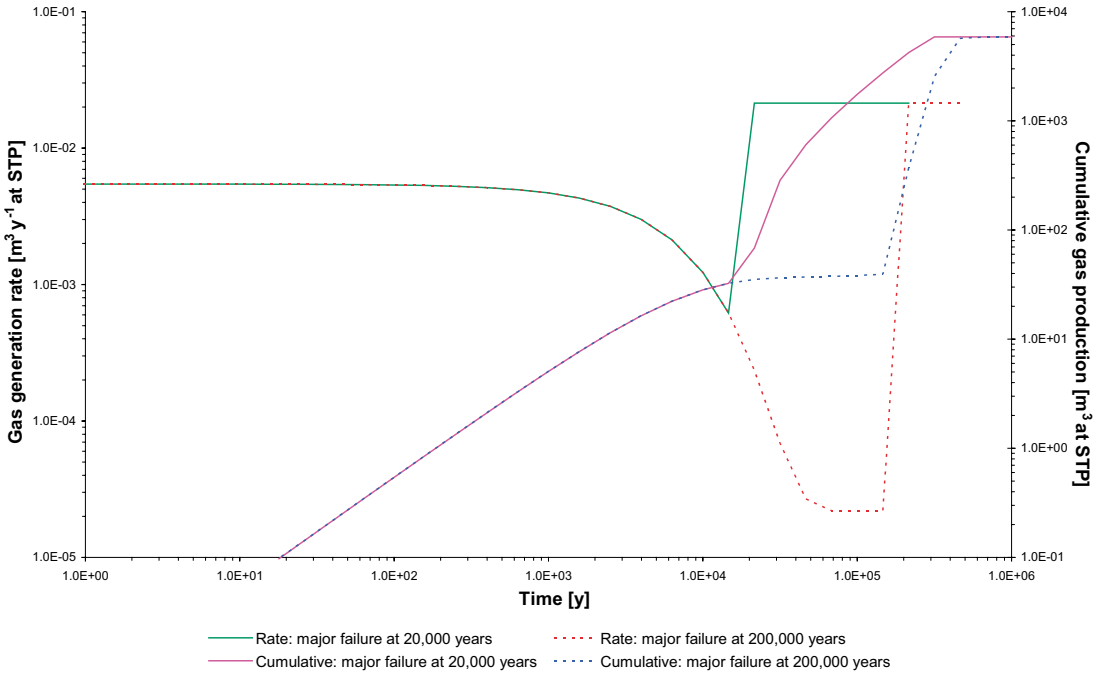

Figure 5-5. *Estimated rate of gas production and cumulative gas production over an extended timescale.*

deposition holes in that there are no seals between these spaces and the deposition holes and they are in proximity to some holes. Gas will also be trapped in other repository spaces, such as the access ramp and shafts, transport and main tunnels, ventilation shafts, and central areas. However, there is insufficient information to consider the gas content of these spaces, and it is also reasonable to argue that these spaces are sufficiently isolated from the deposition holes that the gas content from them will not interfere with that from the waste canisters.

In the deposition holes, gas is trapped in the bentonite blocks and rings and in the spaces between the bentonite and the rock and the bentonite and the canister. The blocks are situated above and below the canister and the rings surround the canister along its length.

Table 5-3 shows the properties of the bentonite rings and blocks and the geometrical dimensions from which the gas-filled volume associated with the buffer-filled region of a deposition hole is obtained. The parameters shown are given in SKB R-04-35 /SKB 2004d/.

Based on the figures in Table 5-3, the total gas-filled volume in the deposition hole (neglecting the short upper section filled with backfill) is 2.41 m^3 (Table 5-4). It is assumed that the gas initially trapped is at atmospheric pressure, and the ambient temperature. To the accuracy of the estimates of the trapped gas volume, this can be taken to be standard temperature and pressure.

Table 5-3. Properties and dimensions from which the gas-filled volume in bentonite-filled part of a deposition hole is obtained.

Shape	Inner diameter (m)	Outer diameter (m)	Void ratio	Water saturation	Canister diameter (m)	Hole diameter (m)	Length (m)
Block	–	1.690	0.680	0.70	1.050	1.750	2.5
Ring	1.060	1.690	0.585	0.81	1.050	1.750	4.833

Table 5-4. Gas-filled volumes (or volume fraction) initially present in deposition holes and backfilled tunnels.

Location	Gas-filled void volume (m^3) or volume fraction ($m^3\ m^{-3}$)
Deposition hole (blocks, rings and slots)	2.41
Backfilled tunnel – gas-filled volume fraction	
Rock/bentonite backfill	0.17
Friedland clay	0.34
Backfilled tunnel – gas-filled volume per deposition hole (i.e. per 7.35 m length of tunnel and assuming the cross-sectional area to be 25 m^2)	
Rock/bentonite backfill	31.6
Friedland clay	63.6

Gas will also be trapped in the backfilled tunnels from which the deposition holes are drilled. Two options are being considered for the backfilling: a rock/bentonite mixture, and Friedland clay blocks /SKB 2004d/. The gas-filled void space would be larger if the Friedland clay were used mainly because of the spaces that would be present between the clay blocks on emplacement. The initial void ratios of the rock/bentonite mixture and the Friedland clay themselves are 0.59 and 0.33, and the initial water saturations are 0.54 and 0.27, respectively, but 20% of the tunnel volume is additionally assumed to consist of gas-filled voids in the case of the Friedland clay /SKB 2004d/. The fraction of the tunnel space initially occupied by gas is shown in Table 5-4. Also shown is the volume of gas in the tunnels that may be associated with each deposition hole. This is the gas filled volume in a 7.35 m length of tunnel, this being the average spacing between the deposition holes, taking the tunnel cross-sectional area to be 25 m^2 (this is the cross-sectional area for a tunnel excavated by drilling and blasting; a larger area would result from tunnel boring, but the difference is ignored here). The gas-filled volume in the backfilling of the top of the deposition holes is included in this estimate of gas-filled volume per deposition hole.

As the repository resaturates, the pressures will tend to the hydrostatic pressure of ~ 5 MPa, a 50-fold increase in pressure, which will cause a corresponding decrease in the gas-filled volume. Some of the gas initially present will also dissolve and may be transported from the tunnels in solution. From the data above, the water content of the backfill when it is resaturated can be calculated as a volume fraction of 0.37 and 0.40 for the rock/bentonite and Friedland clay backfill, respectively. The solubility in water of the main constituents of air, nitrogen (78.08%) and oxygen (20.95%), are rather similar, with nitrogen slightly less soluble /Lide 1994/. It can be shown that for the tunnel filled with either rock and bentonite or Friedland clay, enough water will be present after resaturation to dissolve all the trapped air at a pressure of 5 MPa. These issues are discussed below in relation to geosphere gas transport.

The total trapped gas volume of around 30–60 m^3 per deposition hole corresponds to the amount of gas that would be generated in a defective canister over 1,500–3,000 years at the maximum rate considered likely. Since it is estimated that only 0.1% of the canisters could have a hole defect, the initial gas volume in the tunnel per *defective* canister would be $3 \cdot 10^4$–$6 \cdot 10^4$ m^3. This exceeds the $5.9 \cdot 10^3$ m^3 at STP of gas that could be produced by corrosion of the entire cast iron insert in a defective canister (Section 5.1.1).

5.1.3 Natural gases

Natural gases have been detected in groundwater samples from the region around the Laxemar site /SKB 2004e/. The approximate concentrations of the more significant gases at the repository depth of about 520 m, estimated from the plots in reference /SKB 2004e/, are shown in Table 5-5. The solubilities are obtained from /Lide 1994/ assuming that the solubilities are proportional to the gas pressures.

Table 5-5. Measured dissolved natural gas concentrations and expected solubilities at the repository depth (values of measured concentrations are estimates).

Gas	Measured concentration (mol m^3)	Approximate solubility at repository depth (mol m^3)
Nitrogen	2–5	$4.1 \cdot 10^{1}$
Helium	< 0.3	$2.0 \cdot 10^{1}$
Carbon dioxide	$< 5 \cdot 10^{-2}$	$2.5 \cdot 10^{3}$
Hydrogen	$< 1 \cdot 10^{-2}$	$4.3 \cdot 10^{1}$
Methane	$< 6 \cdot 10^{-3}$	$9.3 \cdot 10^{1}$

It can be seen that the measured concentrations are all small compared with the solubilities of the gases at the repository depth. Only nitrogen, which has a concentration about 10% of its solubility at the repository hydrostatic pressure, is present in amounts that could be significant in terms of creating a free gas phase. The solubilities given in Table 5-5 are those in pure water. The presence of dissolved salts will lower the solubilities (the salting-out effect), but this effect is not expected to reduce the nitrogen solubility sufficiently to cause free nitrogen to appear. Free gas could appear as a result of pressure reduction as the groundwater and its dissolved gases moved towards the surface, but on the basis of the solubilities shown in Table 5-5, this would only occur when the groundwater had risen to within about 50 m of the surface.

If a free gas phase was formed as a result of hydrogen production from corrosion, dissolved natural gases could partition into this gas phase until their partial pressures in the gas phase were in equilibrium with the solution concentrations.

5.2 Flow and transport characteristics of gas

As discussed above, ingress of water into a canister through a defect, first mainly by advection, and then, when the gas pressure in the canister has risen to around the hydrostatic pressure, by vapour phase diffusion, will cause hydrogen generation from anaerobic steel corrosion. To demonstrate repository safety, it is necessary to develop an understanding of what will happen to this hydrogen in order, in particular, to show that the gas pressure will not build up in a way that will damage the near-field containment and that migration of the gas through the near and far fields will not have a deleterious effect on water-borne radionuclide transport.

The first barrier to gas migration from the canister is the saturated bentonite buffer. Examination of gas migration through the bentonite buffer is beyond the remit of this work, which is concerned with gas migration through the geosphere. However, it is appropriate to comment briefly on work that has been carried out on this leg of the gas migration pathway as background to the present consideration of gas migration through the geosphere.

As already noted in Section 5.1.1, /Wikramaratna et al. 1993/ have examined transport of dissolved gas by diffusion through the bentonite buffer. The flow rate of gas that can be achieved by this mechanism depends sensitively on the geometry of the diffusion pathway. If it is assumed that the gas diffuses from the area of the defect, the diffusion will, at least initially, follow a radial pathway through an approximate hemisphere centred on the defect (spherical diffusion). It is assumed in this model that gas emerging from the bentonite is transported away from the location sufficiently quickly that the concentration of dissolved hydrogen at the outer boundary of the bentonite can be taken to be zero. Following /Wikramaratna et al. 1993/, an effective diffusion coefficient of $2 \cdot 10^{-11}$ $m^2 s^{-1}$ is used in this calculation. /Tanai et al. 1999/ report measured values for this diffusion coefficient of 10^{-10} –10^{-11} $m^2 s^{-1}$, so the value used is consistent with this range. The value is also consistent with the values used for the diffusion of ions in bentonite in the SR-97 assessment /Lindgren and Lindström 1999/. Diffusion by

this mechanism is found to be small. Updating the calculations to use current parameters gives a flow of $2.2 \cdot 10^{-6}$ m^3 y^{-1} at STP, if the gas pressure is hydrostatic (at 520 m depth). The flow is proportional to the gas pressure, so if the pressure rises to 15 MPa, the flow would be $6.4 \cdot 10^{-6}$ m^3 y^{-1} at STP.

These calculated flows are evidently much smaller than the upper bound to the potential gas generation rate of $2.1 \cdot 10^{-2}$ m^3 y^{-1} at STP. They are also smaller than the estimate of $1.7 \cdot 10^{-5}$ m^3 y^{-1} at STP for the rate of hydrogen production that would occur when the water supply is controlled by vapour diffusion, so that the gas pressure would continue to rise if this was the only gas escape mechanism.

If the gas pressure rises to a level comparable to the stress in the bentonite, it is possible that the gas could deform the bentonite creating a gas-filled gap between the bentonite and the canister (this could take a very long while unless the defect became enlarged – see Section 5.1.1). In these circumstances, gas could diffuse over a much larger surface area of the bentonite than for the case in which diffusion occurs just from the area of the defect. For this scenario, /Wikramaratna et al. 1993/ consider cylindrical diffusion across the thickness of the bentonite buffer, and vertical diffusion through the bentonite blocks at the top of the canister, in both cases assuming that the gas phase has spread across the whole surface of the copper canister. The dissolved hydrogen concentration at the outer surface of the bentonite is again taken to be zero. Given present understanding of the extent of fracturing of the host rock, the cylindrical diffusion scenario is probably optimistic, in that although the source of the gas for the diffusion may spread over the whole of the surface of the canister, the sink will be confined to the lines of around zero to two fracture intersections with the deposition hole.

Diffusion to a line sink, representing the fracture intersection with a deposition hole, may be modelled approximately as cylindrical diffusion in a half cylinder of length equal to the length of the line of intersection of the fracture with the deposition hole (see Figure 5-6). The diffusive flux, Q_{dg} [m^3 s^{-1} at STP], is approximated as:

$$Q_{dg} = 2\pi^2 D_b \frac{r_d}{\log(2r_b/e_f)} H_H p_g \qquad \text{Equation (5-7)}$$

where

D_b is the diffusion coefficient for dissolved hydrogen in buffer bentonite [m^{2}s^{-1}],

r_d is the radius of the deposition hole [m],

r_b is the distance over which the cylindrical diffusion occurs, taken to be the thickness of the bentonite buffer [m],

e_f is the aperture of the fracture intersecting the deposition hole [m],

H_H is a Henry's law constant for hydrogen dissolved in water [m^3 at STP m^{-3}Pa^{-1}],

p_g is the gas pressure in the canister [Pa].

It is assumed that the dissolved hydrogen concentration at the intersection of the fracture and the deposition hole is zero. The parameters relating to the bentonite buffer are shown in Table 5-6.

Table 5-6. Parameters for the saturated bentonite buffer.

Parameter	Value	Unit	Reference
Deposition hole radius	0.875	m	/SKB 2004d/
Radial thickness of buffer	0.35	m	/SKB 2004d/
Intrinsic diffusion coefficient	$2 \cdot 10^{-11}$	m^{2}s^{-1}	/Wikramaratna et al. 1993/ †

† This appears to be an estimated value based on comparison with values for other species. The diffusion coefficient for hydrogen in free water is $4.5 \cdot 10^{-9}$ m^{2}s^{-1} /Cussler 1984/, so the value quoted is considered reasonable for a compacted clay, and is consistent with measurements made in Japanese experiments. (See also discussion in main text.)

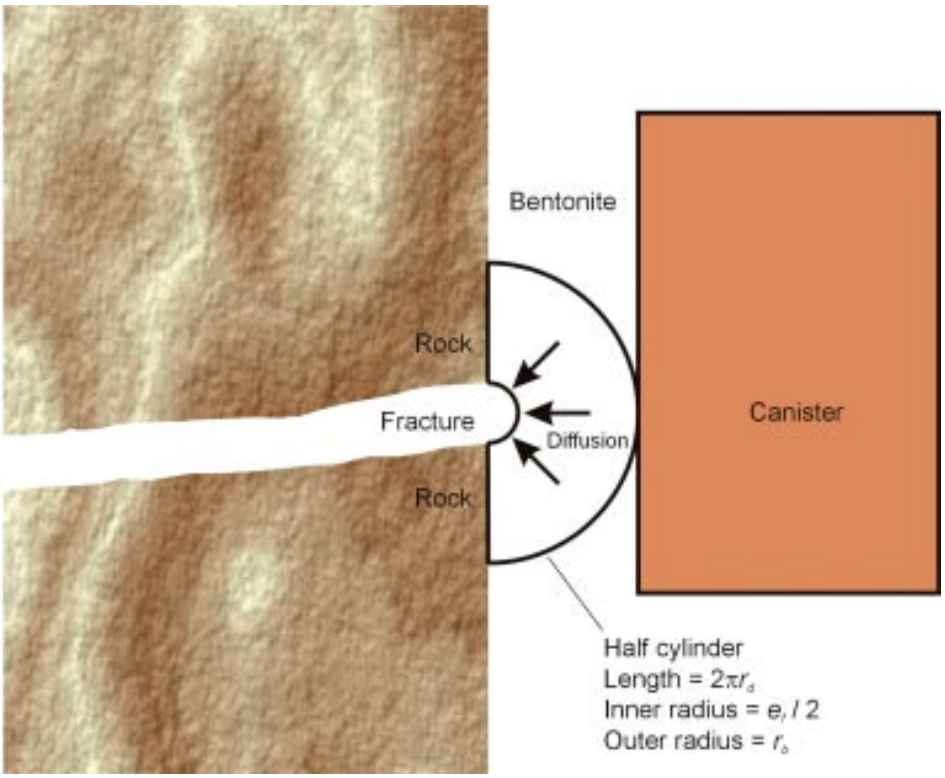

Figure 5-6. *A schematic diagram shows cylindrical diffusion through the bentonite buffer to a fracture intersection with a deposition hole.*

The Henry's law constant is set to $1.9 \cdot 10^{-7}$ m^3 at STP $m^{-3}Pa^{-1}$, to be consistent with the solubility data shown in Table 5-5. If the pressure in the gas phase is taken to 15 MPa (it must exceed the stress in the buffer to create a gap between the canister and the buffer), and the effective fracture transport aperture is taken to be 10^{-4} m, to provide an indicative measure of the diffusive flux, then the calculated flux into the fracture is $3.5 \cdot 10^{-3}$ m^3 y^{-1} at STP. This diffusive flux does depend on the gas source being distributed over a larger area than simply that of the defect in the canister, but appears capable of supporting a hydrogen flow greater than the rate of generation of gas by diffusive supply of water vapour, and comparable to that if the gas generation rate is controlled by supply of water by advection through the bentonite. However, it is less than the rate required to disperse the gas at the upper bound gas generation rate assumed of $2.1 \cdot 10^{-2}$ m^3 y^{-1} at STP.

Vertical diffusion through the bentonite and backfill to the tunnel may also offer a transport path for dissolved gas, particularly if significant groundwater flows are focused along the tunnel, thereby maintaining the dissolved gas concentration at the boundary between the tunnel and the deposition hole at a low value. Assuming that the dissolved gas diffuses from the area of the top of the canister over a distance of 2.5 m to the tunnel, the gas flow would be $6.2 \cdot 10^{-4}$ m^3 y^{-1} at STP. This is again insufficient to remove gas at the maximum rate considered possible, but would be more than adequate to remove gas at the rate at which it could be generated if the process was controlled by vapour diffusion into the canister.

The above discussion indicates that diffusion of dissolved gas directly from the defect hole would be very small and would not prevent the gradual build up of pressure, but, in the very long term, after the gas pressure had built up and if the gas was able to spread out in a gap between the canister and the bentonite, then it is possible that the increased area from which diffusion could occur might allow the gas to escape at the rate at which it would be produced if controlled by water vapour diffusion. However, the time scale for this to occur is so long that it might be unreasonable to assume that further degradation to the copper canister has not occurred to allow freer access of water to the iron insert.

If the gas generated cannot pass through the bentonite by diffusion of dissolved gas, then free gas-phase transport through the bentonite is expected to occur once the pressure has reached a threshold value. The available experimental evidence suggests that this gas-phase transport will occur by fissuring of the buffer, and that the fissures will subsequently self seal, so that as far as the transport through the bentonite buffer is concerned this fissuring will provide a satisfactory method of relieving gas pressure build up in the canister, provided that the threshold pressure is not too high and that the gas can subsequently migrate through the geosphere without the geosphere contributing to a further build up of gas pressure. Note that the creation of gas-filled fissures in the bentonite may create an increased surface area from which dissolved gas can diffuse.

Once the gas has escaped from the buffer, it may directly enter the geosphere via a conducting fracture intersecting the deposition hole, or it may first enter the tunnel (including the EDZ around the tunnel), where it could reside for a time and may travel laterally, before escaping into the fracture network. As with transport through the buffer, gas transport through the geosphere may occur as a dissolved phase or as a free gas. These possibilities are considered in the next subsections.

5.2.1 Dissolved gas

Aqueous phase diffusion of the gas produced through the sparse fracture network of the rock is not expected to make a significant contribution to gas migration through the geosphere. The capacity of gas to disperse in solution through the geosphere depends therefore on the flux of water that is available to carry the gas away and with which the gas makes contact (the latter may be an issue if the groundwater flow is concentrated along paths remote from the pathways followed by the gas). It might be imagined that groundwater flows would be concentrated along excavated structures, in particular tunnels and access roads, including the EDZ's, but the groundwater "pathline" calculations suggest this occurs to an appreciable extent only for some parts of the repository that are located in the low permeability rock domain HRD(D, E, M). This is because of the orientation of the tunnels to the head gradient and the fact that the permeabilities of the tunnels are comparable to those of the host rock.

Given that the solubility of hydrogen at repository depth is about 43 mol m^{-3} (Table 5-5) or 0.97 m^3 at STP m^{-3}, the flow of groundwater required to remove hydrogen at a rate of $2.1 \cdot 10^{-2}$ m^3 y^{-1} at STP would be $2.2 \cdot 10^{-2}$ m^3 y^{-1}, assuming the groundwater was fully saturated with the hydrogen. Using the DFN "base case" model, the geometric mean of the Darcy velocity[6] in the fractures comprising the EDZ close to 7,066 deposition holes from calculations at 2,020 AD is $5.5 \cdot 10^{-3}$ m y^{-1}. (The mean velocities in the tunnels and the rock were much smaller. Groundwater flows are concentrated in the EDZ's because they have much higher permeability than the surrounding material.) This means that to remove the hydrogen generated in solution would require that the gas saturate the flowing groundwater over an area of 4 m^2. It is plausible that the extent of the contact between gas and groundwater flowing through the fractures comprising the EDZ could be sufficient to saturate the groundwater over such a cross-section of its flow-path.

It is also possible that the gas could become trapped, for example in the tunnel, and this could provide an enhanced interface area between the trapped gas and the flowing groundwater from which gas could dissolve and diffuse into the water. At least for rock domain HRD(D, E, M), with the low density of fracturing predicted at the repository depth, intersections of fractures with the deposition holes will be non-existent or sparse, and in the latter case are likely to involve only low transmissivity fractures. It seems likely therefore that the gas will escape

[6] The Darcy velocity has been estimated as $q = \frac{1}{w}\sum_f \frac{Q_f}{\sqrt{A_f}}$, where w is the thickness of the EDZ (assumed to be 0.3 m), Qf is the flow between intersections of the fracture, Af is the area of the fracture, and the sum is over the fractures intersecting a deposition hole.

upwards into the deposition tunnel zone. Depending on the capillary pressure of the backfill in the tunnel, the gas may concentrate in the EDZ around the tunnel, but the available gas storage volume in the EDZ is expected to be small. If not prevented by the capillary entry pressure of the backfill, gas could also collect in the tunnel. The amount of gas that could collect in the tunnel would depend on the capillary entry pressure for the fractures (compared to the backfill), as discussed, for example by /Wikramaratna et al. 1993/, and on the spacing between intersections of fractures with the tunnel.

It will be assumed that the aperture that is relevant for gas migration is the fracture transport aperture, e_t [m], which has been correlated with the transmissivity, T [m^2s^{-1}], according to /Hartley et al. 2004/:

$$e_t = 0.46T^{0.5} \qquad \text{Equation (5-8)}$$

If the capillary pressure in the backfill is negligible compared with that in the fractures (which may not be the case once the backfill has resaturated), the thickness, h [m], of a gas cushion that could collect at the top of the tunnel as a consequence of the capillary pressure that would need to be overcome before gas could enter the fracture is given by:

$$h = \frac{1}{\rho_w g}\frac{2\sigma}{e_t} \qquad \text{Equation (5-9)}$$

where

σ is the surface tension of water [Pa m], which is 0.074 Pa m at 12°C /Lide 1994/.

Table 5-7 shows the estimated fracture transport aperture and gas cushion thickness for fractures with transmissivities in the range 10^{-6}–10^{-10} m^2s^{-1}.

Gas from such a gas cushion may dissolve in water passing around the cushion. The general groundwater flow direction is taken to be at an angle φ to the axis of the tunnel, so groundwater flow through the tunnel could pass across the exposed lower surface of a gas cushion (the upper surface is neglected as there are presumed to be only a few discrete fracture intersections in contact with the gas cushion). Dissolved gas could diffuse into this flowing groundwater. The same general modelling approach could be used to estimate this as is used in estimating radionuclide diffusion into groundwater flowing around a deposition hole /Hartley et al. 2004/. In this approach, the advection-diffusion equation is solved in the boundary layer approximation (diffusion parallel to the groundwater flow is neglected). The flux, Q^t_{dg} [m^3 s^{-1} at STP], of dissolved gas is given by, if $\frac{w_t}{\tan\phi} \le l_c$:

$$\begin{aligned} Q^t_{dg} &\approx 2\int_0^{w_t/\tan\phi} c_s\sqrt{\frac{4D_e t_c(\xi)}{\pi}}q_t\, d\xi\, \sin\phi + \int_{w_t/\tan\phi}^{l_c} c_s\sqrt{\frac{4D_e t_c(\xi)}{\pi}}q_t\, d\xi\, \sin\phi \\ &= c_s l_c\sqrt{\frac{4D_e w_t q_t}{\pi}}\sqrt{\sin\phi}\left(1+\frac{1}{3}\frac{w_t}{l_c\tan\phi}\right) \end{aligned} \qquad \text{Equation (5-10a)}$$

Table 5-7. Dependence of aperture-related properties of fractures on fracture transmissivity.

Transmissivity [m^2s^{-1}]	$1\cdot10^{-6}$	$1\cdot10^{-7}$	$1\cdot10^{-8}$	$1\cdot10^{-9}$	$1\cdot10^{-10}$
Effective aperture [m]	$4.60\cdot10^{-4}$	$1.45\cdot10^{-4}$	$4.60\cdot10^{-5}$	$1.45\cdot10^{-5}$	$4.60\cdot10^{-6}$
Capillary pressure [Pa]	$3.21\cdot10^{2}$	$1.02\cdot10^{3}$	$3.21\cdot10^{3}$	$1.02\cdot10^{4}$	$3.21\cdot10^{4}$
Gas cushion thickness [m]	0.03	0.10	0.33	1.04	3.28

and, if $\frac{w_t}{\tan\phi} \geq l_c$:

$$Q_{dg}^{t} \approx 2\int_{0}^{l_c \tan\phi} c_s \sqrt{\frac{4D_e t_c(\xi)}{\pi}} q_t \, d\xi \, \cos\phi + \int_{l_c \tan\phi}^{w_t} dx \, c_s \sqrt{\frac{4D_e t_c(\xi)}{\pi}} q_t \, d\xi \, \cos\phi$$
$$= c_s w_t \sqrt{\frac{4D_e l_c q_t}{\pi}} \sqrt{\cos\phi}\left(1 + \frac{1}{3}\frac{l_c \tan\phi}{w_t}\right) \qquad \text{Equation (5-10b)}$$

where

φ is the angle between the (horizontal component of the) Darcy velocity of the groundwater and the axis of the tunnel,

w_t is the width of the tunnel [m],

l_c is the length of the gas cushion along the tunnel [m],

c_s is the saturation concentration of dissolved hydrogen at repository depth [m^3 at STP m^{-3}],

D_e is the effective diffusion coefficient for dissolved hydrogen in the saturated backfill [$m^2 s^{-1}$] (the flow area is that of the rock and the dissolved concentration is in terms of pore water volumes),

t_c is the time that the groundwater is in contact with the gas cushion [s],

q_t is the (horizontal component of the) Darcy velocity of the groundwater [m s^{-1}].

The width of a gas cushion in a deposition tunnel would be about 6 m, determined by the tunnel geometry /SKB 2004d/. The geometric mean value of the Darcy velocity at positions in the tunnels close to the deposition holes has been calculated in the DFN "base case" to be about $1.8 \cdot 10^{-5}$ m y^{-1} (i.e. $1.4 \cdot 10^{-5}$ m y^{-1} in rock domain HRD(D, E, M), and $2.4 \cdot 10^{-5}$ m y^{-1} in rock domain HRD(A)). The saturation concentration of hydrogen in water at the repository depth is 0.97 m^3 at STP m^{-3} (compare Table 5-5 and the above text). If the effective diffusion coefficient for hydrogen in the backfill is taken to be that of saturated bentonite, $2 \cdot 10^{-11}$ $m^2 s^{-1}$, and the length of the gas cushion along the tunnel was, say, 10 m, then the flow of dissolved gas from the cushion would be between $2.2 \cdot 10^{-3}$ m^3 y^{-1} at STP for flow parallel to the tunnel and $2.9 \cdot 10^{-3}$ m^3 y^{-1} at STP for flow perpendicular to the tunnel. This is insufficient to remove the gas generated by unrestricted corrosion at $2.1 \cdot 10^{-2}$ m^3 y^{-1} at STP from a defective canister, but could contribute significantly to the removal of gas if the gas generation was significantly constrained by water availability (see Table 5-2). If the diffusion coefficient in the backfill was larger than in pure bentonite, then larger flows of dissolved gas could occur. The flow only depends on the square root of the diffusion coefficient (Equation (5-10)), so an increased diffusion coefficient is not likely to be sufficient to allow all the gas to be removed in solution at the upper bound gas generation rate, but it could result in the dissolution of all the gas produced at lower, more likely, rates.

Gas may dissolve in groundwater as it passes through the formations above the repository. If the horizontal Darcy velocity of the groundwater at depth z above the repository is $q_h(z)$ [m s^{-1}], the capacity of horizontally flowing groundwater to transport gas away from the region above the repository is given by:

$$Q_{dg}^{h} = w_h \int_{0}^{d} q_h(z) H_H \rho_w g z dz$$
$$\approx w_h \frac{H_H \rho_w g}{2} \sum_{i=1}^{n} q_{hi}\left(z_i^2 - z_{i-1}^2\right) \qquad \text{Equation (5-11)}$$

where

Q_{dg}^{h} is the horizontal flow of dissolved gas between repository and the surface [m^3 s^{-1} at STP],

w_h is the width orthogonal to the groundwater flow direction of the region of groundwater that is saturated with gas [m],

d is the repository depth [m],

q_{hi} approximates $q_h(z)$ as constant in the interval (z_i, z_{i-1}), $z_0 = 0$, $z_n = d$.

Average values of the horizontal groundwater flow velocity over the whole repository area have been abstracted from the regional-scale EPM "reference case" calculations at 50 m intervals. Taking these velocities as representative of each 50 m interval, the total flow of dissolved gas that can be transported away from the repository per unit distance orthogonal to the groundwater flow direction is 1.4 m^3 at STP y^{-1} m^{-1}. The width of the region, w_h, that must become saturated with gas to remove in solution all the gas generated from a single defective canister at $2.1 \cdot 10^{-2}$ m^3 y^{-1} at STP is only about 1.5 cm. Without details of the channels followed by the gas it is hard to prove that this amount of groundwater will become saturated with gas, but it is at least plausible that it would be, and certainly at lower gas generation rates it becomes more likely.

This estimate of the amount of gas that would dissolve in flowing groundwater above the repository is only crude, because the groundwater flow above the repository is quite complex, including vertical flows in cells bounded by geological features, as well as horizontal flows. The consideration of the dissolution of gas from a single defective canister also assumes that there are no interactions between canisters; that is, the groundwater does not already contain dissolved gas from another canister before it reaches the region of the canister being considered. Finally, the kinetics of the dissolution process have been neglected.

5.2.2 Gas phase

Gas transport as a free gas through an otherwise water-saturated sparse fracture network is likely to follow a complex behaviour that is difficult to represent. The variable aperture and orientation of fracture planes, and the geometry of fracture intersections will mean that gas will travel in channels of varying width, determined largely by the local capillary pressure variation, which depends on the local fracture aperture. In some places, constrictions in the flow-path, may cause greater filling of the fracture planes with gas upstream of the fracture, compared to places where there are no such constrictions and the gas can flow freely in a narrow channel. Instabilities may also occur in the gas-phase flow, with pathways collapsing and reforming, with some transport occurring as separated bubbles.

Such characteristics of gas transport through water-saturated fractures have been seen in a number of laboratory experiments, and have been explored in modelling studies (see, for example, /Hoch et al. 2001/ and /Rodwell et al. 1999/ and references therein), although the upscaling of these results to the field scale has proved elusive.

Some insight into the potential capacity of the fracture network at Laxemar to transport the gas generated from a defective waste canister through the geosphere can be obtained by considering the width of the channel required to support the flow in an idealised fracture network.

Stable gas channel

In a steady-state situation, it is reasonable to assume that the vertical component of the pressure gradient in the gas phase will be approximately equal to the hydrostatic gradient in the water phase. There will be local variations due to variations in capillary pressure (controlled by fracture aperture variations). Locally, the steady-state gas flow rate, $\mathbf{Q_g}$, [m^3 s^{-1} at STP], is given by:

$$\mathbf{Q_g} = wT(w)\frac{\mu_w}{\mu_g}\left[\mathbf{e_z} + \frac{\nabla p_c(w)}{\rho_w g}\right]\frac{(\rho_w g z + p_s + p_c(w))}{p_s} \qquad \text{Equation (5-12)}$$

where

w is the width of the gas filled channel in the fracture [m],

$T(w)$ is the transmissivity of the gas filled part of the fracture [$m^2 s^{-1}$]. For a uniform, parallel-plate fracture, T would be independent of the gas channel width,

$\mathbf{e_z}$ is the unit vector in the vertical direction,

z is the depth below the surface [m],

p_s is the gas pressure at the surface [Pa],

$p_c(w)$ is the capillary pressure, which, in general, in a rough fracture will depend on the size of the gas channel in the fracture [Pa]. For a uniform fracture, the capillary pressure will be constant.

At the repository depth, the fracture transmissivities are expected to be 10^{-10}–10^{-8} m^2s^{-1}. This range corresponds to an effective fracture aperture range of ~ $5 \cdot 10^{-6}$–$5 \cdot 10^{-5}$ m, or a capillary pressure range of $3 \cdot 10^4$–$3 \cdot 10^3$ Pa. The cushion of gas in saturated rock that could be supported by capillary pressures of this magnitude would have a thickness of 3–0.3 m. This suggests that, although locally the capillary pressure and hence the gas pressure gradient may show considerable variation, when averaged over a length scale of a few metres, and probably a few centimetres, the gas pressure gradient will be close to the hydrostatic pressure gradient. If there is a well connected set of sub-vertical fractures, and if it is assumed that the fractures each have constant aperture (the approximation in the DFN groundwater flow modelling, although it may be better justified there than here), then Equation (5-12) for vertical gas flow becomes:

$$Q_g = wT \frac{\mu_w}{\mu_g} \frac{(\rho_w g d + p_s + p_c)}{p_s} \qquad \text{Equation (5-13)}$$

Assuming the gas flow rate is equal to the upper bound gas generation rate of $2.1 \cdot 10^{-2}$ m^3 y^{-1} at STP, the gas occupied channel widths in sub-vertical fractures of different transmissivities as a function of depth are shown in Figure 5-7. Note that the width of the channel does not necessarily have to comprise a single channel; the channel may well be branched, flowing round asperities and fracture infill, and indeed at any particular depth may be divided between a number of fractures. The division of flow between several fractures may occur if the gas spreads out laterally below some region of restricted vertical flow in the fracture network.

Figure 5-7 shows that below 100 m a channel width of only about 1–5 mm, depending on depth, is needed to support the maximum required gas flow rate, even for fractures with the lowest transmissivity of 10^{-10} m^2s^{-1}. For more transmissive fractures, the channel width required becomes even less. Towards the surface the incidence of more transmissive fractures is expected to increase, offsetting to some extent the effect of gas expansion in increasing the gas channel width.

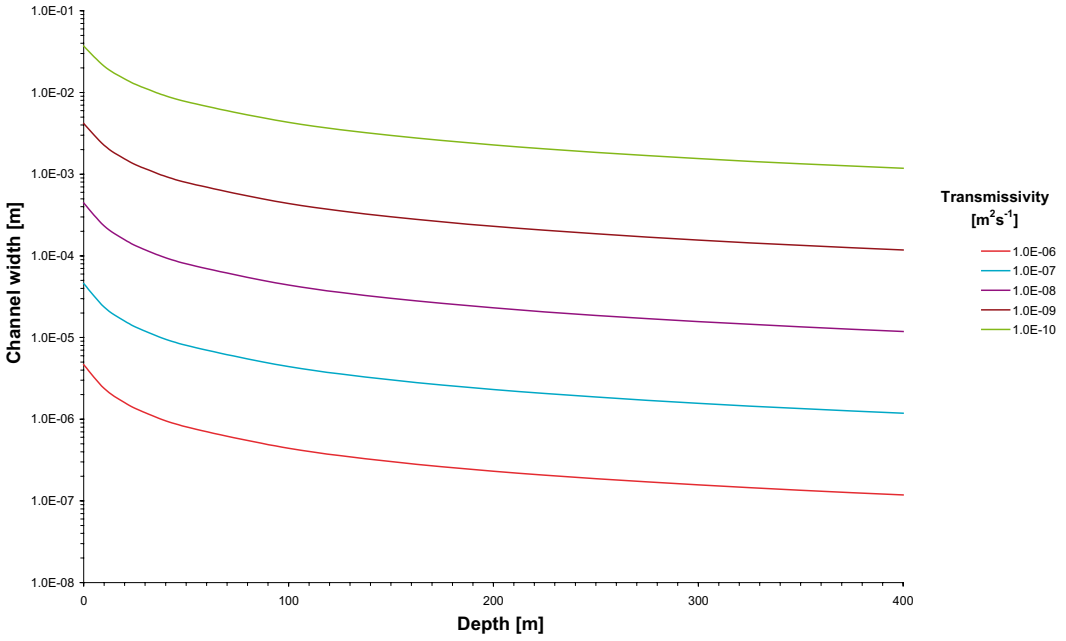

Figure 5-7. *Gas-filled channel width in idealised sub-vertical fractures as a function of depth and fracture transmissivity.*

The travel time, t_t [s], for gas to move from repository to the surface using this model is given by:

$$t_t = d \frac{e_t}{T\left(\frac{\mu_w}{\mu_g}\right)} \qquad \text{Equation (5-14)}$$

where

d is the repository depth [m],

e_t is the fracture transport aperture (see Equation (5-8)).

The travel times obtained for a continuous gas pathway using this model are given in Table 5-8.

These travel times are very short, probably unrealistically so. The concept of a continuous gas channel is invoked to give some feeling for the flow capacity of the rock to transport the gas. As already suggested, it is expected that the gas flow will be broken up by constrictions and intersections in the fracture network, and if the gas flow breaks up into bubbles then the travel time will be longer.

Instability

There have been few experiments on the stability of gas channels in fractured rock. The experimental data that do exist are often for artificial analogues of real fractures (e.g. /Hoch et al. 2001/).

Studies that have been carried out on gas flowing into Hele-Shaw cells[7] (see Figure 5-8) filled with viscous fluid, assuming an initially planar interface, show that:

a) at small inclinations of the Hele-Shaw cell, the interface between the two fluids stays a straight line,

b) at intermediate inclinations of the Hele-Shaw cell, a perturbation to the interface grows to form a stable finger whose width is a calculable fraction of the width of the Hele-Shaw cell,

c) at large inclinations of the Hele-Shaw cell, an apparently chaotic behaviour is observed in which fingers are formed that may branch or split. This is due to a viscous instability, and has been discussed elsewhere, for example /Saffman and Taylor 1958, Chuoke et al. 1959/.

Other relevant experimental work is concerned with the instability of a cylindrical gas jet injected into a liquid phase. At low injection velocities, bubbles form directly at the nozzle, and the forces acting on the forming bubble control their size. However, at higher injection velocities, a jet of gas issues from the nozzle and then breaks up into bubbles in a regular pattern (e.g. /Meister and Scheele 1967, Tomotika 1934/).

These observations suggest that a continuous gas channel in a fracture network may well be unstable.

Effects that could help to stabilise a gas channel include the variability in the capillary pressure due to variations in the fracture aperture, and interactions between the gas channel and the fracture walls.

Table 5-8. Travel time as a function of fracture transmissivity for gas to move along a continuous gas-filled channel from the repository to the surface.

Transmissivity [m^2s^{-1}]	$1.00 \cdot 10^{-6}$	$1.00 \cdot 10^{-7}$	$1.00 \cdot 10^{-8}$	$1.00 \cdot 10^{-9}$	$1.00 \cdot 10^{-10}$
Transport aperture [m]	$4.60 \cdot 10^{-4}$	$1.45 \cdot 10^{-4}$	$4.60 \cdot 10^{-5}$	$1.45 \cdot 10^{-5}$	$4.60 \cdot 10^{-6}$
Travel time [d]	$1.93 \cdot 10^{-2}$	$6.09 \cdot 10^{-2}$	$1.93 \cdot 10^{-1}$	$6.09 \cdot 10^{-1}$	1.93

[7] In a Hele-Shaw cell, the fluid is confined between two closely spaced, parallel, planar surfaces.

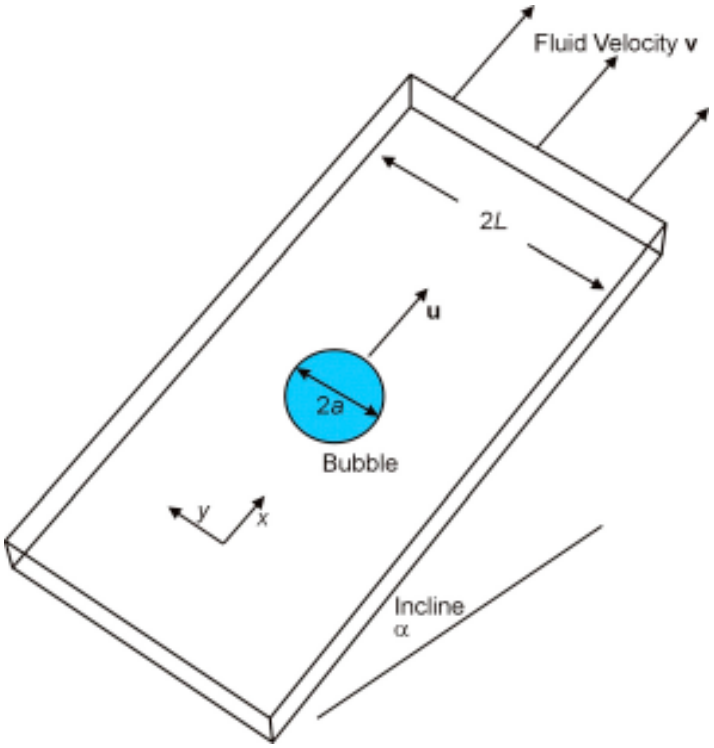

Figure 5-8. *A schematic diagram shows a gas bubble rising in a Hele-Shaw cell.*

The first effect has been observed in experiments with artificial rough fractures, for example /Hoch et al. 2001/.

The second effect has been observed in experiments with a Hele-Shaw cell /Hoch et al. 2001/. When the water in the Hele-Shaw cell was dyed with silicone oil, gas flows through the Hele-Shaw cell were consistent with standard models for such flows (i.e. the gas migrated as bubbles, at speeds consistent with Equation (5-16) given below). However, when the water was dyed with fluorescein, which is a surfactant, it became possible to form a narrow gas channel that persisted for up to a day. The difference between the two experiments is thought to be due to non-wetting of the Hele-Shaw cell surfaces by the water dyed with fluorescein. The gas was able to contact the Hele-Shaw cell surfaces, which stabilised the gas channel, and also led to trapping of gas and caused bubbles to migrate more slowly than expected. A repository for low-level and intermediate-level radioactive waste could contain organics and NAPLs, which might allow the gas that is generated to contact fracture surfaces, thereby stabilising a gas channel. However, the SKB repository for high-level radioactive waste will not contain organics and NAPLs, and it is expected that the geological history of the host rock (i.e. always in contact with water) will ensure that the fracture surfaces are wetted by the water rather than the gas.

On the basis of these considerations, it seems likely, although not proven, that a continuous gas channel will break up into bubbles.

Flow of micro-bubbles

It has been suggested that the gas might flow as ‘micro-bubbles’, understood to be bubbles whose diameter is smaller than the fracture aperture, possibly in the range 10^{-6}–10^{-4} m.

Two arguments can be brought forward against gas migrating in the form of micro-bubbles:

a) It is difficult to form micro-bubbles by conventional snap-off methods /Hoch et al. 2001/.

b) Micro-bubbles dissolve rapidly into the surrounding water /Hoch et al. 2001/ unless the aqueous phase is sufficiently over-saturated with gas.

A simple model has been developed /Epstein and Plesset 1950, Hoch et al. 2001/ for the change in radius R_m [m] of a spherical gas bubble placed in water in which the dissolved gas concentration is c_0 [m^3 at STP m^{-3}]. The derivation assumes that the rate at which mass flows into or out of the bubble can be determined by solving the diffusion equation (with neglect of the motion of the bubble boundary), and that the ideal gas law applies to the gas in the bubble. The differential equation describing the change in radius of the bubble with time is:

$$\frac{dR_m}{dt} = p_s \frac{1}{\left(p_w + \frac{4\sigma}{3R_m}\right)} D_w \left[c_0 - H_H\left(p_w + \frac{2\sigma}{R_m}\right)\right]\left(\frac{1}{R_m} + \frac{1}{\sqrt{\pi D_w t}}\right) \qquad \text{Equation (5-15)}$$

where

p_s is standard pressure (101,325 Pa),

p_w is the ambient water pressure [Pa],

σ is the surface tension of water [Pa m],

D_w is the diffusion coefficient for dissolved hydrogen in water [$m^2 s^{-1}$],

H_H is a Henry's law constant for hydrogen dissolved in water [m^3 at STP $m^{-3} Pa^{-1}$].

This model was used to calculate the approximate lifetimes of micro-bubbles of various sizes present in water. Two saturation conditions, unsaturated and saturated, and two ambient pressure conditions, near surface and deep, were considered. The gas bubbles are unstable unless the surrounding water is sufficiently over-saturated, and in the case of micro-bubbles lifetimes are short (see Table 5-9).

This leads to a conceptual model in which any small bubbles formed at depth might grow in size because of local over-saturation of the groundwater (if smaller than a critical size for the given over-saturation and pressure they will dissolve, otherwise they will grow). The bubbles continue to grow unless they migrate to a region of lower gas saturation, in which case they will start to re-dissolve. This process just helps to propagate the dissolved gas saturation front.

The above arguments suggest that it is unlikely that micro-bubbles (i.e. bubbles whose diameters are less than 10^{-4} m) will contribute significantly to gas migration.

Flow of Hele-Shaw bubbles

It therefore seems that the likely mechanism by which gas will migrate through a fracture network is as a stream of Hele-Shaw bubbles (i.e. bubbles whose diameters are larger than the fracture aperture). By assuming this mechanism, it is possible to develop an understanding of gas and induced groundwater flows in planar, constant aperture fractures, which then can be used as a guide for discussing the flows in a fracture network.

Table 5-9. The lifetime of a gas bubble as a function of its initial radius, R_0, its depth below the surface, z, and the saturation state of the groundwater.

Near surface bubble, *z* = 0 m			
Saturation state	**Bubble lifetime [s]**		
	***R*0 = 10^{-6} m**	***R*0 = 10^{-5} m**	***R*0 = 10^{-4} m**
unsaturated	$7.8 \cdot 10^{-3}$	$9.6 \cdot 10^{-1}$	$10.3 \cdot 10^{1}$
saturated	$12.0 \cdot 10^{-3}$	$6.3 \cdot 10^{0}$	$5.9 \cdot 10^{3}$
Bubble at depth, *z* = –520 m			
Saturation state	**Bubble lifetime [s]**		
	***R*0 = 10^{-6} m**	***R*0 = 10^{-5} m**	***R*0 = 10^{-4} m**
unsaturated	$10.2 \cdot 10^{-3}$	$10.4 \cdot 10^{-1}$	$10.4 \cdot 10^{1}$
saturated	$3.0 \cdot 10^{-1}$	$3.0 \cdot 10^{2}$	$3.0 \cdot 10^{5}$

The speed at which a Hele-Shaw bubble rises upwards is taken to be /Hoch et al. 2001/:

$$u = -\frac{e_f^2}{12\mu_w}\left(\rho_w - \rho_g\right)\mathbf{g}\cdot\mathbf{e_x} \qquad \text{Equation (5-16)}$$

where

e_f is the aperture of the Hele-Shaw cell (an analogue for a planar, constant aperture fracture) [m],

ρ_g is the density of the gas [kg m^{-3}],

g×ex is the magnitude of the acceleration due to gravity in the plane of the Hele-Shaw cell [m s^{-2}].

This expression is reasonably accurate provided that:

a) the Hele-Shaw cell is sufficiently wide compared to bubble size that the side walls do not cause the bubble to distort, and

b) the water wets the surfaces of the Hele-Shaw cell.

The bubble speed depends mainly on the fracture aperture. In particular, an aperture of 10^{-5} m implies a speed in a vertical fracture of $6.6\cdot10^{-5}$ m s^{-1} or $2.1\cdot10^{3}$ m y^{-1}, and so the travel time to the surface would be 91 days. The bubble speed increases (and the travel time decreases) by a factor of 100 if the fracture aperture is 10^{-4} m.

These travel times, which have been derived for an idealised model of a fracture, are unrealistically short. It is expected that constrictions and intersections in the fracture network will break up the gas flow; in some places gas will be trapped, thereby delaying the migration of the gas back to the surface.

The other parameter which affects the quantity of gas that can be transported by a stream of Hele-Shaw bubbles is the largest radius of bubble that is stable. To the best of our knowledge, this issue has not been studied rigorously. However, it may be acceptable to adapt models for the break-up of three-dimensional bubbles in viscous fluids /Grace et al. 1978/ to this case. In such models, a disturbance to the surface of a bubble grows in two stages:

a) In the first, the amplitude is small with respect to the wavelength of the disturbance λ, and a characteristic growth time can be predicted using the theory of unstable interfacial waves incorporating effects of viscosity and surface tension /Plesset and Whipple 1974/. The indentation grows exponentially and moves along the interface at (approximately) the local velocity in the undisturbed system.

b) In the second, the indentation grows at a nearly constant rate, and its motion along the interface is greatly inhibited.

Break-up of the bubble occurs if the first (exponential) growth stage is complete before the disturbance has reached the side of the bubble.

Now, the interface is unstable only for disturbances with wavelengths λ greater than λ_c, where /Plesset and Whipple 1974/:

$$\lambda_c = 2\pi\sqrt{\frac{\sigma\frac{\pi}{4}}{\left(\rho_w - \rho_g\right)\left|\mathbf{g}\cdot\mathbf{e_x}\right|}} \qquad \text{Equation (5-17)}$$

If the aperture of the Hele-Shaw cell, e_f, is small enough, a bubble will move so slowly that any disturbance can not be expelled from the region of instability before it has time to grow. In this case, the stable bubble radius, R_h, is actually determined by λ_c, i.e.

$$R_h = \frac{\lambda_c}{\pi} \qquad \text{Equation (5-18)}$$

Equation (5-18) is assumed to apply to planar, constant aperture fractures with apertures less than about 10^{-4} m, and for these fractures the critical, or maximum, Hele-Shaw bubble radius is about $5 \cdot 10^{-3}$ m.

Finally, for a stream of Hele-Shaw bubbles the total gas flow rate is given by:

$$Q_g = 2\alpha_g u R_h e_f \qquad \text{Equation (5-19)}$$

where α_g is the gas volume fraction, defined to be the volume fraction that contains gas in the region where bubbles are flowing.

Combining Equations (5-16) to (5-19), for a single stream of Hele-Shaw bubbles which are rising vertically and just touching (i.e. $\alpha_g = \pi/4$), it can be shown that the minimum fracture aperture required to support the upper bound gas generation rate of $2.1 \cdot 10^{-2}$ m^3 y^{-1} at STP is about $14 \cdot 10^{-6}$ m at the depth of the repository and about $50 \cdot 10^{-6}$ m at the surface.

How does this minimum fracture aperture compare to the apertures predicted by the DFN model for those fractures that intersect the deposition tunnels? The repository at Laxemar is designed to straddle two rock domains. The south-western part of the repository will be in rock domain HRD(D, E, M), with a lower intensity of fracturing than the rest, which will be in rock domain HRD(A). The analysis presented here is specifically for domain HRD(D, E, M), since if gas can migrate from a defective canister to the surface through this part of the fracture network, then it will be able to do so also for domain HRD(A).

Considering only stochastic fractures with sizes greater than 10 m, P10 varies between 0.0266 m^{-1} for deposition tunnels oriented roughly West-East and 0.0347 m^{-1} for deposition tunnels oriented roughly South-North. In other words, even for the least favourable alignment, on average[8] about 8 fractures from the stochastic fracture network will intersect the axis of a 300 m long deposition tunnel. This number increases to about 15 if the deposition tunnel is modelled as a cylinder 3 m in radius and 300 m long. However, a percolation study[9] suggests that just 60% of these fractures are connected to the surface. A typical deposition tunnel is therefore intersected by about 9 fractures that belong to the fracture network connecting the tunnel to the surface. Figure 5-9 shows the distribution of transport apertures (see Equation (5-8)) for the fractures that intersect the deposition tunnel. The minimum transport aperture is $15 \cdot 10^{-6}$ m.

These observations suggest that at Laxemar there will be sufficient fractures with large enough apertures to transport the gas generated from a defective waste canister through the geosphere. Even for the upper bound gas generation rate, the discrete fracture network should have the capacity to carry the gas from a defective canister to the surface.

5.3 Implications for groundwater flow modelling

The question then arises as to the implications of gas transport as a free gas for the flow of groundwater. In this subsection, previously derived results for single Hele-Shaw bubbles will be used to estimate the effects of a stream of Hele-Shaw bubbles on the entrainment of water in a vertical, planar, constant aperture fracture (this model was developed originally in /Nash et al. 1997/).

---

[8] The stochastic fractures are generated by a Poisson process. Hence, the separation of fracture intersections, x, is given by the cumulative density function $D(x) = 1 - \exp[-\lambda x]$, where $\lambda = 0.0266$ m^{-1}, and the number of fracture intersections, n, per deposition tunnel (assumed to be 300 m long) is given by the probability density function $P(n) = \frac{(300\lambda)^n \exp[-300\lambda]}{n!}$. It follows that it is extremely unlikely that a deposition tunnel will have no intersections.

[9] The study was for a single tunnel. The presence of other deposition tunnels will increase the connectivity.

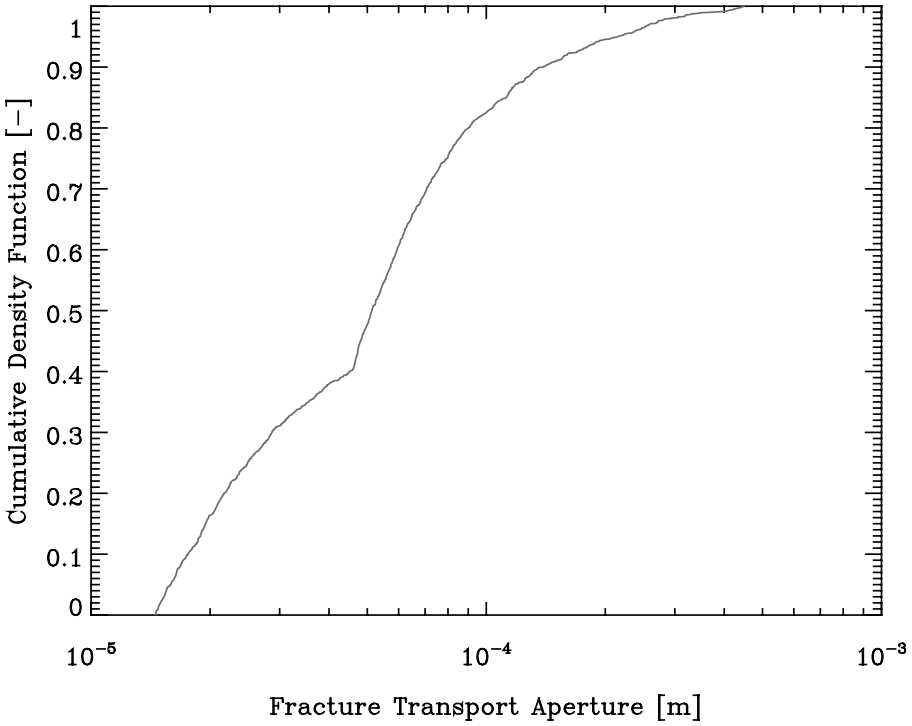

Figure 5-9. *Cumulative density function for the transport apertures of stochastic fractures greater than 10 m in size that intersect a deposition tunnel in domain HRD(D, E, M) at Laxemar.*

For a circular gas bubble rising in a fracture, the radial and tangential components of the velocity of the surrounding groundwater are given by:

$$u_{w,r} = u\frac{R_h^2}{r^2}\cos(\theta)$$
$$u_{w,\theta} = u\frac{R_h^2}{r^2}\sin(\theta)$$

Equation (5-20)

where

u is the terminal velocity of the bubble (see Equation (5-16)) [m s^{-1}],

r is the radial coordinate [m], which is measured relative to the centre of the circular bubble, and

θ is the angular coordinate, which is measured from vertical.

Therefore, the vertical component of the velocity of the groundwater is:

$$u_{w,z} = u\frac{R_h^2}{r^2}\cos(2\theta)$$

Equation (5-21)

This result can be used to estimate the effects of a stream of bubbles on the entrainment of liquid. The assumption will be made that the velocity field surrounding a stream of bubbles can be calculated by linear superposition of the solution for a single bubble. This assumption is accurate only for a disperse system of bubbles, where the distance between the bubbles is large enough for bubble-bubble interactions to be negligible.

An infinite stream of Hele-Shaw bubbles, with centres separated by distance s and with radii R_h, rising in a line is considered. The vertical component of the velocity at a point with co-ordinates (x,z) in the liquid is given by:

$$\bar{u}_{w,z}(x,z) = \sum_{j=-\infty}^{\infty} u \frac{R_h^2}{r_j^2} \cos(2\theta_j) \qquad \text{Equation (5-22)}$$

where

$$r_j^2 = x^2 + (z - js)^2$$
$$\sin(\theta_j) = \frac{x}{r_j} \qquad \text{Equation (5-23)}$$

Symmetry of the bubble stream implies that the liquid velocity between each adjacent pair of bubbles must be similar. Hence, by integrating over the region of symmetry, it is possible to calculate an average vertical flow rate:

$$Q_{w,z} = \frac{1}{s} \int_{-\infty}^{\infty} dx \int_0^s dz\, e_f\, \delta(x,z) \bar{u}_{w,z}(x,z) \qquad \text{Equation (5-24)}$$

where δ(x, z) is an indicator function, which equals one if the point (x, z) is in the liquid surrounding the gas bubbles, and equals zero if the point is inside the gas bubbles.

This integral can be simplified to give (cf. Equation (2.3.6) in /Nash et al. 1997/):

$$\frac{Q_{w,z}}{2uR_h e_f} = \frac{8}{\pi} \alpha_g^2 \int_0^1 d\eta\, \mathrm{Im}\left\{ \coth\left[2\alpha_g \left(\eta - i\sqrt{1-\eta^2} \right) \right] \right\} \qquad \text{Equation (5-25)}$$

where

α_g is the gas volume fraction, that is the fraction of the bubble region, $x<R_h$, containing gas, i.e. $\alpha_g = \frac{\pi R_h}{2s}$. Note that $0 \le \alpha_g < \frac{\pi}{4}$.

The model predicts that there is no contribution to the average liquid flow rate from liquid movement outside the bubble region. This does not imply that the liquid particles outside the bubble region are stationary, but that they move on a circulatory path such that there is no net liquid displacement from each rising bubble.

The right-hand side in Equation (5-25) can be evaluated using standard numerical methods.

The model can be extended to include a first approximation to the effects of bubble-bubble interactions on the gas phase by assuming that each bubble feels the influence of the other bubbles due to the velocity they induce in the surrounding groundwater. The velocity of an individual bubble is assumed to increase by an amount equal to the sum of the liquid velocities from adjacent bubbles, calculated at the origin of the bubble under consideration. Thus the increased bubble velocity is:

$$u^* = u\left(1 + \frac{4}{3}\alpha_g^2\right) \qquad \text{Equation (5-26)}$$

and the total gas flow rate becomes:

$$\frac{Q_g^*}{2uR_h e_f} = \alpha_g \left(1 + \frac{4}{3}\alpha_g^2\right) \qquad \text{Equation (5-27)}$$

The non-dimensional gas flow rate and the non-dimensional induced groundwater flow are plotted as a function of the gas volume fraction in Figure 5-10.

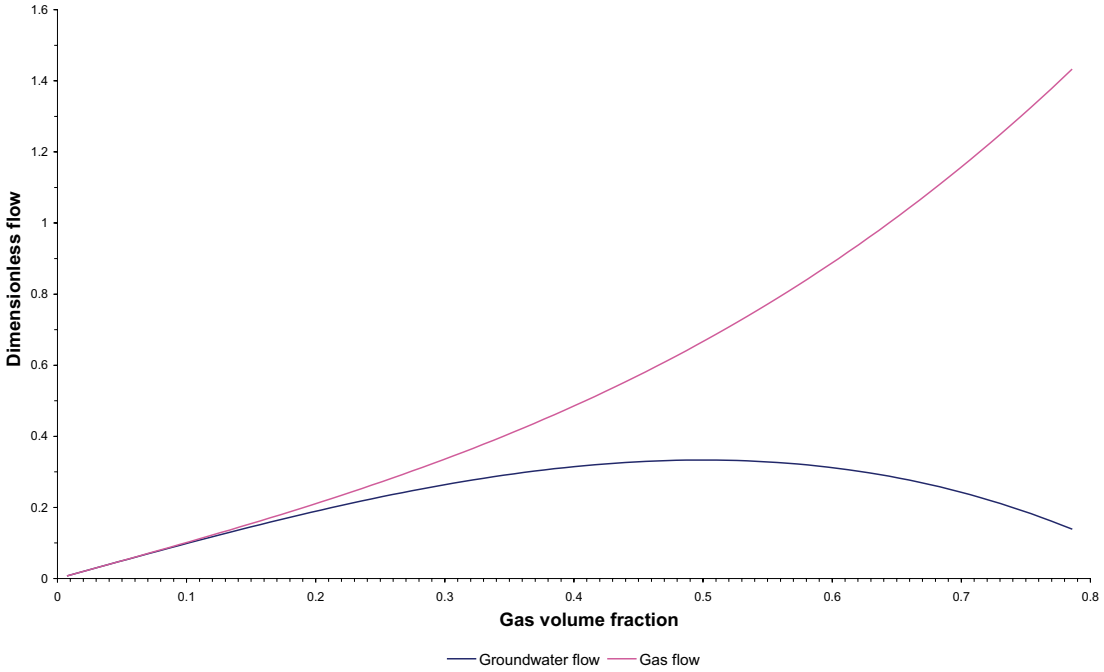

Figure 5-10. *The non-dimensional induced groundwater flow, $Q_{w,z}/2uR_he_f$, and the non-dimensional gas flow rate,$Q_g^*/2uR_he_f$, as a function of gas volume fraction.*

It follows that, in this simple model, the induced groundwater flow is always less than the corresponding gas flow rate, and that becomes more so as the gas volume fraction increases. The maximum induced groundwater flow occurs when the bubbles are very far apart, and then is equal to the gas flow rate[10].

To summarise, the model suggests:

a) A stream of gas bubbles will entrain groundwater.

b) The net flow of groundwater will be confined mainly to the bubble region.

c) It can be assumed, conservatively, that the induced groundwater flow is equal to the gas flow rate.

The conceptual model does not imply that groundwater will be transported rapidly to the surface. Rather, because of the inclination of the fractures, and constrictions and intersections in the fracture network, gas will be trapped in some places and that will disrupt any induced groundwater flow back to the surface. Groundwater possibly may flow quite quickly between pockets of trapped gas, but will be unable to cross those gas pockets.

At the depth of the repository the upper bound gas generation rate, and hence by implication the maximum induced groundwater flow, will be $4.3\cdot10^{-4}$ m^3 y^{-1}.

A stream of gas bubbles rising from the repository may be expected to perturb the pre-existing groundwater flow near the repository over an area that is large enough to supply the induced groundwater flow. The geometric mean value of the Darcy velocities at positions in the tunnels close to the deposition holes has been calculated in the DFN "base case" model to be about $1.8\cdot10^{-5}$ m y^{-1}. The area through which this flow occurs that would be required to supply the maximum possible induced groundwater flow (i.e. $4.3\cdot10^{-4}$ m^3 y^{-1}) is just 24 m^2. Since the width

[10] This is just a consequence of Darwin's Theorem /Darwin 1953/, which states that "the added mass for a body translating uniformly in an infinite expanse of perfect fluid equals the drift-volume times the density of the fluid".

of a deposition tunnel is 5.5 m, the length of the tunnel that might be affected by the induced groundwater flow is 4.4 m. The part of the tunnel affected will be longer if the local Darcy velocity is smaller.

This result suggests that gas transport as a free gas would be expected to perturb the groundwater flow only locally to a defective waste canister that is generating the gas.

5.4 Implications for radionuclide transport

Should a separate gas phase flow appear then there are three mechanisms by which this might affect radionuclide transport:

a) the gas phase may transport volatile radionuclides,

b) as discussed in Section 5.3, the migrating gas may modify the groundwater flow with a corresponding effect on the transport of water-borne radionuclides,

c) it is known that colloids or other species may concentrate at the gas-water interface, and so may be transported along with any migrating gas bubbles that are formed.

The only volatile radionuclides that have been considered as potentially important for a copper canister spent fuel repository are ^{14}C in the form of carbon dioxide or methane and ^{222}Rn. The first has been assessed as radiologically insignificant even if it is released directly from a canister to the biosphere with no delay or dispersion in the geosphere /SKB 1999/.

Substantial quantities of ^{222}Rn may build up in a canister from in-growth of its parent ^{226}Ra from uranium decay, although this takes time. A canister is estimated to contain around 10^{11} Bq of ^{222}Rn after a few hundred thousand years /SKB 1999/. This corresponds to a generation rate of 6.6 TBq y^{-1}. What proportion of this release rate could be propagated to the surface would depend on the travel time to the surface, and the consequences would depend on the exposure pathway (accumulation in an occupied building is likely to be the most significant scenario). Some of the repository derived ^{222}Rn may dissolve in groundwater during transport as well as decaying. ^{222}Rn could also be released from fracture surfaces into a flowing gas stream, but this source is insignificant compared with the spent fuel.

Migrating gas may also affect the movement of groundwater and hence the transport of dissolved radionuclides. The potential consequences of such interactions will be mitigated by the following observations:

- With a small defect, it is not possible to get release of dissolved radionuclides and gas at the same time. The situation may be different if a large hole develops.
- Gas migration can only affect transport of dissolved radionuclides released from a different canister.
- Migrating gas is only likely to affect groundwater flows in the neighbourhood of a small number of canisters local to the canister generating gas, and there is a low probability that one of these also may be defective and releasing radionuclides.

A model study has been carried out to ascertain the importance of radionuclide transport on colloids attached to gas bubbles /Neretnieks and Ernstson 1997/. In the study it was assumed that all gas from a damaged canister is released in the form of small bubbles covered with montmorillonite particles from the bentonite buffer. The clay was further assumed to have sorbed radionuclides from the leaching of the fuel. The particles were assumed to remain irreversibly bound to the bubbles, while all gas was assumed to reach the ground surface. The actinides remained irreversibly bound to the clay particles, while caesium and strontium desorbed from the bentonite clay and underwent matrix diffusion combined with sorption during transport through the rock. The results of the calculations showed that the releases to the biosphere were very limited for all nuclides even with these very pessimistic assumptions.

5.5 Summary of issues relating to far field gas migration at Laxemar

In this section (Section 5), aspects are addressed of the consequences of the production of gas from iron corrosion in the small proportion of canisters (< 0.1%) that it is considered may have manufacturing defects that will allow water ingress. The main issues considered are:

a) The potential rate of gas generation from a defective canister (necessary in order to assess the effects of this gas generation).

b) The fate of gas in the geosphere (gas migration through bentonite buffer is part of buffer performance assessment and is considered elsewhere).

c) The transport of volatile radionuclides by migrating gas.

d) The effect of migrating gas on groundwater flow and the transport of dissolved radionuclides.

Gas is generated in defective canisters by anaerobic corrosion of the cast iron insert as a result of water ingress through the defect. The rate of gas generation is determined by the iron corrosion rate, the iron surface area exposed to water, and the availability of water. The corrosion rate of cast iron, once a passivating layer has formed, has been measured at 0.1 μm y^{-1}. At this corrosion rate and assuming that the whole surface of the iron insert is exposed to an unlimited supply of water, the rate of hydrogen production would be $2.1 \cdot 10^{-2}$ m^3 y^{-1} at STP. This is an upper bound to the rate of gas production from a canister as in practice there are a number of factors which will limit the production of gas.

Water availability from ingress through the defect in the canister will be limited by the flow capacity of the bentonite, the build up of gas pressure in the canister opposing water ingress through the defect, and the capacity of the geosphere to supply groundwater:

a) The constraint on water flow through the bentonite is estimated to limit gas production to about $7.1 \cdot 10^{-3}$ m^3 y^{-1} at STP.

b) The build up of gas pressure will limit liquid water ingress through the defect, reducing the influx by an order of magnitude over an estimated 15,000 years after the bentonite buffer has become resaturated and water ingress into the canister has begun. Eventually the influx of liquid water will become so low that the diffusion of water vapour through the defect will become the main mode of water ingress into the canister. The maximum gas generation rate that can be supported by water vapour diffusion through the defect is estimated to be $1.7 \cdot 10^{-5}$ m^3 y^{-1} at STP.

c) The capacity of the geosphere to supply groundwater to support corrosion in a defective canister will vary substantially between deposition holes because it depends on the nature and number of flowing fractures intersecting the deposition hole. For about half of the deposition holes, the available local groundwater flow may be sufficient to support corrosion at the measured unconstrained rate. For the remaining deposition holes this will not be the case, many (particularly those in rock domain HRD(D, E, M)) having no intersections with flowing fractures.

Gas generation may also be limited by restrictions on movement of water within a canister, in particular, in the long term, from the build up of corrosion product.

The net result of the above considerations is that the upper bound gas generation rate of $2.1 \cdot 10^{-2}$ m^3 y^{-1} at STP is unlikely to be realised in most defective canisters whilst these contain only a single small hole. The generation rate for these is unlikely to exceed ~ 10^{-2} m^3 y^{-1} at STP, and the build up of gas pressure is likely to reduce the rate to less than ~ 10^{-4} m^3 y^{-1} at STP. Bear in mind that no gas escapes from the defective canister until the gas pressure has reached at least hydrostatic. Gas generation will continue, but possibly only at these very low rates, for at least 250,000 years.

Should the build up of corrosion product, or some other event, produce a larger hole in a canister, some of the above constraints would have less effect; in particular, the build up of gas pressure may not limit water ingress so effectively. It has been estimated that it would take 200,000 years before the build up of corrosion product would start to disrupt a canister. Even if an enlarged defect were formed, water supply from the geosphere would still limit water supply to many defective canisters.

The amount of gas that would be trapped in backfilled tunnels on repository closure is significant, on a repository scale, compared with that produced from corrosion in a defective canister. $3 \cdot 10^4$–$6 \cdot 10^4$ m^3 of air at surface conditions would be trapped per *defective* canister in tunnels. This is more than the $5.9 \cdot 10^3$ m^3 of gas at STP that could be produced from each defective canister. However, the gas from a defective canister may not enter a tunnel or disperse along a tunnel very far from the location of the canister, and the volume of gas produced in a defective canister is substantially more than that trapped in the segment of the tunnel local to that borehole. The gas trapped in a tunnel will largely dissolve as the tunnel re-saturates and the pressure is restored to hydrostatic.

The quantities of natural gases dissolved in the groundwater at Laxemar are assessed as unlikely to have a significant effect on repository performance.

Gas released from a defective canister needs to pass through the bentonite buffer if it is to escape from the vicinity of the canister. Even at the constrained gas generation rates discussed above, gas transport through the bentonite by diffusion in solution from the small defect will be inadequate to remove all the gas generated. However, if the gas pressure opens a gap between the canister and the buffer into which the gas can spread, the contribution of diffusion of dissolved gas to gas transport through the buffer may become more significant. In any event, is expected that, if the gas pressure rises sufficiently, movement of a free gas phase through the bentonite buffer will occur.

Once the gas has passed through the bentonite, it might collect in the tunnel and the EDZ associated with the tunnel, and it might enter the fracture network either from the tunnel or directly from the deposition hole. Some of the gas will dissolve in the groundwater and be transported away by the groundwater flow. However, the groundwater flow at the repository depth is very slow, and it is unlikely that gas generated at the upper bound generation rate of $2.1 \cdot 10^{-2}$ m^3 y^{-1} at STP could all dissolve and be transported away in groundwater flowing through the neighbourhood of the repository. If, as seems quite probable for most defective canisters, the gas release rate is 1–2 orders of magnitude less than the upper bound, it is possible that much if not all of the gas could be transported away in solution. A difficulty in demonstrating how much gas might dissolve is in establishing the degree of contact between the gas and water phases, particularly in a fracture network.

Depending on the degree of contact between the migrating gas and the groundwater, and on the groundwater flow rates in the rock between the repository and the surface, more gas might disperse into solution during its migration to the surface. If flowing groundwater to a width of 1.5 cm normal to the horizontal component of the groundwater flow direction becomes saturated with gas, then the gas from a single canister produced at $2.1 \cdot 10^{-2}$ m^3 y^{-1} at STP could all dissolve before it reaches the surface.

Should the gas not all dissolve, simple estimates show that the gas transport capacity of the fracture network, assuming that it is sufficiently connected between the location of the defective canister and the surface, should be more than adequate to easily transport the gas to the surface without any significant increase in gas pressure in the neighbourhood of the repository.

Should free gas phase migration be sustained between the repository and the surface, this would be capable of transporting volatile radionuclides relatively rapidly from the repository to the surface. The only significant such radionuclides identified in the waste canisters are ^{14}C and ^{222}Rn. Direct release of the volatile ^{14}C in defective canisters to the surface has been previously

assessed as not causing a significant radiological hazard and so the capacity of migrating gas to transport this radionuclide is immaterial. Similar conclusions were reached for ^{222}Rn release, although it may be desirable to assess the consequences of ^{222}Rn release into an occupied dwelling.

Migrating gas may also affect the movement of groundwater and hence the transport of dissolved radionuclides. Such transport is mitigated by the following observations:

- With a small defect, it is not possible to get release of dissolved radionuclides and gas at the same time. The situation may be different if a large hole develops.
- Gas migration can only affect transport of dissolved radionuclides released from a nearby different canister, and the probability of two defective canisters being present close together must be quite small.
- Migrating gas is only likely to affect groundwater flows in the neighbourhood of a small number of canisters local to the canister generating gas, and there is a low probability that one of these also may be defective and releasing radionuclides.

6 Conclusions

This hydrogeological study of L 1.2 within the SR-Can project has considered two main issues:

1. Groundwater flow and transport from a repository to the surface to provide input to SA calculations at a range of release times throughout the temperate period;
2. An assessment of gas generation, migration and its potential effect on groundwater flow.

The findings are summarised below.

6.1 Conclusions for groundwater flow

As part of the assessment of the groundwater pathway, models on two different scales were constructed: regional-scale transient porous medium models, and more detailed repository-scale steady-state models using a DFN representation. The regional-scale was used to assess the effects of transient processes such as land-rise and the evolution of hydro-geochemistry coupled to groundwater flow, as well as to perform a sensitivity study of transport performance measures (PM's) to conceptual and parameter uncertainties. The repository-scale modelling was performed with much more detail to resolve the flow around individual deposition holes and calculate flow-paths to the surface for input to SA calculations. For all models, transport was characterised by four main PM's for each canister position in terms of travel-time, initial Darcy velocity, path-length and F-factor along flow-paths started from each canister position. Additional PM's were derived for the DFN repository-scale models such as distances and travel-times in the EDZ and tunnels, as well as equivalent flow-rates, *Qeq*, used in near-field models. Finally, the DFN model is also used to simulate the deposition hole screening process to give three extra PM's to be used in SA analyses.

The reference case from the SDM L 1.2 has been utilised here to quantify SA performance measures based on particle tracking for a release from the canister positions at times in the past, present and future to study the evolution of discharge areas and performance measures over the current temperate climatic period, and to be used as an analogue for future temperate periods. The model uses an ECPM conceptual model, where hydraulic properties are based on upscaling a Hydro-DFN. The simulations are transient and model the effects of shore-level displacement and changes in the salinity in the Baltic Sea on groundwater flow and hydro-geochemical mixing. The time period modelled is from 8,000 BC to 20,000 AD. At chosen release times, particles are released from the canister positions to calculate pathlines using the instantaneous velocity field at the chosen times. This gave ensemble statistics for performance measures as well as the spatial distribution of exit locations.

It was found that least favourable performance measures are found between about 2,000 BC and 1,000 BC. This time-frame coincides with that at which the coastline is directly above the starting positions. After the present-day, the performance measures are generally very constant. The only significant changes take place in the 20–30% of flow-paths that discharge at the shoreline which slowly retreats in the future. Based on the evolution of performance measures and exit locations, 6,000 BC, 2,000 BC, 2,020 AD and 6,000 AD were chosen as representative times to be used in the more detailed repository-scale modelling.

A series of variants have been simulated to explore the sensitivity of the SA performance measures, exit locations and groundwater chemistry to various uncertainties that were highlighted in the SDM or were considered important for SA. One group of simulations were performed to study the sensitivity to the deterministic deformation zones, including cases with spatial variability within deformation zones, and with low confidence zones absent. Another group included variants based on variations in the Hydro-DFN model. A third group investigated sensitivities to transport parameters. Finally, the sensitivity to the hydraulic soil domain model was addressed. One variant that stood out has a higher transmissivity in the sub-vertical Set_C giving greater heterogeneity than the reference case since it gave the least favourable performance measures of the cases

explored, although the predicted salinities for this case suggest it perhaps has implausibly high hydraulic conductivities. The variants with stochastic variability within the deterministic deformation zones suggested that plausible variants are found when the standard deviation in transmissivity is reduced by subtracting 0.5 from std. log(T) to give values of std. log(T) around 1.0. A variant with a correlated relationship between fracture transmissivity-size resulted in slightly worse performance measures than the reference case with a semi-correlated model. Not surprisingly, the case with low confidence deterministic deformation zones removed gave improved performance measures.

In the cases where all deterministic deformation zones were used, about 3% of the start positions start within the HCD, but a clear effect could be observed by removing these low confidence zones. Consideration was also given to the difference in starting particles in the different hydraulic rock domains. The initial Darcy velocity in HRD(A) is significantly higher than HRD(D, E, M) and has less spread between the 25th and 75th percentiles. Similarly the F-factor has a median about half an order of magnitude higher in HRD(D, E, M) than HRD(A). Considering how performance measures vary between tunnel locations, the shortest travel times occur in repository subareas 2 and 3, and the longest travel times are in the southern part of subarea 1, subareas 5 and 7.

Detailed repository-scale models have been used to derive near-field and far-field performance measures for input to SA calculations. A DFN conceptual model has been applied to represent the entire repository and flow in the bedrock around each deposition hole down to the scale of a few metres or less. Groundwater flow-paths are calculated at the representative times 6,000 BC, 2,000 BC, 2,020 AD and 6,000 AD with boundary conditions and the salinity distribution being interpolated on to the steady-sate repository-scale models from ECPM transient regional-scale coupled groundwater flow and salt transport models based on a consistent underlying DFN. Particles are released from three points around each canister position to provide equivalent flow rates for the near-field (COMP23) SA models, and transport statistics along the pathway to the surface for input to far-field (FAR31) SA models. The release points give the three paths: Q1, a release in a fracture abutting the deposition hole; Q2, a release point in the EDZ at the top of the deposition hole; Q3, a release in the tunnel above the canister.

In terms of the SA performance measures for a release at 2,020 AD, the DFN model predicts travels times with a median about 60 years; initial velocity has a median around $2 \cdot 10^{-4}$ m/y with a standard deviation of 1.3 orders of magnitude; the F-factor has a median of $5.4 \cdot 10^{5}$ y/m with a standard deviation of about 1.0 in log-space. At later times in the future, the performance measures are very similar. At 2,000 BC the performance measures are less favourable with a median travel time of 32 years, median initial velocity of $3 \cdot 10^{-4}$ m/y and an F-factor of $4.8 \cdot 10^{5}$ y/m. At 6,000 BC when the site is covered by a shallow sea, the performance measures are the best.

The DFN is sparsely connected, especially in hydraulic rock domain HRD(D, E, M), and so there is not always an advective pathway through a fracture that intersects the deposition holes via the fracture network to the surface. Overall, about 34% of deposition holes are not intersected by a connected fracture, and a further 11% are in areas of stagnant flow without a connected path away from the canister. Only about 3% of particles become stuck due to mass balance problems in the numerical solution. This leaves about 52% of deposition holes that have a Q1 path, i.e. a path to the surface via an intersecting fracture. Of these, only about 47% of canisters are intersected by a connected fracture above the PFL detection limit of around 10^{-9} m^2/s. For the releases in the EDZ and the tunnel, Q2 and Q3, about 10% of particles remain close to the repository due to stagnant flow, and over 80% make it to the surface of the model. The reason there are areas of stagnant flow in the tunnel and EDZ is that the end of each deposition tunnel opposite the main tunnel is essentially a dead-end. That is, to get advection along or out of the tunnel there must be a head gradient along it, which requires that at least two moderate to large water-bearing fractures intersects the tunnel, and the portion outside of these connections is subject to stagnant flow conditions. Travel-time and F-factor are almost identical for each of the release points around the canister, which suggests that the flow-path is the same for each release point and that flow does not diverge down different flow conduits around the repository. Considering the individual rock domains, HRD(A) has 74% of deposition holes with an advective Q1 path to the surface via and adjoining fracture, while HRD(D, E, M) has only 40%.

Generally flow-paths tend to be focussed toward the deterministic deformation zones and the larger stochastic fractures since these are more connected, have higher transmissivity, and hence carry more

flow. Typically, there are few long horizontal flow-paths that discharge away from the site area. This is due to the limited horizontal connectivity and geometry of the fracture network. One exception is the gently northward dipping and extensive zone ZSMEW007A that outcrops in the centre of the repository, which provides a shallow but long horizontal flow-path running west to east. This is interesting since it suggests major sub-horizontal deformation zones could have a significant positive impact on radionuclide transport making flow-paths longer, whereas sub-vertical deformation zones tend to have the negative impact of shortening flow-paths. One clear characteristic of this overall picture of path trajectories is the greater dispersion of paths in the northern and eastern parts of the repository which correspond with rock domain HRD(A) compared with the southern part where particles concentrate on a small number of discrete conduits in rock domain HRD(D, E, M). The cause is the difference in fracture connectivity. In HRD(A) the network is relatively connected, so particles tend to be dispersed through the many connections through the network, while in HRD(D, E, M), particles tend to follow the tunnel or EDZ before they find a connection to a handful of deformation zones or large stochastic fractures that provide the only connections to the surface.

Particles are released in three hydraulic rock domains: HRD(A) in the north and east of the repository, HRD(D, E, M) in the south and west, and 3% in low confidence HCD. Comparing performance measures for these 3 different rock domains, travel-time in the rock indicates that at release times 6,000 BC and 2,000 BC, particles released in the different hydraulic domains have distributions of similar shape. However, particles released in the HCD have slightly shorter median travel-times compared to those for particles released in HRD(A), which have shorter median travel-times than those for particles released in HRD(D,E,M). For example, at 6,000 BC for path Q1, the median travel-time for release in the HCD is 130 years, compared to 180 years for release in HRD(A), and 333 years for HRD(D,E,M). At later release times, median travel-times for particles released in the HCD are significantly shorter than those for particles released in the HRD and median travel-times for the two rock domains are closer to each other. For example, at 2,020 AD for path Q1, the median travel-time for release in the HCD is 13 years, compared to 55 years for release in HRD(A), and 63 years for HRD(D,E,M). The results would suggest that the hydraulic gradient in the HCD increases after 2,000 BC giving faster travel times. For all release times, the median F-factor for releases in the HCD is lower than that corresponding to releases in the HRD, and the median F-factor for a release in HRD(A) is lower than that for a release in HRD(D,E,M).

Sensitivities to the tunnel and EDZ properties have been considered as well as the relationship used between fracture transmissivity and size. The sensitivity of the performance measures in the rock to backfill and EDZ properties is relatively small since the repository does not form a complete path to the surface. Even in the pessimistic variants the 90th percentile for the distance in the EDZ or tunnel is about 100 m, so at worst it only provides a short-cut from the deposition hole to the fracture system about 1 tunnels length away. This suggests flow tends to be limited by what the fracture system can supply and paths have to leave the tunnel or EDZ after a relatively short distance to find a flow-path to the surface through the fracture network.

The variant cases for the DFN using a higher transmissivity in Set_C and correlated fracture transmissivity-size relationship also indicate the performance measures are relatively insensitive to these uncertainties.

For the current fracture model, avoiding locations where fractures intersect the full perimeter of a tunnel seems to be a sufficient test for screening out the worst deposition hole locations without having to perform flow tests of fracture transmissivity in deposition pilot holes.

6.2 Conclusions for gas migration and its effects on groundwater flow

The consequences of the production of gas from iron corrosion in the small proportion of canisters (< 0.1%) that may have manufacturing defects allowing water ingress were addressed.

Gas is generated in defective canisters by anaerobic corrosion of the cast iron insert as a result of water ingress through the defect. The rate of gas generation is determined by the iron

corrosion rate, the iron surface area exposed to water, and the availability of water. Assuming that the whole surface of the iron insert is exposed to an unlimited supply of water, the rate of hydrogen production would be $2.1 \cdot 10^{-2}$ m^3 y^{-1} at STP. This is an upper bound to the rate of gas production from a canister as in practice water availability will be limited by the flow capacity of the bentonite, the build up of gas pressure in the canister opposing water ingress through the defect, and the capacity of the geosphere to supply groundwater. The generation rate for these is unlikely to exceed ~ 10^{-2} m^3 y^{-1} at STP, and the build up of gas pressure is likely to reduce the rate to less than ~ 10^{-4} m^3 y^{-1} at STP. Bear in mind that no gas escapes from the defective canister until the gas pressure has reached at least hydrostatic. Gas generation will continue, but possibly only at these very low rates, for at least 250,000 years.

Gas released from a defective canister needs to pass through the bentonite buffer if it is to escape from the vicinity of the canister. Even at the constrained gas generation rates discussed above, gas transport through the bentonite by diffusion in solution from the small defect will be inadequate to remove all the gas generated. However, if the gas pressure opens a gap between the canister and the buffer into which the gas can spread, the contribution of diffusion of dissolved gas to gas transport through the buffer may become more significant. In any event, is expected that, if the gas pressure rises sufficiently, movement of a free gas phase through the bentonite buffer will occur.

Once the gas has passed through the bentonite, it might collect in the tunnel and the EDZ associated with the tunnel, and it might enter the fracture network either from the tunnel or directly from the deposition hole. Some of the gas will dissolve in the groundwater and be transported away by the groundwater flow. However, the groundwater flow at the repository depth is very slow, and it is unlikely that gas generated at the upper bound generation rate of $2.1 \cdot 10^{-2}$ m^3 y^{-1} at STP could all dissolve and be transported away in groundwater flowing through the neighbourhood of the repository. If, as seems quite probable for most defective canisters, the gas release rate is 1–2 orders of magnitude less than the upper bound, it is possible that much if not all of the gas could be transported away in solution.

Should the gas not all dissolve, simple estimates show that the gas transport capacity of the fracture network, assuming that it is sufficiently connected between the location of the defective canister and the surface, should be more than adequate to easily transport the gas to the surface without any significant increase in gas pressure in the neighbourhood of the repository.

Should free gas phase migration be sustained between the repository and the surface, this would be capable of transporting volatile radionuclides relatively rapidly from the repository to the surface. The only significant such radionuclides identified in the waste canisters are ^{14}C and ^{222}Rn. Direct release of the volatile ^{14}C in defective canisters to the surface has been previously assessed as not causing a significant radiological hazard and so the capacity of migrating gas to transport this radionuclide is immaterial. Similar conclusions were reached for ^{222}Rn release, although it may be desirable to assess the consequences of ^{222}Rn release into an occupied dwelling.

Migrating gas may also affect the movement of groundwater and hence the transport of dissolved radionuclides. Such transport is mitigated by the following observations:

- With a small defect, it is not possible to get release of dissolved radionuclides and gas at the same time. The situation may be different if a large hole develops.
- Gas migration can only affect transport of dissolved radionuclides released from a nearby different canister, and the probability of two defective canisters being present close together must be quite small.
- Migrating gas is only likely to affect groundwater flows in the neighbourhood of a small number of canisters local to the canister generating gas, and there is a low probability that one of these also may be defective and releasing radionuclides.

References

Bond A E, Hoch A R, Jones G D, Tomczyk A E, Wiggin R M, Worraker W J, 1997. Assessment of a spent fuel disposal canister: assessment studies for a copper canister with cast steel inner component, SKB TR 97-19, Svensk Kärnbränslehantering AB.

Börgesson L, Johannesson L-E, Sandén T, Hernelind J, 1995. Modelling of the physical behaviour of water saturated clay barriers: laboratory tests, material models, and finite element application, SKB R-95-20, Svensk Kärnbränslehantering AB.

Börgesson L, Karnland O, Johannesson L-E, 1996. Modelling of the physical behaviour of clay barriers close to water saturation, Eng. Geol, 41, 127–144.

Byegård J, Gustavsson E, Tullborg E-A, 2006. Bedrock transport properties. Data evaluation and retardation model. Preliminary site description Simpevarp subarea – version 1.2, SKB R-06-27, Svensk Kärnbränslehantering AB.

Carrera J, Sanchez-Vila X, Benet I, Medina A, Galarza G, Guimera J, 1998. On Matrix Diffusion: Formulations, Solution Methods and Quantitative Effects, Hydrogeology Journal, 6, No. 1, 178–190.

Chuoke R L, van Meurs P, van der Poel C, 1959. The instability of slow, immiscible, viscous liquid-liquid displacements in permeable media, Pet. Trans. AIME, 216, 188–194.

Cussler E L, 1984. Diffusion: mass transfer in fluid systems, Cambridge University Press.

Darwin, C, 1953. Note on hydrodynamics, Proc. Camb. Phil. Soc., 49, 342–354.

Dershowitz W, Winberg A, Hermanson J, Byegård J, Tullborg E-L, Andersson P, Mazurek M, 2003. Äspö Hard Rock Laboratory. Äspö Task Force on modelling of groundwater flow and transport of solutes – Task 6C – A semi-synthetic model of block scale conductive structures at the Äspö HRL, SKB Report IPR-03-13, Svensk Kärnbränslehantering AB.

Epstein P S, Plesset M S, 1950. On the stability of gas bubbles in liquid-gas solutions, J. Chem. Phys. 18, 1505–1509.

Follin S, Stiggson M, Svensson U, 2006. Hydrogeological DFN modelling using structural and hydraulic data from KLX04, Preliminary site description, Laxemar subarea – version 1.2, SKB R-06-24, Svensk Kärnbränslehantering AB.

Grace J R, Wairegi T, Brophy J, 1978. Break-up of drops and bubbles in stagnant media, Can. J. Chem. Eng., 56, 3–8.

Hartley L, Cox I C S, Holton D, Hunter F M I, Joyce S, Gylling B, Lindgren M, 2004. Groundwater flow and transport modelling using CONNECTFLOW in support of the SR-Can assessment, SKB R-04-61, Svensk Kärnbränslehantering AB.

Hartley L, Hoch A, Hunter F, Jackson P, Marsic N, 2005. Regional hydrogeological simulations – Numerical modelling using Connectflow, Preliminary site description Simpevarp subarea – version 1.2, SKB R-05-12, Svensk Kärnbränslehantering AB.

Hartley L, Cox I, Hunter F, Jackson P, McCarthy R, Gylling B, Marsic N, 2006a. Regional Hydrogeological Simulations– Numerical Modelling Using CONNECTFLOW, Preliminary site description, Laxemar subarea – Version 1.2, SKB R-06-23, Svensk Kärnbränslehantering AB.

Hartley L, Hoch A, Jackson P, Joyce S, McCarthy R, Rodwell W, Marsic N, 2006b. Groundwater flow and transport modelling during the temperate period for the SR-Can assessment, Forsmark area – version 1.2, SKB R-06-98, Svensk Kärnbränslehantering AB.

Hermanson J, Forsberg O, Fox A, La Point P, 2005. Statistical model of fractures and deformation zones: Preliminary site description, Laxemar subarea, version 1.2. SKB R-05-45, Svensk Kärnbränslehantering AB.

Hoch A R, Swanton S W, Manning M C, Rodwell W R, Swift B T, Duddridge G A, 2001. Gas migration in low-permeability fractured rock: theoretical and experimental studies, AEA Technology Report AEAT/ERRA-0323.

Hoch A R, Jackson C P, 2004. Rock-matrix Diffusion in Transport of Salinity. Implementation in CONNECTFLOW, SKB R-04-78, Svensk Kärnbränslehantering AB.

Jackson C P, Hoch A R, Todman S J, 2000. Self-consistency of a Heterogeneous Continuum Porous Medium Representation of a Fractured Medium, Water Resources Research, 36, No. 1, 189–202.

Laaksoharju M et al. 1999. Multivariate Mixing and Mass Balance (M3) Calculations, A New Tool for Decoding Hydrogeochemical Information, Applied Geochemistry 14, 861 871, (1999).

La Pointe P R, Wallmann P, Follin S, 1995. Estimation of Effective Block Conductivities Based on Discrete Network Analyses Using Data from the Äspö Site, Tech. Rep. TR 95-15, Svensk Kärnbränslehantering AB.

Lide D (ed), 1994. CRC handbook of chemistry and physics, CRC Press.

Lindgren M, Lindström F, 1999. SR 97: radionuclide transport calculations, SKB TR-99-23, Svensk Kärnbränslehantering AB.

Marsic N, Hartley L J, Jackson C P, Poole M J, Morvik A, 2001. Development of Hydrogeological Modelling Tools Based on NAMMU, SKB R-01-49, Svensk Kärnbränslehantering AB.

Meister B J, Scheele G F, 1967. Generalized solution of the Tomotika stability analysis for a cylindrical jet, AIChE Journal, **13**, 682–688.

Moreno L, Gylling B, 1998. Equivalent flow rate concept used in near field transport model COMP23 – Proposed values for SR 97, SKB R-98-53, Svensk Kärnbränslehantering AB.

Munier R, 2004. Statistical analysis of fracture data, adapted for modelling Discrete Fracture Networks-Version 2, SKB R-04-66, Svensk Kärnbränslehantering AB.

Nash P J, Cox I C S, Rodwell W R, 1997. Gas-water interactions in gas migration from a deep repository in fractured hard rock, UK Nirex Report NSS/R251.

Neretnieks I, 1979. Transport Mechanism and Rates of Transport of Radionuclides in the Geosphere as Related to the Swedish KBS-Concept, Proc. Symp. Underground Disposal of Radioactive Wastes, Otaniemi, Finland, July 2–6, 1979, Vol II. p 108, International Atomic Energy Agency.

Neretnieks I, Ernstson M-L, 1997. A note on radionuclide transport by gas bubbles. In: W J Gray and I R Triay (eds.), MRS symposium proceedings 465, Scientific basis for nuclear waste management XX, 855–862, MRS, Pittsburgh, Pennsylvania, USA.

Neretnieks I, 2006. A Note on flow and transport in a damaged zone due to spalling. Department of Chemical Engineering and Technology, Royal Institute of Technology, KTH, Stockholm, Sweden.

Påsse T, 1997. A mathematical model of past, present and future shore level displacement in Fennoscandia, SKB TR 97-28, Svensk Kärnbränslehantering AB.

Plesset M S, Whipple C G, 1974. Viscous effects in Rayleigh-Taylor instability, Phys. Fluids, 17, 1–7.

Rhén I, Forsmark T, Forsman I, Zetterlund M, 2006. Evaluation of hydrogeological properties for Hydraulic Conductor Domains (HCD) and Hydraulic Rock Domains (HRD), Preliminary site description, Laxemar subarea – version 1.2. SKB R-06-22, Svensk Kärnbränslehantering AB.

Rodwell W R, Harris A W, Horseman S T, Lalieux Ph, Müller W, Ortiz Amaya L, Pruess K, 1999. Gas migration through engineered and geological barriers for a deep repository for radioactive waste. A joint EC/NEA status report published by the European Commission, European Commission Report EUR 19122 EN.

Saffman P G, Taylor G, 1958. The penetration of a fluid into a porous medium or Hele-Shaw cell containing a more viscous liquid, Proc. R. Soc. Lond., A245, 312–329.

Serco Assurance, 2005a. CONNECTFLOW Release 9.0 Technical Summary Document, Serco Assurance Report SA/ENV/CONNECTFLOW/15.

Serco Assurance, 2005b. NAMMU Release 9.0 Technical Summary Document, Serco Assurance Report SA/ENV/CONNECTFLOW/8.

Serco Assurance, 2005c. NAPSAC Release 9.0 Technical Summary Document, Serco Assurance Report SA/ENV/CONNECTFLOW/12.

SKB, 1997. ZEDEX – A study of damage and distrurbance from tunnel excavation and tunnel boring. SKB TR-97-30, Svensk Kärnbränslehantering AB.

SKB, 1999. Deep repository for spent nuclear fuel. SR 97: post-closure safety (main report Summary, main report Volume 1, and main report Volume 2), SKB TR-99-06, Svensk Kärnbränslehantering AB.

SKB, 2004a. Interim main report of the safety assessment SR-Can, SKB TR-04-11, Svensk Kärnbränslehantering AB.

SKB, 2004b. Preliminary site description of the Forsmark area (Version 1.1), SKB R-04-15, Svensk Kärnbränslehantering AB.

SKB, 2004c. Interim process report for the safety assessment SR-Can, SKB R-04-33, Svensk Kärnbränslehantering AB.

SKB, 2004d. Interim data report for the safety assessment SR-Can, SKB R-04-34, Svensk Kärnbränslehantering AB.

SKB, 2004e. Interim initial state report for the safety assessment SR-Can, SKB R-04-35, Svensk Kärnbränslehantering AB.

SKB, 2005. Preliminary site description, Forsmark subarea – version 1.2, SKB R-05-18, Svensk Kärnbränslehantering AB.

SKB, 2006a. Hydrogeochemical evaluation, Preliminary site description, Laxemar subarea – version 1.2, SKB R-06-12, Svensk Kärnbränslehantering AB.

SKB, 2006b. Preliminary site description, Laxemar subarea – version 1.2, SKB R-06-10, Svensk Kärnbränslehantering AB.

SKB, 2006c. Data report for the Safety assessment SR-Can, SKB R-06-xx, Svensk Kärnbränslehantering AB.

Smart N R, 2001. The anaerobic corrosion of carbon steel and cast iron in artificial ground-waters, SKB TR-01-22, Svensk Kärnbränslehantering AB.

Svenson U, 2006. The Laxemar repository – Modelling changes in the flow, pressure and salinity fields, due to a repository for spent nuclear fuel, SKB R-06-57, Svensk Kärnbränslehantering AB.

Tanai et al. 1999. Measurements of diffusion coefficients for hydrogen in bentonite, communicated by P Sellin.

Tomotika S, 1934. On the instability of a cylindrical thread of a viscous liquid surrounded by another viscous liquid, Proc. R. Soc. Lond., A150, 322–337.

Wikramaratna R S, Goodfield M, Rodwell W R, Nash P J, Agg P J, 1993. A preliminary assessment of gas migration from the copper/steel canister, SKB TR 93-31, Svensk Kärnbränslehantering AB.

Werner K, Bosson E, Berglund S, 2005. Laxemar 1.2. Background report for climate, surface hydrology and near-surface hydrogeology. SKB R-05-61, Svensk Kärnbränslehantering AB.

Westman P, Wastegård S, Schoning K, Gustafsson B, Omstedt A, 1999. Salinity change in the Baltic Sea during the last 8500 years: evidence, causes and models. SKB TR-99-38, Svensk Kärnbränslehantering AB.

Appendix A

Glossary of abbreviations and symbols

For clarity, the SKB advised terminology for referring to fracture size is as follows.

r Equivalent fracture radius (m)
Fractures are modelled as squares. However, an equivalent fracture radius,
$r = \sqrt{\frac{A}{\pi}}$,
where A is fracture area, is used to describe fracture size throughout this report

k The shape parameter for a general power-law distribution

kr The shape parameter for the power-law distribution for fracture radii

x0 The location parameter of a general power-law distribution (m)

r0 The location parameter of the power-law distribution for fracture radii (m)

Other abbreviations and notation used are:

a_r Fracture surface area per unit volume (2×P32) ($m^2\ m^{-3}$)

BC Boundary condition

CPM Continuum porous medium

DFN Discrete fracture network

DZ Deformation zone

ECPM Equivalent continuum porous medium

e_t Fracture transport aperture (m)

F_r F-factor in the rock (year/m)

F 1.2 Forsmark version 1.2

FWS Flow-wetted surface, same as a_r ($m^2\ m^{-3}$)

GWF Groundwater flow

HCD Hydraulic conductor domains

HRD Hydraulic rock domains

HSD Hydraulic soil domains

IC Initial condition

IFZ Implicit fracture zone

K Hydraulic conductivity (m/s)

K_{eff} Effective isotropic hydraulic conductivity (m/s)

K_{hmax} Maximum horizontal hydraulic conductivity (m/s)

K_{hmin} Minimum horizontal hydraulic conductivity (m/s)

K_x Hydraulic conductivity in the E-W direction (m/s)

K_y Hydraulic conductivity in the N-S direction (m/s)

K_z Hydraulic conductivity in the vertical direction (m/s)

KAV Cored borehole at Ävrö

KAS Cored borehole at Äspö

KLX Cored borehole at Laxemar

KSH Cored borehole at Simpevarp

L 1.2 Laxemar version 1.2

L_{EDZ}	Path-length in the EDZ (m)
L_r	Path-length in the rock (m)
L_T	Path-length in the tunnel (m)
M3	Mixing and mass-balance modelling
n_e	Kinematic porosity (–)
$n_{e,b}$	Kinematic porosity for a model block (–)
n_m	Matrix porosity (–)
P10	Linear fracture intensity: number of fractures per metre along a borehole (m^{-1})
$P10_c$	Linear fracture intensity of connected fractures: number of connected fractures per metre along a borehole (m^{-1})
$P10_{corr}$	Terzaghi corrected linear fracture intensity: 'true' number of fractures per metre along a borehole corrected for the bias introduced by the angle of the borehole made with fractures (m^{-1})
$P10_{PFL}$	Linear fracture intensity of PFL-anomalies: number of PFL anomalies per metre along a borehole (m^{-1})
P21	Area fracture intensity: total fracture trace lengths per square metre of outcrop ($m\ m^{-2}$)
P32	Volumetric fracture intensity: total fracture surface area per cubic metre of rock ($m^2\ m^{-3}$)
$P32_c$	Volumetric fracture intensity of connected fractures: total connected fracture surface area per cubic metre of rock ($m^2\ m^{-3}$)
PDF	Probability distribution function
PFL	Posiva flow-log
PFL-f	Posiva flow-anomaly logging is made with a test section length of 1 m and a step length of 0.1 m
PFL-s	Posiva flow section logging is made with a test section length of 5 m and a step length of 0.5 m
PM	Performance measure
PSS	Pipe-string system
Q	Groundwater flux ($m^3\ s^{-1}$)
q	Darcy velocity ($m\ s^{-1}$)
RD	Rock domain
r_{min}	Minimum fracture radius used in DFN simulations (m)
RVS	Rock visualisation system (a tool used by SKB for their structural modelling)
RMD	Rock matrix diffusion
S 1.2	Simpevarp version 1.2
SA	Safety assessment
SDM	Site descriptive modelling
t_{EDZ}	travel-time in the EDZ (year)
t_r	travel-time in the rock (year)
t_T	travel-time in the tunnel (year)
TDS	Total dissolved solids
U_r	Initial Darcy velocity in the rock (m/year)
μ	Mean of normal distribution
σ	Standard deviation of normal distribution

Appendix B

Summary of statistics for regional-scale ECPM modelling

Table B-1 to Table B-3 tabulate the performance measures for the reference case at all release times.

Table B-1. Log_{10} travel time statistics for the reference case at different release times.

Log_{10}(tr) [yrs]	–7,980	–6,000	–4,000	–3,000	–2,000	–1,000	0	1,000	2,020	4,000	6,000	8,000	9,000
Mean	3.617	2.963	2.967	3.133	3.010	3.156	3.343	3.255	3.261	3.118	3.148	3.149	3.171
Median	3.515	2.868	2.965	3.049	2.984	3.049	3.158	3.053	3.004	2.920	2.955	2.969	2.981
5th percentile	2.241	2.029	1.868	1.880	1.708	1.853	1.903	1.928	1.938	1.915	1.930	1.932	1.939
10th percentile	2.433	2.149	2.076	2.130	1.912	2.033	2.111	2.137	2.147	2.146	2.176	2.177	2.188
25th percentile	2.908	2.375	2.458	2.576	2.346	2.489	2.582	2.596	2.612	2.530	2.565	2.574	2.584
75th percentile	4.340	3.520	3.501	3.691	3.661	3.848	4.199	4.065	4.041	3.471	3.679	3.679	3.724
90th percentile	4.901	3.927	3.862	4.182	4.093	4.310	4.773	4.566	4.775	4.801	4.584	4.461	4.418
95th percentile	5.182	4.091	3.993	4.464	4.337	4.669	4.996	4.758	5.029	5.029	4.860	4.838	4.810
Std deviation	0.917	0.697	0.675	0.797	0.848	0.889	0.978	0.916	0.953	0.911	0.869	0.846	0.852
Variance	0.840	0.486	0.455	0.634	0.719	0.790	0.957	0.840	0.909	0.830	0.756	0.715	0.726
Max value	6.487	5.303	5.299	6.265	5.934	5.926	6.188	6.025	5.790	5.617	5.550	5.477	5.473
Min value	1.580	1.004	1.114	0.961	0.856	0.800	1.190	1.188	1.188	1.190	1.182	1.176	1.182
Fraction OK	0.991	1.000	0.990	0.888	0.915	0.991	0.968	0.983	0.981	0.865	0.904	0.908	0.930

Table B-2. Log_{10} initial flux at starting positions for the reference case at different release times.

Log_{10}(Ur) [m/y]	–7,980	–6,000	–4,000	–3,000	–2,000	–1,000	0	1,000	2,020	4,000	6,000	8,000	9,000
Mean	–4.334	–4.145	–3.961	–3.928	–3.727	–3.502	–3.411	–3.381	–3.369	–3.363	–3.362	–3.361	–3.361
Median	–4.237	–3.917	–3.767	–3.738	–3.532	–3.349	–3.257	–3.237	–3.232	–3.226	–3.225	–3.225	–3.225
5th percentile	–6.709	–6.575	–6.226	–6.197	–5.904	–5.810	–5.738	–5.711	–5.704	–5.697	–5.695	–5.693	–5.693
10th percentile	–6.121	–6.235	–5.688	–5.830	–5.552	–5.426	–5.342	–5.320	–5.311	–5.311	–5.314	–5.313	–5.314
25th percentile	–5.128	–4.735	–4.535	–4.505	–4.380	–4.150	–4.069	–4.058	–4.054	–4.055	–4.056	–4.056	–4.057
75th percentile	–3.445	–3.297	–3.171	–3.123	–2.947	–2.633	–2.519	–2.479	–2.462	–2.455	–2.452	–2.450	–2.450
90th percentile	–2.658	–2.757	–2.668	–2.625	–2.403	–2.095	–1.932	–1.886	–1.867	–1.860	–1.857	–1.857	–1.857
95th percentile	–2.178	–2.576	–2.483	–2.218	–1.975	–1.815	–1.711	–1.658	–1.641	–1.633	–1.633	–1.633	–1.633
Std deviation	1.315	1.182	1.100	1.164	1.153	1.175	1.189	1.200	1.204	1.206	1.207	1.207	1.207
Variance	1.728	1.398	1.211	1.354	1.328	1.381	1.415	1.439	1.450	1.455	1.456	1.456	1.456
Max value	–1.250	–1.947	–1.752	–1.207	–1.140	–1.134	–1.133	–1.131	–1.118	–1.111	–1.110	–1.110	–1.109
Min value	–8.232	–7.706	–7.256	–7.780	–7.190	–7.039	–6.907	–6.876	–6.863	–6.851	–6.845	–6.845	–6.842
Fraction OK	1.000	1.000	1.000	1.000	1.000	1.000	1.000	1.000	1.000	1.000	1.000	1.000	1.000

Table B-3. Log_{10} F-factor statistics for the reference case at different release times.

Log_{10}(Fr) [y/m]	–7,980	–6,000	–4,000	–3,000	–2,000	–1,000	0	1,000	2,020	4,000	6,000	8,000	9,000
Mean	6.593	5.988	5.944	6.259	6.131	6.015	6.076	5.939	5.970	5.873	5.914	5.914	5.940
Median	6.581	5.842	5.877	6.220	6.121	5.929	5.966	5.873	5.836	5.696	5.751	5.757	5.788
5th percentile	5.304	5.207	5.107	5.161	4.839	4.817	4.844	4.778	4.773	4.703	4.732	4.740	4.749
10th percentile	5.474	5.295	5.272	5.322	5.045	5.004	5.004	4.934	4.924	4.854	4.870	4.876	4.881
25th percentile	5.942	5.497	5.512	5.677	5.418	5.375	5.407	5.305	5.290	5.196	5.238	5.246	5.265
75th percentile	7.218	6.427	6.316	6.766	6.822	6.668	6.808	6.502	6.635	6.295	6.398	6.360	6.425
90th percentile	7.638	6.837	6.737	7.211	7.274	7.152	7.250	6.952	7.214	7.270	7.173	7.067	7.037
95th percentile	7.944	7.127	6.998	7.486	7.498	7.396	7.449	7.263	7.449	7.501	7.442	7.384	7.456
Std deviation	0.826	0.619	0.590	0.772	0.848	0.834	0.851	0.820	0.857	0.927	0.927	0.940	0.947
Variance	0.683	0.384	0.348	0.596	0.720	0.695	0.725	0.672	0.734	0.859	0.860	0.884	0.897
Max value	9.958	10.072	8.814	9.489	10.104	10.093	10.134	10.097	9.597	10.017	10.021	9.976	9.970
Min value	4.521	4.155	4.233	4.210	4.143	3.977	4.188	4.188	4.188	4.188	4.182	4.179	4.182
Fraction OK	0.991	1.000	0.990	0.888	0.915	0.991	0.968	0.983	0.981	0.865	0.904	0.908	0.930

Appendix C

Summary of statistics for the DFN modelling

C.1 Reference case

Table C-1. Summary statistics for travel-time in the rock for the reference case of the amalgamated repository-scale and regional-scale DFN model. At each of the times 6,000 BC, 2,000 BC, 2,020 AD, and 6,000 AD, three paths Q1, Q2, and Q3 were tracked for each of 7,483 release locations in the amalgamated model.

Log10(tr) [yrs]	6,000 BC			2,000 BC			2,020 AD			6,000 AD		
	Q1	Q2	Q3	Q1	Q2	Q3	Q1	Q2	Q3	Q1	Q2	Q3
Mean	2.398	2.362	2.359	1.551	1.478	1.517	1.765	1.683	1.708	1.822	1.744	1.762
Median	2.378	2.361	2.357	1.497	1.428	1.458	1.758	1.684	1.704	1.795	1.740	1.763
5th percentile	1.589	1.557	1.585	0.567	0.519	0.561	0.751	0.690	0.708	0.750	0.695	0.707
10th percentile	1.758	1.730	1.748	0.741	0.688	0.717	0.947	0.866	0.907	0.941	0.864	0.889
25th percentile	2.023	1.996	1.994	1.086	1.020	1.067	1.350	1.288	1.326	1.366	1.291	1.308
75th percentile	2.711	2.683	2.675	1.967	1.881	1.927	2.186	2.096	2.102	2.324	2.200	2.232
90th percentile	3.090	2.986	2.984	2.439	2.337	2.375	2.546	2.431	2.454	2.623	2.535	2.547
95th percentile	3.329	3.246	3.231	2.691	2.594	2.638	2.759	2.649	2.654	2.824	2.734	2.761
Std deviation	0.540	0.525	0.514	0.662	0.651	0.649	0.621	0.597	0.601	0.667	0.664	0.643
Variance	0.292	0.275	0.264	0.439	0.424	0.421	0.386	0.356	0.361	0.445	0.441	0.414
Max value	6.116	6.423	6.423	5.132	6.488	6.380	7.873	5.567	6.537	7.244	7.873	5.481
Min value	0.265	0.356	0.692	–0.091	–0.151	–0.293	–0.043	–0.092	–0.001	–0.094	–0.164	–0.007
Fraction OK	0.479	0.714	0.751	0.511	0.742	0.791	0.524	0.768	0.806	0.474	0.694	0.723

Table C-2. Summary statistics for initial Darcy velocity in the rock for the reference case of the amalgamated repository-scale and regional-scale DFN model. At each of the times 6,000 BC, 2,000 BC, 2,020 AD, and 6,000 AD, three paths Q1, Q2, and Q3 were tracked for each of 7,483 release locations in the amalgamated model.

Log10(Ur) [m/y]	6,000 BC			2,000 BC			2,020 AD			6,000 AD		
	Q1	Q2	Q3	Q1	Q2	Q3	Q1	Q2	Q3	Q1	Q2	Q3
Mean	–3.955	–4.024	–4.397	–3.623	–3.640	–4.047	–3.670	–3.482	–4.061	–3.667	–3.476	–4.062
Median	–3.910	–3.893	–4.356	–3.560	–3.506	–3.965	–3.608	–3.396	–3.966	–3.604	–3.393	–3.963
5th percentile	–6.025	–5.654	–6.238	–5.721	–5.289	–5.986	–5.757	–4.724	–6.072	–5.755	–4.716	–6.111
10th percentile	–5.577	–5.060	–5.773	–5.299	–4.671	–5.436	–5.357	–4.250	–5.483	–5.341	–4.251	–5.511
25th percentile	–4.796	–4.376	–4.998	–4.487	–3.957	–4.647	–4.522	–3.782	–4.652	–4.519	–3.778	–4.657
75th percentile	–3.197	–3.496	–3.814	–2.831	–3.143	–3.463	–2.892	–3.055	–3.438	–2.888	–3.046	–3.431
90th percentile	–2.465	–3.200	–3.262	–2.119	–2.853	–2.910	–2.151	–2.786	–2.910	–2.145	–2.775	–2.897
95th percentile	–1.921	–3.034	–2.668	–1.570	–2.686	–2.306	–1.581	–2.647	–2.398	–1.576	–2.632	–2.398
Std deviation	1.279	0.782	1.115	1.302	0.763	1.115	1.302	0.641	1.130	1.304	0.644	1.136
Variance	1.637	0.612	1.243	1.694	0.582	1.242	1.695	0.411	1.276	1.700	0.415	1.290
Max value	1.163	–0.011	1.518	1.911	–0.189	0.767	1.937	–1.396	0.470	1.938	–1.397	0.564
Min value	–8.674	–8.281	–9.674	–8.506	–8.181	–9.914	–8.508	–6.779	–10.193	–9.241	–6.736	–10.199
Fraction OK	0.666	0.952	1.000	0.665	0.951	1.000	0.664	0.945	1.000	0.664	0.944	1.000

Table C-3. Summary statistics for path-length in the rock for the reference case of the amalgamated repository-scale and regional-scale DFN model. At each of the times 6,000 BC, 2,000 BC, 2,020 AD, and 6,000 AD, three paths Q1, Q2, and Q3 were tracked for each of 7,483 release locations in the amalgamated model.

Log10(Lr) [m]	6,000 BC			2,000 BC			2,020 AD			6,000 AD		
	Q1	Q2	Q3	Q1	Q2	Q3	Q1	Q2	Q3	Q1	Q2	Q3
Mean	3.110	3.115	3.113	3.081	3.088	3.091	3.173	3.182	3.185	3.165	3.169	3.171
Median	3.068	3.065	3.064	3.053	3.054	3.059	3.125	3.130	3.135	3.121	3.123	3.128
5th percentile	2.850	2.841	2.844	2.870	2.863	2.867	2.926	2.919	2.921	2.922	2.919	2.919
10th percentile	2.885	2.879	2.881	2.902	2.898	2.902	2.973	2.969	2.967	2.969	2.967	2.966
25th percentile	2.964	2.955	2.957	2.972	2.968	2.974	3.041	3.045	3.045	3.037	3.039	3.041
75th percentile	3.209	3.217	3.217	3.154	3.167	3.171	3.273	3.298	3.304	3.253	3.259	3.262
90th percentile	3.388	3.416	3.411	3.282	3.305	3.304	3.471	3.493	3.495	3.443	3.448	3.445
95th percentile	3.522	3.552	3.566	3.391	3.427	3.429	3.548	3.564	3.564	3.554	3.567	3.559
Std deviation	0.212	0.230	0.226	0.171	0.183	0.179	0.191	0.200	0.201	0.190	0.197	0.194
Variance	0.045	0.053	0.051	0.029	0.033	0.032	0.036	0.040	0.040	0.036	0.039	0.038
Max value	4.252	4.270	4.263	4.116	4.200	4.110	4.178	4.224	4.252	4.326	4.325	4.270
Min value	2.750	2.696	2.724	2.768	2.742	2.722	2.781	2.750	2.763	2.785	2.778	2.775
Fraction OK	0.479	0.714	0.751	0.511	0.742	0.791	0.524	0.768	0.806	0.474	0.694	0.723

Table C-4. Summary statistics for F-factor in the rock for the reference case of the amalgamated repository-scale and regional-scale DFN model. At each of the times 6,000 BC, 2,000 BC, 2,020 AD, and 6,000 AD, three paths Q1, Q2, and Q3 were tracked for each of 7,483 release locations in the amalgamated model.

Log10(Fr) [y/m]	6,000 BC			2,000 BC			2,020 AD			6,000 AD		
	Q1	Q2	Q3	Q1	Q2	Q3	Q1	Q2	Q3	Q1	Q2	Q3
Mean	6.133	5.979	6.014	5.622	5.440	5.521	5.655	5.463	5.541	5.679	5.495	5.573
Median	6.126	5.968	6.027	5.683	5.528	5.600	5.731	5.550	5.601	5.732	5.564	5.655
5th percentile	4.849	4.759	4.748	3.929	3.697	3.839	3.853	3.762	3.864	3.938	3.758	3.937
10th percentile	5.160	5.044	5.067	4.405	4.195	4.314	4.456	4.312	4.419	4.478	4.287	4.448
25th percentile	5.648	5.500	5.543	5.079	4.910	4.991	5.116	4.962	5.072	5.152	4.980	5.069
75th percentile	6.623	6.462	6.489	6.227	6.033	6.113	6.240	6.033	6.098	6.269	6.073	6.125
90th percentile	7.117	6.913	6.954	6.746	6.568	6.603	6.817	6.517	6.584	6.811	6.541	6.607
95th percentile	7.462	7.215	7.262	7.097	6.893	6.939	7.129	6.795	6.889	7.159	6.900	6.951
Std deviation	0.790	0.758	0.755	0.943	0.950	0.925	0.969	0.908	0.908	0.963	0.928	0.913
Variance	0.625	0.575	0.570	0.889	0.903	0.856	0.938	0.824	0.824	0.928	0.862	0.833
Max value	9.411	9.299	9.880	9.073	8.534	8.746	9.356	9.283	9.868	10.424	10.424	10.061
Min value	3.303	3.329	3.422	2.294	2.270	2.308	2.207	2.335	2.233	2.031	2.389	2.220
Fraction OK	0.479	0.714	0.751	0.511	0.742	0.791	0.524	0.768	0.806	0.474	0.694	0.723

Table C-5. Summary statistics for travel-time in the tunnel for the reference case of the amalgamated repository-scale and regional-scale DFN model. At each of the times 6,000 BC, 2,000 BC, 2,020 AD, and 6,000 AD, three paths Q1, Q2, and Q3 were tracked for each of 7,483 release locations in the amalgamated model.

Log10(tT) [yrs]	6,000 BC			2,000 BC			2,020 AD			6,000 AD		
	Q1	Q2	Q3	Q1	Q2	Q3	Q1	Q2	Q3	Q1	Q2	Q3
Mean	5.548	5.322	5.785	5.178	4.974	5.454	5.161	4.978	5.450	5.150	5.014	5.442
Median	5.681	5.474	5.747	5.340	5.135	5.450	5.306	5.137	5.442	5.336	5.162	5.428
5th percentile	3.644	3.379	4.675	3.215	3.044	4.330	3.210	3.076	4.306	3.176	3.134	4.321
10th percentile	4.125	3.774	4.866	3.706	3.422	4.521	3.687	3.469	4.544	3.718	3.529	4.542
25th percentile	4.908	4.480	5.234	4.523	4.157	4.916	4.524	4.258	4.953	4.493	4.297	4.942
75th percentile	6.298	6.140	6.296	5.968	5.795	5.964	5.919	5.764	5.927	5.897	5.764	5.917
90th percentile	6.780	6.691	6.777	6.420	6.306	6.387	6.394	6.247	6.362	6.356	6.268	6.378
95th percentile	7.041	7.013	7.030	6.663	6.567	6.634	6.652	6.494	6.622	6.595	6.544	6.628
Std deviation	1.051	1.124	0.726	1.084	1.108	0.720	1.066	1.069	0.705	1.071	1.054	0.704
Variance	1.104	1.263	0.527	1.175	1.228	0.518	1.135	1.142	0.497	1.148	1.111	0.495
Max value	8.619	8.910	8.234	8.406	7.928	8.195	8.162	7.690	8.299	8.194	8.279	7.837
Min value	–0.011	1.348	3.552	–0.466	1.006	2.958	–0.867	1.462	3.351	–1.684	1.632	3.219
Fraction OK	0.341	0.595	0.751	0.364	0.617	0.791	0.369	0.639	0.806	0.336	0.574	0.723

Table C-6. Summary statistics for path-length in the tunnel for the reference case of the amalgamated repository-scale and regional-scale DFN model. At each of the times 6,000 BC, 2,000 BC, 2,020 AD, and 6,000 AD, three paths Q1, Q2, and Q3 were tracked for each of 7,483 release locations in the amalgamated model.

Log10(LT) [m]	6,000 BC			2,000 BC			2,020 AD			6,000 AD		
	Q1	Q2	Q3	Q1	Q2	Q3	Q1	Q2	Q3	Q1	Q2	Q3
Mean	1.051	0.960	1.123	1.062	0.982	1.155	1.046	0.972	1.144	1.025	0.982	1.149
Median	1.088	0.980	1.090	1.085	1.006	1.121	1.073	0.989	1.117	1.069	1.000	1.120
5th percentile	0.120	0.002	0.488	0.103	–0.001	0.495	0.123	0.036	0.527	0.065	0.055	0.525
10th percentile	0.381	0.195	0.636	0.338	0.198	0.631	0.379	0.260	0.666	0.287	0.279	0.664
25th percentile	0.756	0.609	0.848	0.751	0.618	0.861	0.754	0.626	0.872	0.715	0.637	0.877
75th percentile	1.374	1.332	1.376	1.409	1.376	1.420	1.383	1.343	1.400	1.382	1.348	1.407
90th percentile	1.661	1.665	1.649	1.712	1.703	1.714	1.672	1.638	1.673	1.641	1.656	1.669
95th percentile	1.848	1.854	1.836	1.887	1.887	1.900	1.842	1.822	1.835	1.829	1.837	1.857
Std deviation	0.513	0.563	0.405	0.539	0.581	0.423	0.505	0.532	0.391	0.528	0.536	0.399
Variance	0.264	0.317	0.164	0.290	0.338	0.179	0.255	0.283	0.153	0.279	0.287	0.159
Max value	3.161	3.230	2.969	3.471	3.530	3.199	2.797	2.812	2.793	2.652	2.933	3.126
Min value	–0.860	–1.125	0.135	–1.102	–1.125	0.146	–0.764	–1.072	0.115	–0.970	–0.913	0.134
Fraction OK	0.341	0.595	0.751	0.364	0.617	0.791	0.369	0.639	0.806	0.336	0.574	0.723

Table C-7. Summary statistics for travel-time in the EDZ for the reference case of the amalgamated repository-scale and regional-scale DFN model. At each of the times 6,000 BC, 2,000 BC, 2,020 AD, and 6,000 AD, three paths Q1, Q2, and Q3 were tracked for each of 7,483 release locations in the amalgamated model.

Log10(tEDZ) [yrs]	6,000 BC			2,000 BC			2,020 AD			6,000 AD		
	Q1	Q2	Q3	Q1	Q2	Q3	Q1	Q2	Q3	Q1	Q2	Q3
Mean	0.138	0.065	0.269	–0.205	–0.261	–0.074	–0.223	–0.307	–0.109	–0.203	–0.304	–0.105
Median	0.170	0.116	0.304	–0.163	–0.194	–0.023	–0.184	–0.241	–0.078	–0.169	–0.236	–0.071
5th percentile	–1.117	–1.410	–1.068	–1.561	–1.794	–1.340	–1.499	–1.862	–1.376	–1.464	–1.830	–1.379
10th percentile	–0.809	–1.048	–0.710	–1.191	–1.390	–1.016	–1.207	–1.436	–1.051	–1.152	–1.424	–1.016
25th percentile	–0.326	–0.434	–0.183	–0.672	–0.743	–0.534	–0.671	–0.783	–0.567	–0.658	–0.787	–0.546
75th percentile	0.628	0.637	0.761	0.302	0.299	0.428	0.264	0.254	0.388	0.249	0.252	0.372
90th percentile	1.043	1.056	1.181	0.729	0.719	0.826	0.663	0.665	0.758	0.696	0.669	0.762
95th percentile	1.290	1.332	1.429	0.969	0.953	1.039	0.936	0.905	1.010	0.971	0.923	0.995
Std deviation	0.730	0.822	0.753	0.749	0.819	0.730	0.740	0.827	0.737	0.728	0.832	0.726
Variance	0.533	0.676	0.567	0.561	0.670	0.533	0.547	0.685	0.544	0.531	0.692	0.527
Max value	2.551	3.024	3.244	2.302	2.754	2.582	2.339	2.276	2.548	2.353	2.558	2.594
Min value	–2.303	–3.585	–2.822	–2.974	–3.267	–3.106	–2.937	–3.671	–2.792	–2.612	–3.296	–2.786
Fraction OK	0.244	0.693	0.442	0.265	0.726	0.490	0.269	0.768	0.483	0.241	0.694	0.432

Table C-8. Summary statistics for path-length in the EDZ for the reference case of the amalgamated repository-scale and regional-scale DFN model. At each of the times 6,000 BC, 2,000 BC, 2,020 AD, and 6,000 AD, three paths Q1, Q2, and Q3 were tracked for each of 7,483 release locations in the amalgamated model.

Log10(LEDZ) [m]	6,000 BC			2,000 BC			2,020 AD			6,000 AD		
	Q1	Q2	Q3	Q1	Q2	Q3	Q1	Q2	Q3	Q1	Q2	Q3
Mean	1.204	1.124	1.243	1.254	1.194	1.320	1.285	1.192	1.336	1.316	1.192	1.351
Median	1.257	1.177	1.303	1.300	1.243	1.361	1.331	1.256	1.378	1.365	1.257	1.395
5th percentile	0.298	0.048	0.302	0.274	0.053	0.349	0.376	0.048	0.423	0.425	0.043	0.433
10th percentile	0.544	0.338	0.546	0.542	0.354	0.604	0.601	0.333	0.663	0.673	0.325	0.700
25th percentile	0.875	0.803	0.899	0.913	0.829	0.978	0.942	0.828	0.995	1.022	0.830	1.023
75th percentile	1.564	1.526	1.608	1.627	1.617	1.703	1.641	1.621	1.704	1.662	1.619	1.723
90th percentile	1.788	1.783	1.851	1.911	1.907	1.983	1.896	1.890	1.964	1.907	1.901	1.977
95th percentile	1.920	1.907	1.983	2.068	2.056	2.127	2.078	2.038	2.110	2.061	2.045	2.113
Std deviation	0.487	0.538	0.505	0.528	0.575	0.530	0.510	0.574	0.509	0.492	0.578	0.508
Variance	0.237	0.290	0.255	0.278	0.330	0.281	0.260	0.329	0.259	0.242	0.335	0.258
Max value	2.310	2.552	2.351	2.428	2.566	2.485	2.471	2.595	2.527	2.491	2.516	2.475
Min value	–0.492	–0.968	–0.528	–0.691	–0.828	–0.691	–0.828	–0.892	–0.547	–0.746	–0.900	–0.231
Fraction OK	0.244	0.693	0.442	0.265	0.726	0.490	0.269	0.768	0.483	0.241	0.694	0.432

C.2 Variant case: Transport aperture

Table C-9. Summary statistics for travel-time and for initial Darcy velocity in the rock for the cubic-law aperture variant case of the amalgamated repository-scale and regional-scale DFN models. For release time 2,020 AD, three paths Q1, Q2, and Q3 were tracked for each of 7,483 release locations in the amalgamated model.

	Log10(tr) [yrs] 2,020 AD			Log10(Ur) [m/y] 2,020 AD		
	Q1	Q3	Q3	Q1	Q2	Q3
Mean	1.563	1.471	1.493	–3.670	–3.482	–4.061
Median	1.550	1.468	1.490	–3.608	–3.396	–3.965
5th percentile	0.566	0.517	0.529	–5.757	–4.724	–6.070
10th percentile	0.716	0.646	0.678	–5.358	–4.250	–5.487
25th percentile	1.060	0.989	1.020	–4.522	–3.782	–4.652
75th percentile	2.057	1.874	1.893	–2.892	–3.055	–3.438
90th percentile	2.369	2.270	2.284	–2.151	–2.786	–2.910
95th percentile	2.602	2.523	2.538	–1.581	–2.647	–2.400
Std deviation	0.682	0.653	0.648	1.302	0.641	1.130
Variance	0.466	0.426	0.420	1.696	0.411	1.277
Max value	7.886	8.191	7.886	1.937	–1.396	0.470
Min value	–0.288	–0.363	–0.284	–8.508	–6.779	–10.193
Fraction OK	0.527	0.764	0.805	0.664	0.945	1.000

Table C-10. Summary statistics for path-length and F-factor in the rock for the cubic-law aperture variant case of the amalgamated repository-scale and regional-scale DFN models. For release time 2,020 AD, three paths Q1, Q2, and Q3 were tracked for each of 7,483 release locations in the amalgamated model.

	Log10(Lr) [m] 2,020 AD			Log10(Fr) [y/m] 2,020 AD		
	Q1	Q3	Q3	Q1	Q2	Q3
Mean	3.172	3.181	3.184	5.652	5.461	5.547
Median	3.124	3.128	3.134	5.715	5.547	5.603
5th percentile	2.926	2.919	2.919	3.886	3.734	3.890
10th percentile	2.973	2.969	2.967	4.458	4.309	4.420
25th percentile	3.041	3.043	3.044	5.113	4.953	5.069
75th percentile	3.277	3.298	3.299	6.241	6.038	6.105
90th percentile	3.468	3.492	3.492	6.811	6.528	6.588
95th percentile	3.543	3.561	3.564	7.128	6.784	6.900
Std deviation	0.190	0.200	0.201	0.967	0.915	0.909
Variance	0.036	0.040	0.040	0.935	0.838	0.826
Max value	4.084	4.218	4.079	9.356	9.283	9.868
Min value	2.781	2.750	2.763	2.207	2.387	2.233
Fraction OK	0.527	0.764	0.805	0.527	0.764	0.805

Table C-11. Summary statistics for travel-time and path-length in the tunnel for the cubic-law aperture variant case of the amalgamated repository-scale and regional-scale DFN models. For release time 2,020 AD, three paths Q1, Q2, and Q3 were tracked for each of 7,483 release locations in the amalgamated model.

	Log10(tT) [yrs] 2,020 AD			Log10(LT) [m] 2,020 AD		
	Q1	Q3	Q3	Q1	Q2	Q3
Mean	5.154	4.966	5.454	1.043	0.964	1.149
Median	5.291	5.119	5.440	1.069	0.984	1.119
5th percentile	3.233	3.070	4.307	0.125	0.017	0.530
10th percentile	3.678	3.447	4.544	0.370	0.236	0.669
25th percentile	4.517	4.237	4.960	0.753	0.612	0.874
75th percentile	5.908	5.759	5.932	1.380	1.337	1.408
90th percentile	6.396	6.245	6.373	1.671	1.627	1.680
95th percentile	6.650	6.488	6.652	1.849	1.811	1.844
Std deviation	1.067	1.071	0.711	0.506	0.539	0.394
Variance	1.138	1.147	0.505	0.256	0.291	0.155
Max value	8.162	7.782	8.299	2.797	2.812	2.833
Min value	–1.071	1.462	3.351	–0.853	–1.072	0.115
Fraction OK	0.372	0.634	0.805	0.372	0.634	0.805

Table C-12. Summary statistics for travel-time and path-length in the EDZ for the cubic-law aperture variant case of the amalgamated repository-scale and regional-scale DFN models. For release time 2,020 AD, three paths Q1, Q2, and Q3 were tracked for each of 7,483 release locations in the amalgamated model.

	Log10(tEDZ) [yrs] 2,020 AD			Log10(LEDZ) [m] 2,020 AD		
	Q1	Q3	Q3	Q1	Q2	Q3
Mean	–0.220	–0.309	–0.102	1.287	1.189	1.339
Median	–0.183	–0.239	–0.079	1.331	1.254	1.382
5th percentile	–1.482	–1.848	–1.357	0.386	0.048	0.445
10th percentile	–1.181	–1.431	–1.047	0.599	0.325	0.669
25th percentile	–0.673	–0.795	–0.558	0.945	0.828	0.998
75th percentile	0.258	0.252	0.390	1.639	1.616	1.708
90th percentile	0.661	0.668	0.760	1.893	1.887	1.965
95th percentile	0.933	0.907	1.014	2.068	2.033	2.110
Std deviation	0.729	0.829	0.736	0.508	0.572	0.507
Variance	0.531	0.688	0.542	0.258	0.327	0.258
Max value	2.339	2.276	2.715	2.471	2.595	2.527
Min value	–2.937	–3.671	–3.225	–0.828	–0.892	–0.547
Fraction OK	0.270	0.764	0.481	0.270	0.764	0.481

C.3 Variant case: Enhanced EDZ

Table C-13. Summary statistics for travel-time and initial Darcy velocity in the rock for the enhanced EDZ variant case of the amalgamated repository-scale and regional-scale DFN models. For release time 2,020 AD, three paths Q1, Q2, and Q3 were tracked for each of 7,483 release locations in the amalgamated model.

	Log10(tr) [yrs] 2,020 AD			Log10(Ur) [m/y] 2,020 AD		
	Q1	Q3	Q3	Q1	Q2	Q3
Mean	1.718	1.611	1.656	–3.605	–2.740	–3.747
Median	1.707	1.623	1.651	–3.550	–2.599	–3.536
5th percentile	0.720	0.596	0.664	–5.731	–4.287	–6.164
10th percentile	0.889	0.764	0.833	–5.318	–3.619	–5.558
25th percentile	1.277	1.152	1.226	–4.502	–3.025	–4.579
75th percentile	2.147	2.034	2.080	–2.774	–2.269	–2.789
90th percentile	2.506	2.387	2.426	–2.087	–1.989	–2.347
95th percentile	2.716	2.624	2.666	–1.559	–1.834	–2.038
Std deviation	0.645	0.637	0.633	1.311	0.751	1.319
Variance	0.415	0.405	0.400	1.719	0.564	1.740
Max value	6.739	6.405	6.398	1.937	0.091	0.715
Min value	–0.058	–0.156	–0.124	–8.256	–6.467	–10.053
Fraction OK	0.529	0.784	0.799	0.664	0.961	1.000

Table C-14. Summary statistics for path-length and F-factor in the rock for the enhanced EDZ variant case of the amalgamated repository-scale and regional-scale DFN models. For release time 2,020 AD, three paths Q1, Q2, and Q3 were tracked for each of 7,483 release locations in the amalgamated model.

	Log10(Lr) [m] 2,020 AD			Log10(Fr) [y/m] 2,020 AD		
	Q1	Q3	Q3	Q1	Q2	Q3
Mean	3.165	3.167	3.172	5.575	5.281	5.415
Median	3.117	3.115	3.118	5.592	5.336	5.460
5th percentile	2.922	2.914	2.924	3.904	3.453	3.661
10th percentile	2.966	2.963	2.964	4.396	4.027	4.234
25th percentile	3.035	3.032	3.033	5.007	4.743	4.873
75th percentile	3.264	3.272	3.281	6.171	5.866	5.972
90th percentile	3.464	3.481	3.486	6.755	6.437	6.553
95th percentile	3.533	3.550	3.554	7.123	6.820	6.951
Std deviation	0.189	0.195	0.199	0.960	0.974	0.963
Variance	0.036	0.038	0.039	0.922	0.949	0.928
Max value	4.312	4.181	4.312	9.683	9.458	9.265
Min value	2.797	2.754	2.767	2.224	2.287	2.277
Fraction OK	0.529	0.784	0.799	0.529	0.784	0.799

Table C-15. Summary statistics for travel-time and path-length in the tunnel for the enhanced EDZ variant case of the amalgamated repository-scale and regional-scale DFN models. For release time 2,020 AD, three paths Q1, Q2, and Q3 were tracked for each of 7,483 release locations in the amalgamated model.

	Log10(tT) [yrs] 2,020 AD			Log10(LT) [m] 2,020 AD		
	Q1	Q3	Q3	Q1	Q2	Q3
Mean	5.184	5.036	5.480	1.046	0.984	1.137
Median	5.333	5.160	5.458	1.086	1.019	1.110
5th percentile	3.272	3.212	4.371	0.131	0.021	0.506
10th percentile	3.706	3.580	4.592	0.368	0.217	0.646
25th percentile	4.568	4.366	4.976	0.754	0.629	0.875
75th percentile	5.919	5.773	5.959	1.373	1.355	1.391
90th percentile	6.363	6.267	6.413	1.651	1.677	1.675
95th percentile	6.632	6.586	6.679	1.833	1.845	1.817
Std deviation	1.038	1.035	0.710	0.511	0.554	0.392
Variance	1.077	1.072	0.504	0.261	0.307	0.154
Max value	7.761	8.007	8.173	2.809	2.842	2.563
Min value	–0.508	1.634	3.347	–1.047	–0.919	0.132
Fraction OK	0.382	0.633	0.799	0.382	0.633	0.799

Table C-16. Summary statistics for travel-time and path-length in the EDZ for the enhanced EDZ variant case of the amalgamated repository-scale and regional-scale DFN models. For release time 2,020 AD, three paths Q1, Q2, and Q3 were tracked for each of 7,483 release locations in the amalgamated model.

	Log10(tEDZ) [yrs] 2,020 AD			Log10(LEDZ) [m] 2,020 AD		
	Q1	Q3	Q3	Q1	Q2	Q3
Mean	–0.839	–0.878	–0.731	1.481	1.403	1.533
Median	–0.811	–0.810	–0.703	1.544	1.476	1.592
5th percentile	–2.149	–2.391	–1.975	0.533	0.182	0.617
10th percentile	–1.741	–1.921	–1.636	0.806	0.581	0.835
25th percentile	–1.289	–1.359	–1.161	1.169	1.061	1.227
75th percentile	–0.351	–0.345	–0.255	1.858	1.834	1.901
90th percentile	0.042	0.069	0.125	2.101	2.098	2.153
95th percentile	0.303	0.340	0.370	2.228	2.235	2.264
Std deviation	0.753	0.825	0.752	0.520	0.587	0.510
Variance	0.566	0.680	0.565	0.270	0.345	0.260
Max value	1.977	2.425	2.432	2.625	2.658	2.635
Min value	–4.065	–4.106	–4.116	–1.211	–0.690	–0.587
Fraction OK	0.310	0.784	0.519	0.310	0.784	0.519

C.4 Variant case: Enhanced tunnel backfill

Table C-17. Summary statistics for travel-time and for initial Darcy velocity in the rock for the degraded tunnel backfill variant case of the amalgamated repository-scale and regional-scale DFN models. For release time 2,020 AD, three paths Q1, Q2, and Q3 were tracked for each of 7,483 release locations in the amalgamated model.

	Log10(tr) [yrs] 2,020 AD			Log10(Ur) [m/y] 2,020 AD		
	Q1	Q3	Q3	Q1	Q2	Q3
Mean	1.670	1.608	1.577	–3.546	–3.446	–3.616
Median	1.664	1.608	1.581	–3.490	–3.346	–3.580
5th percentile	0.694	0.630	0.636	–5.601	–4.586	–5.658
10th percentile	0.850	0.789	0.786	–5.179	–4.224	–5.088
25th percentile	1.221	1.140	1.128	–4.429	–3.734	–4.227
75th percentile	2.123	2.024	1.973	–2.726	–3.030	–2.990
90th percentile	2.436	2.366	2.318	–2.054	–2.813	–2.354
95th percentile	2.674	2.625	2.580	–1.554	–2.681	–1.773
Std deviation	0.627	0.631	0.614	1.277	0.601	1.171
Variance	0.393	0.398	0.378	1.630	0.361	1.371
Max value	4.428	5.628	6.325	1.938	–1.773	1.137
Min value	0.008	0.001	–0.189	–7.778	–6.291	–9.573
Fraction OK	0.527	0.747	0.820	0.658	0.922	1.000

Table C-18. Summary statistics for path-length and F-factor in the rock for the degraded tunnel backfill variant case of the amalgamated repository-scale and regional-scale DFN models. For release time 2,020 AD, three paths Q1, Q2, and Q3 were tracked for each of 7,483 release locations in the amalgamated model.

	Log10(Lr) [m] 2,020 AD			Log10(Fr) [y/m] 2,020 AD		
	Q1	Q3	Q3	Q1	Q2	Q3
Mean	3.158	3.167	3.168	5.459	5.249	5.234
Median	3.112	3.116	3.118	5.487	5.278	5.272
5th percentile	2.919	2.917	2.914	3.833	3.697	3.646
10th percentile	2.958	2.963	2.965	4.356	4.139	4.080
25th percentile	3.035	3.034	3.035	4.965	4.744	4.733
75th percentile	3.249	3.270	3.275	6.022	5.776	5.764
90th percentile	3.453	3.480	3.478	6.541	6.284	6.305
95th percentile	3.524	3.552	3.552	6.885	6.652	6.651
Std deviation	0.184	0.194	0.192	0.903	0.892	0.904
Variance	0.034	0.038	0.037	0.815	0.795	0.817
Max value	4.131	4.245	4.183	8.691	9.925	9.925
Min value	2.778	2.754	2.772	2.112	2.264	2.357
Fraction OK	0.527	0.747	0.820	0.527	0.747	0.820

Table C-19. Summary statistics for travel-time and path-length in the tunnel for the degraded tunnel backfill variant case of the amalgamated repository-scale and regional-scale DFN models. For release time 2,020 AD, three paths Q1, Q2, and Q3 were tracked for each of 7,483 release locations in the amalgamated model.

	Log10(tT) [yrs] 2,020 AD			Log10(LT) [m] 2,020 AD		
	Q1	Q3	Q3	Q1	Q2	Q3
Mean	4.892	4.970	4.527	1.356	1.316	1.464
Median	4.987	5.222	4.333	1.390	1.357	1.475
5th percentile	2.903	2.636	2.890	0.373	0.225	0.643
10th percentile	3.420	3.469	3.158	0.624	0.492	0.803
25th percentile	4.088	4.236	3.701	0.998	0.928	1.109
75th percentile	5.824	5.879	5.433	1.759	1.768	1.821
90th percentile	6.357	6.327	6.145	2.040	2.067	2.097
95th percentile	6.652	6.582	6.454	2.170	2.216	2.234
Std deviation	1.223	1.261	1.120	0.555	0.601	0.487
Variance	1.494	1.589	1.253	0.309	0.361	0.237
Max value	8.176	8.008	8.602	2.867	3.099	3.029
Min value	–0.140	–0.364	1.633	–0.694	–0.737	0.165
Fraction OK	0.400	0.630	0.820	0.400	0.630	0.820

Table C-20. Summary statistics for travel-time and for path-length in the EDZ for the degraded tunnel backfill variant case of the amalgamated repository-scale and regional-scale DFN models. For release time 2,020 AD, three paths Q1, Q2, and Q3 were tracked for each of 7,483 release locations in the amalgamated model.

	Log10(tEDZ) [yrs] 2,020 AD			Log10(LEDZ) [m] 2,020 AD		
	Q1	Q3	Q3	Q1	Q2	Q3
Mean	–0.328	–0.344	–0.335	1.225	1.185	1.147
Median	–0.289	–0.300	–0.273	1.264	1.246	1.184
5th percentile	–1.559	–1.675	–1.695	0.368	0.179	0.188
10th percentile	–1.239	–1.311	–1.357	0.607	0.454	0.382
25th percentile	–0.754	–0.785	–0.833	0.870	0.825	0.771
75th percentile	0.130	0.144	0.177	1.589	1.571	1.562
90th percentile	0.542	0.534	0.548	1.835	1.832	1.831
95th percentile	0.766	0.761	0.838	1.968	1.965	1.961
Std deviation	0.710	0.745	0.773	0.487	0.531	0.553
Variance	0.504	0.555	0.598	0.237	0.282	0.306
Max value	1.847	2.216	3.233	2.452	2.609	2.787
Min value	–3.359	–3.281	–2.970	–0.690	–1.097	–1.149
Fraction OK	0.265	0.747	0.383	0.265	0.747	0.383

C.5 Variant case: Anisotropy

Table C-21. Summary statistics for travel-time and initial Darcy velocity in the rock for the anisotropy variant case of the amalgamated repository-scale and regional-scale DFN models. For release time 2,020 AD, three paths Q1, Q2, and Q3 were tracked for each of 7,483 release locations in the amalgamated model.

	Log10(tr) [yrs] 2,020 AD			Log10(Ur) [m] 2,020 AD		
	Q1	Q3	Q3	Q1	Q2	Q3
Mean	1.700	1.616	1.653	–3.512	–3.409	–3.949
Median	1.688	1.631	1.657	–3.448	–3.326	–3.868
5th percentile	0.643	0.554	0.601	–5.729	–4.678	–5.930
10th percentile	0.839	0.770	0.814	–5.260	–4.193	–5.417
25th percentile	1.280	1.221	1.249	–4.406	–3.696	–4.572
75th percentile	2.112	2.013	2.045	–2.684	–2.984	–3.318
90th percentile	2.451	2.344	2.389	–1.935	–2.715	–2.776
95th percentile	2.699	2.545	2.600	–1.329	–2.549	–2.107
Std deviation	0.683	0.643	0.656	1.350	0.645	1.168
Variance	0.466	0.414	0.430	1.823	0.416	1.363
Max value	7.223	7.605	6.898	2.001	–1.281	0.616
Min value	–0.371	–0.300	–0.249	–8.323	–6.653	–9.206
Fraction OK	0.502	0.734	0.769	0.664	0.943	1.000

Table C-22. Summary statistics for path-length and F-factor in the rock for the anisotropy variant case of the amalgamated repository-scale and regional-scale DFN models. For release time 2,020 AD, three paths Q1, Q2, and Q3 were tracked for each of 7,483 release locations in the amalgamated model.

	Log10(Lr) [m] 2,020 AD			Log10(Fr) [y/m] 2,020 AD		
	Q1	Q3	Q3	Q1	Q2	Q3
Mean	3.183	3.193	3.197	5.500	5.308	5.398
Median	3.137	3.150	3.148	5.549	5.380	5.438
5th percentile	2.919	2.913	2.918	3.786	3.588	3.755
10th percentile	2.964	2.964	2.963	4.330	4.104	4.262
25th percentile	3.044	3.047	3.047	4.944	4.803	4.892
75th percentile	3.282	3.300	3.307	6.102	5.882	5.963
90th percentile	3.472	3.503	3.516	6.664	6.375	6.476
95th percentile	3.569	3.590	3.612	7.006	6.678	6.834
Std deviation	0.208	0.215	0.223	0.970	0.929	0.930
Variance	0.043	0.046	0.050	0.942	0.862	0.866
Max value	4.270	4.192	4.326	8.988	9.221	9.094
Min value	2.800	2.770	2.773	2.043	2.139	2.334
Fraction OK	0.502	0.734	0.769	0.502	0.734	0.769

Table C-23. Summary statistics for travel-time and path-length in the tunnel for the anisotropy variant case of the amalgamated repository-scale and regional-scale DFN models. For release time 2,020 AD, three paths Q1, Q2, and Q3 were tracked for each of 7,483 release locations in the amalgamated model.

	Log10(tT) [yrs] 2,020 AD			Log10(LT) [m] 2,020 AD		
	Q1	Q3	Q3	Q1	Q2	Q3
Mean	5.106	4.890	5.389	1.050	0.963	1.142
Median	5.261	5.024	5.365	1.088	0.990	1.118
5th percentile	3.170	2.963	4.302	0.133	0.027	0.543
10th percentile	3.633	3.383	4.520	0.395	0.225	0.673
25th percentile	4.489	4.128	4.899	0.756	0.623	0.887
75th percentile	5.829	5.679	5.853	1.385	1.340	1.383
90th percentile	6.344	6.167	6.296	1.655	1.639	1.651
95th percentile	6.600	6.440	6.562	1.812	1.811	1.801
Std deviation	1.059	1.069	0.692	0.508	0.543	0.382
Variance	1.122	1.144	0.479	0.258	0.295	0.146
Max value	8.330	8.484	8.376	2.948	2.959	3.408
Min value	–0.350	1.542	3.286	–0.856	–0.976	0.147
Fraction OK	0.346	0.605	0.769	0.346	0.605	0.769

Table C-24. Summary statistics for travel-time and path-length in the EDZ for the anisotropy variant case of the amalgamated repository-scale and regional-scale DFN models. For release time 2,020 AD, three paths Q1, Q2, and Q3 were tracked for each of 7,483 release locations in the amalgamated model.

	Log10(tEDZ) [yrs] 2,020 AD			Log10(LEDZ) [m] 2,020 AD		
	Q1	Q3	Q3	Q1	Q2	Q3
Mean	–0.336	–0.406	–0.202	1.236	1.133	1.273
Median	–0.323	–0.336	–0.174	1.294	1.180	1.305
5th percentile	–1.603	–1.951	–1.438	0.304	0.044	0.390
10th percentile	–1.266	–1.527	–1.127	0.581	0.303	0.616
25th percentile	–0.818	–0.913	–0.671	0.920	0.798	0.933
75th percentile	0.161	0.167	0.283	1.582	1.541	1.640
90th percentile	0.596	0.568	0.696	1.846	1.826	1.891
95th percentile	0.833	0.798	0.923	1.989	1.979	2.034
Std deviation	0.757	0.827	0.732	0.498	0.559	0.501
Variance	0.573	0.684	0.536	0.248	0.313	0.251
Max value	2.943	2.524	2.589	2.785	2.508	2.524
Min value	–2.897	–3.270	–2.801	–1.211	–0.968	–1.211
Fraction OK	0.244	0.734	0.440	0.244	0.734	0.440

C.6 Variant case: Correlated transmissivity model

Table C-25. Summary statistics for travel-time and initial Darcy velocity in the rock for the correlated transmissivity model variant case of the amalgamated repository-scale and regional-scale DFN models. For release time 2,020 AD, three paths Q1, Q2, and Q3 were tracked for each of 7,483 release locations in the amalgamated model.

	Log10(tr) [yrs] 2,020 AD			Log10(Ur) [m/y] 2,020 AD		
	Q1	Q3	Q3	Q1	Q2	Q3
Mean	1.735	1.649	1.667	–3.696	–3.463	–4.054
Median	1.708	1.636	1.645	–3.681	–3.375	–3.971
5th percentile	0.755	0.666	0.679	–5.819	–4.713	–5.978
10th percentile	0.915	0.813	0.846	–5.358	–4.231	–5.467
25th percentile	1.261	1.149	1.198	–4.554	–3.753	–4.686
75th percentile	2.154	2.093	2.095	–2.906	–3.045	–3.411
90th percentile	2.509	2.433	2.450	–2.169	–2.779	–2.911
95th percentile	2.763	2.706	2.721	–1.591	–2.593	–2.334
Std deviation	0.668	0.673	0.661	1.305	0.656	1.132
Variance	0.446	0.453	0.437	1.703	0.431	1.282
Max value	8.101	6.188	7.796	0.776	–1.391	0.900
Min value	0.052	0.144	0.061	–8.641	–7.281	–9.589
Fraction OK	0.554	0.796	0.831	0.672	0.941	0.976

Table C-26. Summary statistics for path-length and F-factor in the rock for the correlated transmissivity model variant case of the amalgamated repository-scale and regional-scale DFN models. For release time 2,020 AD, three paths Q1, Q2, and Q3 were tracked for each of 7,483 release locations in the amalgamated model.

	Log10(Lr) [m] 2,020 AD			Log10(Fr) [y/m] 2,020 AD		
	Q1	Q3	Q3	Q1	Q2	Q3
Mean	3.160	3.161	3.160	5.673	5.505	5.583
Median	3.121	3.119	3.118	5.722	5.601	5.668
5th percentile	2.918	2.916	2.917	4.017	3.804	3.961
10th percentile	2.964	2.963	2.961	4.568	4.327	4.485
25th percentile	3.037	3.035	3.036	5.163	4.990	5.090
75th percentile	3.264	3.267	3.264	6.238	6.099	6.139
90th percentile	3.431	3.428	3.421	6.748	6.567	6.599
95th percentile	3.500	3.502	3.501	7.090	6.885	6.949
Std deviation	0.180	0.185	0.184	0.914	0.919	0.892
Variance	0.032	0.034	0.034	0.836	0.845	0.795
Max value	4.148	4.200	4.166	9.489	8.853	9.018
Min value	2.748	2.758	2.745	2.368	2.267	2.329
Fraction OK	0.554	0.796	0.831	0.554	0.796	0.831

Table C-27. Summary statistics for travel-time and path-length in the tunnel for the correlated transmissivity model variant case of the amalgamated repository-scale and regional-scale DFN models. For release time 2,020 AD, three paths Q1, Q2, and Q3 were tracked for each of 7,483 release locations in the amalgamated model.

	Log10(tT) [yrs] 2,020 AD			Log10(LT) [m] 2,020 AD		
	Q1	Q3	Q3	Q1	Q2	Q3
Mean	5.106	4.943	5.433	1.020	0.940	1.127
Median	5.243	5.100	5.413	1.047	0.958	1.100
5th percentile	3.185	3.059	4.341	0.095	0.015	0.496
10th percentile	3.636	3.411	4.569	0.357	0.219	0.637
25th percentile	4.467	4.192	4.924	0.726	0.596	0.862
75th percentile	5.858	5.709	5.899	1.339	1.295	1.380
90th percentile	6.297	6.197	6.313	1.628	1.612	1.653
95th percentile	6.557	6.480	6.615	1.798	1.794	1.813
Std deviation	1.037	1.065	0.702	0.501	0.533	0.392
Variance	1.074	1.134	0.492	0.251	0.284	0.154
Max value	8.722	9.414	9.181	2.979	3.034	2.765
Min value	–0.741	1.250	3.012	–0.864	–0.754	0.111
Fraction OK	0.381	0.653	0.831	0.381	0.653	0.831

Table C-28. Summary statistics for travel-time and path-length in the EDZ for the correlated transmissivity model variant case of the amalgamated repository-scale and regional-scale DFN models. For time 2,020 AD, three paths Q1, Q2, and Q3 were tracked for each of 7,483 release locations in the amalgamated model.

	Log10(tEDZ) [yrs] 2,020 AD			Log10(LEDZ) [m] 2,020 AD		
	Q1	Q3	Q3	Q1	Q2	Q3
Mean	–0.241	–0.292	–0.103	1.305	1.209	1.339
Median	–0.202	–0.212	–0.059	1.352	1.257	1.384
5th percentile	–1.541	–1.821	–1.419	0.390	0.080	0.412
10th percentile	–1.225	–1.408	–1.064	0.600	0.393	0.667
25th percentile	–0.734	–0.778	–0.593	0.958	0.843	1.004
75th percentile	0.266	0.262	0.381	1.666	1.624	1.710
90th percentile	0.657	0.679	0.788	1.957	1.914	1.982
95th percentile	0.943	0.947	1.072	2.106	2.066	2.120
Std deviation	0.763	0.838	0.770	0.522	0.570	0.518
Variance	0.582	0.703	0.593	0.273	0.325	0.268
Max value	3.442	4.268	4.022	2.569	2.689	2.669
Min value	–3.382	–3.489	–2.870	–0.603	–0.885	–0.603
Fraction OK	0.278	0.796	0.490	0.279	0.794	0.489

Appendix D

Modifications to equivalent flow-rates for spalling and advective flow in the tunnels

Two effects that may potentially lead to higher equivalent flow-rates (*Qeq*) arise from mechanical effects of spalling in deposition holes induced by the waste heat, and advective flow within the tunnel backfill. The effects of spalling change conditions for mass exchange between the buffer and the fractures intersecting the deposition hole, in the form of an altered Q_{eq} for the Q1 path. Advective flow in the tunnels enhances the outflow to the Q3 path, such that *Qeq* is calculated as a sum of a term representing diffusive flux from the tunnel back fill into a fracture intersecting the tunnel, as well as the advective flux through and out of the tunnel. The methods used to quantify these two effects are given in the following sections.

D.1 Effects on flow and transport due to spalling

This section summarises the definitions and data used for the calculations of the increase in water flow rate in the damaged zone due to spalling. Spalling occurs when the rock nearest to the surface of the deposition hole for the waste canisters is damaged due to natural stress distribution in the rock and due to stresses induced due to heating by the waste in the canister /Neretnieks 2006/.

A wedge formed region of fractured rock on both sides of the deposition hole may form. The damaged zone is envisaged to extend some 10 cm into the rock and be 15 to 20 cm wide. The zone will contain several small fractures that form a connected network for flow. The porosity and hydraulic transmissivity of the damaged zone is assumed to be higher than that of the surrounding rock. A water conducting fracture that intersects the deposition hole will also intersect the zone with the damaged rock and allow water to flow through it. Water that enters the zone from the upstream side of a fracture will spread out in the zone both upward and downward before it again leaves at the downstream side. Because the hydraulic conductivity of the damaged zone is higher than the undamaged rock it may allow more water to be drawn in from the flowing fracture. The water in the porous damaged rock will have a longer residence time in contact with the buffer and may therefore have more time to equilibrate with pore water of the backfill /Neretnieks 2006/.

The flow rate of water will increase due to the presence of the damaged zone. However, only a fraction of that water will exchange solutes with the buffer. Nevertheless, the equivalent flow rate Q_{eqDZ} due to the presence of a damaged zone could be considerably larger than when there is no damage. Scoping calculations indicate that the increase can be on the order of up to ten times depending on the angle at which the deposition hole is intersected. For every canister position the flow rate q in the fracture that intersects the deposition hole has been determined from hydraulic calculations. To the Q_{eq} for a deposition hole without spalling should be added a Q_{eqDZ} caused by the presence of the damage /Neretnieks 2006/.

$$Q_{eq,tot} = Q_{eq} + Q_{eqDZ}$$

Q_{eqDZ} is defined slightly different depending on what type of hydrogeological model, CPM or DFN, that was used, see below. A more detailed description of the spalling phenomenon is presented in /Neretnieks 2006/.

CPM model

For a CPM model Q_{eqDZ} is defined as,

$$Q_{eqDZ} = 1.13\sqrt{\frac{D_p \cdot q \cdot W_{zone} \cdot L_{zone} \cdot \varepsilon_{zone}}{d_{zone}}}$$

where all parameter values and definitions are given in Table D-1 except for the flow rate q which is calculated from

$q = U_{r0} \times A$

where U_{r0} is the Darcy velocity and A the capture area. The Darcy velocity, and hence q, is determined from hydraulic calculations.

DFN model

For a DFN model Q_{eqDZ} is defined as,

$$Q_{eqDZ} = 1.13\sqrt{\frac{D_p \cdot q \cdot W_{zone} \cdot L_{zone} \cdot \varepsilon_{zone} \cdot f}{d_{zone}}}$$

where all parameter values and definitions are given in Table D-1 except for the flowrate q which is calculated from

$q = U_{r1} \times w_c \times \min[2L_{zone}, L_{fracture}]$

where $L_{fracture}$ is the length of the fracture intersecting the spalled zone. The minimum value of $2 \cdot L_{zone}$ and $L_{fracture}$ is used. $L_{fracture}$ is obtained from the hydrogeological model used for the calculations. U_{r1} is the Darcy velocity for path Q1 and is determined from hydraulic calculations.

Figure D-1 present the cumulative distribution function of Q_{eq1} at 2,020 AD with and without spalling included for the reference case in L 1.2.

Table D-1. Definitions and data as used in the spalling calculations /Neretnieks 2006/.

Entity	Description	Value	Unit
QeqDZ	Equivalent flow rate in zone	–	m^3/s
q	Flow rate	–	m^3/s
Dp	Pore diffusion coefficient	10^{-10}	m^2/s
Wzone	Width of damaged zone	0.2	m
Lzone	Length of damaged zone	8	m
εzone	Porosity of damaged zone	0.01	–
dzone	Thickness of damaged zone	0.1	m
f	Fraction of zone where water effectively flows	0.5	–
Ur0	Darcy velocity in a CPM model	Determined from hydraulic calculations	m/s
Ur1	Darcy velocity in a DFN model	Determined from hydraulic calculations	m/s
A	Capture area	12.8	m^2
wc	Canister height	5	m
Lfracture	Length of the fracture intersecting the spalled zone		m

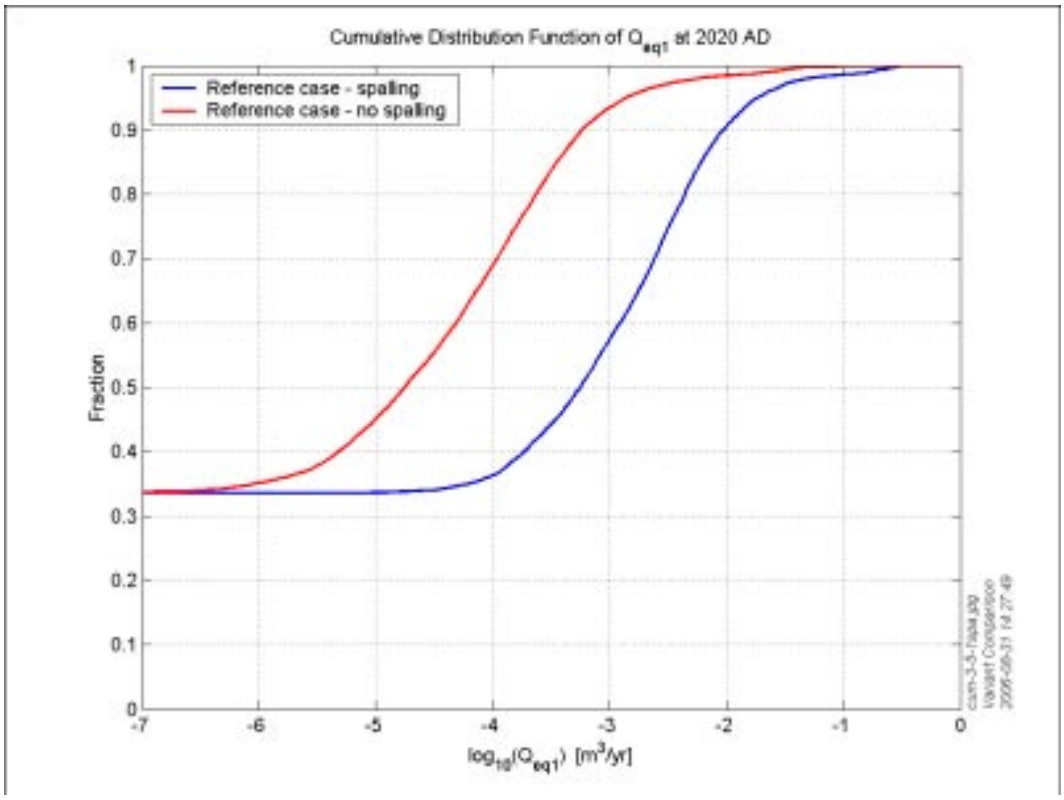

Figure D-1. *Cumulative distribution function of Qeq1 at 2,020 AD with and without spalling included for the reference case of the amalgamated repository-scale and regional-scale DFN model.*

D.2 Additional advective component to Q_{eq3}

This section summarises the definitions and data used for calculating the additional advective component to Q_{eq3} that arises when flow is present in the backfill of the tunnel.

Path Q3 considers the release of radionuclides into a fracture that intersects the tunnel. It is assumed that diffusive equilibrium of radionuclides is achieved in the tunnel backfill and advection takes place into fractures surrounding the tunnel. Hence, an equivalent flow-rate, Qeq_3, is required for advective flow in the first fracture encountered along the path after a particle is released in the tunnel backfill above the deposition hole. For a DFN model, the equivalent groundwater flow-rate, Q_{eq3} is calculated from the flow-rate in the first fracture the particle enters after leaving the tunnel. The equation for calculating Q_{eq3} assumes no flow in the backfill. When there is flow in the backfill, an additional advective component needs to be added to Q_{eq3} given by

$$Q_{eq3,adv} = \frac{L_{tunnel-fracture}}{t_{tunnel-fracture}} \cdot \varepsilon_{tunnel} \cdot A_{tunnel}$$

$L_{tunnel\text{-}fracture}$, $t_{tunnel\text{-}fracture}$, ε_{tunnel} and A_{tunnel} are the length and advective travel time in the tunnel from the top of the deposition hole to the fracture intersecting the tunnel, the porosity of the back-filled tunnel, and the cross-sectional area of the tunnel, respectively. Parameter values and definitions are given in Table D-2. $L_{tunnel\text{-}fracture}$ and $t_{tunnel\text{-}fracture}$ are determined from hydraulic calculations /SKB 2006c/.

Table D-2. Definitions and data as used when calculating the additional advective component to Q_{eq3}. /SKB 2006c/.

Entity	Description	Value	Unit
Qeq3,adv	Equivalent flow rate, advective component	–	m^3/s
Ltunnel-fracture	Path length in the tunnel from the top of the deposition hole to the fracture intersecting the tunnel	Determined from hydraulic calculations	m
ttunnel-fracture	Advective travel time in the tunnel from the top of the deposition hole to the fracture intersecting the tunnel	Determined from hydraulic calculations	s
εtunnel	Porosity of the back-filled tunnel	0.35	–
Atunnel	Cross-sectional area of the tunnel	12.566	m^2

Figure D-2 and Figure D-3 present the cumulative distribution function of Q_{eq} for different paths at 2,020 AD for the reference case in SR-Can Laxemar v1.2. In Figure D-2, the sum of Q_{eq3} and $Q_{eq3,adv}$ is presented for path Q3. In Figure D-3, Q_{eq3} and $Q_{eq3,adv}$ are presented separately.

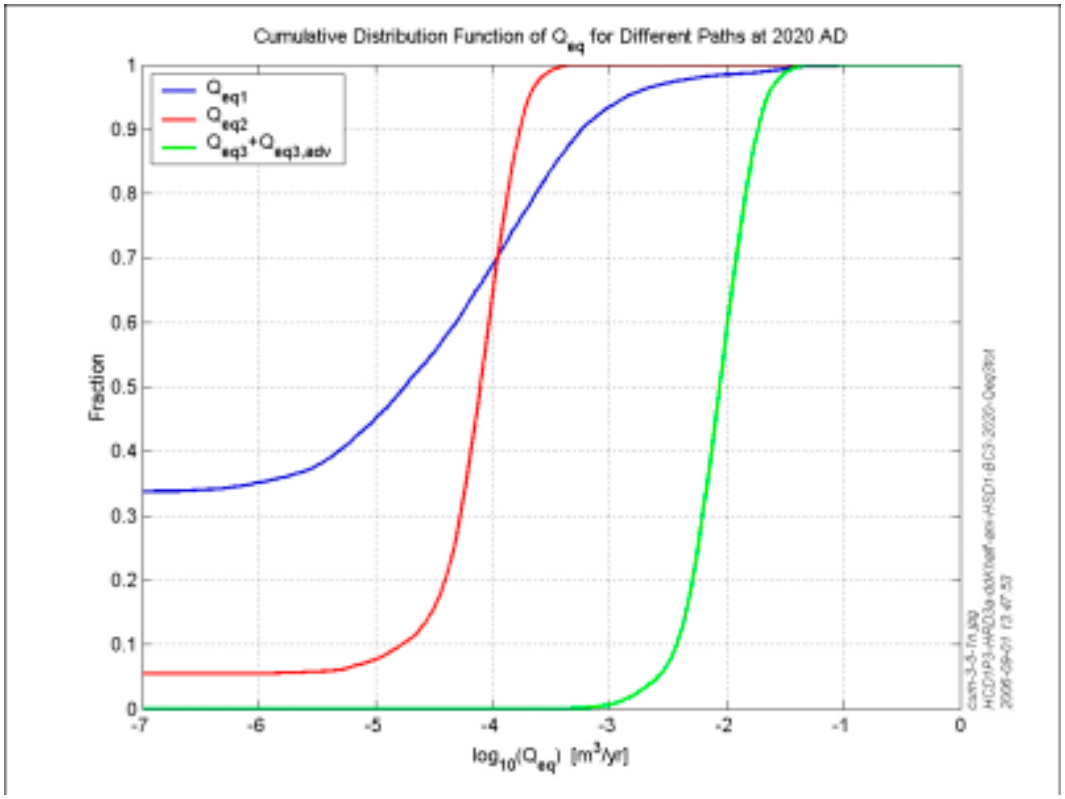

Figure D-2. *Cumulative distribution function of Q_{eq} for different paths at 2,020 AD for the reference case of the amalgamated repository-scale and regional-scale DFN model. For path Q3 the sum of Q_{eq3} and $Q_{eq3,adv}$ is presented.*

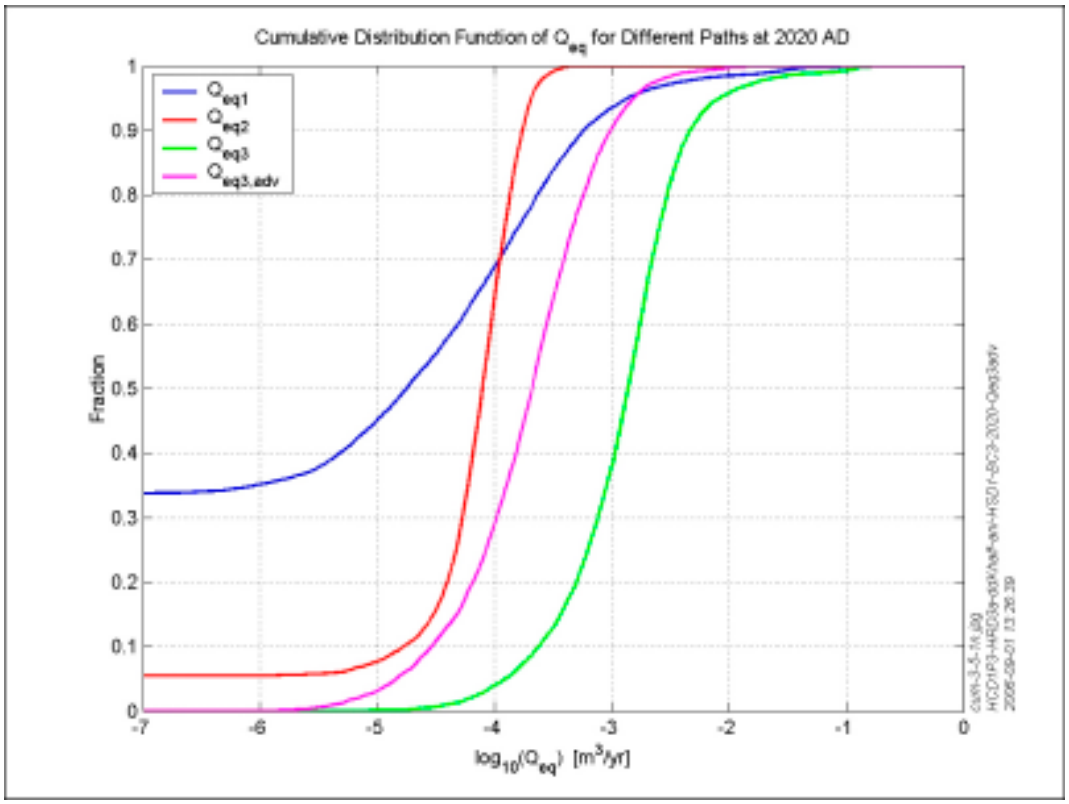

Figure D-3. *Cumulative distribution function of Q_{eq} for different paths at 2,020 AD for the reference case of the amalgamated repository-scale and regional-scale DFN model. For path Q3, Q_{eq3} and $Q_{eq3,adv}$ are presented separately.*